THE UNIVERSITY *of* EDINBURGH

Visible light response semiconductor nanomaterials for heterogeneous photocatalysis in liquid phase

Dávidné NAGY

This thesis is submitted for the degree of

Doctor of Philosophy

The University of Edinburgh

2017

”Nem a nagy sereg segíti
győzelemre a királyt,
nem a nagy erő menti meg a hőst.
Csalódik, aki lovaktól vár segítséget,
mert nagy erejük nem ment meg.
De az Ùr szeme ügyel az istenfélőkre,
akik szeretetében bíznak.
Megmenti őket a haláltól,
éhinség idején is megtartja életüket.”

Zsolt, 33, 16-19

Declaration

Hereby I declare that the work presented in the thesis has been originated, performed and written by myself. The help and contribution of others has been clearly indicated and acknowledged to the best of my knowledge. This work has not been submitted for any other degree or qualification in this or any other institution or university.

Dávidné NAGY
2017

Acknowledgements

I am thankful to my primary and co-supervisors Dr Maria-Chiara Ferrari, Dr Xianfeng Fan, Prof Neil Robertson and Dr Imre Miklós Szilágyi who guided and supported me throughout my PhD. The helpful discussions, their devoted time and motivation, the guidance and the opportunities they gave me are greatly acknowledged.

I am also thankful for the help of academics from the University of Edinburgh who provided me with access and assistance in the use of various equipments. With this regard, Dr Nicola Cayzer is acknowledged for the SEM, Dr Bart Marzec and Dr Fabio Nudelman for TEM, Prof Neil Robertson for the UV-vis diffuse reflectance and Dr Gary S. Nichol for the XRD facility. I also would like to thank the help of all collaborators, academics and students from Hungary. I would also like to thank my fellow PhD students who were always open to chat with me and help me with my questions. Special thanks goes to Gylen Odling, John Mallows, James Young, Patrick Schmidt and Ebraheam Al-Zaidi.

For the financial support, I would like to greatly acknowledge the University of Edinburgh for awarding me with the Principal Career Development Scholarship. For travel grants to symposia and conferences the Royal Society of Chemistry and the Solar Fuel Network is thanked.

Last, but certainly not least I would like to give thanks to those friends and family members who supported me at times of difficulties and rejoiced with me at times of happiness. I am thankful for their never ceasing prayers and help in all sorts of ways. I am especially thankful for Tim and Annalauren's friendship, delicious cooking and the beautiful paintings and flags made by Evangeline and Eliana. I will always be thankful to my mom and dad who supported and believed in me from the beginning. To Edit and Miklós who so often carried me in prayers. I am happy to know the support and love of our siblings and grandparents, our friends Anna, Gábor, Barni, Kinga, Márk, Dávid, Fanni, Bandi, Elisabeth, Jonathan, the Packer's, the MacMillan's, Ian, Emily, Collin and the whole Cornerstone family. And finally leaving to last the two most important friends and love of my life. I am grateful for my beloved husband, Dávid and to God who were always with me. Their support, patience and never ending love is indescribable. I dedicate this work to them. Soli Deo Gloria.

Abstract

The development of sustainable and green technologies powered by renewable energy sources is highly desired to address the growing global energy need and water scarcity problems.

Heterogeneous photocatalysis emerged in the past decades as promising solar-powered technology for environmental remediation applications such as wastewater treatment. The photoactivity of the materials is believed to be governed by complex mechanisms, still it was shown that it may be critically dependent on the following material properties (i) ability and effectiveness to absorb incident photons, (ii) charge separation efficiency, (iii) charge utilization efficiency, (iv) morphology including the size and shape of the nanostructure and its distribution and (v) the crystal structure, phase composition and crystallinity...*etc* Hence, most strategies aiming to improve the performance of photocatalytic materials may focus on one or more of the aforementioned aspects.

Beside developing new materials or modifying existing systems, the development of sustainable, easy-to-operate systems are highly desired for developing countries such as Africa where almost half of the population are affected by water scarcity of some sort. For this motivation the immobilization of powder catalyst could be one attractive solution.

In this thesis three experimental systems are presented. In the first two the effect of material properties on the photoactivity whereas in the third chapter the immobilization of powder catalyst was investigated.

The first experimental project aimed to study the effect of synthesis parameters of WO_3 nanostructures on its morphology, phase composition, optical properties and ultimately on the photoactivity. Understanding the role of process parameters to gain control over

the material properties is still a challenge but is of great interest in photocatalysis. Here, a hydrothermal synthesis method was employed to synthesize WO_3 nanostructures with various morphologies, crystal phases and optical properties. The effect of the solution pH, the polymeric surface modulator and the added EtOH was investigated on the material properties and on the photocatalytic activities. It was found that the crystal structure and the morphology of WO_3 was influenced by the solution pH in the first place. It was proposed that stabilization effects between the crystal phase and the morphology could also influence the crystallization process beside supersaturation. It was revealed that despite the highest surface area of W-2.01-P20E, reduced oxidation state did not promote high photoresponse. Instead the photoactivity of WO_3 was seen as the compromise of the material properties including the optical, structural properties and the oxidation state.

In the second experimental project the effect of Ag co-catalysis was studied on TiO_2-Cu_2O heterostructure formation. Coupling a wide band gap (TiO_2) and a narrow band gap (Cu_2O) semiconductor could benefit from extended light absorption properties and additionally from enhanced charged separation. In this study a facile wet chemical synthesis method was coupled with a UV treatment step to fabricate TiO_2-Ag-Cu_xO ternary hybrid nanomaterials. The effect of the Ag loading (1-5%) and the synthesis sequence of the Ag deposition step was evaluated on the material properties as well as on the visible photocatalytic activity. It was revealed that both the amount and the order of the Ag-deposition altered the material properties considerably. Typically TiO_2/Cu_xO/Ag (TCA) catalysts had better visible light absorption properties but reduced affinity to adsorb methyl orange (MO) to their surface. Whereas, TiO_2/Ag/Cu_xO (TAC) catalysts in general had better dye adsorption properties relative to TCA and had more efficient decoloration properties under visible light. TOC and HPLC-MS analysis revealed that MO and possibly its degradation products were mainly mineralized and/or adsorbed to the surface of TAC catalyst with 5% nominal Ag content in the visible process generating limited amount of byproducts in the final solution.

The third experimental project focused on the immobilization of the previously prepared powder TiO_2-Cu_2O nanostructure. In this work a fluorine-doped tin oxide (FTO) glass sheet was used as a substrate and the doctor-blade coating technique has been employed to make TiO_2-Cu_2O thin films. Although this technique has a widespread use in the fabrication of solar cells to the best of our knowledge this is the first report on supported TiO_2-Cu_2O photocatalytic systems prepared by this method. To optimize the performance of the TiO_2-Cu_2O thin film under visible light irradiation, the chemical composition of the doctor-blading paste and the temperature of the final thermal treatment step was studied. It was found that both the paste composition and the heat treatment step played an important role in the material properties. When the film contained ethyl cellulose the minimum temperature to remove organic additives was 350 °C. Whereas for the films containing only alpha terpineol 300 °C was sufficient. It was revealed that the higher temperature treatment resulted in more oxidized films which were also shown in their deeper colour. The most effective film under visible light irradiation was TC-0-300 which contained no cellulose and was treated at the lowest temperature.

Lay Summary

Photocatalysis is a process where a solid material makes use of the energy of the light. The interaction of the light and the solid material (also called catalyst) can initiate chemical reactions. This is interesting because these reactions can be potentially used to decompose harmful chemicals from water for example. This way the purification of wastewater may be possible by solar light using a photocatalytic material. Unfortunately, it is not easy to find and develop a material which can effectively eliminate toxic chemicals from water and at the same time work under solar light.

The sunlight mainly consists of visible light but about 5-8% of it falls into the UV range. Because of this, Visible active materials are preferred to be used in photocatalysis to maximize light harvesting. Because WO_3 structures can utilize part of the visible light, in the first part of the work we focues on WO_3 materials. We prepared these materials in the nano range in various sizes and shapes to take advantage of the high surface area. Our aim was to study how the different synthesis conditions affect the material properties and performance in photocatalysis to find the best WO_3 materials.

It was earlier observed that the combination of different photocatalytic materials could positively affect the photoactivity. Therefore, in the second project we turned our attention towards more complex systems. To still benefit from visible light response, a TiO_2-Cu_2O material was modified by metallic Ag. The effect of the Ag amount and the preparation order was studied on the material properties and photocatalytic activities.

It was also noted that the handling and recycling of powder catalysts is not ideal. The catalyst recycling could be more difficult and they could also represent health and safety

issues. Therefore, nanomaterials can be either fixed on macroscopic supports or be directly prepared on them. In our final project, our aim was to transfer the previously prepared TiO_2-Cu_2O material onto a glass slide as a thin film. By changing the temperature and the chemicals used in the fixing process, we wanted to find the best preparation conditions.

Table of contents

List of figures **xvii**

List of tables **xxi**

1 Introduction **1**
1.1 Motivation 1
1.2 Structure of thesis 3

2 Theory and Literature Review **5**
2.1 Photocatalysis 5
2.1.1 Benefits and challenges 5
2.1.2 Fundamentals 6
2.1.3 Nanomaterials in photocatalysis 9
2.1.4 Influencing factors 11
2.2 Material development techniques 13
2.2.1 Doping 13
2.2.2 Semiconductor heterostructure formation 22
2.2.3 Modifications with non-semiconductors 28
2.3 Immobilization techniques 36
2.3.1 *In-situ* synthesis coating techniques 39
2.3.2 Immobilization of powder catalyst 42
2.3.3 Summary of literature review 46

3 Materials and Methods **49**
3.1 Materials 49
3.2 Experimental procedures and nomenclatures 50
3.2.1 Synthesis of WO_3 nanostructures 50
3.2.2 Synthesis of TiO_2/Cu_2O and Ag co-catalyzed nanostructures 50
3.2.3 Preparation method for TiO_2/Cu_2O thin films 51

3.3 Characterization techniques . . . 52
3.4 Photocatalytic testing . . . 56
3.5 Models and calculations . . . 58
3.5.1 Calculation of the MO concentration . . . 58
3.5.2 Estimating the crystallite size . . . 60
3.5.3 Estimating the optical band gap . . . 61

4 Photoactivity of WO_3 nanocrystals 63
4.1 Introduction . . . 63
4.2 Results and Discussion . . . 65
4.2.1 Nomenclature . . . 65
4.2.2 Investigated process parameters . . . 65
4.2.3 Crystal structure . . . 66
4.2.4 Morphological structure . . . 68
4.2.5 Crystallite size calculation . . . 72
4.2.6 Mechanism of nanocrystal formation . . . 74
4.2.7 Optical properties and chemical states . . . 77
4.2.8 Photocatalysis . . . 83
4.3 Conclusion . . . 86

5 Effect of Ag co-catalysis on TiO_2/Cu_2O 89
5.1 Introduction . . . 89
5.2 Results and Discussion . . . 91
5.2.1 Nomenclature . . . 91
5.2.2 Crystal structure . . . 92
5.2.3 Morphological structure . . . 94
5.2.4 Optical properties . . . 96
5.2.5 Dark adsorption . . . 102
5.2.6 Apparent visible photoactivity . . . 107
5.2.7 Mechanism . . . 116
5.3 Conclusion . . . 117

6 TiO_2/Cu_2O nanofilms 121
6.1 Introduction . . . 121
6.2 Results and Discussion . . . 124
6.2.1 Nomenclature . . . 124
6.2.2 Crystal structure and surface properties . . . 124

6.2.3 Morphological structure 128
6.2.4 Optical properties 135
6.2.5 Temperature effect on the organic composition of the nanofilm . . . 136
6.2.6 Visible photocatalytic activities and dark adsorption 138
6.2.7 Recycling test 144
6.3 Conclusion 147

7 Conclusion **149**
7.1 Future improvements 152

References **155**

List of figures

1.1 Pie chart showing the contribution of energy sources in the past 15 years. Figure is taken from the following source: [1] 2
1.2 Graphical representation of localized water withdrawal given as a percentage of the total available water. Figure is taken from the following source: [4] . 3

2.1 General pathway of photocatalysis showing the generation of light-induced charge carriers and their possible surface redox reactions 7
2.2 Band structure positions of a few semiconductor materials relative to the normal hydrogen reference electrode (NHE) 8
2.3 Representation of the energy level distribution for bulk and nano-sized semiconductor material along with the distinct energy levels of an individual molecule which highlights the influence of the scale of the material on the width of the forbidden band gap 9
2.4 Possible routes of incorporating impurities into the host lattice a) and b) shows substitution of homo-valence ions with small or large ionic radius, respectively c) and d) depicts the substitution of hetero-valence ions with interstitial ion or vacancy formation due to charge balance requirement, respectively and finally e) shows interstitial dopant occupation. This figure is reproduced from [39] (http://dx.doi.org/10.1039/C3NR00368J) with permission of The Royal Society of Chemistry 15
2.5 Schematic representation of the semiconductor heterostructure classification based on the band structure a) depicts type I band alignment b) shows quasi-type II and c) represents type II configuration between two semiconductor materials 23
2.6 Schematic representation of the work function values for an n-type semiconductor (TiO_2), a p-type semiconductor (Cu_2O) and for a metal (Ag) 30

2.7 Schematic representation of the charge transfer mechanism between a dye and a semiconductor in a dye sensitized photocatalyst. This figure is reproduced from [103] with permission of Springer. 32
2.8 Schematic representation of doctor blading coating technique shown on the left whereas ”knife-over-edge” coating technique is depicted on the right. This figure is reproduced from [141] with permission of the Royal Society of Chemistry. 44

3.1 Background spectrum measured in the ATR-FTIR equipment 55
3.2 Schematic figure of the photocatalytic set-up a) for powder catalysts and b) for the supported catalyst 57
3.3 Chemical formula of methyl orange 59
3.4 Calibration curve of MO absorbance plotted in the function of concentration 59

4.1 XRD diffractograms of the WO_3 nanostructures a) W-0.10-P20E, b) W-0.51-P20E, c) W-1.05-P20E, d) W-1.52-P20E and e) W-2.01-P20E 67
4.2 Effect of the chain length of the polymeric surface modulator a) SEM image of W-0.10-P200E as an example for typical morphology prepared at pH 0.10, b) SEM image of W-1.52-P3350 as an example for typical morphology prepared at pH 1.52 and c) XRD diffractograms of the WO_3 nanostructures: W-1.52-P3350, W-1.52-P20E and W-1.52-P200E prepared at pH level 1.52 and W-0.10-P3350 and W-0.10-P200E prepared at pH level 0.10 69
4.3 Effect of the presence of EtOH in the reaction mixture a) SEM image, b) TEM image and c) XRD diffractogram of W-EtOH with reference card . . . 69
4.4 SEM images of the WO_3 nanostructures a) W-0.10-P20E, b) W-0.51-P20E, c) W-1.05-P20E, d) W-1.52-P20E and e) W-2.01-P20E 70
4.5 Box plot showing the change in the aspect ratio of the WO_3 nanostructures prepared at various pH levels 71
4.6 On the left the crystallite size estimation for W-0.10-P20E sample is shown using shape factor k between 0.8 and 1.1 is shown. On the right the relative change in crystallite sizes is shown with respect the neigbouring peak. . . . 73
4.7 Optical properties of the WO_3 nanostructures as shown in the Tauc plot (top figure) and in the Kubelka-Munk function versus photon energy plot (bottom figure) 78
4.8 Correlation between the band gap energies of the WO_3 nanostructures and the solution pH 80

4.9 Typical high resolution XPS spectra a) O 1s, c) W 4d and e) W 4f for for W-EtOH (blue) and b) O 1s, d) W 4d and f) W 4f for W-0.10-E20E (pale yellow) WO_3 nanostructures 82
4.10 Photocatalytic activities of the WO_3 nanostructures in the photobleaching reaction of methyl orange 85
4.11 Repeated photocatalytic test of W-0.10-P20E nanostructure 87

5.1 XRD diffractograms of the nanostructures 93
5.2 SEM images of a) Cu_2O, b) TC, c) TA1C, d) TA5C, e) TCA1 and f)TCA5 nanostructures 95
5.3 TEM images of a) TC b) TA5C and c)TCA5 nanostructures 96
5.4 The light absorption properties of the nanostructures shown a) in the diffuse reflectance spectrum and b)-d) in the Tauc plot 97
5.5 Band gap estimation based on the differential reflectance method for selected nanostructures 99
5.6 Comparison of the estimated band gap values by direct and indirect Tauc plot and by differential reflectance method for a) TC and b) TA1C catalyst . 101
5.7 Kinetic models for TC, TA5C and TCA5 catalyst a) q_t versus time plot b) Lagergren pseudo-first order model c) pseudo-second order model d) Weber and Morris intra-particle diffusion model 104
5.8 Apparent visible activities of TC, TA5C and TCA5 nanomaterials after 60 min dark stirring shown with solid lines and dark activity shown with dotted lines 108
5.9 a) Pseudo-zero order kinetic model and b) pseudo-first order model tested for the catalysts 110
5.10 Apparent visible activity of TC nanostructure after 20 min dark stirring shown with solid line and reference dark activity shown with dotted line . . 111
5.11 TOC conversion showed for TA5C catalyst in the function of time a) when it is stirred in darkness and b) when exposed to visible light 112
5.12 HPLC-MS analysis of the MO solution after 90 min visible light irradiation when using TA5C catalyst, a)-c) MS spectra of the recognised products and d) HPLC chromatogram 114
5.13 HPLC chromatograms of the MO solutions when stirred in the dark for a) 0 min and b) 60 min and c) when irradiated with visible light for 90 min . . . 115

6.1 Images showing the colour evolution of TC thin films treated at different temperatures 125

6.2 XRD patterns of (a) TC-100-550 b) TC-100-350 c) TC-0-350 and d) TC-0-300 nanofilms 126
6.3 SEM1 130
6.4 TEM1 131
6.5 XPS spectra of Cu 2p of a) TC-0-300 b) TC-0-350 c) TC-100-350 d) TC-100-550 where the black line represents the measured spectra, the orange line shows the theoretical overall fit and the dotted green lines show the fitted peaks 133
6.6 XPS spectra of Ti 2p of a) TC-0-300 b) TC-0-350 c) TC-100-350 and d) TC-100-550 along with the O 1s XPS spectra of e) TC-0-300 f) TC-0-350 g) TC-100-350 and h) TC-100-550 133
6.7 UV-vis diffuse reflectance spectra shown for the unheated TC film along with TC-0-300, TC-0-350, TC-100-350 and TC-100-550 thin films 136
6.8 ATR spectra revealing the effect of temperature treatment on the organic composition of the nanofilms a) sintering at or below 300 °C the cellulose-free nanofilm and b) sintering at or below 350 °C the cellulose-containing nanofilm. In the bottom row the ATR spectrum of alpha-terpineol and ethyl-cellulose is shown from the left to the right, respectively. 138
6.9 Apparent visible photoactivity measured after 60 min dark stirring is shown with red line and as a reference dark stirring is shown with black line for a) TC-0-300 b) TC-0-350 c) TC-100-350 and D) TC-100-550 nanofilms . . . 139
6.10 Theoretical band structure alignment between CuO, TiO_2 and Cu_2O when all three semiconductor phases are present at the heterointerface. 143
6.11 ATR-IR spectrum showing the effect of 0, 1.5 and 4 hours of NaCl soaking of TC-0-300 nanofilm after the visible photocatalysis test 144
6.12 Recycling experiments showing the apparent visible efficiency of TC-0-300 nanofilm over three repeated cycles, the vertical lines indicate the points when the visible ligth was turned on 145
6.13 XPS spectrum of TC-100-350 as recorded after the first photocatalytic test followed by recovery, the black line represents the measured spectra, the orange line shows the theoretical overall fit and the dotted green lines show the fitted peaks 145

List of tables

3.1 Photocatalytic testing conditions for powder catalysts 57

4.1 Synthesis conditions and characterization of WO_3 nanostructures 72
4.2 Specific surface area of the WO_3 nanostructures 72

5.1 Summary of the estimated band gap values for the nanostructures by direct and indirect Tauc plot and by differential reflectance method 100
5.2 Kinetic parameters of Weber-Morris intra-particle diffusion model 106
5.3 Kinetic model parameters for the apparent visible activities after 60 min dark stirring 109
5.4 MO concentrations in the Visible process of the different photocatalysts tabulated in the function of irradiation times 110

6.1 Scherrer dimensions calculated based on specific peaks from the XRD pattern of nanofilms of TC-0-300, TC-0-350, TC-100-350 and TC-100-550 127

Chapter 1

Introduction

1.1 Motivation

The concerning global trends of growing energy demand and water shortage problems are driving the development of novel sustainable technologies.

It was forecasted by the World Energy Council that the global energy consumption may reach 30 TW by 2050 which is double as much as the demand in 2012 [1]. Figure 1.1 shows that in the past decade and still currently over 80% of the global energy consumption was provided by fossil fuels such as coal, oil and natural gas [1, 2]. This trend cannot be sustained endlessly since fossil fuels are effectively non-renewable energy resources and additionally they have a negative impact on the environment.

Due to climatic change and rapidly growing population it was reported that in 2005 about one third of the population experienced water scarcity of some sort [3]. Predictions indicate that the number of people affected by shortages of clean water would continue to increase and it can reach 3 billion by 2025. A geographical highlight for water usage and availability is shown in Figure 1.2 [4]. The map shows that by 2025 prominent decrease in the available water could be experienced in local areas within America, Europe, Africa and Asia compared to historical data from 1995. For example, in 1995 the US typically used up 20% of the available water sources whereas it is estimated that by 2025 the water consumption would

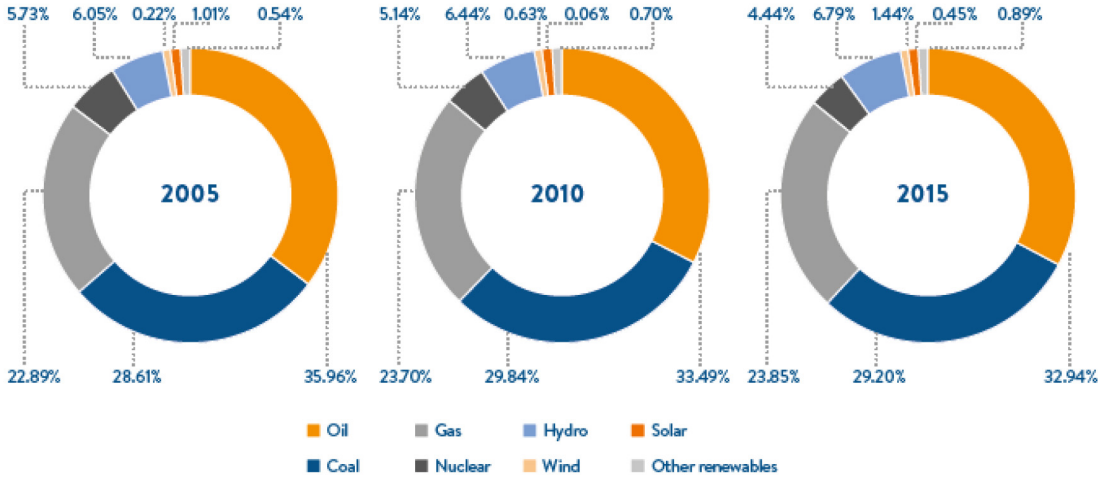

Fig. 1.1 Pie chart showing the contribution of energy sources in the past 15 years. Figure is taken from the following source: [1]

increase up to 40%. As a consequense of unsafe drinking water about 3.1% of the population is reported to die worldwide [5]. Current water remediation technologies include membrane filtration, advanced oxidation processes or even biological methods, however most of them are limited by high operating cost, low efficiency and negative enviromental impact [6].

Because of these, producing energy and purifying water in an energy- and cost-effective way by enviromental-friendly technologies is highly desired.

As an alternative, solar energy is one of the most abundant renewable energy sources. It is estimated that about 36 thousand TW power provided by the Sun is available to be harvested on the Earth which is orders of magnitudes higher than the worldwide energy consumption of 17 TW reported in 2012. Beside its abundance, it is also a waste- and a greenhouse gas emission-free energy source [7]. These benefits make the solar energy driven applications as a promising way to generate clean energy and play a role in environmental remediation.

Solar light utilization is possible by the direct conversion of solar energy into electricity by photovoltaic devices or by solar energy conversion into chemical energy in photocatalytic processes [2]. Contaminants could be decomposed using chemical energy. In a photocatalytic

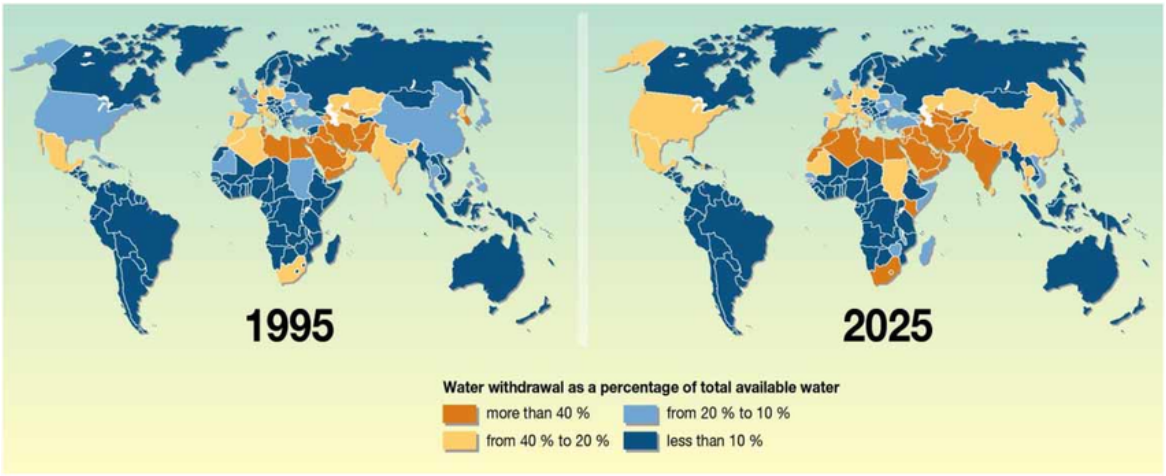

Fig. 1.2 Graphical representation of localized water withdrawal given as a percentage of the total available water. Figure is taken from the following source: [4]

water treatment process the photocatalytic material would be activated ideally by solar light which could convert toxic chemicals into harmless compounds such as water and carbon dioxide. The utilization of solar light in enviromental remediation is a promising green alternative to current technologies and therefore it represents an active research area.

In this thesis, photocatalytic material development and immobilization was in the research focus to contribute in research for water treatment application. To aid sustainable material development, my goal was to work towards photocatalytic systems that would work with visible light for easiness of operation and that would have low-toxicity. By investigating catalyst immobilization, my motivation was to study easy-to-use and cost-effective photocatalytic systems to be used in developing countries such as Africa.

1.2 Structure of thesis

The thesis is structured into seven main chapters.

The second chapter is the literature review and theory part that presents detailed background for the original research projects that includes the discussion of the principle and benefits of photocatalysis, material modification approaches and immobilization techniques.

In each part highlights of the relevant literature are given with the presentation of key concepts and theories.

The third chapter details the experimental procedures and methodologies that were used in multiple chapters.

The fourth, fifth and sixth chapters contain the original research works. These chapters give a short introduction of the research goals that is followed by the presentation of the results and discussion. In the fourth chapter a single semiconductor oxide, WO_3 is investigated in its different structural and crystal forms. The effect of synthesis conditions and material properties is presented for the visible photocatalytic activities of the materials. In the fifth chapter a ternary hybrid structures containing Cu_2O, TiO_2 and Ag are studied. In this work the effect of Ag-cocatalysis with respect to the amount of Ag and to the synthesis sequence are studied. Detailed work is presented for the optical properties of the nanostructures. Study on the dark adsorption and apparent visible activities of the nanomaterials is also performed. The sixth chapter focuses on the development of an immobilization procedure for a TiO_2/Cu_2O system. The effect of the preparation conditions such as the heat treatment and chemical composition of the paste is investigated. The characterization of the prepared thin films are provided along with the apparent visible activities.

And finally the seventh chapter concludes the thesis and summarizes the key findings. Additionally, improvements and future research investigations are proposed at the end of the conclusion chapter.

Chapter 2

Theory and Literature Review

2.1 Photocatalysis

2.1.1 Benefits and challenges

Since the discovery of light-induced water-splitting on a TiO_2 photoanode presented by Fujishima and Honda in 1972, the interest in light conversion systems by means of photocatalytic processes increased exponentially [8–10]. Photocatalytic processes are attractive options to decompose harmful chemicals from wastewater because the process takes place at ambient conditions, it has the potential to be fuelled by solar energy and to fully decompose contaminants to harmless compounds such as water or CO_2. Moreover, the oxygen need of the process can be conveniently supplied from air [9].

The early research works predominantly focused on TiO_2 nanostructures since then several other semiconductor materials (ZnO, WO_3, Fe_2O_3, SnO_2, Cu_2O *etc*) have been associated with photocatalytic activities, too [11–13]. Nevertheless TiO_2 has not lost attention in photocatalytic material development and became a benchmark material for its numerous benefits [14, 15]. As a wide band gap semiconductor oxide ($E_g \approx 3.2$ eV) it exhibits excellent stability and chemical resistance which makes it a robust catalyst in versatile

systems with good retained activity over multiple cycles [14]. Thanks to the suitable position of its conduction and valence band edges it can facilitate water splitting into oxygen and hydrogen without applying external voltage [15, 8]. Also its adequate redox potential could enable the complete mineralization of organic contaminants into CO_2 and H_2O [16]. Its application is environmental friendly and economical considering its lack of toxicity, low cost and widespread availability. Most of these parameters are key requirements for an ideal photocatalytic system.

However, from the photocatalytic material development viewpoint TiO_2 comes with certain shortcomings, too. Importantly, its light absorption ability is restricted to the UV range which takes up only 3-5% of the solar spectrum resulting in a rather poor solar light utilization [14]. On the other hand, as most single materials it could suffer from relatively short diffusion length (around 100-1000 nm) for holes which may limit its photoefficiency [17, 18]. The penetration depth of photons typically lies in the micrometer range (*circa* 10 μm) whereas the diffusion lenght of electrons or holes of most semiconductors ranges from 20 nm to several hundreds of nm [19]. The mismatch between these two characteristics could cause recombination of a substantial part of the charge carriers before successful migration to the catalyst/liquid interphase and participation in photocatalytic reactions. Therefore intensive research effort has been paid to overcome these challenges and improve on the photocatalytic character of TiO_2 and develop novel systems.

2.1.2 Fundamentals

In principle, in photocatalysis band-to-band promotion of electrons takes place after the material absorbs the incident light which inevitably results in the production of positive holes in the valence band [20]. The electronic structure of semiconductors is ideal for light switched activation due to the width of their forbidden band gap over which electrons can be excited typically by UV or visible light. After light-activation the photo-generated electrons

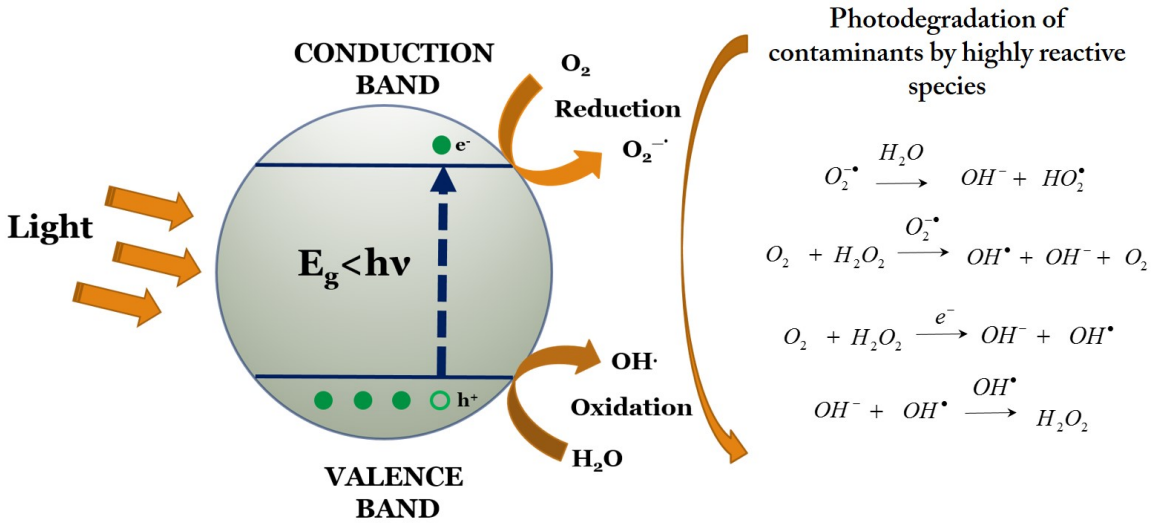

Fig. 2.1 General pathway of photocatalysis showing the generation of light-induced charge carriers and their possible surface redox reactions

and holes could undergo two distinct pathways [21]. They may migrate to the surface of the catalyst given the long-enough lifetime of the charge carriers or alternatively they may relax back to the ground state by recombination via radiative (like fluorescence, phosphorescence) or non-radiative routes.

Importantly, the photo-generated electrons and holes could participate in reduction or oxidation reactions with surface-adsorbed species, respectively. Figure 2.1 depicts the general pathway of activation and subsequent surface reactions of photocatalytic systems. Large variety of surface redox reactions may be possible which could involve the generation of $OH^{\cdot}$ radicals or O^{2-} species from water or surface-adsorbed oxygen, respectively. These radicals may participate in further reactions or directly photodegrade the organic contaminants [16, 22].

However, it is worth mentioning that there is a thermodynamic precondition for generating certain radicals and participating in redox reactions which lies in the position of the conduction (CB) and valence band edge (VB) of the catalyst. In fact, the bottom of CB should be more negative and the upper edge of VB should be more positive with respect to the standard electrode potential of the electron acceptor or donor system for reduction or

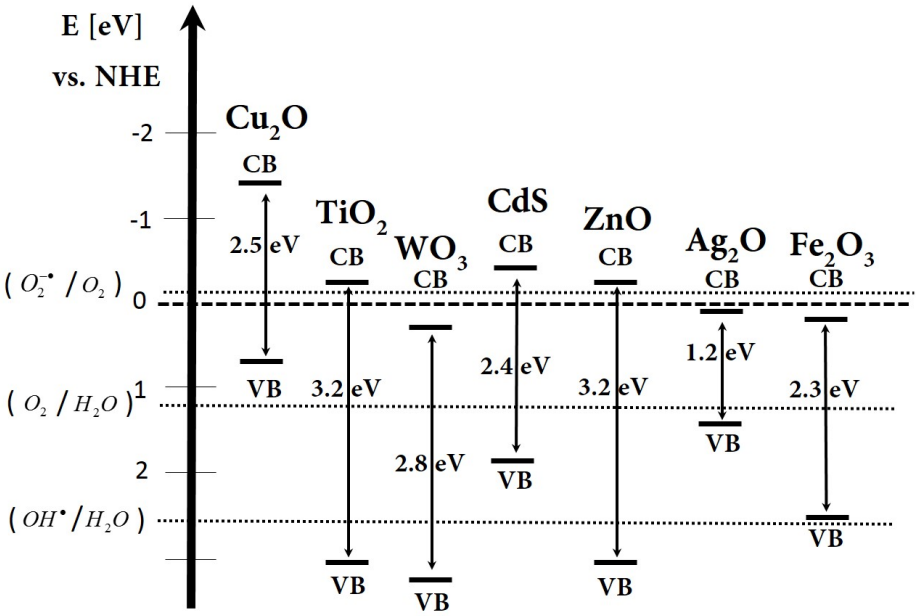

Fig. 2.2 Band structure positions of a few semiconductor materials relative to the normal hydrogen reference electrode (NHE)

oxidation to occur, respectively [20]. Figure 2.2 shows the approximate band structure of common semiconductors based on literature data [23, 21]. It can be seen from the position of the valence and conduction band edges of typical photocatalytic materials that wide band gap semiconductors such as TiO_2 or ZnO could benefit from the possibility to generate both $OH^{\cdot}$ and O^{2-} radicals while narrow band gap semiconductors such as CdS or Cu_2O could form only one type of radical. On the other hand, due to the wide band gap of TiO_2 and ZnO, they could only be excited by more energetic light radiation like UV light. To benefit from both systems the formation of semiconductor heterostructures are commonly performed. When a narrow and a wide band gap semiconductor is coupled, the composite system could take advantage of improved ligth utilization and interfacial electron transfer between the semiconductors that could potentially promote photocatalysis. Considerations of the band structures and thermodynamic conditions are important aspects of photocatalyst material design. Further discussion on this topic is presented in Section 2.2.2.

2.1.3 Nanomaterials in photocatalysis

Nanomaterials have gained key importance in photocatalysis. The growing interest in nanoscale architectures is driven by the unique properties of nanomaterials relative to their bulk counterparts. Since their size is comparable to the wavelength of photons and to the length of the electronic wave function, quantum mechanical rules start to dictate the properties of these structures [24]. In nanoscale, owing to the substantially reduced number of building constituents distinct energy levels starts to dominate the material character in contrast to the quasi-continuous energy band structure of bulk materials [25]. This quantization has a prominent effect on the material properties which will be discussed shortly.

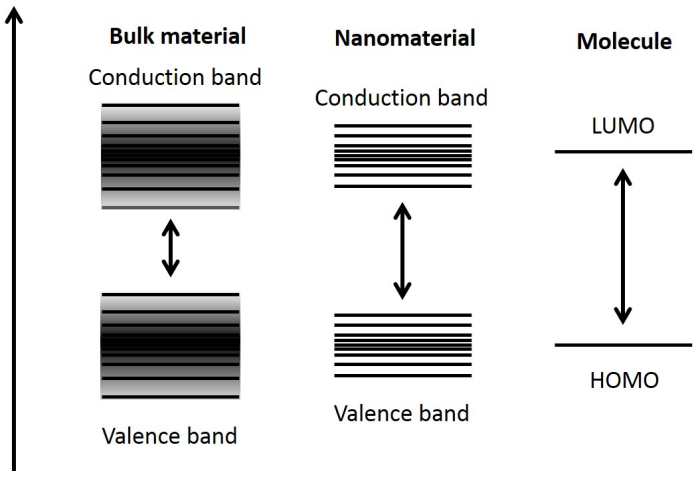

Fig. 2.3 Representation of the energy level distribution for bulk and nano-sized semiconductor material along with the distinct energy levels of an individual molecule which highlights the influence of the scale of the material on the width of the forbidden band gap

When the size of semiconducting materials is reduced to nanoscale, the electronic band structure is affected. Figure 2.3 depicts the effect of energy level separation on the effective band gap of a general semiconductor. Both theoretical and experimental results confirmed that size reduction close to the Bohr radius of a material (see Equation 2.1) could lead to the broadening of the effective band gap between the upper edge of the valence band and the bottom of the conduction band [26]. This phenomenon in often referred as quantum

confinement effect in the literature. Based on the extent of the band gap widening weak or strong quantum confinement (QC) effect can be defined. In particular, weak QC effect occurs at sizes exceeding the Bohr radius (a_B) whereas strong QC effect is expressed at sizes smaller than the a_B.

$$a_B = \frac{\varepsilon \hbar}{\mu_0 e^2} \tag{2.1}$$

$$\mu_0 = \frac{m_e \cdot m_h}{m_e + m_h} \tag{2.2}$$

Where ε is the dielectric constant, $\hbar$ is the reduced Planck constant, μ_0 is defined as the fraction of the product of the effective mass of the electron and the hole and the sum of the effective mass of the electron and the hole in the semiconductor given as $(m_e \cdot m_h)/(m_e + m_h)$ and finally e is the charge of the electron [27]. The concept of effective mass was firstly introduced for the description of the parabolic curvature of the energy spectrum (E(p)) (which correlates the energy to the quasi-momentum (p)) close to its minimum and maximum value. And hence the effective mass of the electrons and holes (m_e and m_h) written for the conduction and valence band (E_c and E_v), respectively can be expressed as shown in Equation 2.3 and 2.4 [28].

$$m_e = \frac{p^2}{2E_c} \tag{2.3}$$

$$m_h = -\frac{p^2}{2E_v} \tag{2.4}$$

This phenomenon is particularly important to light-driven applications such as photocatalysis since the optical properties of the nanomaterial defines the longest wavelength from which the activation of the catalyst could take place and the amount of the irradiated light that could potentially be harvested.

Another appealing feature of nanomaterials is the possibility for versatile structure formulation that could offer increased surface area relative to their bulk counterparts. High surface area catalyst was shown to lead to increased photoactivities in the past [29].

2.1.4 Influencing factors

It is known that the photocatalytic efficiency is the complex functions of many parameters [20]. The material properties such as the structural and optical characteristics along with the operation conditions of the photocatalytic reaction could both play an important role in the overall photodegradation efficiency [9]. In this section, some of the common factors will be reviewed starting the discussion with the material characteristics followed by the operating conditions.

It has been generally accepted that structural properties such as the morphology and the crystalline phase of the nanostructures could have a profound effect on the photocatalytic activity. Smaller nanocrystals may exhibit higher surface area that was shown to typically enhance the photoactivity. Also, the shape and the exposed crystal facets of the nanomaterials was linked to the effectiveness of charge transport and to the adsorption properties of the material towards reactant molecules which could greatly influence the photoactivity. Moreover, the crystallinity and the number of microstrains and defect sites in the material was found to impact the e^-/h^+ recombination which has a reversed effect on the photoactivity [30].

In line with this, high surface area mesoporous TiO_2 nanofibers were prepared by *Zhang et al.* that exhibited superior photoactivity over P25 nanoparticles towards Rhodamin B. The authors reported that the TiO_2 nanofibers could be characterized with high surface area, faster electron transport, longer-lived charges and higher dye adsorption relative to P25. The enhanced photocatalytic activity was attributed to the benefits of these factors [31]. Similarly, other high surface area nanostructures such as CdTe quantum dot decorated ZnO nanowires

and hierarchical nanostructures such as hollow sphere WO_3 were shown to exhibit improved photocatalytic activities [32, 29].

Morphology-dependent photocatalytic activity was noted by *Ho et al.* who prepared cubic Cu_2O with distinct morphologies of cubic, octahedral and hexapod shapes. It was found that the various morphologies exhibited significantly different photoactivities. Octahedral Cu_2O possessed the highest whereas cubic shaped Cu_2O nanomaterials showed the lowest photoactivity. The authors suggested that the $\{111\}$ crystal facet which dominated the octahedral but not the cubic morphology could cause such a prominent difference in the photoactivity of Cu_2O. It was also noted that the $\{111\}$ crystal facet favoured the adsorption of negatively charged dye molecules which could lead to the promoted photoactivity [33].

By varying the synthesis conditions *Cui et al.* prepared a low-defected C_3N_4 photocatalyst with 6-times higher photocatalytic hydrogen evolution efficiency than a reference C_3N_4 nanostructure. The authors revealed that the different synthetic approach provided more structural control and resulted in a nanostructure with high surface area, fewer defects and ordered crystallinity [34].

Beside structural characters, the optical property of nanomaterials is highly relevant to the photocatalytic activity. With respect to the light utilization, the width of the forbidden band gap defines the threshold of lowest energy incident photons that could activate the photocatalyst. Additionally, nanomaterials with direct electron transition over the band gap typically possess high absorption coefficient that increases the probability of efficient light absorption [21]. However, in this type of semiconductors not only the excitation of electrons is likely to take place but the recombination of the photo-induced charges as well. As the diffusion of charge carriers is limited in most semiconductors the high light absorption ability in the subsurface areas could promote the photoactivity [20, 35].

It is also known that by varying the operation conditions the effectiveness of the photocatalytic material can be altered. For example, it was shown that a Cu_2O thin film in the absence

of H_2O_2 exhibited only minimal photocatalytic activity while the same film in the presence of H_2O_2 could considerably improve the photoefficiency of methyl orange degradation. The enhancement of the photobleaching reaction was explained by the role of H_2O_2 as an electron acceptor agent which could hinder the fast electron/hole recombination of the Cu_2O thin film [36].

To optimize the performance of the photocatalytic system *Byrappa et al.* investigated the effect of the solution pH, the reactant and photocatalyst concentration and finally the effect of the temperature on the photocatalytic activity of ZnO nanocrystals towards Rhodamin B. It was found that high Rhodamin B dye concentrations led to decreasing photoefficiency which was explained by the reduced path length of the incident photons at higher dye concentrations. The effect of the ZnO loading was found to drop dramatically beyond the optimal level which could be caused by increased light scattering. The photobleaching efficiency was found to reach a minimum at pH 7 whereas more acidic and alkaline conditions increased the photoactivity considerably. The authors attributed the increased degradation rate to the facilitated radical formation at both higher and lower pH values. Increasing temperature was found to promote photocatalysis which was explained by the mitigation of electron/hole recombination [37].

Also other factors such as the light characteristics and various reactor designs could affect the photoactivity which is not detailed further in this thesis [9].

2.2 Material development techniques

2.2.1 Doping

The desire for developing efficient photo-response catalysts has been the subject of intensive research since decades. However, the exclusive UV activity of photocatalyst such as TiO_2 or ZnO practically limits their application. Various approaches aiming to overcome this limita-

tion were proposed for extending the light absorption to the Vis range. Among others, doping is one of the techniques which enables the band structure engineering of semiconductors. Although doping has been carried out with various semiconductor oxides (*e.g.* ZnO) the most extensive research in the field still belongs to TiO_2 therefore in this thesis we primarily focused on TiO_2 to discuss doping processes.

Doping is associated with heteroatom introduction into the crystal lattice in the effort to engineer the band gap and enhance photoactivity. In a special situation when similar effects are achieved but without external heteroatom introduction the process is often referred as self-doping [38]. These modulations ultimately alters the local symmetry of the crystals and changes the character of the intrinsic semiconductor. Figure 2.4 highlights the different possible routes for heteroatom incorporation into a host lattice. Dopants may be incorporated into the crystal lattice by means of substitution or interstitial occupation [39]. In the former case the dopant substitutes some of the host cations or anions in the crystal lattice whereas in the latter case the dopants are located in a lattice site and are able to diffuse throughout the lattice. Depending on the homo-valence or hetero-valence nature of the dopant additional ions or vacancies may be formed in the lattice as shown in Figure 2.4 a) and d). The material properties such as the band structure, the spatial distribution of the dopant, the level of lattice distortion and the amount of O-vacancies were shown to be affected by multiple factors such as the synthetic approach, the ionic radius, concentration and the nature (anionic or cationic) of the dopant. The photocatalytic activity is believed to be the complex function of these and similar effects [40].

Metal doping

By incorporating metal cations into the crystal lattice of TiO_2 the visible light utilization can be enhanced. The improvement in the optical properties is typically explained by the generation of new impurity bands in the forbidden band gap which can be responsible for

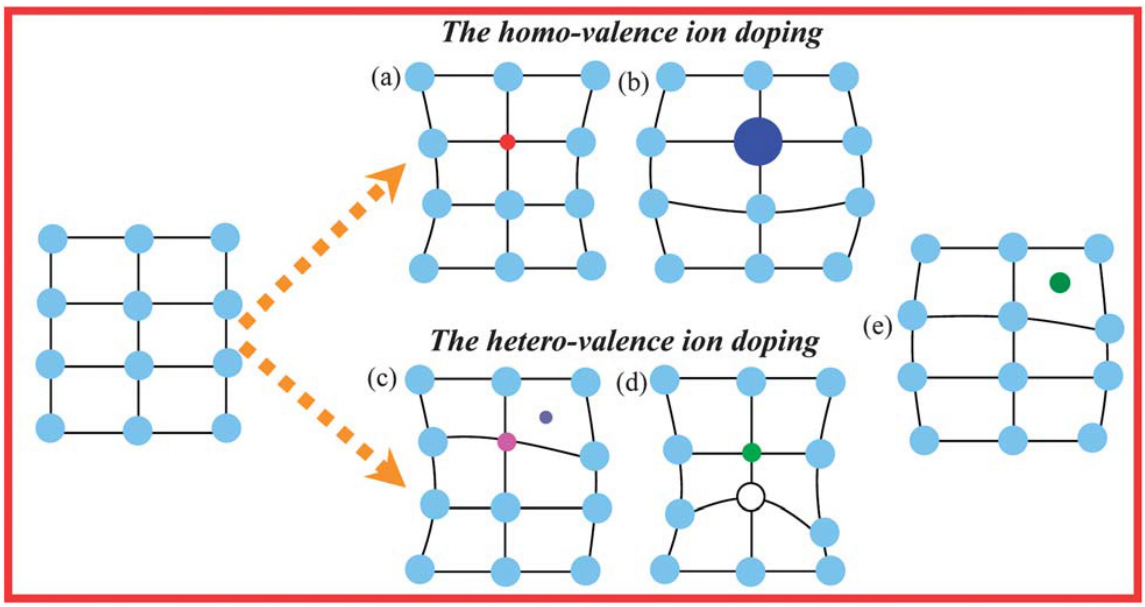

Fig. 2.4 Possible routes of incorporating impurities into the host lattice a) and b) shows substitution of homo-valence ions with small or large ionic radius, respectively c) and d) depicts the substitution of hetero-valence ions with interstitial ion or vacancy formation due to charge balance requirement, respectively and finally e) shows interstitial dopant occupation. This figure is reproduced from [39] (http://dx.doi.org/10.1039/C3NR00368J) with permission of The Royal Society of Chemistry

secondary absorption [41]. Both theoretical and experimental results showed that for example Mn is a capable transition metal to significantly extend the light absorption properties of TiO_2 to the visible region [42]. Among others also Fe-, V-, W- and Cr-doped TiO_2 showed enhanced optical properties relative to undoped TiO_2 [43–46]. In agreement with experimental findings, the theoretical calculation of *Khan et al.* demonstrated that substitutional or interstitial W-doping of TiO_2 could result in significantly altered optical properties. Their calculations revealed that substitutional W-doping induces the formation of W 5d states below the conduction band of TiO_2 whereas interstitial W-doping results in the formation of localized interband 5d states. Owing to this distinct mechanism the optical properties of substitutional doped TiO_2 is more enhanced than the interstitial doped one they found [46].

However, in some cases instead of shifting the light absorption into the visible range, blue-shift in the optical band gap edge has been noticed when doped with certain metal

cations. For example, the band gap of a Zr^{4+}-doped TiO_2 was shifted towards higher energies to an extent proportional to the amount of doped Zr^{4+} [47]. Also, Nb- and Ta-doping of TiO_2 was found to increase the energy of the effective band gap as reported by *Cimieri et al* [48].

Concerning the photoactivity of metal-doped TiO_2 both positive and negative outcomes have been reported. Although the Zr^{4+}-doped TiO_2 showed no enhancement in the light absorption still improved photoactivities were measured for the doped semiconductor oxide. The authors believe that the Zr^{4+} sites could enhance the separation efficiency and the lifetime of the electron-hole pairs by acting as an electron trap [47]. A number of other authors also support the idea that by trapping one type of charge carriers metal dopants could influence the lifetime of the counter charge carrier which may enhance the likeliness of successful surface migration and photocatalytic reactions to take place [49, 46]. Elsewhere, a 10% Ta-doped TiO_2 was shown to have improved photoactivity compared to 10 or 20% V-, Nb- and 20% Ta-doped TiO_2. The photocatalytic test was carried out in a stainless steel batch type reactor under Ar/O_2 atmosphere to degrade gaseous ethanol into CO_2 and H_2O under visible light irradiation. The authors suggested that the enhanced properties could be related to the close matching ionic radius and crystallite size of Ta to that of Ti [48].

Beside the benefits, also detrimental effect on the photoactivity was reported when doping or codoping TiO_2 with certain metal cations [50, 51]. The negative effect was mostly explained by the generation of the newly formed in-gap states that could act as recombination centers for the charge carriers which impair the photocatalytic activity. *Obata et al.* found that a substitutional Cr-doped TiO_2 was deactivated compared to undoped TiO_2 in the photodecomposition reaction of NH_3 into H_2 and N_2 under UV light irradiation. They argued that due to the charge balance requirement, beside Cr^{3+} ions Cr^{6+} could also be formed in the crystal lattice when substituting Ti^{4+}. These Cr^{6+} sites were accounted for the reduced photoactivity by serving as recombination centers for the photo-generated charges [43]. Elsewhere, a Fe/Zn-codoped TiO_2 catalyst has been investigated with 2:1

Fe:Zn ratio and doping concentration ranging from 0.06 to 1.2% with respect to the Fe content. It was found that the Fe/Zn-codoping approach worsened the photoactivity of TiO_2 towards phenol under UV-Vis light irradiation. Under visible light irradiation up to circa 9% improvement in the photodecomposition has been achieved at a doping concentration of 0.24%. The authors accounted the loss of efficiency in the UV-visible test for the reduced crystallinity of the samples and highlighted that excess level of metal doping could diminish the photoactivity [52].

To prepare metal-doped TiO_2 different synthesis strategies have been presented. Among others sol-gel, hydrothermal, solid-state and microemulsion approaches has been explored for fabricating metal-doped TiO_2. The importance of the various methods on the optical and photocatalytic properties of the materials has been highlighted by some research works. According to *Venkatachalam*, although most metal doping processes employ impregnation and co-precipitation methods, the effectiveness of substitutional doping is low for wet-impregnation processes [47]. Similar conclusion has been drawn by *Obata et al.* who attempted to synthesize Fe-doped TiO_2 by both solid-state reaction and impregnation method. They found that substitutional Fe-doping was only achieved by the former process. As a consequence, the visible light absorption property of the materials was only improved when the Fe-doped TiO_2 has been prepared via solid-state reaction route. Similarly, the photocatalytic activity of the substitutional Fe-doped TiO_2 was also superior over the impregnated catalyst [43].

Non-metal doping

Similarly to metal-doping, non-metal elements are typically incorporated into the crystal lattice of TiO_2 in order to extend its light absorption character into the visible range and enhance its photoactivity. Non-metal elements such as N, C or S can alter the optical properties of TiO_2 by two distinct mechanism. They could contribute in the narrowing of

the effective band gap by mixing N, C or S respective 2p or 3p orbitals with O 2p orbitals which could result in the upward shift of the valence band maximum of TiO_2 [53]. Or alternatively, they may create localized mid-gap states in the forbidden band gap of TiO_2 [54, 44]. Depending on several factors such as the type of the dopant or the spatial distribution of the non-metal element, one of the aforementioned mechanism or the combined effect of these two are normally responsible for the modulation of the optical properties [55, 56].

Positive effect on the visible light harvesting ability of TiO_2 has been demonstrated by several non-metal dopant incorporations. *Yalcin et al.* for example reported that the effective band gap of TiO_2 could be reduced to 2.48 eV from 3.20 eV by 1% of substitutional sulphur doping. The measured band gap of S-doped TiO_2 was even smaller than that of the 1% substitutional N- or interstitial C-doped TiO_2 (2.70 and 2.50 eV, respectively) synthesized by the same author [54]. In another report more modest improvement in the light absorption abilities was reported by similar non-metal elements. Substitutional C-doping of TiO_2 nanotubes was found to only slightly affect the band gap of undoped TiO_2 by red-shifting it to 2.92-2.95 eV [57]. On the contrary, theoretical calculations predicted and experimental results confirmed that other elements such as fluorine atom could not effectively reduce the band gap of TiO_2 due to the F 2p states being positioned below the valence band of TiO_2 [58, 59].

Some authors accounted the limited success of visible light absorption enhancements of non-metal doping to the difficulty to synthesize bulk doped TiO_2 by substitution. They believe that the high energy demand for breaking the Ti-O chemical bond and the limited thermodynamic/kinetic solubility of substitutional dopants in the bulk of the material hinders further improvement of the material properties [55, 56]. To overcome these difficulties *Liu et al.* presented a B,N codoping approach to achieve substitutional doping of TiO_2 with nitrogen by a two-step synthesis approach. Firstly interstitial boron ions were introduced into the crystal structure by hydrothermal and calcination processes which were believed to

weaken the Ti-O bond prior to N-doping. In the second step, substitutional N-doping was achieved in a gaseous ammonia atmosphere. The resulting red catalyst had absorption in the full Vis range with 1.94 eV energy band edge and was tested in visible light induced water splitting reactions [56]. Elsewhere an Al-reduced self-doped TiO_2 was shown to facilitate the substitution of guest heteroatoms into the crystal lattice. The oxygen-deficient structure, which was prepared by reduction, could welcome non-metal elements more easily. *Lin et al.* used this technique to synthesize H, N, I and S doped TiO_2 with the highest solar light utilization efficiency of 85%. Moreover, the authors claim that the as-prepared black N-doped TiO_2 is the best performing titania photocatalyst up to date [55].

Although great improvements have been reported when doping with non-metal elements, some works demonstrated that extended visible light absorption is not always resulted in enhanced photocatalytic activity. For example *Zhou et al.* reported that a B,N-codoped TiO_2 showed extended light absorption character which was found to be the function of the temperature treatment step. High temperate treated samples at 600 and 650 °C showed much improved absorption in the whole visible region which was indicated by their dark green and black colours as well. Whereas samples treated at 500 and 550 °C showed limited improvement by an add-on shoulder peak in the optical properties. Despite the improved light absorption, the high temperature treated samples exhibited the lowest photoactivities both under UV and visible light irradiation among the B,N-codoped TiO_2. The reduced performance was explained by the presence of more abundant oxygen defect states owing to the higher applied temperature that could act as recombination centers for the charge carriers [60]. Due to the hetero-valence nature of nitrogen with respect to O atoms, nitrogen doping has been shown to facilitate the formation of oxygen vacancies in the crystal lattice yielding a highly defective system [53, 41, 61]. In photocatalytic systems the role of oxygen vacancies have been associated with both positive and negative effect.

Self-doping

As the name reflects, self-doping is an intrinsic type of doping without introducing heteroatom from external source into the crystal structure. Similarly to extrinsic heteroatom doping the alteration of the electronic character in self-doped semiconductors may be caused by anion or cation vacancies. For example, in a self-doped TiO_2 donor-type O-vacancies are introduced into the crystal lattice of TiO_2 [62]. Whereas in copper-deficient chalcogenide nanocrystals the generation of cation vacancies leads to the self-doped state [63].

Self-doped TiO_2 nanostructures have been presented by different synthesis techniques including those under harsh and mild conditions. Among techniques employing high temperature, hydrogenation and chemical reduction methods are common techniques. *Zuo et al.* used an ethanol-based combustion technique with 2-ethylimidazole at 500 °C to produce blue-coloured self-doped TiO_2 [64]. Elsewhere *Wang et al.* reported an Al-reduction technique in a tube furnace at temperatures between 400 and 600 °C which resulted in dark grey and black TiO_2 [62].

Also, techniques employing milder conditions have been researched with the hope to fabricate self-doped TiO_2. *Yin et al.* presented a carbon sphere templated sol-gel method using $NaBH_4$ as reducing agent to synthesize off-white self-doped TiO_2 hollow spheres [65]. Others reported a microwave-assisted heating method where ethylene glycol was used as an environmental friendly and mild reducing agent [66]. Also *Zhang et al.* used an electrochemical reduction approach to prepare light grey-coloured Ti^{3+}-doped TiO_2 nanotube arrays [67]. As the lighter colours of the self-doped TiO_2 may suggest typically milder conditions could not achieve as prominent increase in the visible light absorption as the harsh condition routes.

Regarding the photocatalytic activities of the as-prepared self-doped TiO_2 nanostructures, the generation of Ti^{3+} states into the crystal lattice is argued by some researchers to induce fewer structural defects formation in the crystal structure than the traditional heteroatom

doping strategy. Also the improved photoactivities relative to undoped TiO_2 nanoparticles were explained by the presence of O-vacancy donor states [66, 64]. Yet others believe that the generated Ti^{3+} states may mostly act as recombination centers which impair the photoactivity [62, 55]. These questions are not yet clarified in the literature. Furthermore, comparing photoactivities across studies are complicated due to the various testing conditions and apparatus used. Moreover, the reference system is mostly commercial TiO_2 nanoparticles which shows effectively no activity under visible light irradiation and that way it does not serve as a sensitive scale for the improvements.

Despite these, an especially effective model system has been demonstrated by many researchers that combines self-doping and non-metal doping strategies of TiO_2. *Lin et al.* for example achieved substitutional nitrogen doping of a black self-doped TiO_2 which could absorb 85 % of the solar spectrum and was claimed to exhibit superior photocatalytic activity over all previously reported titania catalysts in H_2 generation up to date [55]. Elsewhere *Yang et al.* presented a very similar method to prepare S-doped black TiO_2. In his method oxygen-deficient TiO_2 was achieved by an Al-reduction method which was then heated at 600 °C in H_2S atmosphere [68]. They also reported rapid H_2 evolution in the photocatalytic test. Both authors attributed the excellent photoactivities to the mixed doping strategy where the nonmetal heteroatoms could readily occupy the abundant oxygen vacancies generated in the first step of the process. This process not only resulted in narrowed band gaps but also reduced the number of recombination centers in the TiO_2 in favour of photocatalysis they argued [55, 68].

Besides TiO_2, for example self-doped copper chalcogenide nanocrystals has been reported, too [63, 69]. Interestingly, researchers found that copper cation vacancies arising from the copper-deficient structure could behave as free-moving holes and when at high concentration these structures exhibit increasing plasmonic resonance effect similarly to noble metals (which will be discussed under Section 2.2.3). This unique character was

firstly associated with a $Cu_{2-x}S$ nanocrystal in 2009 by *Zhao et al* [38]. Since then $Cu_{2-x}S$ and similar structures received growing attention. And although stochiometric Cu_2S has been already investigated in photocatalytic reactions, its self-doped form has been rarely studied in photocatalysis [70, 71]. One of the reports is from *Chen et al.* who fabricated a $Cu_{2-x}S$/graphene oxide nanocomposite with a Cu:S ratio of 7:4 that showed photocatalytic activity under solar and visible light irradiation [72].

2.2.2 Semiconductor heterostructure formation

Beside doping, another approach to address the shortcomings of TiO_2 is to form semiconductor heterostructures. The formation of hybrid semiconductor nanostructures has attracted widespread interest due to the potential to prepare highly effective visible-response photocatalytic systems [23]. One attractive feature of such a system is the possibility of effective charge carrier separation which could ensure improved utilization of the photo-generated charges.

Band alignment in heterostructures

Based on the band structure of the materials a number of authors have adopted the classification of semiconductor heterostructures into three groups with some variations [23, 2, 73]. A schematic representation of these groups can be viewed in Figure 2.5.

Type I band alignment shown in Figure 2.5 a) is satisfied when both the valence (VB) and conduction band (CB) edges of one of the semiconductors lie within the respective band edges of the other semiconductor. This is also called straddling configuration in the literature [73]. At this band alignment both the photo-generated electrons and holes would thermodynamically favour to accumulate in the nested narrower band gap semiconductor therefore no electron-hole pair separation would take place. In other words, type I band alignment could support charge carrier recombination which is typically not desired for

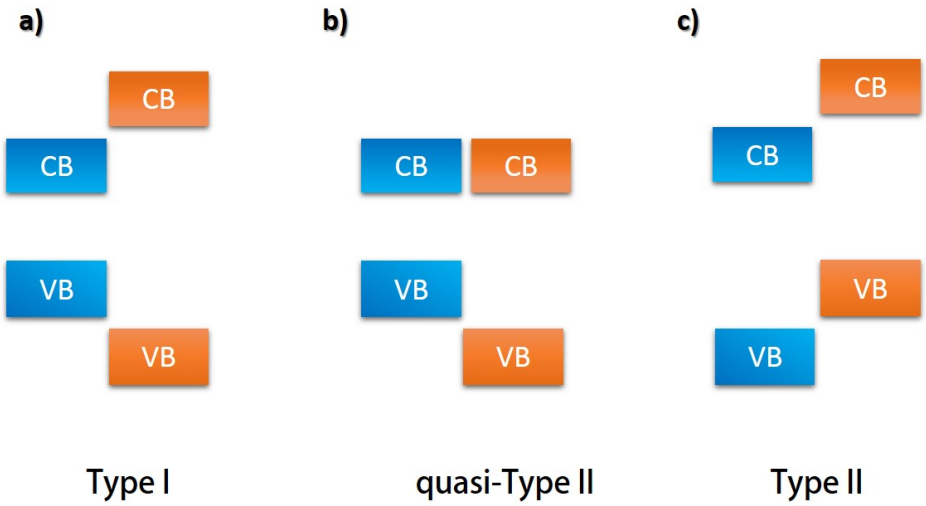

Fig. 2.5 Schematic representation of the semiconductor heterostructure classification based on the band structure a) depicts type I band alignment b) shows quasi-type II and c) represents type II configuration between two semiconductor materials

photocatalytic processes [73]. Examples for type I arrangement would include CdSe/CdS, ZnS/CdSe or CuO/TiO_2 heterojunctions [74].

In the quasi-type II arrangement shown in Figure 2.5 b) either the CB or VB of the two semiconductors are closely located allowing delocalization of one type of charge carrier while the other band confines the counter charge carrier due to the different band positions [2]. In this set-up the electron/hole relaxation could be delayed owing to the delocalized nature of one of the charge carriers. Hence converting type I heterostructures to type II may be beneficial with respect to e^-/h^+ recombination. An experimental example for such a conversion was presented by *Wu et al.* who synthesized CdSe@CdS nanorods with an original type I band alignment which was later tuned to quasi-type II alignment. They achieved the conversion by adjusting the size of the CdSe quantum dots and the thickness of the CdS nanorods that ultimately altered the optical properties of the semiconductors. Tuning the band structures was possible because of the large difference between the valence band edge positions and the small offset between the conduction band edges of CdSe and CdS [75].

The third group is the type II band alignment (in Figure 2.5 c)), also referred as staggered configuration. At this occasion the VB and CB of one of the semiconductors is located at less positive and more negative energies with respect to the other, respectively. Hence this alignment could result in preferential electron and hole accumulation on the CB and VB sites of different semiconductors, respectively. As a result of charge separation the inhibition of fast recombination of the charge carriers could take place in a type II heterojunction that would expectedly increase the photoactivity. For this potential a special interest has been paid to type II systems. Various semiconductor combinations provide with type II alignments such as Cu_2O/g-C_3N_4, TiO_2/Cu_2O, TiO_2/WO_3 ...*etc* [76].

Charge separation efficiency

Beyond meeting the thermodynamic condition for e^-/h^+ separation the structural properties of the heterostructures could have a profound effect on how efficiently the charge carrier separation may take place through a heterojunction [73, 77]. The different synthesis techniques and approaches could have a significant role in providing with different structural configurations influencing the morphology, surface and interphase area, the number of defect states, crystal structure of the semiconductors and other similar material properties mentioned in Section 2.1.4 and 2.1.3. For example it was demonstrated that typically physical mixtures of specific heterostructures are less effective photocatalyst than a nanocomposite material. In agreement with this, *Chen et al.* found that the photocatalytic activities of a mechanically mixed g-C_3N_4-Cu_2O material was lowered compared to the same hybrid structure that was synthesized by one-pot reduction method. It was concluded that thanks to the more intimate contact the nanocomposite structure exhibited more enhanced preformance in photocatalysis [76].

Zheng et al. highlights that the compatibility of crystal phases of the different materials is an important factor in effective heterostructure formation [78]. Closely matching lattice

parameters could support heterostructure formation whereas in the alternative event the heterointerphase formation may need to be aided by auxiliary materials such as surfactants or enhanced by linker molecules. It was also suggested by the same author that increasing lattice mismatch at interphases may result in more abundant defect sites where the charge carriers could possibly recombine.

In accordance with this nanosized alloy formation in the interphase region of a ZnO-CdS core/shell nanocomposite was found to affect the number of defect sites in the interphase which was ascribed to the significantly enhanced photocatalytic activity of the material [79]. The authors believe that the CdZnS alloy could play an important role in the core/shell interphase by suppressing the lattice mismatch between the semiconductor layers. The ZnO-CdS core/shell nanocomposite prepared by chemical vapour deposition exhibited superior performance in photocatalytic H_2 generation over TiO_2-CdS core/shell nanocomposite where no such alloy formation was noticed in the interphase. They argue that the fewer defects could improve the charge carrier transfer efficiency which resulted in the high photoactivity. Elsewhere *Liu et al.* reported a 3-mercaptopropionic acid aided hydrothermal synthesis of a Cu_2O nanocrystal/TiO_2 nanobelt heterostructure with close interaction [80]. The bifunctional acid could act as a linker molecule that could ease the interphase formation between Cu_2O and TiO_2. The highest visible photocatalytic activity measured in a methyl orange solution was presented by the 6% Cu_2O/TiO_2 nanobelts overperforming both bare Cu_2O and TiO_2.

As a means of enhancing interaction between semiconductor nanocrystals and improving the crystallinity of the material, calcination is often performed especially after wet-chemical processes. The benefit of thermal treatment on the photoactivity was demonstrated in a number of cases.

Huo et al. for instance synthesized a CdS-TiO_2 hybrid structure that showed high activity and stability in the photocatalytic degradation of 4-chlorophenol [81]. The calcination of the as-prepared nanomaterials was performed under supercritical condition to ensure strong

interaction between the semiconductor nanocrystals and to retain high surface area at the same time. Elsewhere, *Mioduska et al.* found that higher calcination temperatures between 500 and 800 °C increased the photoactivity of a WO_3/TiO_2 nanocomposite by a factor of 1.5 with respect to the 400 °C treated sample. The authors believe that the crystallinity of the samples was improved by the elevated temperature treatment that could lead to higher performance in the photocatalytic decomposition of phenol [82].

Also fabricating core-shell materials is considered as a promising way to enhance contact area between the semiconductors which could promote the charge separation efficiency in type II heterojunctions [83]. Semiconductor thin films have been synthesized around the core materials by different methods including various deposition techniques (chemical vapour deposition, atomic layer deposition, sputter deposition), sol-gel or hydrolysis approaches. For example, *Su et al.* coated uniformly octahedral Cu_2O nanoparticles with TiO_2 film by a hydrolysis method [84]. *Myung et al.* deposited CdS shell on pre-grown ZnO nanowires by chemical vapour deposition technique with controlled shell thickness [79]. Others presented a method to fabricate WO_3/TiO_2 core/shell nanowires by the combination of sputtering deposition and thermal oxidation [85]. Elsewhere, WO_3/TiO_2 core/shell nanofibers were prepared by electrospinning and atomic layer deposition techniques [86]. In certain cases it was reported that the core/shell configuration showed superior performance over single materials and other nanocomposite structures. *Chu et al.* presented a Cu_2O/TiO_2 core/shell material that overperformed both Cu_2O/TiO_2 nanocomposite and physically mixed Cu_2O and TiO_2. The authors attributed the high photocatalytic activity towards methyl orange to the enhanced interphase and close contact of the core/shell nanocomposite [87].

Photocorrosion

Although narrow band gap semiconductors such as Cu_2O (2.4 eV), CdS (2.4 eV) or Ag_2O (2.39 eV) could act as effective visible photosensitizers and by rational material design they

may also suppress fast charge carrier recombination, they often suffer from photocorrosion over the course of photodecomposition [77, 81, 88]. The poor stability could significantly affect their activity over repeated cycle of use. Therefore, different approaches has been trialed to overcome this shortcoming.

Liu et al. presented that partial coverage of Cu_2O nanospheres with TiO_2 nanoislands could effectivily enhance the stability of Cu_2O over multiple cycles. The heterojunction was prepared by a two-step method including a hydrolyzation and a solvent-thermal step. They proposed that the improved stability could be accounted for the partially covered surface which allowed the holes accumulated on the VB of Cu_2O to react with water [89].

Elsewhere, atomic layer deposition (ALD) was employed to deposit a conformal TiO_2 layer over a CdS quantum dot decorated TiO_2 nanorod arrays [90]. It was reported that the photodecomposition rate of methyl orange was enhanced by the deposition of TiO_2 overlayer compared to the bare heterojunction. The ALD layer was also shown to serve as protection against photocorrosion of CdS. The authors suggest that the passivation of the CdS surface and the more enhanced charge separation provided by the TiO_2 thin film could play role in the improved stability. Independently, other researchers also found that the passivation of CdS surface by one layer of ALD-deposited TiO_2 or Al_2O_3 thin film enhanced its stability by the factor of 14 [91].

Improved stability was also reported by *Huo et al.* who investigated a CdS-TiO_2 photocatalyst prepared by supercritical *in-situ* sulfurization reaction of doped TiO_2. The authors believe that the inherent interaction between the CdS and TiO_2 nanocrystals could protect CdS from serious photocorrosion [81].

2.2.3 Modifications with non-semiconductors

The third main approach to improve the efficiency of solar absorption and/or the photoactivity of semiconductor materials is the modification with non-semiconductor materials or elements.

This category could include *e.g.* surface modification with metal elements, visible active dyes or carbon-related material.

Modification with metals

Metals alone are typically not great photocatalysts but as surface deposits on semiconductor materials they were demonstrated to be able to improve the photoactivity [92]. The enhancement of photocatalytic processes may stem from improved light absorption by surface plasmon resonance effect and/or facilitated charge separation.

Surface plasmon resonance effect (SPR) of metal nanoparticles arises from the collective oscillation of surface electrons when they interact with light [93]. The SPR phenomenon is based on the matching frequency of incident photons and oscillating electrons which is characteristic for the particular metallic element. It is well-established that beyond the nature of the metal, its size and geometry also significantly affects the intensity and wavelength of SPR [94]. The improved light absorption properties induced by plasmonic metals were typically attributed to the so-called near-field enhancement phenomenon and to increased light scattering [93]. In the former case, the generated surface plasmons could induce local electric field in the proximity of the metal nanoparticles that concentrate the light flux and may create a local ”hot spot” [94]. Thanks to these high intensity spots, the generation of photo-induced charges is facilitated locally. Additionally, the improved light scattering character of plasmonic photocatalyst could enhance the light utilization efficiency by reflecting some of the unabsorbed portion of the light back to the catalyst surface [93].

In order to understand the characteristics of charge separation induced by plasmonic metal nanoparticles, we need to consider the semiconductor-metal interphase that is formed when a metal is brought in contact with a semiconductor. To describe the underlying mechanism of interfacial electron transfer between metal and semiconductor, the concept of work function (written in Equation 2.5) is generally introduced.

$$\phi = E_F - E_I \tag{2.5}$$

where E_F is the Fermi energy and E_I is the ionization energy. Considering a p-type semiconductor (S) the relationship between the work function (ϕ) of the semiconductor and the metal (M) should satisfy $\phi_M < \phi_S$ in order to electron transfer to occur from the metal to the semiconductor until thermodynamic equilibrium is reached [95, 96]. For example Cu_2O (ϕ: ca. 5.0 eV) and Ag (ϕ: 4.7 eV) fulfills the above condition, therefore it is expected that the Fermi level of Cu_2O is upward shifted to establish a new equilibrium [97, 98]. This way the projection of visible light excited electrons from the conduction band of Cu_2O to metallic Ag became favoured which could limit fast charge recombination and accordingly enhance photocatalysis.

Similarly when an n-type semiconductor and a metal gets in contact and $\phi_M > \phi_S$ holds true then electron flow from the semiconductor to the metal may occur. For example at a TiO_2 (ϕ: ca. 4.6-4.7 eV) and Pt (ϕ: 5.4-5.6 eV) interphase the electron transfer is favored as described above. In contrast, at a TiO_2-Ag interphase where the Ag (ϕ: 4.7 eV) represents close values for the work function of TiO_2 no significant electron transfer would be expected to take place between the two materials. This was previously supported by experimental findings as well when the photocatalytic activities of a Pt- (ϕ: 5.4-5.6 eV) and Ag-modified TiO_2 was studied [99]. The authors found that Ag had only minor effect on the overall photocatalytic performance whereas the Pt notably enhanced the photoactivity of TiO_2. The better performance of TiO_2/Pt catalyst was attributed to the more beneficial work potentials of Pt relative to TiO_2 that could promote effective charge separation.

Plasmonic photocatalysts with different morphologies can be fabricated by various methods including chemical reduction and photoreduction routes. A range of noble metals including Ag, Au, Pt or Pd has been already coupled with various semiconductors in the literature and utilized as plasmonic photocatalysts.

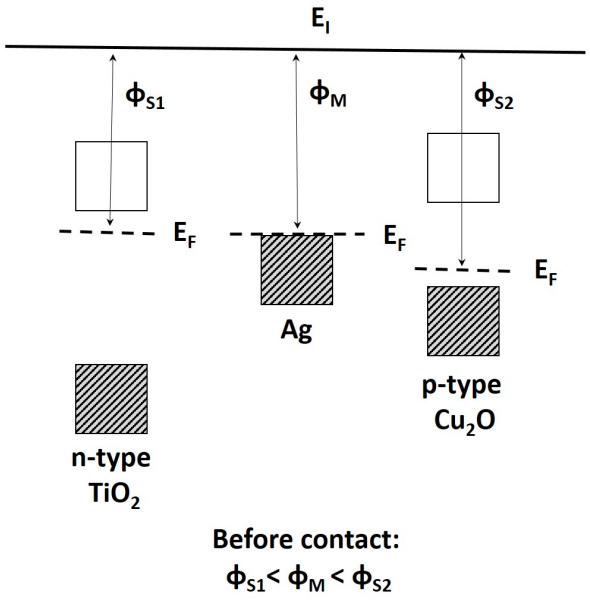

Fig. 2.6 Schematic representation of the work function values for an n-type semiconductor (TiO_2), a p-type semiconductor (Cu_2O) and for a metal (Ag)

A chemical reduction technique has been employed by *Dinesh et al.* who used functionalized ZnO nanorods to prepare ZnO/Ag core/shell nanostructures. Significant visible light absorption has been shown by the core/shell nanomaterials thanks to the electronic coupling of ZnO and Ag. The photocatalytic studies revealed that the hybrid ZnO/Ag nanorods could faster eliminate the R6G dye compared to ZnO nanorods [100]. Elsewhere, the chemical reduction of Ag nanoparticles was performed in a successive ionic layer adsorption reaction (SILAR) onto WO_3-loaded TiO_2 nanowires. The enhanced photocatalytic activity of the ternary nanostructure over TiO_2 nanowires was attributed to the extended visible light absorption and the effective charge separation. Although it was noted that excessive Ag coverage hindered the photoactivity probably due to the increased reflection of the metal nanoparticles and to the reduced level of methyl orange adsorption [101].

Having employed a photoreduction approach *Qamar et al.* presented the synthesis of Au- and Pt-WO_3 nanostructures. The authors found that the Pt-deposition onto WO_3 beneficially affected the photoactivity while the Au modification reduced its performance.

The negative effect on the photodegradation of methyl orange was accounted for the different size distribution of 2-4 nm and 10-15 nm of Pt and Au noble metals, respectively [12].

Beside deposition techniques, direct mixing of metal and semiconductor nanostructures has been presented as well. *Pan et al.* for example separately synthesized 3-5 nm small Au nanoparticles functionalized with oleylamine and Cu_2O nanowires protected with an *o*-anisidine layer by a chemical reduction approach and hydrothermal reaction, respectively. In the final step the pre-synthesized and functionalized materials were ultrasonically treated in chloroform to prepare Cu_2O-Au nanostructures. The light absorption of bare Cu_2O was improved by the Au nanoparticles that exhibited a plasmon resonance peak at around 517 nm. The coupled Cu_2O-Au hybrid structures were also shown to exhibited superior photoactivity over Cu_2O in the degradation of methylene blue [13].

Beyond the benefits of plasmonic metals, some research works highlighted that the metal deposites might not always show excellent stability over multiple cycle of use in photocatalytic reaction [93]. Also some authors mentioned the increasing price of using noble metals and the possibility of undesired secondary pollution as challenges of plasmonic photocatalysis [101].

Dye sensitization

Another strategy to extend the light absorption of semiconductors further to the visible range is to couple them with visible-response dyes [102]. In a semiconductor-dye arrangement, the dye can effectively absorb the incident photons and act as a photosensitizer to generate the electron-hole pairs. In the event of adequate band alignment between the dye and the semiconductor the separation of charge carriers could be established by transferring the photo-generated electrons from the CB of the dye to the CB of the semiconductor [103]. Then the injected electrons can be utilized in surface reactions as it is depicted in Figure 2.7. Same Figure also shows that as an alternative route the dye may go through degradation

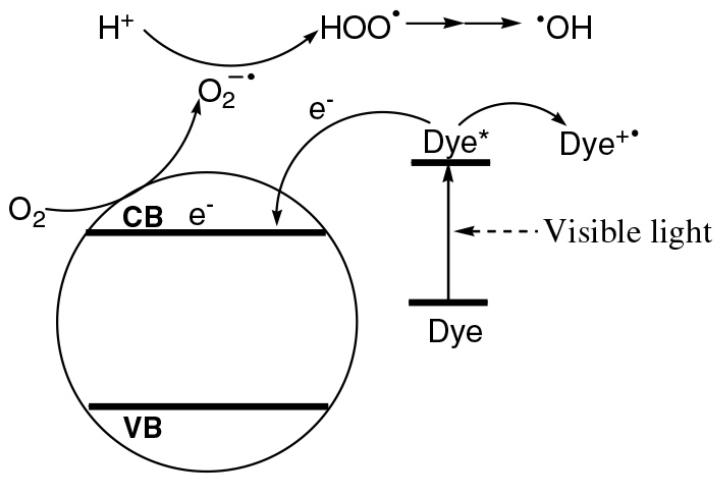

Fig. 2.7 Schematic representation of the charge transfer mechanism between a dye and a semiconductor in a dye sensitized photocatalyst. This figure is reproduced from [103] with permission of Springer.

processes in the presence of oxygen which is an undesired process. Despite this challenge, this mechanism has gained widespread utilization in dye-sensitized solar cells and also has been researched for photocatalytic application.

Varius dyes has been coupled with semiconductors including those of natural and synthetic origins. For example, *Wahyuningsih et al.* prepared a natural anthocyanin dye sensitized TiO_2 photocatalytic system by adsorbing the dye onto the semiconductor surface. The authors highlighted that the benefit of this system was the non-toxic nature of the dye and the ability to completely photomineralize the target organics, namely Rhodamine B. However, it was also noted that the dye was inactivated in the first run of the photocatalytic process therefore TiO_2 needed to be retreated with the dye for further use [104]. Elsewhere, TiO_2 thin film was sensitized by the natural dye extract of *Picramnia sellowii* and tested for the photocatalytic treatment of real waste water. It was reported that the natural dye could cover the entire visible spectrum. Furthermore, the total organic carbon measurements revealed that the senzitised thin film was more efficient relative to reference TiO_2 thin film. It was

also found that the recycling of the sensitized thin film was possible up to five cycles without major loss of photoactivity [105].

Beside TiO_2 other complex systems have been coupled with dyes, too. *Jin et al.* presented an eosin Y-sensitized CuO/TiO_2 system for photocatalytic hydrogen evolution under visible light irradiation in the presence of diethanolamine that acted as a sacrificial electron donor [106]. It was found that the complex photocatalytic system overperformed both CuO/TiO_2 and a Rhodamine B-sensitized CuO/TiO_2 catalyst. The authors attributed the enhanced photoactivity to the Eosin Y dye that significantly improved the light absorbance of CuO/TiO_2 and could transfer electrons to the CB of TiO_2 and finally to the CB of CuO. The dye sensitized CuO/TiO_2 system has also demonstrated good stability over several tens of hours. Elsewhere a range of different dyes including thionine, eosin Y, methylene blue ...*etc* has been employed to sensitize TiO_2 and TiO_2/Pt systems. The authors found that the eosin Y-sensitized TiO_2/Pt produced the highest amount of hydrogen over visible light irradiation in the presence of electron donors. It was also concluded that for the sake of catalyst stability the photocatalytic system should be freed from oxygen [107]. Similarly a cyanoacrylic acid synthetic dye/TiO_2/Pt photocatalyst has been presented by *Kang et al.*. The authors believe that the organic dye derivatives could establish strong adsorption to the TiO_2 surface via chemical bonding thanks to the -COOH side chains. The photocatalytic H_2 generation was performed under nitrogen atmosphere in the presence of electron donors. It was found that the functional groups of the dye critically affected the effeciency. In fact, it was concluded that hydrophilic side groups were more beneficial for the photocatalytic hydrogen generation over hydrophobic ones [108].

Modification with inorganic carbon materials

Inorganic carbon-semiconductor nanocomposites has attracted considerable attention for their benefits to improving the photocatalytic activities of semiconductor nanomaterials. It

was revealed that using for example graphene, graphene oxide (GO), reduced graphene oxide (rGO) or carbon nanotubes (CNTs) in conjunction with other semiconductors or composite structures could effectively improve the material properties that may include retarded electron/hole recombination, improved stability or hindered aggregation of the nanocrystals. It has been recognized that these carbon related materials could mediate electrons and holes effectively which could promote interfacial charge transfer and may enhance the lifetime of the charge carriers [5]. This mechanism could be especially adventageous in semiconductors with limited charge carrier mobility and short diffusion length of charges [23].

Jin et al. reported that a Cu-TiO_2 structure that was homogeneously distributed on a graphene nanosheet could significantly enhance both the optical and visible photocatalytic properties of TiO_2. The authors suggested that the graphene sheet could facilitate the adsorption of methylene blue to the catalyst surface via $\pi - \pi$ stacking between the dye and the graphene sheet which could promote the photoactivity. Also the inhibited charge recombination by Cu and graphene was accounted for the better photoactivity [109].

Some researchers argue that the relatively few functional groups on the surface of graphene makes it difficult to utilize it in nanocomposite material formation. As alternative materials graphene oxide and reduced graphene oxide are commonly used. *Kim et al.* for example coupled Cu_2O with GO by an electrochemical deposition technique and tested the photoelectrochemical performance of the material. The amount of GO was varied in the composite thin film between 1% and 30%. It was found that the 1% GO-Cu_2O film could achieve the highest activity that was ascribed to its reduced band gap of 1.94 eV which was the smallest among the prepared thin films [110].

Xu et al. synthesized a Ag-Cu_2O/rGO hybrid material by a one-pot and two-stage reduction method. The authors found that the absorption edge of the Ag-Cu_2O could be further red-shifted by coupling with rGO which resulted in the best visible light utilization among single and binary hybrid reference materials. The highest photoactivity measured in

the photobleaching reaction of methyl orange also belonged to the ternary hybrid material. The enhanced performance was explained by the improved charge separation and better light harvesting properties of Ag-Cu_2O/rGO. Additionally it was also noted that coupling with rGO could significantly improve the stability of Ag-Cu_2O possibly through encapsulation or protective layer formation over the nanocrystals that inhibited oxidative degradation of Cu_2O [96]. Elsewhere, *Vinoth et al.* synthesized rGO with AgI-mesoTiO_2 composite material in a sonochemical procedure. The authors found that the presence of rGO reduced the optical band gap of the nanocomposite from 2.80 to 2.65 eV. It was suggested that the chemical bonding between rGO and TiO_2 could lead to narrowed band gap. The authors also reported that the visible photoactivity of the ternary hybrid material toward methyl orange was enhanced by 60% when compared to AgI-mesoTiO_2. The good methyl orange adsorption, the reduced electron/hole recombination and the fast charge carrier transport properties of rGO was accounted for the improved photoactivity [111].

Carbon nanotubes (CNTs) are also an attractive option to fabricate nanocomposite materials with semiconductors thanks to their unique tubular structure, enhanced surface area and good electron transport properties. In the literature, carbon nanotubes with single- (SWCNTs) and multiwall (MWCNTs) has been already synthesized and coupled with other materials for photocatalytic application. For example single-walled CNTs has been linked to a ZnO-TiO_2 heterostructure by *Liu et al.* in a microwave-assisted chemical reaction. The as-prepared ternary nanostructure was tested in the photocatalytic reduction of Cr(VI) under UV light. The authors found that the 3 weight % CNTs containing nancostructure exhibited the highest performance that was attributed to the improved light absorption and electron-hole separation of the ternary hybrid structures [112]. *Natarajan et al.* fabricated multi-walled CNTs/TNTs nanocomposites by a hydrothermal method in different weigth ratios. They reported that the nanocomposites exhibited increased light absorption in the visible range. The narrowing of their band gap was more pronounced for nanocomposites with higher

MW-CNTs weight percentages. It was also found that the photodegradation of RhB-6G dye under UV light was enhanced by the presence of carbon nanotubes with highest degradation rate achieved by 10% MWCNTs/TNTs. This was explained by the enhanced dye adsorption, increased surface area and porous structure of the nanotubes along with the reduced charge recombination across the heterojunction which was proved by photoluminescence [113].

2.3 Immobilization techniques

In the past decades, immobilization of powder photocatalysts has gained increasing research interest in circumventing difficulties associated with powder photocatalyst utilization in potential environmental remediation technologies.

Although nano-sized powder catalysts are typically characterized of high surface area and good mass transfer character between the liquid and solid phase, they are accounted for complex post-treatment recovery, increased danger of leaching out and health and safety concerns of breathing in fine powders when working with loose nanomaterials [114]. Also the light utilization efficiency of suspended powders could be limited by increased turbidity in liquid phase [14, 115]. To aid complete removal of suspended photocatalyst, the combination of different techniques may be required such as sedimentation and high performance filtration processes. However, fine powders could require long hours to sediment along with big capacity tanks and expensive filtration equipments which considerably increase both the capital and running cost of the process [9].

In this regard, immobilized photocatalysts are considered to be a promising option to facilitate the post-treatment separation process, minimize the loss of photocatalyst and ensure safer handling of the catalytic material [116]. Also with carefully designed and selected support matrices enhanced light utilization could be achieved as well.

Immobilization of photocatalyst has been achieved on various type of solid materials. For example glass, polymer, ceramics, silica, metal substrates possessing various shapes

like sheets, beads, fibers, fiber mats or membranes have been already tested to support photocatalytic materials [117, 118]. In some cases, the direct coverage of reactor walls or other reactor specific parts have been also demonstrated [119]. Ideally support materials are desired to be chemically and mechanically stable, to provide high surface area and strong attachment of the catalyst and to retain or further improve the photocatalytic activity. However, in reality meeting all these conditions is very challenging.

Various substrates were found to exhibit adequate inertness and chemical stability over the photocatalytic process including ceramics, glass, metal or certain polymeric supports. However, depending on the operation conditions the stability of these substrates could be significantly affected. It was noted by *Geltmeyer et al.* that under non-harsh conditions polyamide 6 membrane could be an ideal economical support material, while under highly acidic conditions a silica based nanofibrous membrane could be effectively utilized [115]. In another study, *Chin et al.* compared the stability of various polymeric membranes under UV light irradiation and oxidative conditions. They found that polytetrafluoroethylene and polyvinylidene fluoride polymers exhibited good stability under these conditions whereas polyacrylonitrile was found to be instable [120].

By immobilizing photocatalyst the mass transfer becomes limited as the contact area of the catalyst typically gets reduced. To mitigate these difficulties substrates with increased surface area could be used to support the photocatalyst such as nanofibrous mats or membranes. For example, *Geltmeyer et al.* fabricated silica and polyamide 6 nanofibrous membranes that were loaded with TiO_2 nanoparticles for water treatment application to benefit from the high surface area and the porosity of the support materials. The authors reported that the prepared membranes exhibited high photoactivity towards methylene blue and isoproturon thanks to the optimized TiO_2 loading strategy [115]. Elsewhere a flexible fiberglass cloth was used by *Tasbihi et al.* and his co-workers to provide high surface area support for commercially available TiO_2 nanoparticles. They used a ”binder”-sol to firmly attach the TiO_2 powders

to the flexible surface by a dip-coating method. The prepared fiberglass cloth showed high potential to effectively degrade toluene in gaseous phase [118].

Beside the surface area, the light utilization efficiency is also an important factor for photochemical application. To maximize light harvesting, floating photocatalyst has been developed and tested for water remediation application [14]. The low relative density of the support material could allow the catalyst to float in the liquid medium resulting in better exposure to light and oxygen. This could represent a comparative advantage over suspended powder catalyst that generally exhibit significant light scattering when suspended in water. It is also worth noting that only a fraction of the light reaches the deeper regions of water due to light attenuation [121]. In contrast, buoyant photocatalyst could effectively utilize light and effectively target surface accumulated contaminations such as oil spills. *Magalhaes et al.* has reported a floating photocatalyst by preparing TiO_2/low-density polyethylene (LDPE) composite beads. The photocatalytic activity was performed in methylene blue solution under restricted conditions including the absence of agitation and/or oxygenation. Under identical conditions, the immobilized catalyst showed significantly higher efficiency than P25 powder catalyst. The authors proposed that floating catalyst could be directly utilized in the treatment of contaminated wastewater reservoirs eliminating the need of special equipments providing stirring and oxygenation. The improved efficiency of the immobilized catalyst was attributed to the better light and oxygen utilization [122]. Others used polypropylene fabric or polystyrene beads to prepare buoyant TiO_2 and ZnO photocatalyst, respectively [121, 123].

To retain high light harvesting ability of the photoactive materials, transparent solid supports can be also used such as borosilicate, quartz, Pyrex or conductive glasses. Glass beads and sheets have been extensively used to support various photocatalysts [124]. For example, a TiO_2 film/Cu_2O microgrid has been fabricated by *Zhang* and his co-workers on a quartz substrate [125]. Others used a microscope slide to deposit Cu_2O thin film [36]. *Wang*

et al. prepared porous glass beads supported TiO_2 photocatalyst for the photobleaching of methyl orange with high efficiency [126].

Immobilization of various semiconductor photocatalyst can be achieved by two main approaches, namely by *in-situ* synthesis/deposition of the active photocatalyst or by the direct immobilization of powder catalyst to the substrate surface.

2.3.1 *In-situ* synthesis coating techniques

One approach to fabricate immobilized photocatalysts is the *in-situ* synthesis of the photoactive compound on the support material. These synthesis processes may be gaseous- or liquid-phase approaches. Among the gaseous-phase techniques physical (PVD) and chemical vapour deposition (CVD) methods are commonly utilized such as magnetron sputtering and atomic layer deposition (ALD), respectively. Whereas typical liquid-phase techniques could include chemical bath deposition, successive ionic layer adsorption and reaction (SILAR), sol-gel or hydrothermal methods. Also, electrochemical routes can be utilized to coat substrates with photocatalytic materials.

Physical vapour deposition techniques may apply different approaches like thermal heating or ion bombardment to evaporate or sputter a source material that finally forms a thin film via condensation [127]. Among PVD techniques, for example a radio-frequency magnetron sputtering method has been used to deposite TiO_2 film layer over a quartz substrate. The as-prepared thin films were further modified with Au and Ag to create a plasmonic composite film [128]. Others fabricated a TiO_2/Cu_2O microgrid heterojunction over a quartz substrate where direct-current magnetron sputtering technique was used to deposite Cu_2O over the TiO_2 film [125].

CVD methods are based on the chemical reaction facilitated on the surface of a substrate material between gaseous reactants. It is widely utilized to coat substrates of different geometries and complex shapes. For example, a fiberglass substrate has been coated by

Cu_2O using an atmospheric CVD method [129]. Elsewhere, a flame-assisted CVD technique was employed to prepare Cu_2O films on a glass substrate that exhibited high antibacterial photoactivity [130]. Atomic layer deposition (ALD) is a modified CVD method that further benefits from high level of control over the deposited film thickness. Due to the alternate introduction of the reactant gases, in an ALD process, the film deposition is self-limited by surface saturation and in theory the film thickness can be controlled by the number of ALD cycles [131]. *Levchuk* and his co-workers used ALD to coat an aluminium foam substrate by TiO_2. The immobilized photocatalyst was tested in the photodegradation reaction of formic acid and phenol and compared to the activity of suspended P25. It was found that although the aluminum foam-supported TiO_2 exhibited good photocatalytic performance, the quantum efficiency of the powder P25 catalyst was still higher [132]. Also, *Cheng et al.* reported the fabrication of a core-shell nanopillar-array SnO_2-TiO_2 thin film on a ITO glass substrate. Both SnO_2 and TiO_2 layers were deposited by ALD technique over an anodic alumina oxide (AAO) template that was removed by post-chemical dissolution. The nanopillar-array composite film exhibited high surface area and good charge separation character that promoted the photodecomposition of MB. It was found that the as-prepared film could overperform even the flat layer-by-layer configuration of the SnO_2-TiO_2 composite film [11].

In general, liquid-phase synthesis processes are facile and low-cost techniques by which a range of semiconductors can be produced. The substrate may be immersed into the reaction mixture or alternatively, especially for sol-gel processes, the precursor sol could be sprayed or spread over the support material. Most of these processes are followed by post-thermal treatment which was shown in some cases to improve the crystallinity of the nanostructures and promote strong adherence to the substrate [133]. The combination of different wet-chemical approaches is also commonly performed to fabricate e.g. high aspect-ratio nanostructures or composite heterostructures.

Multiple wet-chemical approaches have been employed by *Nan et al.* to fabricate ZnO nanoarrays and ZnO/CdS core/shell heterostructures on an FTO glass substrate. The ZnO nanoarrays were hydrothermally grown over a ZnO seed layer that was deposited by a sol-gel spin-coating method. The ZnO seed layer was also thermally annealed at 510 °C after deposition. To prepare the ZnO/CdS core/shell film a chemical bath deposition technique has been employed that was followed by a calcination step up to 600 °C. The highest photocatalytic hydrogen evolution was noted for the composite thin film annealed at 550 and 600 °C. The enhanced performance was believed to be caused by the reduced number of defect sites at the interphase and by the improved crystallinity thanks to the thermal treatment [134]. Others prepared WO_3 and Ag-doped WO_3 thin films on a microscope glass slide by a chemical bath deposition method. The authors reported improved crystallinity when the film was annealed at 600 °C. The characterisation of the thin film revealed a uniform and dense coverage over the substrate. Additionally, the photodegradation reaction of methyl orange and phenol was significantly improved by Ag-doping which was attributed to the reduced charge recombination [135].

The SILAR approach is a modified chemical bath reaction where instead of using a one-pot reaction mixture the substrate is sequentially made in contact with separate precursor solutions. Similarly to ALD, the number of repetitions provide control over the thickness of the deposited film [136]. *Lv et al.* used SILAR approach to deposit Bi_2S_3 and CdS quantum dots (QDs) onto TiO_2 nanotube arrays that was supported on a Ti foil. The highest photocatalytic activity towards methyl orange dye was noted when the CdS deposition was repeated 4 times and the Bi_2S_3 one time. The improved photoactivity was attributed to the increased light absorption and enhanced charge separation [137]. Elsewhere $BiVO_4$ film layer has been deposited onto TiO_2 thin film by SILAR technique. The heterojunction exhibited improved light utilization in the visible range and showed good activity to decompose Rhodamine 6G dye [138].

Electrodeposition is another commonly employed technique to fabricate immobilized photocatalyst. In this process, electrical current is applied to facilitate redox reactions to take place such as the reduction of metal cations from their electrolyte solution [128]. Direct-current electrodeposition and atmospheric-pressure chemical vapour deposition techniques were employed by *Chen* and his co-workers to fabricate ordered TiO_2-Pt nanotube arrays on a Ti substrate. The Pt nanotubes were prepared via an anodic aluminium oxide (AAO) templated electrodeposition method onto which the TiO_2 film layer was deposited by CVD technique followed by thermal treatment at 430 °C. The photoactivity of the as-prepared composite film was tested against phenol which showed a significant improvement relative to TiO_2 reference film. The enhancement was attributed to the effective charge separation between TiO_2 and Pt [139].

2.3.2 Immobilization of powder catalyst

Beside the *in-situ* synthesis approach the direct utilization of powder photocatalyst is an alternative technique. To immobilize powder catalysts mainly liquid based approaches are employed where the suspension of the powder may be distributed by dipping, spraying, spreading or spin-coating techniques, alternatively by impregnation. Strong adhesion of the photocatalyst to the substrate surface are usually established by means of chemical bonding and/or physical interactions over a thermal treatment step [124]. Non-liquid based methods may attach the powder catalyst directly by thermal treatment.

During dip-coating the substrate is withdrawn from the catalyst suspension to form a film layer. In an automated environment the pull-out rate can be adjusted to optimize the film characteristics [124]. Spray-coating is another alternative technique in which the solution is sprayed over the substrate surface. In both cases complex geometries such as spherical beads or fibers can be coated as an advantage [116].

For example, *Park et al.* used a set of organic and inorganic binders including poly(methyl methacrylate) (PMMA), poly(vinyl alcohol) (PVA), sodium silicate and zinc phosphate to immobilize ZnO and TiO_2 powders by dip-coating and spray-coating methods. The strong attachment of the nanoparticles was confirmed by XRD measurements before and after 10 minutes of sonication. The photocatalytic activities of the immobilized ZnO and TiO_2 structures were tested in a photocatalytic Ag ion extraction reaction which revealed that ZnO immobilized by zinc phosphate exhibited the highest performance among the supported catalysts. As a reference the catalysts were also tested in a suspended powder form which showed about 25% higher Ag extraction after 60 minutes than the best performing immobilized system. Surprisingly immobilized TiO_2 catalysts were inactived in the photocatalytic process [114].

Some researchers argue that binders could potentially encapsulate the photocatalyst that may significantly reduce their respective surface area and hence reduce their photoactivity [116]. To minimize embedding of the photocatalyst by the substrate *Matsuzawa et al.* presented a dip-coating method to prepare polymer-supported TiO_2 photocatalyst based on electrostatic interaction between the surface of the catalyst and the substrate. To achieve this the polyester nonwoven fiber was firstly coated with a SiO_2 layer followed by a thin film of polyvinyl chloride-polyvinyl acetate copolymer coating. The former layer was implemented to protect the polymer fiber from photocatalytic damage whereas the second layer modulated the surface properties of the polymer to favour electrostatic interaction with TiO_2. The photocatalytic test was performed both in liquid and gaseous phase using dyes (MO and MB) and toluene, respectively. It was found that the immobilized TiO_2 possessed high performance in the degradation of different chemicals [140].

Beside dip-coating and spray-coating techniques another route to immobilize powder photocatalyst is spread-coating. One way to achieve this is doctor blading. In this approach, a coating knife fixed at a given distance is moved along the length of the substrate to uniformly

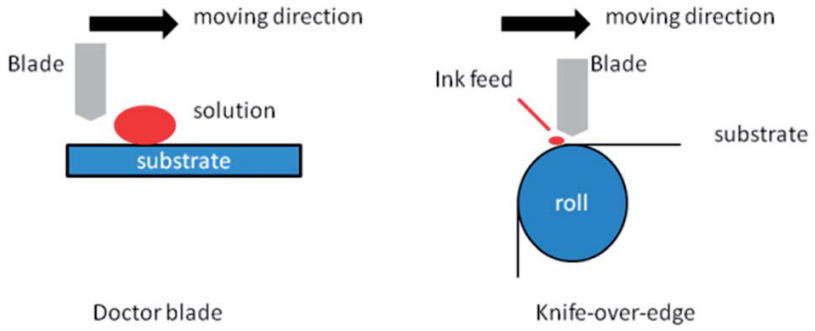

Fig. 2.8 Schematic representation of doctor blading coating technique shown on the left whereas "knife-over-edge" coating technique is depicted on the right. This figure is reproduced from [141] with permission of the Royal Society of Chemistry.

spread the paste over its surface [141]. In laboratory, tapes can be used to mask the surface of the substrate and to control the deposited layer thickness. In industry, this process can be also used in a continuous fashion that is often referred as "knife-over-edge" coating technique. Figure 2.8 shows a schematic representation of both laboratory and industrial scale utilization of this technique.

Jonstrup et al. fabricated borosilicate glass supported TiO_2 thin films by a spread-coating technique. An ethanol based TiO_2 paste was spread over the glass surface and subsequently treated at 550 °C. The photobleaching reaction of Remazol Red dye showed that the performance of the immobilized catalyst was only slightly reduced compared to that of the slurry TiO_2 photocatalytic system [142]. Elsewhere, *Lamdab et al.* prepared an $InVO_4$-$BiVO_4$ composite thin films with varying film thickness by doctor-blade coating method. The deposited films were annealed at 250 °C. They found that the three-layer coating heterojunction film exhibited the highest visible photoactivity in the photobleaching reaction of methylene blue [143].

Impregnation is another method to coat porous or non-porous substrates. For example *Rachel et al.* impregnated porous lavas with TiO_2 that served as support matrices for the photocatalyst. A TiO_2 slurry was spread over the lava stone by a brush. To exhaust the pores and to aid the penetration of the photocatalyst into the porous structure reduced

pressure was applied. Finally the stones were left to dry at 100 °C. In the photodegradation of 3-nitrobenzenesulfonic acid the pumice strone supported TiO_2 showed higher activities than dip-coated cement or red brick substrates [144]. Elsewhere, *Shephard et al.* prepared TiO_2 impregnated fiberglass sheets that were used in a special "falling film" reactor. The impregnated sheets were vertically fixed in the reactor and by a peristaltic pump a continuous recirculation of the reaction mixture was provided as a falling film flow from the top of the sheet. The photocatalytic activity of the impregnated TiO_2 sheet was tested in the degradation reaction of microcystins under UV light irradiation with fast degradation rates [145].

Other immobilization techniques may include thermal fixing or non-liquid based approaches. A dry immobilization procedure was presented by *Tennakone* and his co-workers to immobilize TiO_2 on a polythene film by simple heat treatment. The dry powder was evenly spreaded over the polymer film, then covered by a paper and ironed at 74 °C. In the final step the film was rinsed with NaOH and water and was left to dry. The as-prepared film was shown to be active to decompose phenol under solar irradiation [146]. Others, reported a thermal fixing immobilization approach where the polymeric substrates were heated to their melting points. *Velasquez et al.* coated selected polymeric substrates such as polypropylene and low-density polyethylene with TiO_2 using a heat treatment method. The photocatalyst was suspended in glycerine and mixed with the polymeric supports then heated to the melting temperature of the particular polymer. The authors reported strong adhesion and good stability of the immobilized photocatalyst along with high activity in the degradation of 4-chlorophenol [147].

2.3.3 Summary of literature review

This literature review had three main parts. In the first part the benefits, basic principles and fundamentals of photocatalysis and nanomaterials were outlined. In the second part

the different material modification techniques were reviewed which included doping and heterostructure formation. In the final part immobilization techniques were presented.

It was seen that semiconductor nanomaterials have the potential to photodegrade contaminants in solution or split water. However, as a single material their application is limited by shortcomings. The motivation of material modifications often includes the desire for extended light absorption into the visible range and the development of more efficient photocatalytic systems.

By doping impurity heteroatoms into the crystal lattice good improvements were reported in the light absorption properties of the materials especially in the case of non-metal doping. However, these modifications often resulted in limited enhancement in the photoresponse due to the generated recombination centers. Effective doped systems in photocatalysis were reported in cases when the lattice distortion was minimized by closely matching the ionic radius of the dopant to the host system like in the case of 10% Ta-doped TiO_2 reported by *Cimieri et al* [48]. Also, high photoactivities were reported by *Lin et al.* an N-doped black TiO_2 catalyst which was claimed to be the best performing titania up to date due to the successful substitutional doping process [55].

Similarly to doping, heterostructure formation also showed good achievements in extending light absorption and improving the photoactivity. Effective charge separation was commonly reported for type II heterostructure systems. However, negative effects of lattice mismatch and photocorrosion of small band gap semiconductors was shown to limit the efficiencies of these structures. To overcome this difficulty, *Myung et al.* reported an effective ZnO-CdS core/shell nanocomposite system where they believed the interfacial CdZnS alloy could mitigate the effect of lattice mismatch between the semiconductor layers and hence further promote the photoactivity [79]. Also photocorrosion was shown to be effectively hindered by the deposition of TiO_2 nanoislands onto the surface of Cu_2O nanospheres according to the report of *Liu et al* [89].

In the literature immobilized systems were seen to hold benefits for special applications. By the formation of photocatalyst loaded nanofibrous membranes or flexible fiberglass, treatment of wastewater could be effectively performed by filtration or water circulation for example. Also, buoyant photocatalysts was shown to have the potential to be effectively utilized in wastewater reservoirs where enhanced solar light harvesting and oxygen utilization could be achieved compared to suspended catalysts. For instance, *Magalhaes et al.* reported the development of a TiO_2/low-density polyethylene system which showed higher photoactivity than P25 under restricted testing conditions in a methylene blue solution [122].

Chapter 3

Materials and Methods

3.1 Materials

All chemicals were purchased from Sigma-Aldrich unless otherwise specified and were used without further purification. Sodium tungstate dihydrate ($Na_2WO_4 \cdot 2H_2O$, 99+%, ACS reagent) and ammonium nitrate (NH_4NO_3, 99+%, ACS reagent) were purchased from Acros Organics. Hydrochloric acid (HCl, 37%, ACS reagent), poly(ethylene glycol) powder (PEG, average M_n 3,350 $gmol^{-1}$), poly(ethylene glycol) flakes (PEG, average M_n 20,000 $gmol^{-1}$), poly(ethylene oxide) powder (PEG, average M_n 200,000 $gmol^{-1}$) and methyl orange (MO, Reag. Ph. Eur) were purchased for the synthesis of WO_3 nanostructures. TiO_2 P25 nanopowder (Aeroxide® P25, 99.5%) exhibited 21 nm of primary particle size. Polyvinylpyrrolidone (PVP, average M_n 40,000 $gmol^{-1}$), copper(II) chloride dihydrate ($CuCl_2 \cdot 2H_2O$, 99.0%, ACS reagent), anhydrous sodium hydroxide pellets (NaOH, 98%, reagent grade), L-ascorbic acid (BioXtra, 99.0%) and silver-nitrate ($AgNO_3$, 99.0%, ACS reagent) were used to synthesize Cu_2O and related heterostructures. Ethyl cellulose powder (viscosity 10 cP, 5% in toluene/ethanol 80:20 L) was purchased from Sigma-Aldrich and alpha-terpineol (97+%) from Acros Organics. The FTO glass sheets (TCO30-8) were purchased from Solaronix.

3.2 Experimental procedures and nomenclatures

3.2.1 Synthesis of WO_3 nanostructures

The WO_3 nanostructures were prepared via a hydrothermal synthesis process which was inspired by an earlier publication [148]. In a typical synthesis, 2.0 g of $Na_2WO_4 \cdot 2H_2O$ was dissolved in 45 mL water, then 30 mL of 0.03 g/mL and 0.05 g/mL poly(ethylene glycol) (PEG) and NH_4NO_3 solutions were added to the transparent Na_2WO_4 solution, respectively. The pH was adjusted by 6 M HCl. All chemicals were analytical grade reagents. For the ethanol/water based system the ratio of EtOH/H_2O was set to 1:3 in volume. All the as-prepared solutions were aged at room temperature for an additional 1.5 hours and then transferred to a 150 mL Teflon-lined autoclave. The as-prepared mixtures were treated at 200 °C for 24 hours in a furnace, then left to cool down naturally. The solid precipitates were collected by centrifugation using a Clinispin CT20 type centrifuge at 6500 rpm for 10 min and then washed with distilled water and ethanol for several times. Finally, the as-prepared powders were dried at 100 °C for 12 hours.

3.2.2 Synthesis of TiO_2/Cu_2O and Ag co-catalyzed nanostructures

Synthesis of TiO_2/Cu_2O nanostructure

In a typical synthesis route to make TiO_2/Cu_2O catalyst, firstly 30 mg P25 was suspended in 190 mL water in an Erlenmeyer flask. Then based on a literature procedure, 400 mg polyvinylpyrrolidone (PVP) was dissolved in distilled water followed by the dropwise addition of 10 mL, 0.04 M $CuCl_2$ and 4 mL, 0.4 M NaOH solution [89]. Finally, 4 mL, 0.2 M ascorbic acid solution was added dropwise to the reaction mixture. The as-prepared solution was stirred for 5 more minutes and then centrifuged using a Clinispin CT20 type centrifuge at 6500 rpm for 10 min and washed by distilled water and ethanol several times. The solid matter was dried at 85 °C for 12 h.

Synthesis of TiO_2/Ag/Cu_2O nanostructures

The method was inspired by previous publications [100, 149, 101]. In a typical synthesis process, 300 mg P25 was suspended in 100 mL water in a beaker, then the required volume of a 0.04 M $AgNO_3$ solution was added dropwise to produce 1 w/w%, 3 w/w% or 5 w/w% nominal Ag content. For example, to produce 5 w/w% nominal Ag content, 3.5 mL of 0.04 M $AgNO_3$ solution was added. The as-prepared solution was stirred under UV irradiation by a PLS-SXE300 xenon arc lamp equipped with a PE300BF type light bulb (total Vis light output between 390 nm- 770 nm: 5000 lumen, total UV output for $\lambda < 390$ nm: 2.6 Watts) for 3 hours. Finally, the solution was centrifuged as previously, washed and the solid matter was dried at 85 °C for 12 h.

Synthesis of TiO_2/Cu_xO/Ag nanostructures

For preparing TiO_2/Cu_xO/Ag catalysts, 30 mg of TiO_2/Cu_2O catalyst were suspended in 40 mL water followed the required volume of a 0.004 M $AgNO_3$ solution to produce 1 w/w%, 3 w/w% or 5 w/w% nominal Ag content. For example, to produce 1 w/w% nominal Ag content, 0.7 mL of 0.004 M $AgNO_3$ solution was added. The as-prepared solution was stirred under UV irradiation under the same conditions as TiO_2/Ag/Cu_2O catalysts. Finally, the solution was centrifuged as previously, washed and the solid matter was dried at 85 °C for 12 h.

3.2.3 Preparation method for TiO_2/Cu_2O thin films

FTO glass sheets were used as substrates to prepare TiO_2/Cu_2O thin films. Firstly, the FTO glass substrates were cut into 0.9 cm wide and 4.0 cm long pieces and cleaned ultrasonically in a *circa* 5% detergent solution (Decon 90). Then the glass substrates were rinsed with tap water, distilled water, ethanol and finally dried on air.

Then the TiO_2/Cu_2O paste with either 0% or 100% ethyl cellulose content were prepared as follows. In a general process, TC powder catalyst which were synthesized as described in Section 3.2.2 were used to make TiO_2/Cu_2O paste. Firstly, 50 mg TC powder were ground in a mortar for a few minutes. Then dropwise 0.05 mL distilled water was added under continuous grinding. Then 0.3 mL ethanol was added gradually. The suspension was transferred into a vial with 1 mL ethanol and stirred and sonicated for 10 minutes for each step. While continuously stirred 0.22 mL terpineol was slowly added to the mixture followed by further 10 minutes of stirring and sonication. If the TC paste contained ethyl cellulose then 0.38 mL, 10 w/w% ethanol based ethyl cellulose solution was added dropwise to the mixture and again stirred and sonicated for 10-10 minutes. Finally, a rotary evaporator was used to evaporate the ethanol over the as-prepared mixture [133].

The TC thin films were prepared by doctor-blading technique. The clean FTO glass substrates were masked by Scotch tape to allow a 0.9 cm x 2 cm active area to be covered by the TC paste. After removal of the tape, the thin films were exposed to heat treatment at specific temperatures of 300 °C , 350 °C or 550 °C under N_2 atmosphere in a glass reactor over a hot plate.

3.3 Characterization techniques

Scanning and transmission electron microscope images were recorded to study the morphology and related crystal properties such as the crystal shape and the size distribution of the nanomaterials. For WO_3 nanostructures a LEO 1540XB type RÖNTEC Quantax field emission scanning electron microscope (SEM) and a Philips/FEI CM120 Biotwin transmission electron microscope (TEM) were used. The rest of the catalysts were studied by a FEI F20 type transmission electron microscope equipped with a 8k x 8k CMOS camera and a Carl Zeiss SIGMA HD VP Field Emission scanning electron microscope equipped with Oxford AZtec energy dispersive X-ray analysis system (EDX). To record TEM images of the thin

films part of the film was scrapped off the glass substrate for sample preparation. Samples were prepared by depositing 4 µL ethanol suspension of the samples on a carbon film coated 200 mesh gold grid from Agar Scientific. In a typical TEM measurement 200 kV accelerating voltage was applied. For the SEM imaging, the thin films on the FTO substrate were used. A typical SEM image was taken with 20 kV accelerating voltage and by using a inlens detector for the WO_3 and secondary electron detector for the rest of the catalyst.

The crystal phases of the nanostructures were investigated by X-ray powder diffraction (XRD) by a Bruker D2 PHASER diffractometer using the Cu Kα radiation wavelength ($\lambda = 1.542$ Å). The powders were gently placed onto a glass sample holder and placed into the machine. The diffractograms were collected with the following parameters: scan speed: 0.35 sec/step, high voltage: 30 kV, current: 10 mA , increment: 0.05°. In the case of the thin films, a 2 cm x 2 cm dimension ordinary glass substrate was used to make the thin films specially for the XRD measurement to fit the specific sample holder in the diffractometer.

To estimate the forbidden band gap of the nanostructures solid-phase UV-Visible diffuse reflectance spectra (DR) were recorded by a JASCO V-670 spectrophotometer equipped with an integration sphere. The spectra were taken in the spectral range of 200-850 nm using KBr or $BaSO_4$ as a white reference. The immobilized photocatalyst were scrapped off the glass support and were diluted with the white background material similarly to the powder catalysts. The samples were thoroughly mixed with KBr in a mortar for several minutes to give a homogeneous mixture with 1-5% sample concentration. The as-prepared mixture was loaded into the sample holder and placed into the spectrophotometer for measurement. The spectra were taken with the following parameter settings: data interval: 0.5 nm, UV-vis bandwidth: 1.0 nm, scan speed 100 nm/min.

The solid samples were sent to the University of Birmingham for measurement and calculation of the BET surface areas. The measured BET areas are reported in the thesis but unfortunately the raw BET data are no longer available due to a hardware failure. The

apparent surface areas of the catalysts were measured by a NOVA 2000 gas sorption analyser from Quantachrome Corporation at the temperature of liquid nitrogen and calculated by using the BET (Brunauer–Emmett–Teller) model. In the BET model the surface area of the material is determined by means of physisorption of a non-absorbing gas onto the material surface. The measurement is commonly carried out at the boiling temperature of nitrogen. Usually the BET measurements are performed in a restricted range of relative pressure (between 0.05 and 0.3). The linearized form of the BET equation can be seen in Equation 3.1 where w is the weight of the absorbed gas, p/p_0 is the relative pressure, w_m is the weight of monolayer absorbed gas and c is a constant. By plotting $\frac{1}{w[p/p_0-1]}$ versus p/p_0 a straight line can be obtained. From the slope and from the intercept constant c and w_m can be worked out which can be used to calculate the surface area according to Equation 3.2 where N_{Av} is the Avogadro number and σ_0 is the cross-sectional area of the nitrogen [150].

$$\frac{1}{w[p/p_0-1]} = \frac{1}{w_m c} + \frac{c-1}{w_m c} \cdot \frac{p}{p_0} \tag{3.1}$$

$$S = w_m \sigma_0 N_{Av} \tag{3.2}$$

For surface analysis with regard the composition and chemical states of the catalysts X-ray Photoelectron Spectroscopy (XPS) was employed. The samples were sent to the University of Debrecen in Hungary to be measured by Prof. Erdélyi Zoltán's research group. XPS experiments were conducted by using Al k-α anode (E = 1486 eV) as a source of X-ray and Phoibos 100 MCD-5 series hemispherical energy analyzer produced by Specs.

Attenuated total reflectance of the thin films (ATR-FTIR) was measured by a Perkin-Elmer Spectrum65 type Fourier Transform Infrared Spectrometer (FTIR) with a MIRacle^{TM} Single Reflection ATR attachment from PIKE Technologies which were fitted with a diamond/ZnSe crystal cell. The background measurement was taken in the empty equipment which is shown in Figure 3.1. Subtraction of the background from the measurement spectrum was

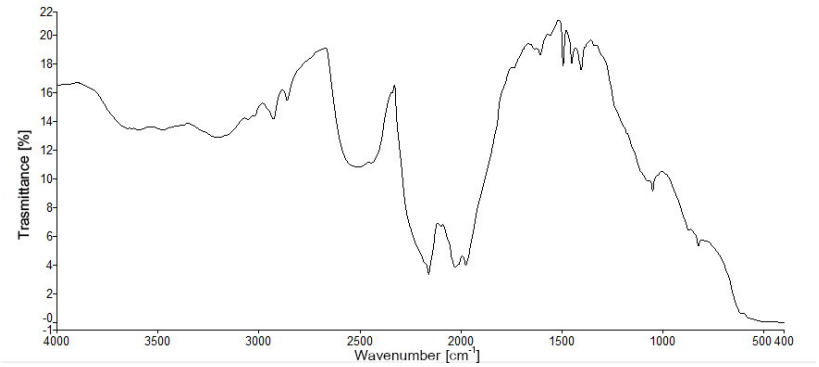

Fig. 3.1 Background spectrum measured in the ATR-FTIR equipment

automatically done by the Perkin-Elmer Spectrum^{TM} software. Typically the transmittance values were measured between 3500 and 600 cm^{-1} with 0.2 sec/step scan speed.

For the total organic carbon (TOC) measurement a SHIMADZU Oceania TOC-V CS instrument was used. The measurement was undertaken at the Budapest University of Technology and Economics at the Department of Chemical and Environmental Process Engineering. The process parameters were set to the following: air flux was set to 150 cm^3/min, 200 kPa pressure was maintained and the combustion temperature of 680 °C was employed. The TOC measurement required 10 mL sample and the analyzer repeated the measurements three times.

High performance liquid chromatography (HPLC) mass spectroscopy (MS) analysis was performed by a Shimadzu Nexera X2 HPLC-AB Sciex 6500 QTrap MS instrument. The measurements were done by the Bálint Analitika Mérnöki Kutató és Szolgáltató Kft. An Agilent PoroShell 120, 50*3 mm, 2.7 µm column was used applying the following process conditions: elution mixture: A: 10 mM aqueous ammonium acetate, B: 10mM acetonitrile, gradient program: 10% B hold for 1.5 min, 90% B reached by 7 min, hold for 1 min, reaching 10% B in 0.1 min. The flow rate was set to 0.5 mL/min.

3.4 Photocatalytic testing

For testing the photocatalytic activity of the powder catalysts and the thin films, seperate photocatalytic testing systems were employed whose schematic representations are shown in Figure 3.2 a) and b), respectively.

The powder catalysts were studied in a batch-type jacketed quartz reactor under continuous air bubbling and agitation. In the jacket of the quartz reactor cooling water was circulated in order to prevent heating of the reaction mixture. The reactor was irradiated from 6 cm above the liquid level by a PLS-SXE300 xenon arc lamp. The lamp was equipped with a PE300BF type light bulb which has an input power of 300 Watts and a total radiant output power of 50 Watts which involves a total Vis light output of 5000 lumen between 390 nm–770 nm and 2.6 Watts of total UV output for $\lambda < 390$ nm. The light intensity for the UV-Vis photocatalytic tests was calculated to be *circa* 5.5 Wcm^{-2}. When using a 420 nm cut-off filter the light intensity was calculated to be *circa* 0.4 Wcm^{-2}. In a typical photocatalytic test, a given amount of powder catalyst was suspended in methyl orange (MO) dye solution. The photocatalytic testing conditions for the powder catalysts are summarized in Table 3.1. Before light exposure, the suspension was left to be stirred in darkness to allow adsorption of the dye to the catalyst surface. At regular intervals, samples were taken from the reaction mixture and the solid matter was separated from the solution by centrifugation. Then using a UV-Vis spectrophotometer (Analytic Jena Specord250) the dye concentration was determined from the absorption maximum at $\lambda = 465$ nm using WinASPECT Software. Reference measurements were also carried out in complete darkness. In order to perform repeated experiments after each cycle of use the powder catalysts were washed with distilled water several times, rinsed with ethanol and dried at room temperature.

The photocatalytic activities of the thin films were studied in a quartz cell (Hellma® Suprasil® quartz, 3500 µm) under continuous stirring. The quartz cell was irradiated 1 cm apart from the side by a white LED (New Lumileds, LUXEON COB Gen3 White CoB

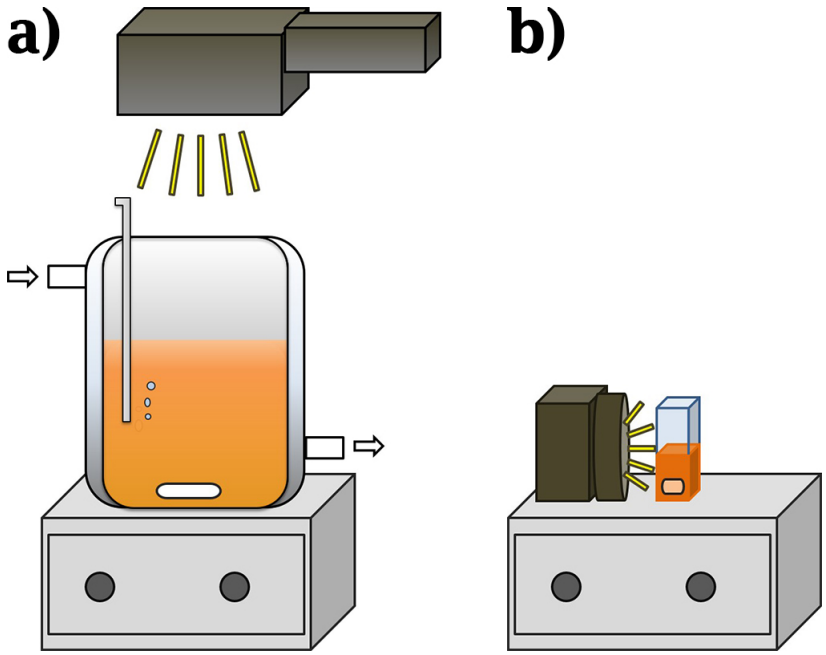

Fig. 3.2 Schematic figure of the photocatalytic set-up a) for powder catalysts and b) for the supported catalyst

Table 3.1 Photocatalytic testing conditions for powder catalysts

Powder catalysts	Catalyst	MO solution		Dark stirring
	mg	mL	mg/L	min
WO_3 nanostructures	50	150	20	60
TiO_2/Cu_2O and Ag-cocatalysed systems	20	60	20	60

LED, 3500K 90CRI) which has emission λ >400 nm and a typical luminous flux of 2533 lm along with 121 lm/W luminous efficacy. In a typical photocatalytic test, the thin films with 0.9 x 1.0 cm active area were immersed into 2.0 mL and 15 mg/L MO solution. Before the light exposure the thin films were left in the stirred MO solution in darkness for 60 min. At regular time intervals the thin films were removed from the solution and the concentration of the MO solution was followed by a UV-visible spectrophotometer using the same equipment and method as for the powder catalyst described previously. Reference measurements were also carried out in complete darkness. The recycling test of the thin films were carried out after the recovery of the films. After each cycle of use the catalysts were left to be stirred in a

9% NaCl solution until complete desorption of the dye has been achieved. The films were subsequently rinsed with distilled water, dried overnight at room temperature and used in a repeated experiment.

3.5 Models and calculations

3.5.1 Calculation of the MO concentration

UV-visible spectroscopy

In the thesis, ultraviolet-visible (UV-vis) spectroscopy was used to follow the concentration of a coloured dye, namely methyl orange (MO). The molecular structure of the dye is depicted in Figure 3.3. In the UV-vis spectroscopy the interaction between the UV or visible light and the chemical substance is recorded. By absorbing portion of the irradiated light, vibrational and rotational electron excitation can be induced in a molecule that reflects the chemical structure of the substance in a given environment [151]. From the incident and transmitted light intensities (I_0 and I_T, respectively), the light absorbance (A) can be defined as shown in Equation 3.3. According to the Lambert-Beer law, the light absorbance (A) may show linear relationship to the solution concentration (c), where ε is the molar absorption coefficient, l is the path length and c is the concentration in the solution (see in Equation 3.4).

$$\mathrm{A} = log\frac{I_0}{I_T} \tag{3.3}$$

$$\mathrm{A} = \varepsilon \cdot \mathrm{l} \cdot \mathrm{c} \tag{3.4}$$

By taking the absorption maximum at $\lambda = 465$ nm which is characteristic for MO, the calibration curve of the dye could be constructed which is shown in Figure 3.4. From the slope of the absorbance versus concentration curve, the molar absorption coefficient of MO

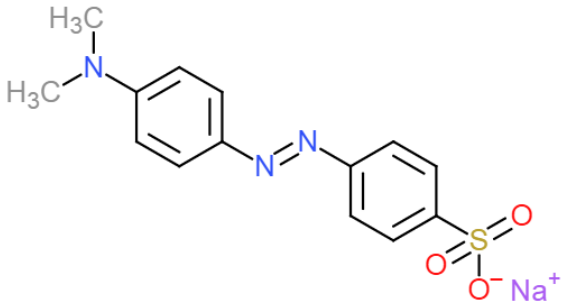

Fig. 3.3 Chemical formula of methyl orange

could be determined. The linear relationship between the absorbance and concentration allowed us to use the Lambert-Beer law to calculate the concentration of the dye. A sample calculation for the MO concentration is given below.

$$c = \frac{A}{\varepsilon[\mathrm{Lmg^{-1}cm^{-1}}] \cdot l[\mathrm{cm}]} = \frac{1.215}{0.0773 \cdot 1} = 15.72 \text{ ppm} \tag{3.5}$$

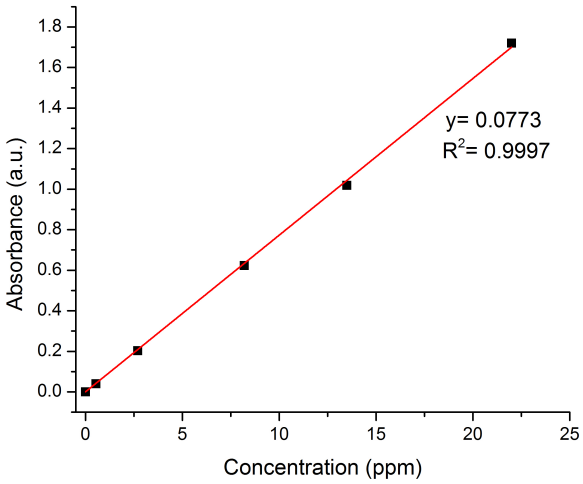

Fig. 3.4 Calibration curve of MO absorbance plotted in the function of concentration

3.5.2 Estimating the crystallite size

Scherrer-Debye formula

The crystallite sizes of the samples were calculated from their respective powder diffraction pattern using the Scherrer-Debye equation (k=1, λ= 1.542 Å) where FWHM is the full width of the peak at half maximum, k is a shape factor, λ is the wavelength, d_s is the Scherrer diameter, θ is the diffraction angle.

$$\text{FWHM} = \frac{k \cdot \lambda}{d_s \cdot cos\theta} \tag{3.6}$$

To provide sample calculation for the crystallite size determination, TC-0-300 thin film sample was chosen as an example. The crystallite size of the anatase TiO_2 content of the film was calculated as follows. The Scherrer dimension was calculated based on the (101) hkl peak of the anatase phase which appeared at 25.3°.

$$d_s = \frac{k \cdot \lambda[\text{Å}]}{\text{FWHM} \cdot cos\theta} = \frac{1 \cdot 1.542}{0.005 \cdot 0.9758} = 320 \text{ Å} = 32 \text{ nm} \tag{3.7}$$

The calculated Scherrer dimensions (d_s) are estimated values that involve certain assumptions. Correction for instrumental peak broadening was taken into account prior to calculation by using reference sample (corundum) provided to the XRD diffractometer. Because the size-related peak broadening is usually notable for crystallites below 100 nm, the instrumental broadening is typically measured by using a large enough well-crystalline material that has only negligible effect on the peak broadening. This allows the determination of the instrumental contribution [152–154]. Peak broadening was measured at the full width at half maximum (FWHM) at a particular peak position for example for corundum reference sample FWHM(25.5°) = 0.06° was measured. The data collection of reference and sample was performed under the same recording conditions. Within the range of (25.5°–52.5°°) the peak broadening was measured to be FWHM= $0.063° \pm 0.006°$. For convenience and due

to limited available peak positions in the reference XRD pattern the sample FWHM was corrected by 0.063.

In reality apart from the instrumental contribution crystal imperfections also contribute to the peak broadening. In the crystallite size calculations however, ideal crystals were assumed that are microstrain-free (with no crystal defects or distortions). Therefore it should be borne in mind that the goodness of estimation is also the function of the crystallinity of the sample [155].

3.5.3 Estimating the optical band gap

Tauc plot and Kubelka-Munk theory

It is known that when the incident photon energy is close to the energy of the forbidden band gap the light absorption of the material starts to follow an exponential trend [156]. This region is often called as Urbach tail region. The exponential trend can be written as a power law in the form shown in Equation 3.8 where α is the molar absorption coefficient, hν is the photon energy, E_g is the forbidden band gap, A is a constant and n takes 1/2 or 2 values depending on the direct or indirect type of electron transition of the material, respectively [157].

$$\alpha h\nu = A(h\nu - E_g)^n \tag{3.8}$$

The calculation of the optical band gap is possible using the above equation. By plotting (αhν) against hν photon energy the so-called Tauc plot can be drawn. Fitting a tangent line to the linear portion of the high absorption region of the plot and extrapolating its value to hν = 0 provides an estimate to the optical band gap [35].

In order to convert the diffuse reflectance spectra into the equivalent absorption coefficient the Kubelka-Munk (K-M) theory was applied [158, 159]. The Kubelka-Munk equation can

be expressed in the following form, where R stands for the absolute reflectance, k is the molar absorption coefficient and s is the scattering coefficient.

$$\mathrm{f(R)} = \frac{(1-R^2)}{2R} = \frac{k}{s} \tag{3.9}$$

Taking the example of R = 0.434 at hν = 3.6 eV, f(R) can be calculated to be 0.934 based on Equation 3.9. Then the as-calculated f(R) can be used to calculate $(\mathrm{h}\nu\mathrm{f(R)})^{(1/2)}$ to construct the Tauc plot for indirect semiconductors such as WO_3. This gives

$$(h\nu f(R))^{1/2} = (3.6 \cdot 0.934)^{1/2} = 1.834 \tag{3.10}$$

After repeating this process for each of the measured reflectance values, the Tauc plot can be constructed and the band gap can be determined as detailed above.

The K-M relationship involves certain assumptions such as that the incident light is perfectly diffuse, the particles are uniformly distributed within a non-absorbing matrix material, the level of dilution is infinite and that the thickness of the measured sample layer is infinite [160].To fulfil these assumptions highly diluted samples were used between 1-5% sample dilution. Also, isotropic sample distribution was ensured by thorough mixing of the white non-absorbing matrix material with the sample in a mortar.

Chapter 4

Photoactivity of WO_3 nanocrystals

This work has been published in the RSC Advances [161] under an Open Access licence. It has been written by the first author who is also the author of present thesis. The introduction and the conclusion part is reproduced from original paper with some modifications.

4.1 Introduction

Semiconductor nanostructures are technologically important materials that have received widespread interest for their unique electrical and optical properties [162, 25, 163]. The striking features of such nanoscale materials are particularly determined by their size and shape. In the mid 1980's quantum dots were shown to exhibit a strong relationship between their size and the longest absorbed wavelength, which was of particular interest for fine-tuning the optical properties of nanostructures by simple size-control [164]. Later, 1D nanomaterials were recognised to have enhanced charge carrier transport properties owing to their beneficial shape, which attains less interfacial interaction with grain boundaries and therefore produces longer-lived charges [165, 166].

Although many applications of nanomaterials are determined by the size- and shape-dependent properties, it is still a great challenge to synthesise these materials by precise

control over their microstructure. WO_3 is an n-type semiconductor oxide which has gained widespread interest due to its attractive properties for enhancing visible photoactivity of wide band gap semiconductors such as TiO_2. It is also widely used for the fabrication of electrochromic devices, cost-effective displays, smart windows, optical switches or gas sensors [167, 26]. Similarly to other materials, WO_3 is popularly synthesised by hydrothermal processes owing to its facile arrangement, cost effective nature and the possibility of versatile product formation [168, 169]. As the shape of nanodimensional materials prepared by wet-chemical processes is mainly driven by nucleation and growth kinetics, many factors were shown to be decisive for the final morphology [170].

A great variety of structure directing agents were found to modulate the crystal growth including inorganic salts, organic acids, polymers and surfactants [171–173, 32]. *Adhikari et al.* used fluoroboric acid to obtain nanocuboid WO_3 and optimized the product morphology by varying the acid concentration, the reaction time and the temperature [174]. Other factors such as the processing temperature, the time, the precursor concentration and the pH were also shown to affect the nanostructures. *Bai et al.* concluded that the temperature and the time of the hydrothermal synthesis influenced strongly the diameter of the obtained WO_3 nanorods [175]. *Peng et al.* showed that the increasing concentration of the capping agent notably changed the morphology of WO_3 [176]. In addition to these, *Sonia et al.* revealed that hexagonal superstructure and twin octahedral WO_3 can be formed at pH 1 and pH 5.25, respectively [177].

Although substantial experimental work has been devoted to interpreting the relationship between process parameters and microstructure in nanomaterial synthesis, theories and the current understanding are still limited to explaining the crystal growth mechanism and limited to fabricating designed nanostructures due to the lack of sufficient and comparable experimental data [178–180]. The classical nucleation theory proposed by LaMer and Dinegar has been widely used to explain the crystal growth mechanism. However, it cannot

be generally applied to explain the effect of process parameters on the microstructure, and experimental results were found to contradict the theory [180–182].

In this study, I focused on WO_3 polymorphs to study the effect of hydrothermal synthesis conditions, such as solution pH, the chain length of polymeric surface modulator and mixed solvent medium on the crystal growth, morphology and on the photocatalytic efficiency. I investigated what is the drive of the morphology evolution beyond the influence of supersaturation. In addition to this, I intended to study the correlation between the optical property and the crystal phase and size of the nanostructures by calculating the band gap energies. The prepared WO_3 nanostructures were characterised by XRD, SEM, TEM, XPS, BET and solid phase diffuse reflectance and tested for photocatalytic application.

4.2 Results and Discussion

4.2.1 Nomenclature

The WO_3 catalysts presented in this thesis are named to reflect the synthesis conditions of the nanostructures. The first number refers to the applied pH of the reaction mixture followed by the indication of the carbon chain length of the applied poly(ethylene glycol) (PEG) additive. For example W-0.10-P3350, W-0.51-P20E, W-1.52-P200E means that the catalysts were prepared at pH 0.10, 0.51 and 1.52, respectively and the PEG additive had an average molecular weight of 3350, 20000 and 200000 g/mol, respectively. The sample prepared in an $EtOH/H_2O$ precursor solution was named as W-EtOH.

4.2.2 Investigated process parameters

The synthesis of WO_3 nanostructures by hydrothermal processes is typically achieved under acidic conditions. Equation 4.1 and 4.2 highlights that the formation of WO_3 nanostructures depends on the concentration of H^+ [183]. Although, relatively few studies reported the

formation of WO_3 nanomaterials either under highly acidic conditions (pH < 1) or above pH 3 [177]. Therefore, in this study in order to investigate the effect of the solution pH, experiments were designed at pH levels of 0.10, 0.51, 1.05, 1.52 and 2.01 while other synthesis parameters such as the process temperature and time along with the amount of reagents (except the acid) was kept constant.

$$WO_4^{2-} + 2H^+ = H_2WO_4 \tag{4.1}$$

$$H_2WO_4 = WO_3 + H_2O \tag{4.2}$$

A second factor studied in this work was the effect of the chain length of PEG. Polymeric surface modulators such as PEG are commonly employed additives in wet-chemical processes to promote anisotropic crystal growth of *e.g.* ZnO or WO_3 nanomaterials [148, 184]. They are believed to act through selective coordination to specific crystal faces of the nanomaterial like WO_3 at the early stages of the crystallisation process [185]. In some cases also the character and chain length of the polymer has been found to affect the nanocrystal formation [184]. In order to study the role of PEG on the crystal growth kinetics, in this work three PEGs with average molecular weights of 3350, 20 000, 200 000 g/mol has been tested at pH levels of 0.10 ± 0.04 and 1.50 ± 0.04.

Furthermore, the affinity of polymeric surface modulators such as PEG towards the crystal nuclei could be also affected by the solvent medium [184]. To explore such influence, as a third factor the effect of EtOH/H_2O ratio of 1:3 at pH 1.68 has been investigated.

4.2.3 Crystal structure

To investigate the effect of the process parameters on the crystal structure, XRD diffractograms of WO_3 nanomaterials were recorded and analysed. Table 4.1 and 4.2 summarizes

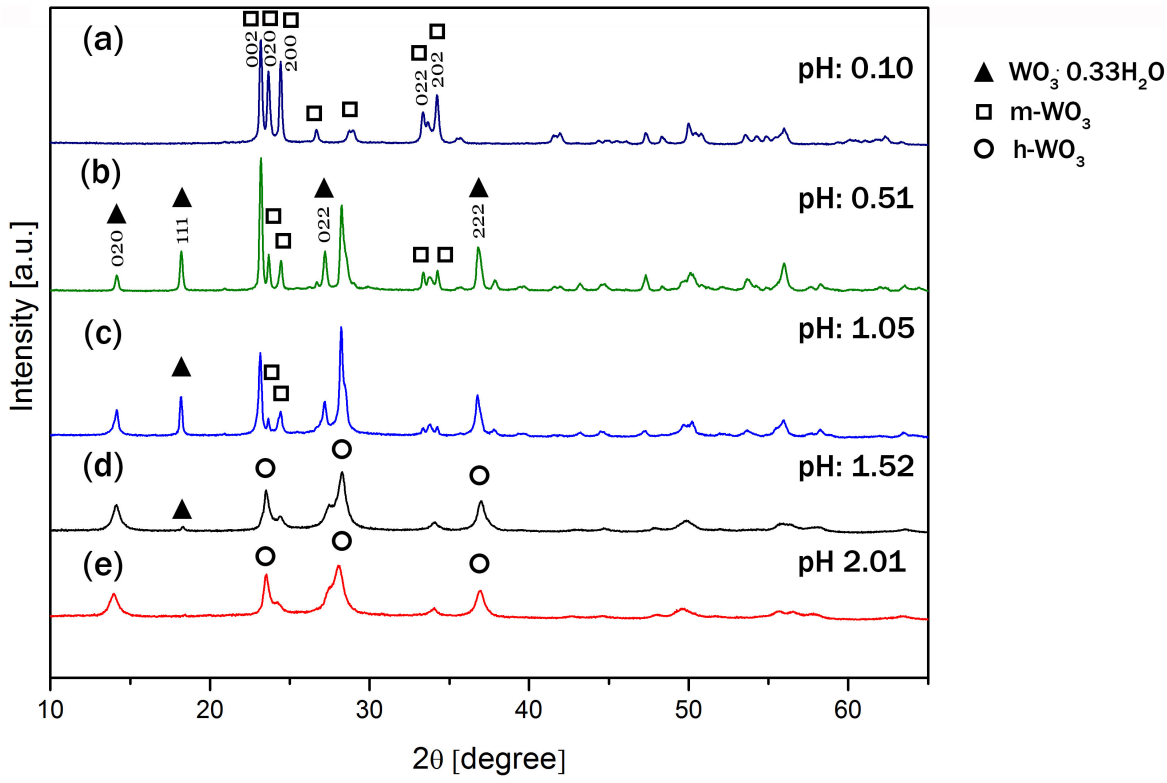

Fig. 4.1 XRD diffractograms of the WO_3 nanostructures a) W-0.10-P20E, b) W-0.51-P20E, c) W-1.05-P20E, d) W-1.52-P20E and e) W-2.01-P20E

the material properties of the prepared nanostructures including the crystal phase, morphology, optical properties and specific surface area values.

It was revealed that by varying the solution pH from 0.10 to 2.01 different crystal phases were favoured. Figure 4.1 shows the XRD diffractograms of the nanostructures. In general, the reflection peaks were sharp and intense which suggested that the obtained nanostructures were well-crystalline. Furthermore, it was found that at the lowest pH level of 0.10 monoclinic phase (m-)WO_3 was obtained which was evidenced by 43-1035 JCPDS card. As a result of elevating the pH to 0.51 and to 1.05 a new crystal phase appeared beside m-WO_3 which could be assigned to orthorombic (o-)$WO_3 \cdot 0.33H_2O$ by 35-0270 JCPDS card. From the XRD pattern no other crystal phases of WO_3 or other crystalline impurities could be identified to either W-0.51-P20E or W-1.05-P20E samples. At pH 1.52, also two crystal phases could be assigned to the reflection peaks. Beside o-$WO_3 \cdot 0.33H_2O$, hexagonal (h)-WO_3 could be

identified with some ammonia incorporated to the crystal lattice as indicated by 58-0151 JCPDS card of $(NH_4)_{0.33-x}WO_{3-z}$. Similarly to W-1.52-P20E, at pH 2.01 h-WO_3 could be assigned to the XRD peaks but this time as a pure phase. For simplicity these phases are referred as h-WO_3 throughout this text.

When altering the chain length of the PEG or studying the effect of EtOH in the reaction mixture, no significant effect on the crystal structure has been revealed by the XRD patterns. At pH 0.1, for all three PEG sources (M_g: 3350, 20 000, 200 000 g/mol) pure m-WO_3 could be assigned to the diffraction peaks whereas at pH 1.5 h-WO_3 with co-existing o-$WO_3 \cdot 0.33H_2O$ crystal phase was identified. Although the main crystal phases have been preserved for the different PEG capping agents at pH 0.1 and pH 1.5, slight changes were noted in the XRD pattern of samples prepared at pH 1.5. It was noted that the relative intensities of h-WO_3 and o-$WO_3 \cdot 0.33H_2O$ crystal phases have been slightly altered. This was indicated by the changing intensity of the reflection peak of the orthorombic phase at *circa* 18° relative to the reflection peak of the hexagonal phase at *circa* 14° when different PEG additives were used. No clear trend could be seen between the chain length of the PEG and the varied relative intensities. Figure 4.2 c) shows the XRD patterns of W-1.52-P3350, W-1.52-P20E, W-1.52-P200E and W-0.10-P3350, W-0.10-P200E prepared at pH levels of 1.52 and 0.10, respectively.

For W-EtOH sample h-WO_3 phase could be assigned to the XRD peaks that can be seen in Figure 4.3 c).

4.2.4 Morphological structure

The morphology of the nanostructures has been investigated by SEM and TEM. The effect of varied pH levels is depicted in Figure 4.4. It can be seen that both the size and the shape of the fabricated nanocrystals changed considerably over the 0.10-2.01 applied pH range. At the lowest pH level of 0.10, cuboidal nanoplates were formed that could be

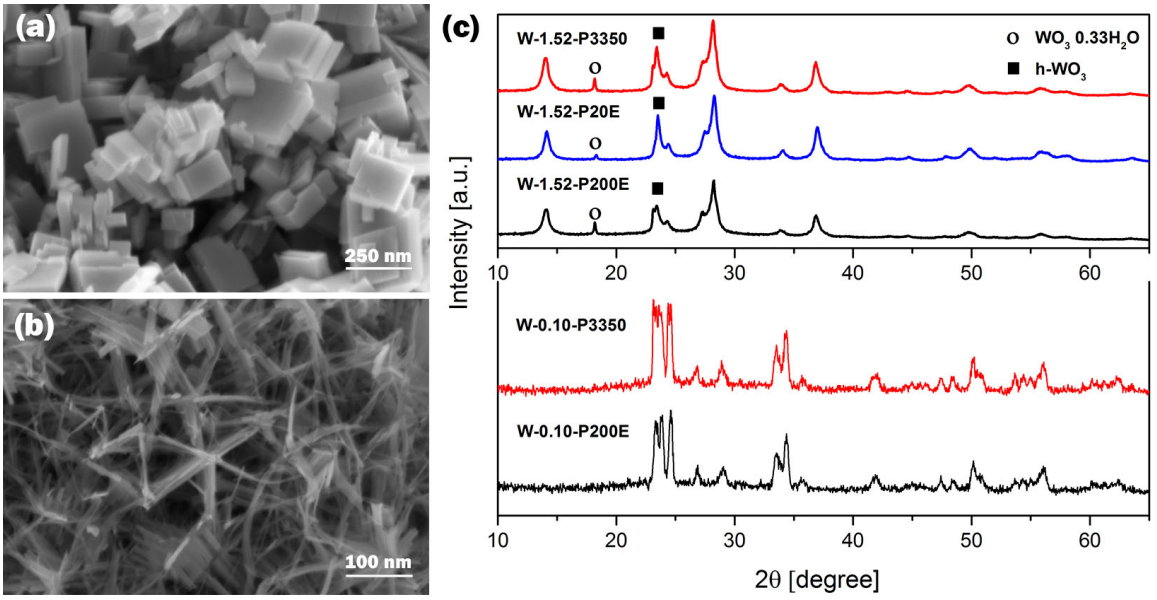

Fig. 4.2 Effect of the chain length of the polymeric surface modulator a) SEM image of W-0.10-P200E as an example for typical morphology prepared at pH 0.10, b) SEM image of W-1.52-P3350 as an example for typical morphology prepared at pH 1.52 and c) XRD diffractograms of the WO_3 nanostructures: W-1.52-P3350, W-1.52-P20E and W-1.52-P200E prepared at pH level 1.52 and W-0.10-P3350 and W-0.10-P200E prepared at pH level 0.10

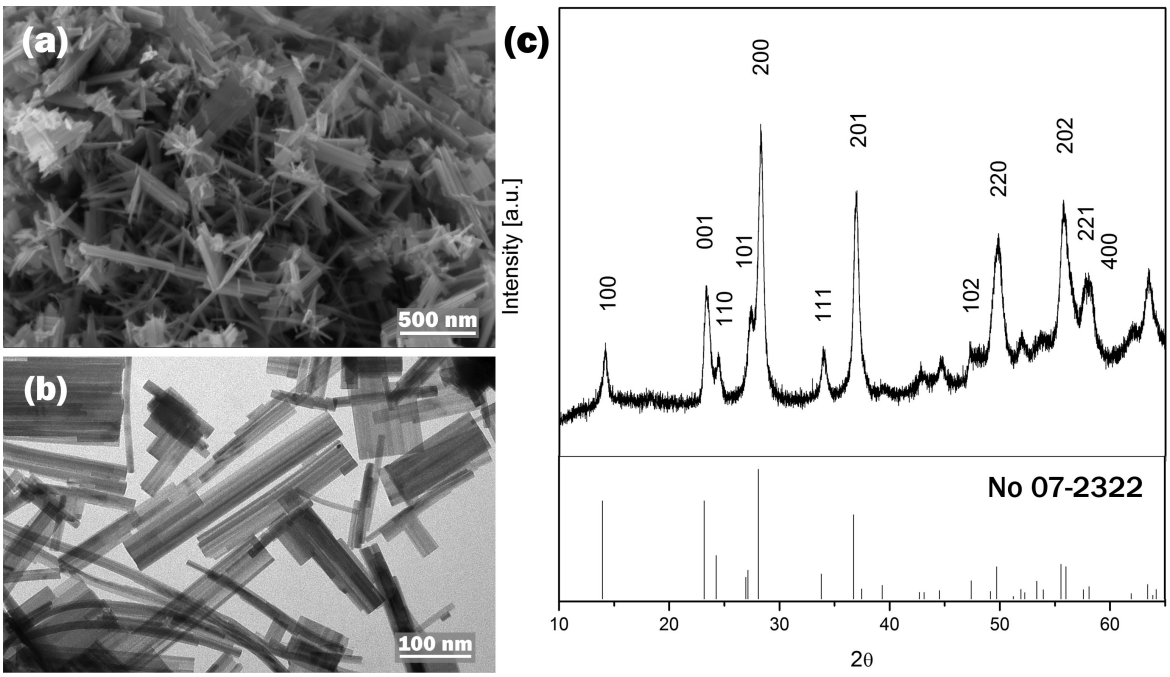

Fig. 4.3 Effect of the presence of EtOH in the reaction mixture a) SEM image, b) TEM image and c) XRD diffractogram of W-EtOH with reference card

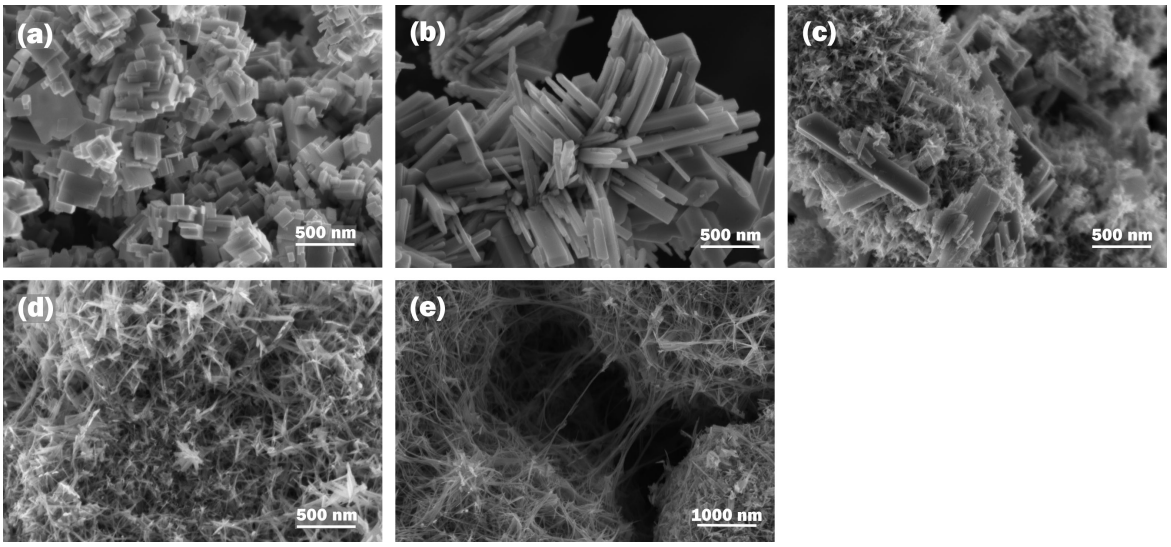

Fig. 4.4 SEM images of the WO_3 nanostructures a) W-0.10-P20E, b) W-0.51-P20E, c) W-1.05-P20E, d) W-1.52-P20E and e) W-2.01-P20E

characterised by 30-50 nm average thickness and couple of hundreds of nanometers of length as it can be seen in Figure 4.4 a). At pH 0.51, considerably bigger nanostructures were synthesised that exhibited nanorod-like shape which is shown in Figure 4.4 b). Typically these nanocrystals were 50-100 nm thick and several hundreds of nanometers long. When the pH further rose to 1.05, mixed morphologies could be observed that is depicted in Figure 4.4 c). Beside the 50-100 nm thick and *circa* 800-1000 nm long nanorod structures, a much finer nanoneedle-shaped crystal phase has appeared. These nanoneedles possessed about 10-15 nm in thickness. Under even less acidic conditions, at pH 1.52, the bigger nanorod structures disappeared and uniform nanoneedles could be identified that is shown in Figure 4.4 d). The pH level of 1.05 was therefore realized as a transition point for the morphology. The nanoneedles structures in W-1.52-P20E typically exhibited about 10 nm in thickness and 200-300 nm in length. And finally at pH 2.01, 5-10 nm thin but significantly longer nanowires were formed. A lower magnification SEM image in Figure 4.4 e) is provided to highlight the length of the 1D nanostructures which was in the micrometer range. Due to the significant increase in the length of W-2.01-P20E, the aspect ratio (that is defined as the ratio between the length and the thickness of the nanostructure) was found to follow an

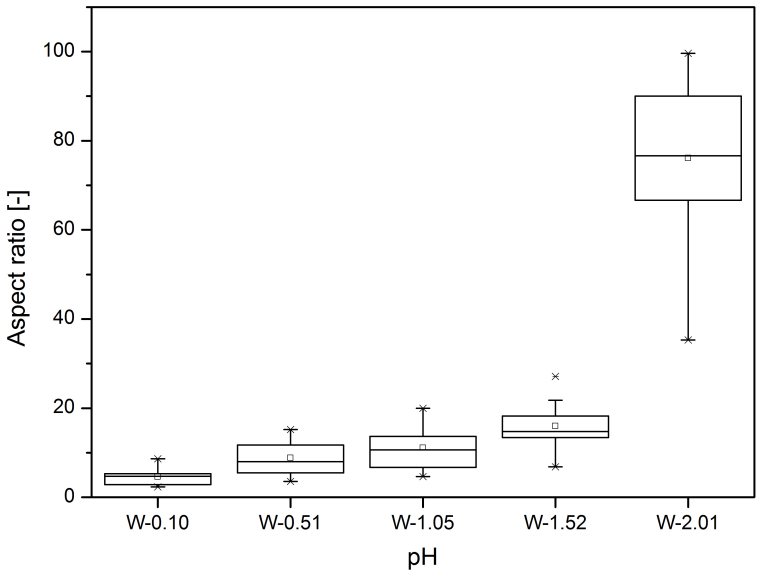

Fig. 4.5 Box plot showing the change in the aspect ratio of the WO_3 nanostructures prepared at various pH levels

exponential trend over the 0.10-2.01 pH range. A Blox plot shown in Figure 4.5 reflects the variation of the aspect ratio with increasing pH levels. The lowest length to thickness ratio could be estimated for W-0.10-P20E nanostructure that gradually increased up to pH 1.52. The aspect ratio of these structures were most typically between 10-20. In contrast, in W-2.01-P20E sample this number was close to 100 showing almost an order of magnitude increase.

When the PEG surface modulators were varied at pH 0.1 and 1.5, typical 30-50 nm thick cuboid nanoplate and 10-15 nm thick nanoneedle morphologies were observed, respectively. Figure 4.2 a) and b) shows the typical SEM images at pH 0.1 and 1.5. Additionally, it was noted that the nanoneedles formed at pH 1.5 often formed star-shaped assemblies. This feature could be observed for all three PEG surface modulators [186].

And finally Figure 4.3 a) and b) shows the SEM and TEM images of W-EtOH sample, respectively. It can be seen that very similar morphologies could be discovered to the EtOH-free samples that were prepared under similar acid concentration as W-EtOH. The star-shaped assemblies were observed for this sample as well.

Table 4.1 Synthesis conditions and characterization of WO_3 nanostructures

Nanostructure	pH	Crystal phases	Morphology	Colour	E_g [± 0.03 eV]
W-0.10-P20E	0.10	m-WO_3	cuboidal nanoplates	yellow	2.70
W-0.51-P20E	0.51	m-WO_3, o-$WO_3 \cdot 0.33H_2O$	nanorods	yellow	2.70
W-1.05-P20E	1.05	m- and h-WO_3, o-$WO_3 \cdot 0.33H_2O$	nanorods, nanoneedles	yellow	3,25
W-1.52-P20E	1.52	h-WO_3, o-$WO_3 \cdot 0.33H_2O$	nanoneedles	yellow	3.10
W-2.01-P20E	2.01	h-WO_3	nanowires	blue, yellow	2.93
W-0.10-P3350	0.10	m-WO_3	cuboidal nanoplates	yellow	
W-0.10-P200E	0.10	m-WO_3	cuboidal nanoplates	yellow	
W-1.52-P3350	1.48	h-WO_3, o-$WO_3 \cdot 0.33H_2O$	nanoneedles	yellow	2.91
W-1.52-P200E	1.45	h-WO_3, o-$WO_3 \cdot 0.33H_2O$	nanoneedles	yellow	2.87
W-EtOH	1.68	h-WO_3	nanoneedles	blue	3.13

Table 4.2 Specific surface area of the WO_3 nanostructures

Nanostructure	Specific surface area $[m^2 g^{-1}]$
W-0.10-P20E	7.8
W-0.51-P20E	6.6
W-1.05-P20E	19.2
W-1.52-P20E	32.3
W-2.01-P20E	43.8

Therefore, it could be concluded that the morphologies of the synthesized WO_3 nanostructures were primarily affected by the solution pH since there was no significant effect associated with the utilization of different PEGs or EtOH/water mixed solvent.

4.2.5 Crystallite size calculation

In addition to the electron microscope images and the XRD crystal structure analysis, the average crystallite sizes of the nanostructures have been calculated by the Scherrer-Debye equation (3.6) using characteristic Bragg reflections of the different crystal phases.

In the calculation it was considered that the shape factor of the crystallites (k) could affect the estimation of the Scherrer dimension. Figure 4.6 shows the influence of shape factor k between 0.8 and 1.1 on the estimated crystallite size of the WO_3 sample synthesized at pH 0.10 (W-0.10-P20E). Although the exact value of k is most of the time unknown, it

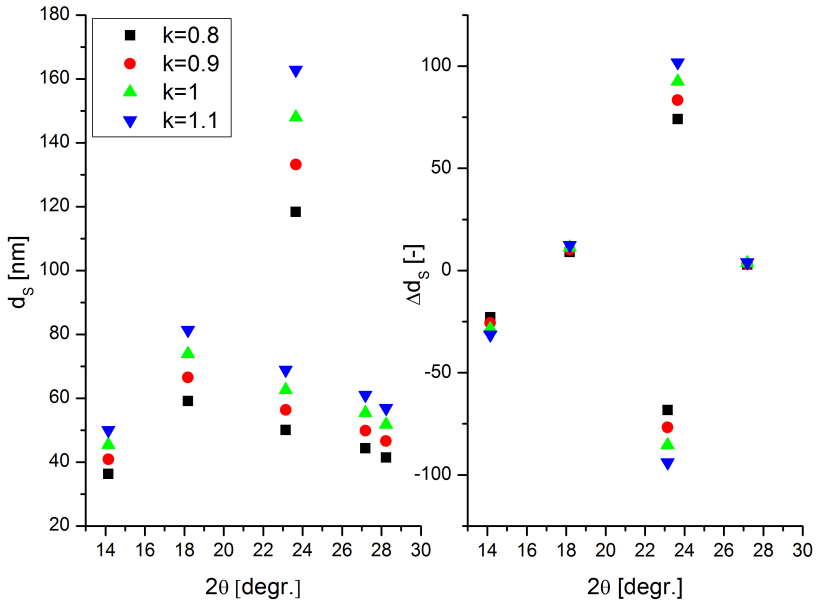

Fig. 4.6 On the left the crystallite size estimation for W-0.10-P20E sample is shown using shape factor k between 0.8 and 1.1 is shown. On the right the relative change in crystallite sizes is shown with respect the neigbouring peak.

typically lies close to unity [152]. For example, in the literature 0.94 and 1.07 typical values are reported for spherical or cubic crystallites [152, 154].

From the left plot of Figure 4.6 it can be seen that for smaller crystallites the alteration of k caused less variation in the calculated sizes regardless of 2θ (in the range of 13-30°), whereas for crystallites larger than 100 nm the deviation showed a considerable increase. This could highlight the limitation of the Scherrer size prediction based on peak broadening for crystallites larger than 100 nm which is in good agreement with literature findings [152].

Furthermore, it could be also found that the Scherrer sizes calculated under different k values effectively followed the same relative trend. This is illustrated on the right handside of Figure 4.6 where the difference between d_s values at neighbouring diffraction angles were plotted. It can be seen that the standard deviation of less than 50 nm size difference ranged from as little as $\pm$0.7 nm to $\pm$4.3 nm by using different k values.

Given the relatively close calculated crystallite sizes for smaller nanostructures and the good correlation between the relative trends when different shape factors were used, k was

approximated with unity in the Scherrer-Debye equation to allow crystallite size estimation of the synthesised WO_3 nanostructures.

In general, it was seen that the Scherrer dimensions revealed anisotropic crystal growth which is in good agreement with the observed WO_3 morphologies in the SEM images. For example, the crystallite dimensions of W-0.51-P20E were found to be 98 and 68 nm for the (020) and (200) crystal planes of m-WO_3, respectively. A sample calculation for the crystallite size determination of W-0.51-P20E can be seen in Equation 4.3. The Scherrer dimension of m-WO_3 was calculated based on the (020) hkl peak which appeared at 23.7°.

$$d_s = \frac{k \cdot \lambda[\text{Å}]}{\text{FWHM} \cdot cos\theta} = \frac{1 \cdot 1.542}{0.0016 \cdot 0.97872} = 980 \text{ Å} = 98 \text{ nm} \tag{4.3}$$

It was also noticed that the increase in the solution pH from 0.10 to 1.05 resulted in a considerable crystallite size growth from 80 nm to 156 nm for the (020) plane of m-WO_3. However, both the m-WO_3 and o-$WO_3 \cdot 0.33H_2O$ phases in W-1.05-P20E revealed crystallite sizes greater than 60 nm which left the nature of fine nanoneedle phase unexplained. Therefore, it is suspected that potentially another crystal phase (h-WO_3) may be present in the W-1.05-P20E sample. This hypothesis is also supported by the fact that at higher pH levels of 1.52 and 2.01 similar fine nanoneedle and nanowire morphology was observed in the SEM images. These phases were pure h-WO_3 with minor o-$WO_3 \cdot 0.33H_2O$ phase in W-1.52-P20E. It is likely that the XRD peaks of a potential h-WO_3 in W-1.05-P20E were more broadened due to their small dimension. Moreover, the characteristic peaks could coincide with other crystal phase reflections. Therefore, an additional h-WO_3 phase could be hidden in the XRD pattern.

4.2.6 Mechanism of nanocrystal formation

Most widely, the classical nucleation theory of LaMer and Dinegar is used to explain the mechanism of nanostructure growth and formation [172, 187, 188]. Although the theory

was found to adequetly describe the formation mechanism of most crystals, there were instances when experimental results were found to contradict the theory [183]. In this study, the morphological evolution of the prepared WO_3 nanocrystals could not be satisfactorily explained exclusively by the classical nucleation theory, therefore other possible influencing factors were investigated and proposed.

In general, two main steps govern the crystallisation process, the formation of crystal nuclei and the subsequent crystal growth. These processes are believed to be influenced by the level of supersaturation. At high supersaturation level, rapid crystal nuclei formation is expected which limits the rate of the crystal growth step and yield many but limited-sized crystals at a given precursor concentration. On the contrary, when the level of supersaturation is low, the crystal nuclei formation step becomes rate-determining that results in the production of fewer but well-developed, bigger nanocrystals.

The level of supersaturation can be modulated *e.g.* by the pH of the reaction mixture. It was earlier shown in Equation 4.1 and 4.2 that the formation of WO_3 nanostructures depends on the solution pH and therefore the generation of initial crystal nuclei and their subsequent growth can be modulated by the level of acidity level. In an acidic medium, the starting material, sodium tungstate could react with H^+ ions to form tungstic acid. Under the hydrothermal reaction conditions tungstic acid may loose stoichiometric amount of water to produce WO_3 precipitates. By influencing the level of supersaturation in the reaction mixture, the number of initial crystal nuclei is affected which could alter the size and morphology of the formed WO_3 nanocrystals. It is also worth mentioning that additives such as PEG are often added to the reaction mixture to influence the crystal formation. These materials are believed to work through selective binding to the crystal faces at the early stages of crystal formation. These specific interactions may lead to diverse morphologies [189]. By changing the pH level the interaction between the developing crystals and the surface modulator could be affected which may also had an impact on the final morphology of the WO_3 nanostructures.

The SEM images in Figure 4.4 along with the calculated crystallite sizes of the WO_3 nanostructures revealed that the decrease in the degree of acidity yielded a prominent growth in the size of nanostructures which finding is in good correlation with the classical nucleation theory. This trend held true up to pH 1.05. However, unexpectedly beyond this point a sudden size drop was observed. The appearance of fine nanoneedles in W-1.05-P20E sample and the formation of thin nanowires in W-2.01-P20E could not be explained as a result of altered level of supersaturation any more.

To further explore the possible reasons for the crystal development, the material characters were carefully investigated over the applied pH range. It was noted that the degree of supersaturation failed to give explanation for the mechanism of the crystal growth beyond pH 1.05. This pH level was also recognised as a transition point not only for the morphology but also for the crystal structure. Below pH 1.05 monoclinic whereas above this pH hexagonal WO_3 formation was preferred. Hexagonal WO_3 is a metastable phase where the presence of stabilizing foreign cations support the hexagonal channel structure [174, 190]. For nanosized materials in general, but especially for metastable crystal phases such as the hexagonal phase of WO_3, the question of stability could be highly relevant. It is believed that the morphology could have stabilizing effect on the formed crystal phase of nanostructures that has been recently highlighted by *Zheng et al.* as well who stated that ”the morphology of the nanostructures can have a significant effect on obtaining stable phases” [26]. Hence it is suggested, that the interaction of the crystal structure and the morphology could possibly be a leading factor in the crystal development observed above pH 1.05. The crystalline structure of the material could favour the formation of certain morphological structure, that in return may have a positive effect on the stability.

This idea is further supported by the fact that h-WO_3 is commonly fabricated in the form of 1D nanostructures that could imply the beneficial effect of this spatial arrangement on the metastable crystal structure [176, 190–194]. In the contrary, monoclinic WO_3 has seldom

been reported in 1D shape. In those few occasions, typically substrates with an initial seed layer were employed to promote the growth of 1D nanostructures [148, 195, 196].

4.2.7 Optical properties and chemical states

To study the light absorption properties of the various WO_3 nanostructures, solid-state UV-vis diffuse reflectance spectra were recorded. The calculation of the optical band gap (E_g) was performed by converting the experimental data into Kubelka-Munk function prior to using the Tauc model. Both of these models are depicted in Figure 4.7. Additionally, the Kubelka-Munk function also served information on the light absorption behaviour of the nanostructures.

The Tauc plot (defined in Equation 3.8) is a widely used model for the estimation of direct and indirect semiconductor materials. As an n-type semiconductor oxide with indirect electron transition, the optical band gap of WO_3 nanostructures are commonly determined from the Tauc plot [157, 35]. To estimate the band gap, firstly the Kubelka-Munk function (f(R)), which is defined in Equation 3.9, was used to obtain the equivalent absorption coefficients from the diffuse reflectance spectra. Then by plotting $(f(R)h\nu)^{1/2}$ versus $h\nu$ the Tauc plot could be constructed. The high absorption region of this plot was used to fit a tangent line and extrapolate to $h\nu$=0 in order to estimate the band gap. Beside the Tauc plot, the K-M function was also plotted against $h\nu$ to observe the absorption properties of the catalysts and to highlight special feature of their absorption behaviour like in the case of the blue samples.

Band gap energies

In general, the forbidden band gap energies of the WO_3 nanostructures ranged from 2.7±0.03 eV to 3.25±0.03 eV. Table 4.1 summarizes the calculated E_g values that were found to be in good agreement with reported band gap energies for nanosized WO_3 structures [197–199].

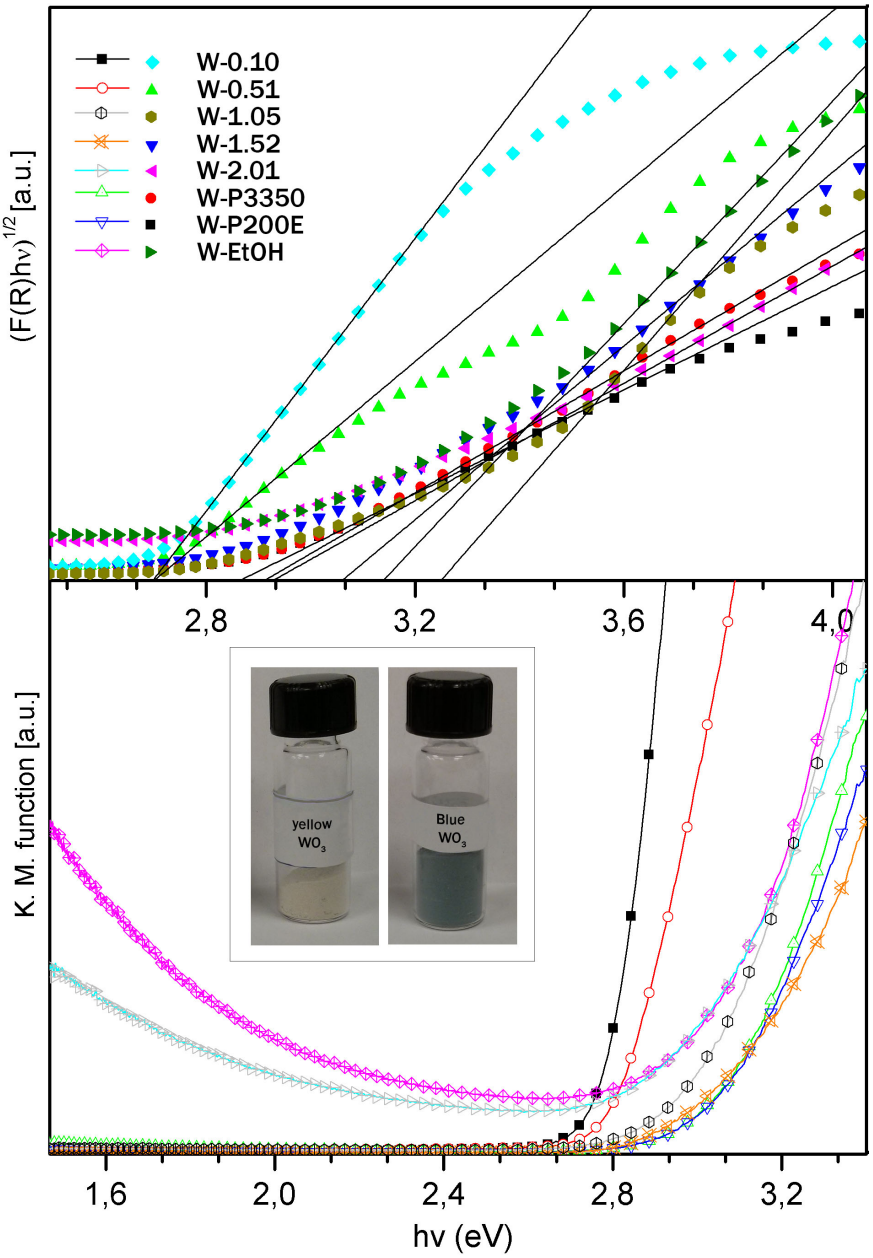

Fig. 4.7 Optical properties of the WO_3 nanostructures as shown in the Tauc plot (top figure) and in the Kubelka-Munk function versus photon energy plot (bottom figure)

It was found that WO_3 nanostructures prepared at low pH levels of 0.10 or 0.52 exhibited the smallest energy band of E_g = 2.70 eV among all the prepared nanomaterials. At higher pH levels in W-1.05-P20E, W-1.52-P20E and W-2.01-P20E samples, the band gap energies were calculated to lie between 2.93 and 3.25 eV that showed a blue shift in the light absorption threshold relative to W-0.10-P20E and W-0.51-P20E. Both theoretical and experimental findings revealed that the distortion of the WO_6 octahedra is typically followed by the widening of the energy band gap [200–202]. In agreement with this, it was also generally found in the literature that m-WO_3 structures possessed smaller whereas h-WO_3 nanomaterials exhibited higher energy gap values [203]. The E_g values calculated for the WO_3 samples are consistent with this expectation since the lowest energy band belonged to W-0.10-P20E and W-0.52-P20E samples that showed monoclinic phase WO_3 while wider energy band gaps were calculated for W-1.52-P20E and W-2.01-P20E samples that showed the presence of hexagonal phase WO_3.

Furthermore, beyond the effect of the crystal structure, the size of the fabricated nanomaterials could have a pronounced effect on the width of the band gap, too. It is known that the reduction of the characteristic dimensions of nanostructures could increase the band gap due to quantum confinement effects [203]. This effect was found to be especially dominant when the size of the nanostructures approaches the Bohr radius of the material which equals to 3 nm for WO_3 [26, 204]. Therefore, the blue shift in the absorption edge of h-WO_3 nanomaterials, like in the case of W-1.52-P20E and W-2.01-P20E, could be also induced by the thin nanoneedle and nanowire morphology that exhibited 5-15 nm in thickness and several hundreds or thousands of nanometers in length, respectively.

It was therefore found that the variation in the solution pH affected remarkably the width of the forbidden band gap. Figure 4.8 shows the general trend between the E_g and the solution pH. It can be seen that the highest energy band was associated with the sample prepared at pH 1.05. At this pH level not only the transition from bigger nanoplates to fine nanoneedle

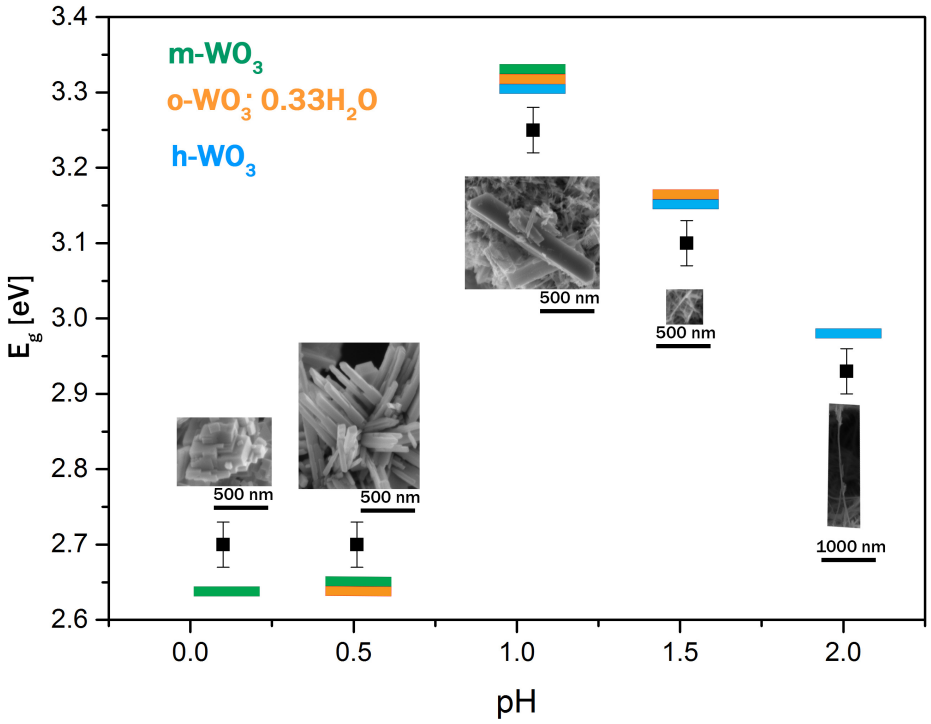

Fig. 4.8 Correlation between the band gap energies of the WO_3 nanostructures and the solution pH

phase took place, but also the crystalline phase changed from monoclinic to hexagonal. At this pH, various morphologies and all three crystal phases co-existed. The pH 1.05 also represented a peak in the band gap energies, lower or higher level of acidity resulted in a decrease in the E_g.

Light absorption

In addition, it was noted that generally the WO_3 samples were pale yellow in colour, except two samples, W-2.01-P20E and W-EtOH. The Kubelka-Munk function revealed that beyond the apparent ligth absorption threshold, the absorption started to rise again in the far-red region of the visible spectrum. This unique optical behaviour, which is shown at the bottom part of Figure 4.7, could cause the greyish blue appearence of these nanomaterials. Switching the color of WO_3 from yellow to blue is a well-known phenomenon that is most typically induced by gasochromism or electrochromism [205, 206]. In the former case reducing gas

medium, whereas in the latter case electricity induced ion insertion leads to blue colour. It is worth mentioning that the colorization of WO_3 is an interesting opportunity for *e.g.* the fabrication of smart windows and energy saving displays [207]. Rarely, other conditions were also reported to lead to colorized WO_3. *Kurumada et al.* found that the fabrication of WO_3 nanostructures with characteristic dimension less than 10 nm resulted in blue colour [208]. However, to the best of our knowledge there was no previous report indicating the colorization of WO_3 by means of EtOH.

The light absorption of W-EtOH and W-2.01-P20E could be characterized by a transmission window between the apparent E_g and the increasing absorption in the far red-region. Similar optical behaviour has been previously associated with the presence of interband localized states of reduced W atoms in the literature [206]. Reduced W atoms may have been generated in the W-EtOH sample by excessive surface OH functional groups due to the EtOH/water mixed solvent phase. To confirm this, the W-EtOH sample was annealed at 250 °C under air for 12 hours. As expected, the initial bluish colour turned into off-white which could be an indication of reoxidation of the sample by for example the removal of the excess amount of hydroxil groups from the surface. For W-2.01-P20E sample, the accommodation of increased amount of NH_4^+ cations into the hexagonal channel could be a reason for the presence of reduced oxidation state W atoms that was also indicated by the XRD diffractogram.

Oxidation states

To further confirm the oxidation states of W atoms in the blue and yellow WO_3 samples, XPS studies have been performed. Figure 4.9 shows the high resolution O 1s, W 4d and W 4f XPS spectra for the nanostructures. It can be seen that distinct binding energies belonged to the O and W atoms in the yellow and the blue WO_3. Both blue and yellow WO_3 samples showed characteristic peaks in the O 1s XPS spectrum for surface adsorbed

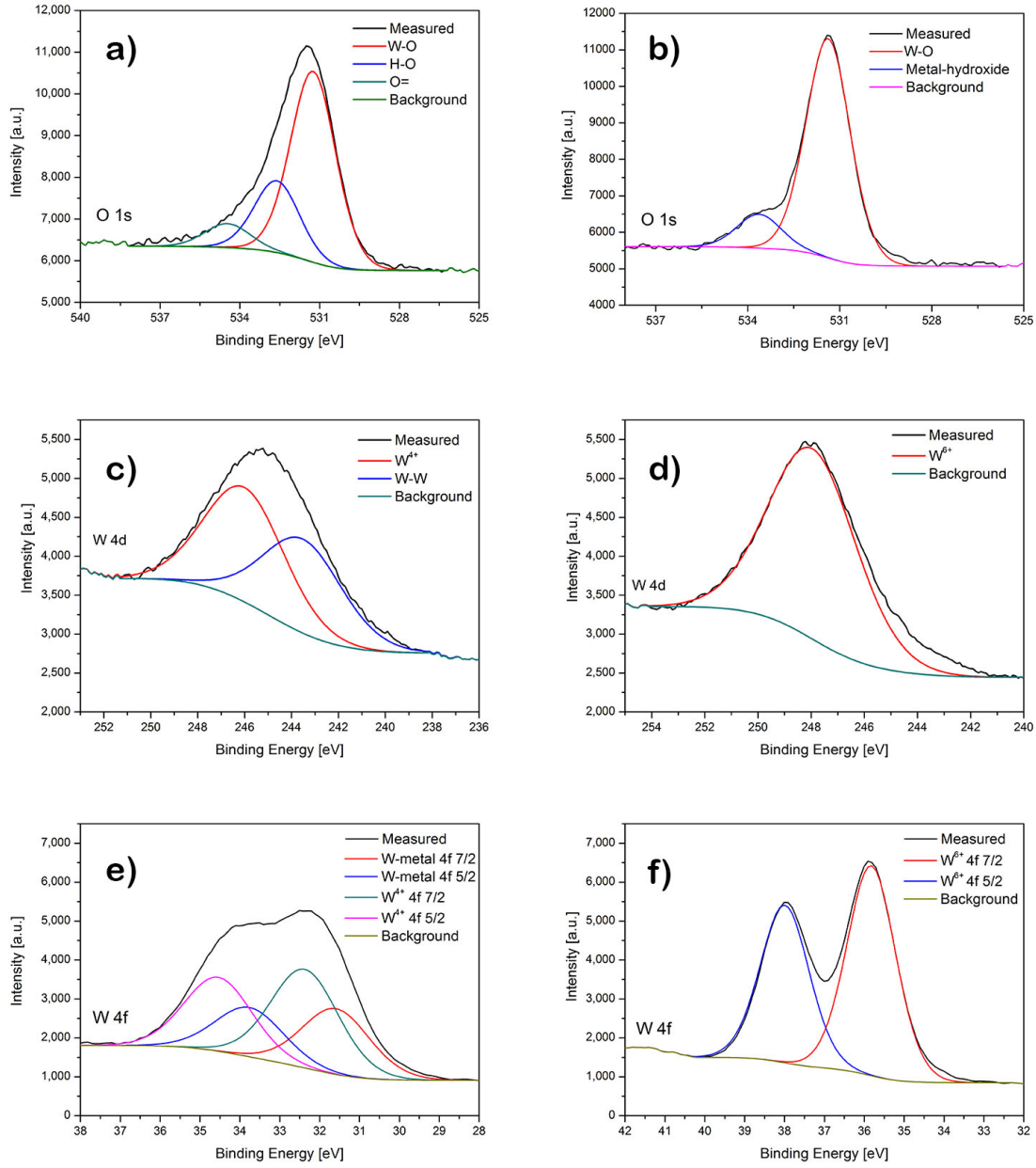

Fig. 4.9 Typical high resolution XPS spectra a) O 1s, c) W 4d and e) W 4f for for W-EtOH (blue) and b) O 1s, d) W 4d and f) W 4f for W-0.10-E20E (pale yellow) WO_3 nanostructures

O in the form of hydroxide at binding energies of 532.6 and 533.7 eV and lattice W-O bonds at 531.2 and 531.4 eV, respectively. These values were found to be in agreement with literature reports [209–212]. In the W 4d spectrum of the blue sample two peaks could be deconvoluted from the XPS spectrum. These peaks could be attributed to reduced W^{4+} and metallic W peaks appearing at 246.2 and 243.8 eV, respectively. In contrast, the yellow sample showed only one peak at 248.1 eV which could be assigned to W^{6+} based on literature references [212, 213]. The W 4f spectrum is used most commonly in the literature to describe WO_3 nanomaterials. In accordance with this, the most remarkable differences between the blue and yellow samples could be seen in this spectrum. Characteristically, the blue sample showed a broad, convoluted spectrum whereas the yellow WO_3 could be described by two slightly overlapping peaks. Similarly to W 4d spectrum both metallic W and reduced W^{4+} peaks could be ascribed to the four resolved peaks. W^{4+} 4f 5/2 and 7/2 peaks appeared at 34.6 and 32.4 eV, respectively. In the yellow sample W^{6+} 4f 5/2 and 7/2 peaks appeared at 37.9 and 35.8 eV, respectively. In agreement with these finding, in the literature reduced WO_3 nanostructures were characterized by peaks appearing at lower binding energies in both W 4d and W 4f XPS spectrum. W^{6+} peaks are typically reported in the range of 35.5-37.6 eV and 36.6-37.9 eV for W 4f 7/2 and 5/2, respectively. While W and W^{4+} peaks are typically reported around 31.0-32.5 and 33.2-34.6 eV for W 4f 7/2 and 5/2, respectively [214–216, 209, 157, 217].

4.2.8 Photocatalysis

The prepared WO_3 nanostructures with various material properties were tested in photocatalysis using methyl orange (MO) as a model compound. The dark adsorption of the MO was typically around 1-2%. The fewest dark adsorption was found for W-0.10-P20E and W-1.05-P20E with only 0.1 and 0.6%, while the highest value was measured for W-EtOH

with 3% MO adsorption in 60 min. A possible route for the photocatalytic degradation of MO in the presence of WO_3 photocatalyst is proposed in Equation 4.4, 4.5 and 4.6.

$$WO_3 + h\nu = WO_3 + e^-_{CB} + h^+_{VB} \tag{4.4}$$

$$h^+_{VB} + H_2O = OH^{\cdot} + H^+ \tag{4.5}$$

$$OH^{\cdot} + MO = \text{degradation products} \tag{4.6}$$

In general, the photocatalytic tests revealed that the photoactivities of WO_3 nanomaterials were a compromise of the crystal structure, morphology, optical properties and the oxidation state. It was found that the best performing catalyst was W-1.52-P20E, closely followed byW-0.10-P20E and W-1.05-P20E. W-EtOH and W-2.01-P20E samples showed considerably lower photocatalytic activities.

Interestingly, the highest photocatalytic performance (under present conditions) belonged to W-1.52-P20E, that exhibited one of the highest band gap energy (E_g = 3.10 eV). This meant that owing to the relatively wide band gap it could harvest less portion of the incident light compared to *e.g.* W-0.10-P20E catalysts that exhibited E_g = 2.70 eV. Regarding the morphology and the crystal phase, W-1.52-P20E possessed 10-15 nm thick nanoneedle structure that mainly consisted of h-WO_3 with coexisting o-$WO_3 \cdot 0.33H_2O$ phase. Compared to W-0.10-P20E, the fine nanoneedle phase could serve higher surface area for the photocatalytic surface reactions which was evidenced by the BET measurements and it is summarized in Table 4.2. However, compared to W-2.01-P20E, which showed high aspect ratio nanowire morphology of pure h-WO_3, W-1.52-P20E had more limited surface area. Still, it showed significantly higher photocatalytic performance than W-2.01-P20E. In this case, it is worth mentioning that the colours of the two catalysts were different. W-1.52-P20E had a pale

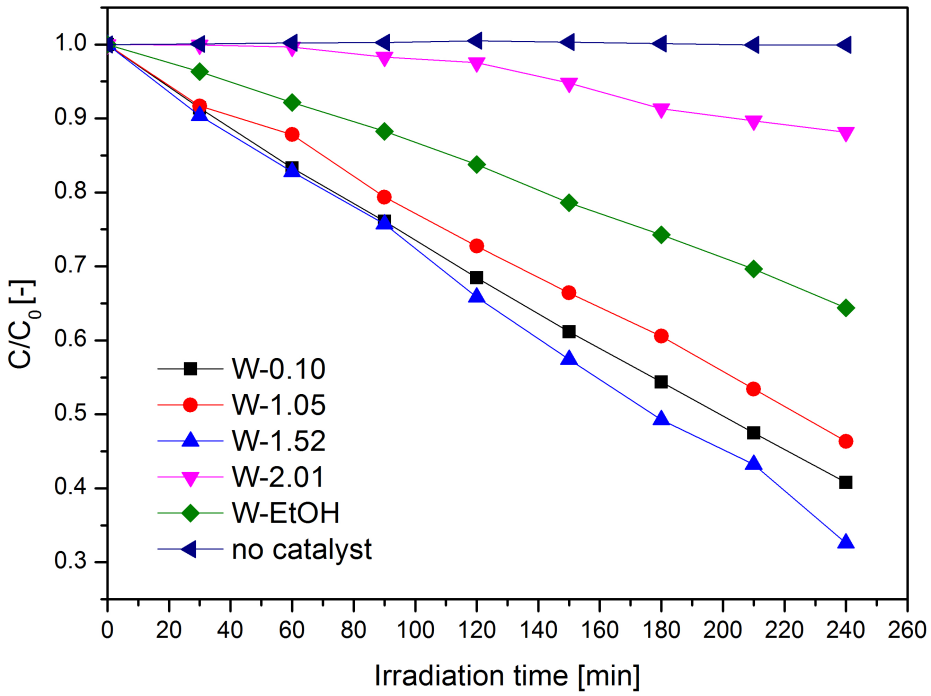

Fig. 4.10 Photocatalytic activities of the WO_3 nanostructures in the photobleaching reaction of methyl orange

yellow colour whereas W-2.01-P20E catalyst was blue. The UV-vis diffuse reflectance and XPS analysis confirmed that the blue WO_3 had unique light absorption behaviour. After the apparent band gap, the light absorption rose again in the far-red region of the visible spectrum. The XPS studies further evidenced the presence of reduced W atoms that could be responsible for the additional light absorbance in the far-red region by the generation of in-gap defect states. It is likely, that at these interband defect sites the photogenerated charges could more easily recombine which had an adverse effect on the photoactivity of blue W-2.01-P20E catalyst. Therefore, the remarkably better photocatalytic activity of W-1.52-P20E with respect to W-2.01-P20E is likely to be the result of the more oxidized composition of the WO_3. This is supported by earlier literature reports which showed that WO_3 nanostructures exhibited significantly different efficiencies in photocatalytic reactions when the oxidation level of the material was altered [206].

In agreement with this, the other pale-yellow catalysts of W-0.10-P20E and W-1.05-P20E showed good photoactivities after W-1.52-P20E, as well. These strucures were characterized by the lowest and highest band gap energies of 2.70 eV and 3.25 eV, respectively. Although W-1.05-P20E showed the highest energy band, the presence of three different crystal phases and various morphologies could compensate the limited light harvesting ability of W-1.05-P20E. In some cases, the contact between different crystal phases was found to enhance the photoactivity. For example, it is well-known that the mixture of anatase and rutile phase TiO_2 in P25 overperforms the single phases in photocatalysis [218]. Also the different morphologies provided somewhat higher surface area for W-1.05-P20E compared to W-0.10-P20E as it can be seen from Table 4.2.

The recycling test of the prepared nanostructures was performed to study the reusability and chemical stability of WO_3 photocatalyst over multiple cycles. To test this, W-0.10-P20E sample has been reused three times. Figure 4.11 shows that the photocatalytic activity of W-0.10-P20E was well-preserved over the three cycles. In all three cases the final c/c_0 was measured to lie around 0.4. No significant loss of photoactivity could be observed over the repeated experiments which suggested good stability of the nanostructure. This finding correlates well with other literature reports where good chemical stability and retained photoactivity was reported for WO_3 nanostructures [219, 12].

4.3 Conclusion

In this work, WO_3 nanostructures were synthesised in nanoplate, nanorod, nanoneedle and nanowire morphology by a facile hydrothermal method. It was found that the crystalline phase and the morphology of the nanomaterials were determined by the solution pH in the first place.

The pH 1.05 was a transition point for the monoclinic/hexagonal phase, crystal size and for the band gap. M-WO_3 was preferentially prepared in a lower pH range of 0.10 and 1.05

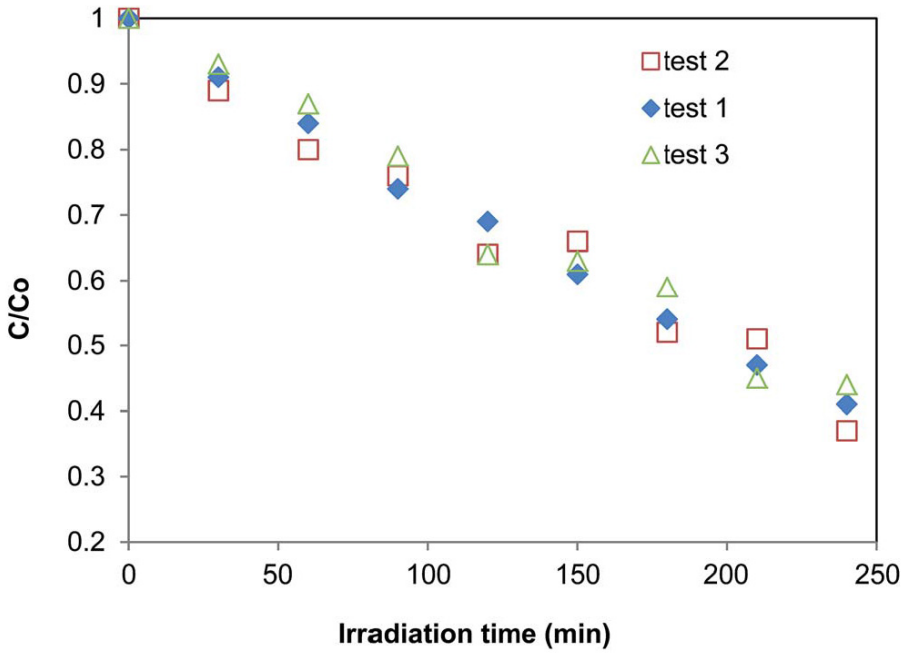

Fig. 4.11 Repeated photocatalytic test of W-0.10-P20E nanostructure

whereas h-WO_3 was favoured at a pH above 1.05. The aspect ratio of WO_3 nanostructures increased significantly with the pH and reached close to 100 at pH 2.01 where good quality nanowires were formed.

The morphological evolution of the WO_3 nanostructures could not be fully explained by the nucleation theory of LaMer and Dinegar. The appearance of fine nanoneedle phase at pH 1.05 could not be interpreted from the viewpoint of supersaturation and crystal nucleation. Considering the metastable nature of h-WO_3 and the potential impact of morphology on the stability of the nanostructure, the crystalline phase may also play an important role in the determination of the morphology.

The band gap energies of synthesised WO_3 nanostructures ranged from 2.70$\pm$0.03 eV to 3.25$\pm$0.03 eV. The highest band gap was observed at pH 1.05, which was the transition point of crystal phases and morphology. The higher band gap energies of h-WO_3 nanostructures in comparison to m-WO_3 can be explained by the effect of QC and the crystal structure. W-EtOH and W-2.01-P20E samples exhibited blue colour while the rest of the samples were

pale yellow. The absorption spectra of the blue samples revealed that the light absorption further increased beyond the apparent band gap energy in the far red region of the visible spectrum. The optical behaviour implied that in-gap states were formed due to reduced W atoms. Additionally, for the W-2.01-P20E the accommodation of NH^{4+} ions into the crystal lattice resulted in a slight band gap narrowing.

The photocatalytic tests showed that the photocatalytic efficiency of nano WO_3 was a compromise of the band gap, crystal phase, morphology, and the oxidation state. The best catalyst was W-1.52-P20E (E_g = 3.10 eV) that was closely followed by W-0.10-P20E (E_g = 2.70 eV) and W-1.05-P20E (E_g = 3.25 eV) samples. W-0.10-P20E and W-1.05-P20E exhibited similar photoefficiencies despite the fact that these samples showed the lowest and highest calculated band gap energies, respectively. It was suggested that the presence of multiple crystal phases and morphologies in W-1.05-P20E could compensate the limited light absorption property of the material. The blue samples (W-2.01-P20E and W-EtOH) typically exhibited reduced photoactivity. It was suggested that the presence of in-gap defect states could act as recombination centres for the photo-generated charges which could result in lowered overall photoefficiency.

Chapter 5

Effect of Ag co-catalysis on TiO_2/Cu_2O

The content of this chapter has been presented at the E-MRS Spring Meeting, in Strasbourg, France between 22-26 May 2017. This project has been also awarded by the Graduate Student Award.

5.1 Introduction

TiO_2 is still one of the most studied photocatalyst owing to its excellent chemical stability, inexpensive and non-toxic nature. It also possesses adequate valence and conduction band edge positions for water-splitting. However, as most single materials its activity was found to be inefficient for industrial processes [16].

Inefficiencies may arise from exclusive light absorption, fast e^-/h^+ recombination and/or short diffusion length of the charge carriers [220]. To improve one or more of these shortcomings, different approaches were investigated in the past including (i) heteroatom doping, (ii) semiconductor coupling or (iii) surface modifications. For instance, by forming a nanocomposite with a narrow band gap semiconductor, both the light absorption can be extended into the visible range and the charge carrier recombination can be suppressed. This holds true when a type II band alignment is induced between the semiconductors [221]. Addi-

tionally it was found that further enhancement in the photoefficiency may be possible by combining one or more approaches. For example, the synergetic effect of noble metal surface modification and semiconductor coupling was reported for a Ag/TiO_2/multi-walled carbon nanotube heterostructure and a g-C_3N_4/Pt/ZnO photoanode [222, 223]. In both cases the ternary hybrid nanostructures overperformed the visible photocatalytic activity and photoelectrochemical performance of the binary counterparts, respectively. In other cases, doping and nanomaterial coupling was found to beneficially affect the photoefficiency. *Chen et al.* for example investigated a nitrogen-doped graphene/ZnSe nanocomposite system that exhibited improved photoactivity towards methyl orange [224]. Elsewhere, *Nguyen-Phan et al.* studied an Sn-doped TiO_2 coupled reduced GO system. The doped nanocomposite was found to exhibit increased specific surface area, enhanced visible light absorption and higher photoactivity than the undoped nanocomposite [225].

Recently Cu_2O, a non-toxic and earth abundant p-type semiconductor, has gained much attention for visible-response photocatalysis, electrochemical and gas sensing applications [226–228].

Its narrow direct band gap (2.2 eV) and high light absorption abilities makes it ideal to be utilized in solar-response systems [229]. However, due to the rapid charge carrier recombination, it is often coupled with other semiconductor oxides such as TiO_2 [230]. In such a system, the adequate band alignment could facilitate effective electron-hole separation which can further promote the photocatalytic performance [231]. Therefore, binary heterostructures such as Cu_2O/Ag, Cu_2O/TiO_2 or Cu_2O/ZnO are commonly prepared in order to mitigate charge recombination [232–235]. Yet, the combination of different approaches like nanocomposite formation and surface modification has been only rarely investigated for Cu_2O type catalysts. For example, an Ag/Cu_2O/ZnO triplejunction photoelectrode has been fabricated by *Liu et al.* for photocatalytic hydrogen generation [227]. Others prepared and tested a Cu_2O/Ag/TiO_2 thin film in photocatalysis [236]. In both cases, promising results

and enhanced performance was reported for the composite structures that was explained by the improved visible light absorption, higher charge separation and enhanced electron transfer. Although some investigations have been already carried out in the preparation of ternary hybrid structures and metal-modified systems, it is still a rather unexplored field for Cu_2O related systems.

Therefore, the motivation of this work was to further extend the current studies on TiO_2-Cu_2O systems by combining different modification techniques. To the best of our knowledge, TiO_2/Ag/Cu_2O powder system has not yet been investigated. Therefore uniquely, in this study not only the amount of Ag content was studied but also the effect of the synthesis sequence of the Ag deposition step as well. The Ag modification was carried out between 1% to 5% which resulted in effective plasmonic photocatalysts in the past [94, 237, 238]. The hybrid nanostructures were prepared by a facile wet-chemical technique and subsequent UV-treatment. The nanostructures were fully characterized by SEM, TEM, XRD and UV-visible diffuse reflectance along with the dark adsorption kinetics. Because the materials exhibited both indirect and direct electron transitions over the forbidden band gap, multiple techniques were employed for the band gap estimation.

5.2 Results and Discussion

5.2.1 Nomenclature

The TiO_2/Cu_2O and Ag related powder catalysts presented in the thesis are named as follows. The first letter indicates the type of semiconductor and the related number refers to the nominal composition. For example catalysts T, C or TA1C stands for TiO_2, Cu_2O or TiO_2/Ag(1%)/Cu_2O catalysts. The TAC and TCA nomenclature reflects the order of synthesis steps. For example, in TA5C catalyst firstly Ag was synthesised in a TiO_2 suspension which

was followed by the Cu_2O synthesis step. TAC or TCA notation is used to discuss general material properties regardless the nominal Ag percentage.

5.2.2 Crystal structure

The crystal structure of the nanomaterials has been investigated by X-ray powder diffraction (XRD).

Figure 5.1 a) shows the diffractogram of C and TC nanostructures. The bare Cu_2O sample was identified as cubic Cu_2O based on 71-3645 JCPDS card. Typical peak positions of 2θ = 29.8°, 36.6°, 42.5° and 61.6° could be assigned to (110), (111), (200) and (220) (hkl) planes, respectively. Additionally, it was also noted that the peaks were intense and sharp which suggested good crystallinity. TC heterostructure showed characteristic peaks of anatase and rutile TiO_2 (based on 21-1272 and 72-7374 JCPDS cards, respectively) and also cubic Cu_2O. No other crystalline structure could be identified from the XRD pattern. Although it was noticed, that the diffraction peaks of the TC sample were less intense compared to the bare Cu_2O.

Figure 5.1 b) depicts the diffractogram of T and TA5 nanostructures for comparison. The bare TiO_2 sample showed anatase and rutile reflection peaks as expected. Whereas the Ag-modified TA5 nanomaterial showed evidence of the Ag-content beside the anatase and rutile peaks of TiO_2. Characteristic Ag diffraction peaks could be identified at peak positions of 2θ = 44.4° and 64.5° that could be assigned to (200) and (220) (hkl) planes of cubic metallic Ag (based on 04-0783 JCPDS card), respectively.

The XRD pattern of TA5C is shown in Figure 5.1 c) in comparison with the binary TC hybrid structure. The diffractogram of TA5C showed characteristic peaks of anatase and rutile TiO_2, cubic Cu_2O and cubic Ag without the indication of other crystalline impurities. The diffraction pattern of TA3C and TA1C samples could be assigned to the same crystal phases as TA5C only the intensity of metallic Ag peaks were found to be less intense.

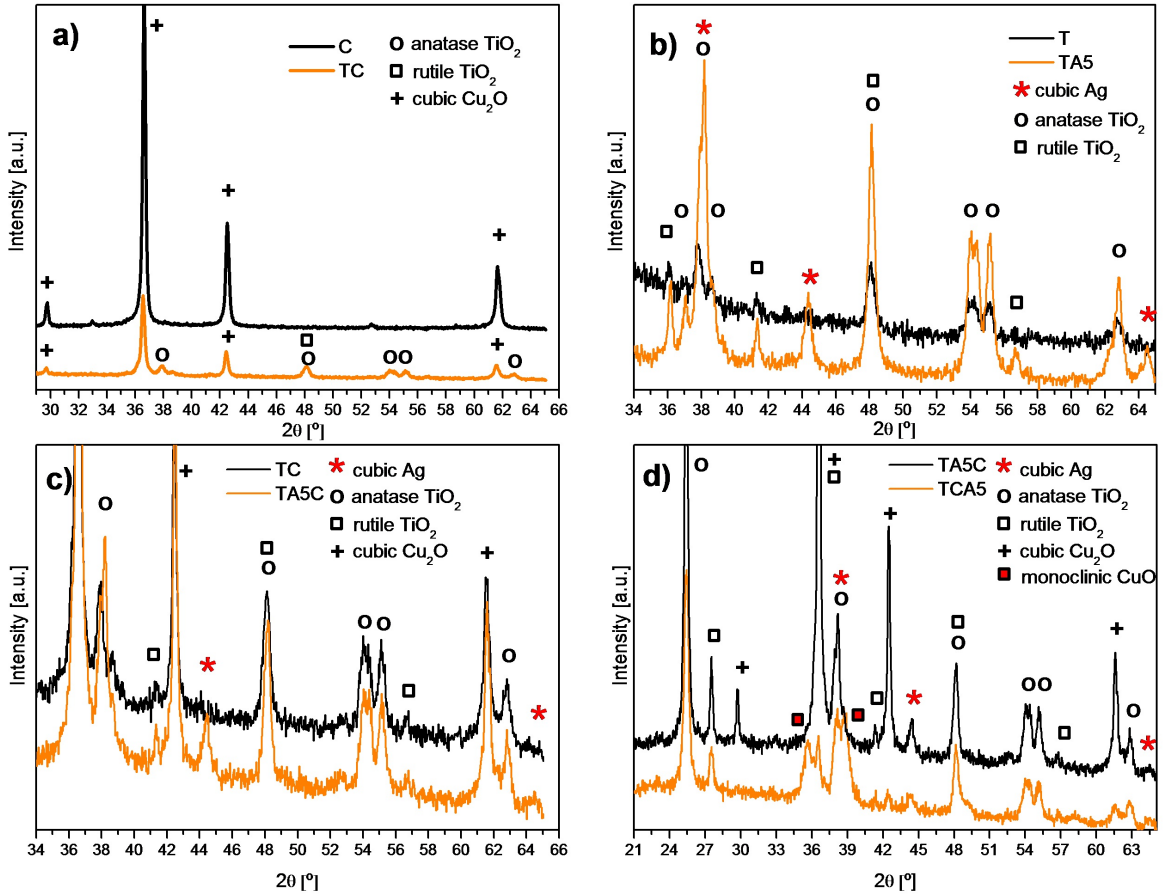

Fig. 5.1 XRD diffractograms of the nanostructures

Finally, Figure 5.1 d) shows the diffraction pattern of TCA5 nanostructure. Uniquely, a new crystal phase could be identified in the TCA hybrid structures. The newly appearing peaks at $2\theta = 35.6^\circ$ and 38.8° positions indicated the presence of face-centered monoclinic CuO (73-6023 JCPDS card) in the ternary TCA5 nanostructure. Although, there was still indication to the presence of co-existing cubic phase Cu_2O at $2\theta = 42.5^\circ$ and 61.6°. Therefore, TCA5 sample was interpreted as a mixture of face-centered monoclinic CuO and cubic Cu_2O. The partial oxidation of Cu_2O is likely to be induced by the Ag-deposition procedure since in TA5C, where the Ag-deposition was performed prior to Cu_2O synthesis, only cubic Cu_2O could be identified in the XRD pattern. The partial oxidation of cubic Cu_2O was also evidenced at 1% Ag loading in TCA1 catalyst. With regard to the peak intensity, it

was found that TCA5 catalyst exhibited less intense peaks in the XRD pattern compared to TA5C sample which could be an indication of reduced crystallinity.

5.2.3 Morphological structure

The morphological structure of the nanomaterials has been explored by recording SEM and TEM images that are presented in Figure 5.2 and 5.3, respectively.

In general, the SEM images revealed that the various nanostructures consisted of cuboidal or irregularly shaped spherical nanocrystals that were typically less than 100 nm in size. Furthermore, the TEM images revealed the co-existence of smaller and bigger nanostructures in the hybrid materials.

It was found that the pristine Cu_2O nanostructure exhibited uniform cuboidal nanocrystals with a characteristic dimension of *circa* 60-75 nm as it can be viewed in Figure 5.2 a). The hybrid nanostructures shown in Figure 5.2 b)-f) revealed more irregularity in the shape and size of the nanocrystals. TC nanomaterial shown in Figure 5.2 b) and Figure 5.3 a) was found to consist of smaller 15-30 nm and bigger *circa* 50-80 nm crystals. The nanoparticles resembled cuboidal and irregular spherical shapes. The wider size distribution could be caused by the hybrid nature of the sample. It was indicated by previous reports that anatase and rutile phases of TiO_2 exhibit different mean crystal sizes in P25 [159]. Also the primary crystal size of TiO_2 was 21 nm according to the analytical report of P25 used for this study which is significantly smaller than the typical crystal size of the reference bare Cu_2O nanomaterial.

The shape and size distribution of TA1C and TA5C which is shown in Figure 5.2 c), d) and Figure 5.3 b) were found to be similar to TC sample. The nanocrystals possessed both cuboidal and spherical shapes and typically ranged from around 20 nm up to 80 nm.

And finally, Figure 5.2 e), f) and Figure 5.3 c) depicts TCA1 and TCA5 nanomaterials. Although the TEM image reveals the presence of both smaller and bigger crystals, there

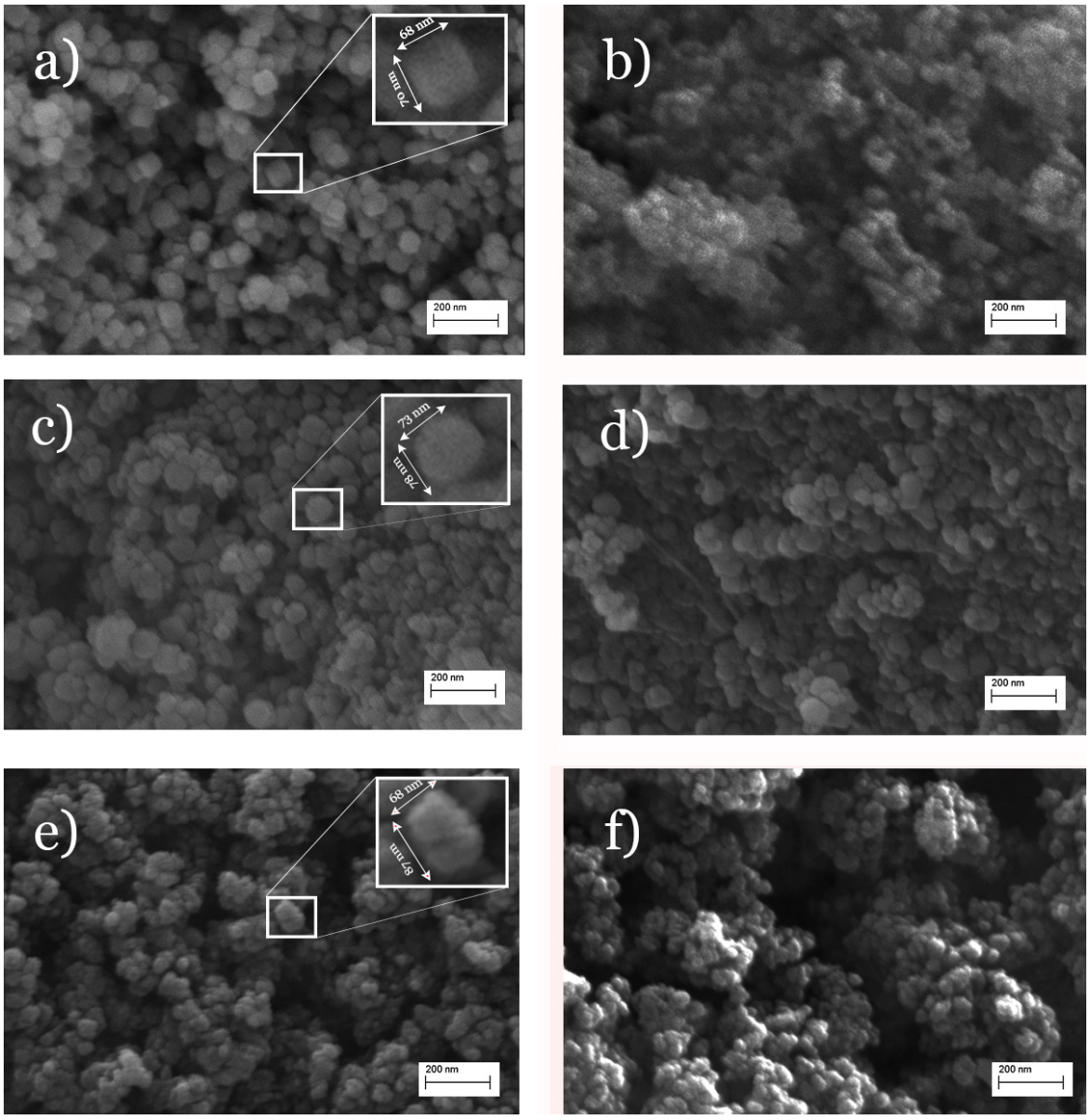

Fig. 5.2 SEM images of a) Cu_2O, b) TC, c) TA1C, d) TA5C, e) TCA1 and f)TCA5 nanostructures

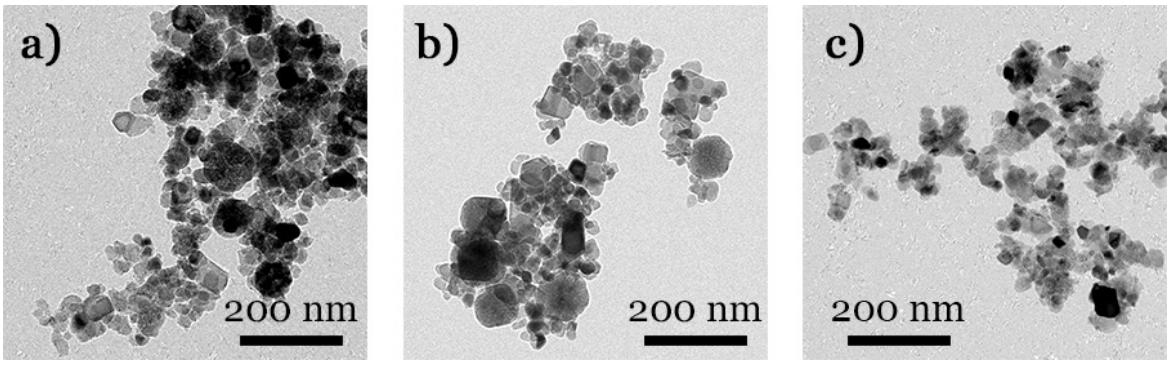

Fig. 5.3 TEM images of a) TC b) TA5C and c)TCA5 nanostructures

are fewer bigger nanoparticles compared to TC or TA5C samples. The reduced number of 50-80 nm nanocrystals correlates with the fact that in TCA samples the cubic Cu_2O was partially oxidized to face-centered monoclinic CuO as revealed by XRD. This could imply that the bigger cuboidal shaped nanostructures are Cu_2O which is also in agreement with the typical morphology of the reference Cu_2O sample. From the SEM image it could be noticed that the nanocrystals in TCA1 and TCA5 samples were typically in close contact with each other and they aggregated to form *circa* 80-100 nm or bigger clusters.

5.2.4 Optical properties

The light absorption properties of the nanostructures were studied by recording the solid-phase diffuse reflectance (DR) spectra which is shown in Figure 5.4 a). To estimate the band gap values (E_g) the Tauc model was used which can be seen in Equation 3.8 and displayed in Figure 5.4 b)-d). As an additional method, differential reflectance method (DRM) was also employed to obtain additional information on the band gap energies of the hybrid nanostructures which is shown in Figure 5.5.

Importantly, in Equation 3.8 n coefficient takes different values depending on the mode of electron transition of the material. In the case of indirect electron transition n= 2 whereas for direct transition n= 1/2.

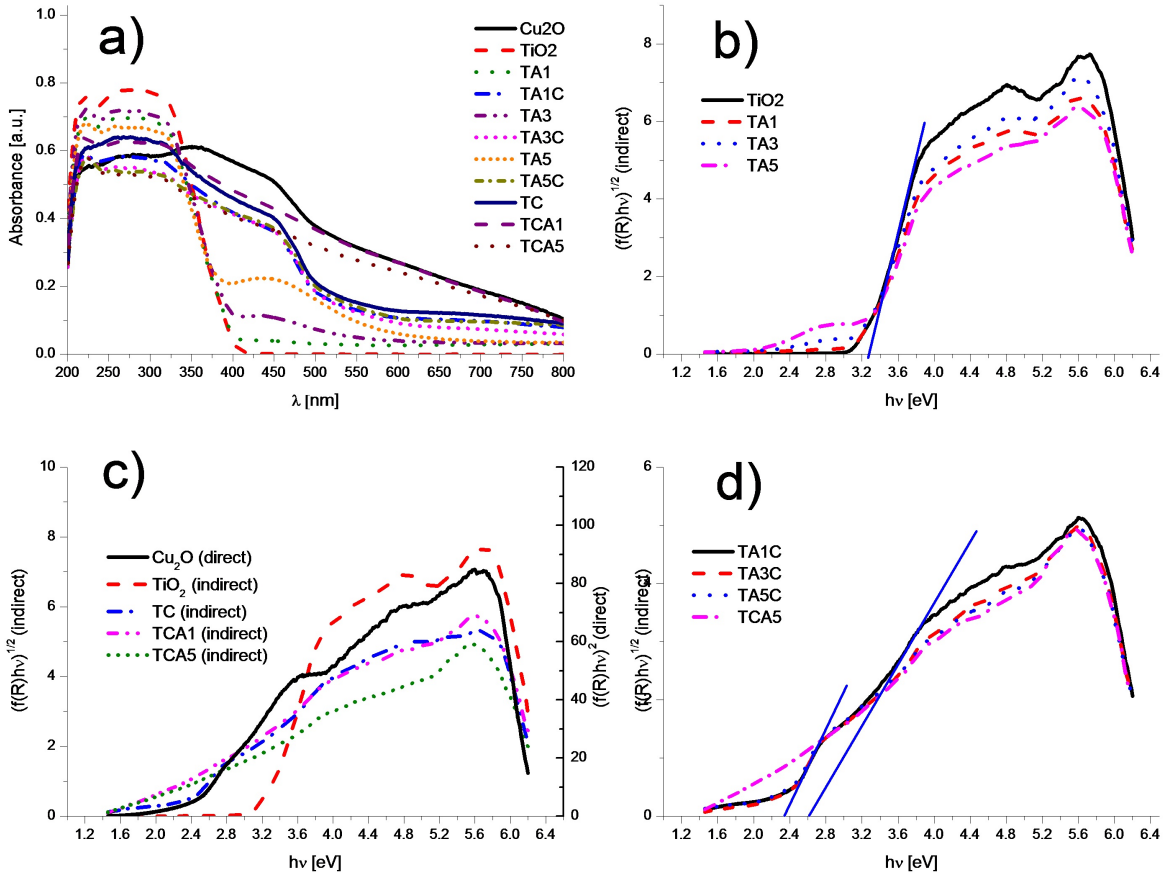

Fig. 5.4 The light absorption properties of the nanostructures shown a) in the diffuse reflectance spectrum and b)-d) in the Tauc plot

It is known that P25, which was used as TiO_2 source in the synthesis processes, is the 3:1 mixture of anatase and rutile phases of TiO_2, respectively. However, the different crystal phases of TiO_2 are typically associated with different electron transition over the forbidden band gap. The anatase phase is most typically reported to possess indirect transition while both indirect and direct band transitions are commonly reported for the rutile phase [159, 35, 158]. Therefore the estimation of the band gap of TiO_2 requires certain assumption. Becauce anatase is the major phase, indirect transition was assumed in the Tauc plot. The calculated band energy was found to be 3.28 ± 0.03 eV which is in good agreement with other literature report [159].

Using indirect Tauc model, it was found that the absorption edge of the Ag-modified TiO_2 samples has slightly red-shifted (ca. 0.05-0.08 eV) compared to the bare TiO_2. Additionally, an absorption peak centred around 450 nm appeared in the absorption spectra of TA1-TA5 samples. This is believed to be caused by surface plasmon resonance effect which is characteristic of metallic Ag and has been previously reported in the literature [239]. It could be noted that with increasing Ag content the intensity and distribution of the characteristic absorption peaks increased. It is known that the resonance effect induced by surface deposited noble-metals such as Ag is influenced by the size and shape of the nanoparticles. *Madhavi et al.* reported that increasing the size of Ag nanoparticles could induce broader absorption peaks which was explained by secondary radiations affecting the surface plasmon resonance [240]. Therefore, it is possible that the increased intensity and broadened absorption peak in TA5 sample is caused by the increasing number and/or size of the Ag nanoparticles.

The optical band gap of Cu_2O sample has been calculated to be E_g = 2.36±0.03 eV by direct Tauc model [241]. The direct band gap of nanostructured Cu_2O was reported to typically range from 2.2 to 2.5 eV while the band gap of bulk Cu_2O is reported to be 2.17 eV [242–244]. Our estimated band gap is in good agreement with reported literate data and higher than that of the bulk form which is consistent with weak quantum confinement effect caused by the nanoformulation.

To estimate the band gap of the hybrid nanostructures such as TC, TAC or TCA by the Tauc model, firstly the mode of electron transition needed to be assumed. However, the presence of both indirect (anatase TiO_2) and direct nanostructures (rutile TiO_2 and cubic Cu_2O or monoclinic CuO) complicated the assumption. In the literature, *Perez-Gonzalez et al.* determined the optical band gap of an anatase TiO_2/ZnO nanocomposite film (prepared in different ratios) where the anatase TiO_2 possessed indirect while the ZnO direct electron transition over the band gap. The authors found that the band energies estimated by Tauc

	E_g [± 0.03 eV] Indirect Tauc plot	E_g [± 0.03 eV] Direct Tauc plot	E_g [± 0.04 eV] Differential reflectance
TC	2.35 2.77	2.50 3.15	2.49 2.57 2.68
TA1C	2.35 2.61	2.50 3.15	2.50 2.56 2.66
TA3C	2.35 2.62	2.50 3.12	2.48 2.56 2.67
TA5C	2.34 2.62	2.48 3.15	2.48 2.56 2.67

Table 5.1 Summary of the estimated band gap values for the nanostructures by direct and indirect Tauc plot and by differential reflectance method

model gave closer agreement with reported values when the major component's mode of transition was assumed in the Tauc relationship [245]. However, SEM-EDS results indicated that in the prepared TiO_2-Cu_2O composite nanostructures the contribution of both direct and indirect transitions was comparable. Therefore, the absorption threshold of the hybrid nanomaterials was estimated by both direct and indirect Tauc plot. Additionally a third approach, the differential reflectance method (DRM) has been also utilized that did not require the assumption of the mode of electron transition. This technique has been previously used in the literature to further validate estimated band gap energies especially for mixed indirect/direct heterostructures [158, 159]. Moreover, *Apopei et al.* claimed that the band gap estimation of mixed phase TiO_2 by differential reflectance method could provide more accurate values than Tauc plot [159]. The band gap estimation by differential reflectance method was performed by plotting $dR/d\lambda$ against the wavelength (λ) from which the maxima of the fitted peaks gave estimates for the band gaps. Figure 5.5 shows the transformed spectra.

In general, it was found that three band gaps could be estimated from the differential reflectance curves for the binary TC and ternary TAC heterostructures while two band gaps

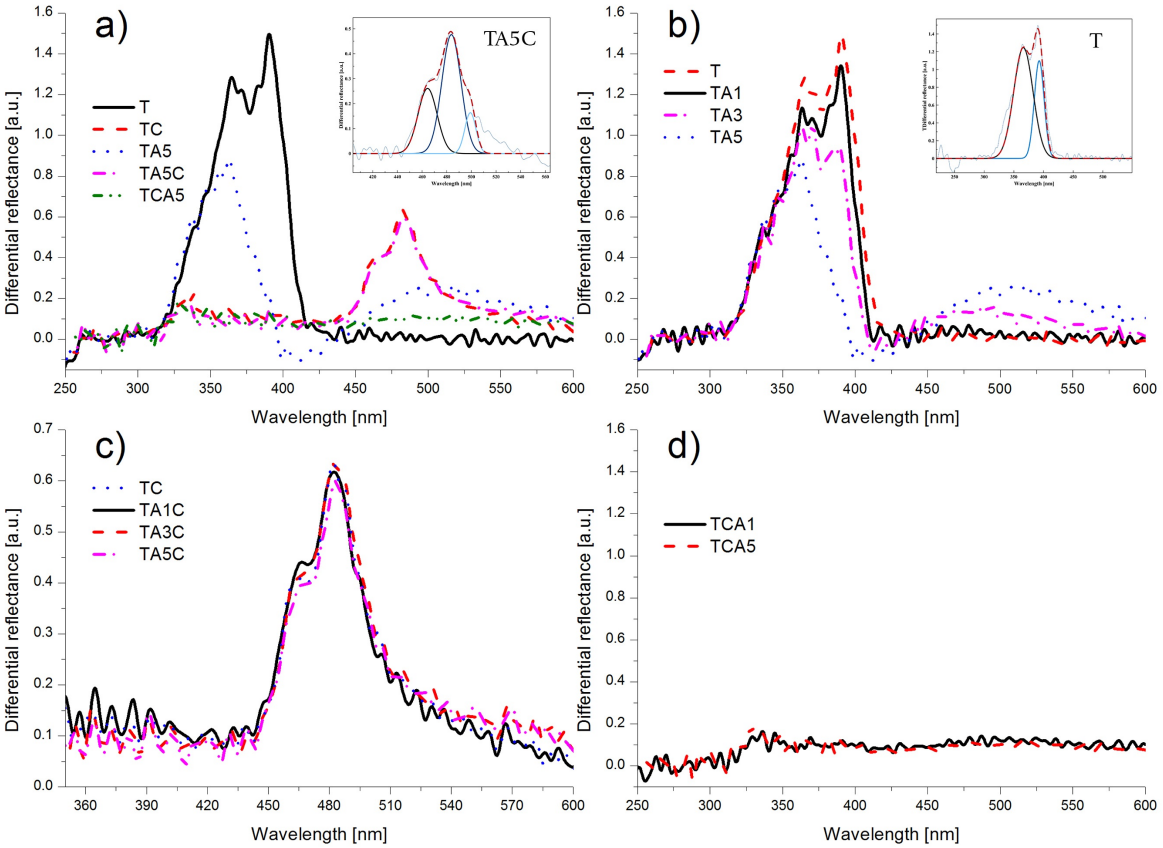

Fig. 5.5 Band gap estimation based on the differential reflectance method for selected nanostructures

could be derived from the Tauc plot both under direct and indirect transitions. Similarly to us, *Li et al.* reported two apparent band gaps for an Ag_2O/TiO_2 double layer thin film by Tauc model. The higher band gap was associated with TiO_2 whereas the smaller band gap with Ag_2O [77]. Additionally, *Apopei et al.* found that in contrast to the Tauc model, by DRM two band gaps could be determined for P25 intstead of one. One for the anatase and one for the rutile phase [159]. Table 5.1 summarizes the calculated band gap energies by the different methods and Figure 5.6 helps to visualize the differences between the estimated values.

The absorbance spectrum of TC catalyst revealed extended light absorption into the visible range compared to bare TiO_2 thanks to light sensitization of Cu_2O. By using different methods, the estimated E_g values for the smallest band gap varied between 2.35 and 2.50 eV.

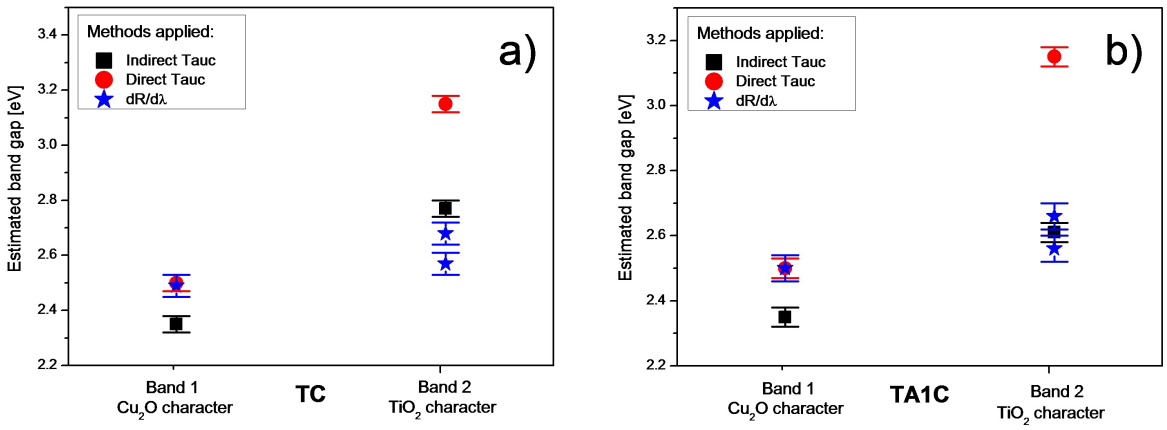

Fig. 5.6 Comparison of the estimated band gap values by direct and indirect Tauc plot and by differential reflectance method for a) TC and b) TA1C catalyst

The closest agreement between the estimated E_g values was found between direct Tauc plot and DRM that differed only by 0.01 eV. This difference is smaller than the error band associated with the E_g estimation ($\pm$ 0.03 eV). On the other hand, the smallest band energy calculated by indirect Tauc model lied 0.14-0.13 eV below these values.

Considering the higher energy gap, it could be noted that the direct Tauc plot estimated significantly higher energy value (by at least 0.47 eV) than the rest of the methods. Whereas the indirect Tauc plot and DRM showed closer matching E_g values that can be seen in Figure 5.6 a).

It is interesting to observe that closer agreeing E_g estimates could be achieved between different methods when the electron transition of the intrinsic semiconductor was used in the Tauc model. For example for the higher band gap, indirect Tauc plot gave close agreement with DRM which is consistent with the electron transition of the major anatase TiO_2 phase. Similarly, for the smallest band gap, direct Tauc plot agreed better with DRM which is consistent with the mode of transition of Cu_2O.

For TAC ternary heterostructures similar light absorption behaviour to TC catalyst was observed. Figure 5.6 b) demonstrates the estimated band gap energies of TA1C catalyst obtained by different methods. It can be seen that TA1C shows very similar trend to TC.

Finally, for TCA ternary nanostructures different optical behaviour was found. In general, the DRM could not derive optical band gap energy for TCA catalysts due to the absence of sharp drop in the absorbance spectra. The absence of sudden decrease in the light absorption suggests light harvesting over the whole visible range although with decreasing intensity. This unique optical behaviour could be most probably ascribed to the partial oxidation of Cu_2O into CuO. In the literature monoclinic CuO is characterised by narrower band gap energy than Cu_2O. Reported E_g values of monoclinic CuO typically lies between 1.55 and 2.00 eV for bulk and nanostructured CuO, respectively [246, 247].

5.2.5 Dark adsorption

Cu_2O has been previously realized as promising photocatalytic adsorber material in the literature [89].

To model dye adsorption most widely Lagergren pseudo-first order or pseudo-second order kinetic models are used in the literature [248]. Therefore, to describe the dark adsorption of the hybrid structures these kinetics models were fitted to our experimental data. Figure 5.7 b) and c) depicts the fitted kinetics models. To gain further insights into the sorption kinetics, the intra-particle diffusion model by Weber and Morris was also applied. This is shown in Figure 5.7 d).

The linearized forms of Lagergren pseudo-first order shown in Equation 5.1, pseudo-second order in Equation 5.2 and intra-particle diffusion models in in Equation 5.3 takes the following forms.

$$log(q_e - q_t) = log(q_e) - \frac{k_1 t}{2.303} \tag{5.1}$$

$$\frac{t}{q_t} = \frac{1}{k_2 q_e^2} + \frac{t}{q_e} \tag{5.2}$$

$$q_t = k_i t^{1/2} + C \tag{5.3}$$

where q_e and q_t are the amount of adsorbed dye at equilibrium and at any time t, respectively and k_1, k_2 and k_i are rate constants, t denotes the time and C is model parameter which indicates the thickness of dye adsorbed at the boundary layer.

The pseudo-second order model shown in Equation 5.2 was first proposed by Ho and McKay to describe the sorption kinetics of metal ions onto a peat sample [249]. The kinetic equation by Ho and McKay could model the chemical bonding between the sorbent and sorbate. The order of the empirical model is reflected from the power of the non-linearized form of the kinetic equation which is shown in Equation 5.4. In the original paper the unit of the pseudo-second order constant k_2 was given as [g/mg min] [250].

$$\frac{dq}{dt} = k_2(q_e - q)^2 \tag{5.4}$$

The amount of dye adsorbed was calculated according to Equation 5.5.

$$q_t = \frac{(c_0 - c_t)V}{m} \tag{5.5}$$

where c_0 and c_t are the initial and final concentration in [mg/L], respectively, V is the volume in [L] and m is the mass of catalyst in [g].

Figure 5.7 a) revealed that the adsorption profile of TC, TA5C and TCA5 catalyst was remarkably different. It could be noticed that the Ag-modified TA5C and TCA5 materials showed lower dye uptake levels over time up to about 175 min. At this point TA5C reached similar levels of dye uptake as TC catalyst. Interestingly, after the first couple of minutes TCA5 sample did not even approach the dye uptake level of TC or TA5C. It showed significantly lower dye adsorption ability which was saturated quickly. This showed that the introduction of Ag into the binary TiO_2-Cu_2O nanostructure had much effect on the catalyst

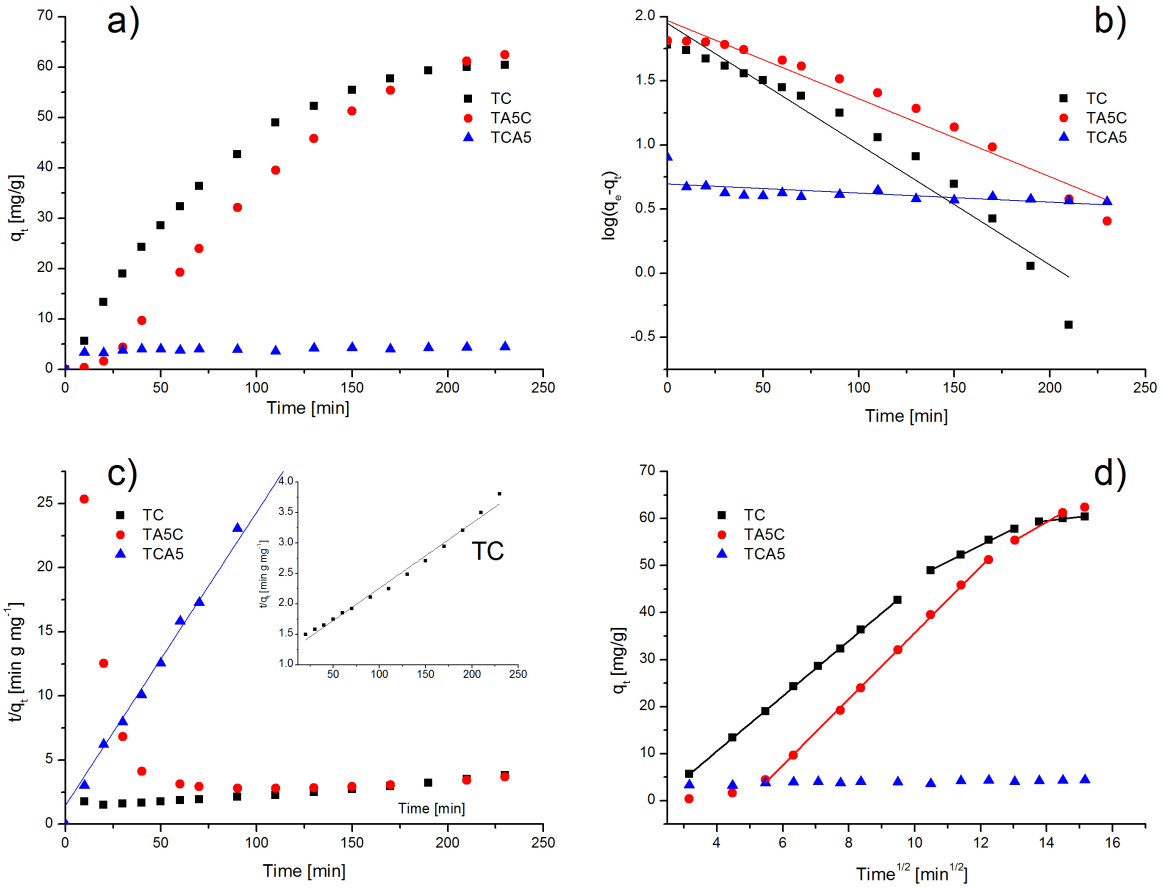

Fig. 5.7 Kinetic models for TC, TA5C and TCA5 catalyst a) q_t versus time plot b) Lagergren pseudo-first order model c) pseudo-second order model d) Weber and Morris intra-particle diffusion model

affinity to adsorb MO onto its surface. Although it is worth noting that in the case of TCA structure beside the Ag modification, the oxidation state of the copper component was also altered. This could also play a prominent role in the much reduced dye adsorption of the catalyst. Typically, the adsorption characteristics reflect the physicochemical properties of the material. And although the surface charge of semiconductor oxides could strongly depend on conditions such as the solution pH, synthesis methods, purity of the material ... *etc*, it was found that bare Cu_2O may possess positively charged surface under ambient conditions [251]. According to the review of Marek Kosmulski, the pH level at the point of zero charge is reported to lie between 5.0-11.5 for Cu_2O [252]. This means that under more acidic conditions than the pH of the point of zero charge, the surface of Cu_2O is expected to become positive. The surface properties of materials can be experimentally determined by *e.g.* Zeta potential measurement. In agreement with this, *Gao et al.* for example realized that bare Cu_2O exhibited positive surface charge while a graphene-Cu_2O composite showed negative Zeta potential values in aqueous solution at 0.4 mg/mL concentration [253].

Silver on the other hand, was reported to show little adsorption towards the anionic MO which was explained by its negatively charged surface character measured by Zeta potential analyzer [254]. Reports suggested that the negative surface charges of silver nanoparticles could originate from chemicals in the synthesis mixture such as citrate [255]. Ag nanoparticles synthesized from aqueous sea weed was also found to result in negatively charged nanoparticles [254]. It is likely, that the opposing surface charges of Cu_2O and Ag could cause different affinity towards MO in the case of the Ag-cocatalyzed materials.

Figure 5.7 b) shows the $\log(q_e\text{-}q_t)$ versus time plot which fits pseudo-first order kinetic model to TC, TA5C and TCA5 catalyst. It was found that TC and TA5C catalysts showed significant deviation from linearity after *circa* 100 min. This was reflected in the correlation coefficients of R^2 = 0.943 and 0.952, respectively. Similarly, TCA5 catalyst showed poor fitting to the Lagergren model.

Sample	k_i [mg g^{-1} $min^{-1/2}$]	C [mg g^{-1}]	$R^2[-]$
TC	3.47	12.64	0.996
TA5C	4.02	2.93	1

Table 5.2 Kinetic parameters of Weber-Morris intra-particle diffusion model

Figure 5.7 c) depicts the regression analysis for the pseudo-second order model which revealed that TC and TA5C nanostructures exhibited significantly different features at the early stages of dark adsorption. The least square linear fit revealed strong correlation coefficient of $R^2 = 0.988$ to the TC data points whereas $R^2 = 0.229$ to TA5C. The poor fitting of TA5C was caused by the significant deviation from linearity especially in the first 50 minutes. The early adsorption showed unique features which can be also viewed on the adsorption capacity (q_t) versus time plot on Figure 5.7 a). It can be seen that the dye started to bind to the catalyst surface at a very slow pace in the first 25 min. After that, a gradual rise in the adsorbed amount could be noted which essentially reached similar dye uptake rate as TC catalyst after 50 minutes. Due to this delayed adsorption behaviour, none of the Lagergren or pseudo-second order models could fully describe the adsorption characteristics of TA5C. However, the dark adsorption of both TC and TCA5 sample could be satisfactorily modelled by pseudo-second order kinetics. This finding correlates well with literature reports where *e.g.* cubic Cu_2O of various sizes and shapes were reported to follow pseudo-second order kinetics for dark adsorption towards organic dyes such as MO or Congo Red [256, 251, 97]. It was also indicated by previous reports that systems obeying pseudo-second order kinetics indicates chemisorption as dominant mechanism in the adsorption process. This reflects dimeric chemical reaction taking place between the sorbent and sorbate mostly through the sharing or exchange of electrons and ions [257–260].

In order to learn more about the adsorption mechanism, the intra-particle diffusion model was also explored. A single linear relationship in the Weber-Morris plot (q_t vs $time^{1/2}$) which passes through the origin implies that intra-particle diffusion is the sole rate-controlling

step [251, 261]. However, in the event of multi-linearity the adsorption process may be governed by multiple mechanism. Figure 5.7 d) depicts the Weber-Morris plot which clearly shows multilinear regression for both TC and TA5C structures. The q_t vs $time^{1/2}$ plot reveals three main linear regions. The first steep linear phase corresponds to external diffusion of the dye molecules to the catalyst surface which also referred as film diffusion [262]. The second linear portion indicates when the intra-particle diffusion is rate-controlling. Over this step gradual adsorption of the dye is taking place. The last rather horizontal linear part is the equilibrium plateau when the adsorption process reaches saturation coverage in the system [263]. For TA5C catalyst it is noteworthy that the first linear portion was delayed in time which is the result of disfavoured adsorption in the early phases of the process. The calculated kinetical parameters which were derived from the intercept and the slope of the linear lines are listed in Table 5.2 where the *C* values indicates the thickness of the boundary layer. For both catalysts it was a non-zero value but it was remarkably higher for TC catalyst. This indicates higher boundary layer effect in the dye adsorption onto TC [248, 263]. The adsorption profile of TCA5 catalyst was different from TC and TA5C. Firstly, the adsorption of MO onto TCA5 reached equilibrium more rapidly than for TC or TA5C. Secondly, the amount of dye adsorbed was significantly less for TCA5 relative to TC or TA5C catalysts.

5.2.6 Apparent visible photoactivity

The apparent visible activities of the prepared heterostructures were studied after 60 minutes of dark stirring under visible light irradiation. Figure 5.8 shows that most typically the light irradiation significantly improved the decoloration efficiency of the Ag-cocatalysed samples compared to the dark reference measurements. However, TC catalyst did not exhibit considerable improvement under light illumination relative to the dark measurement under this testing condition.

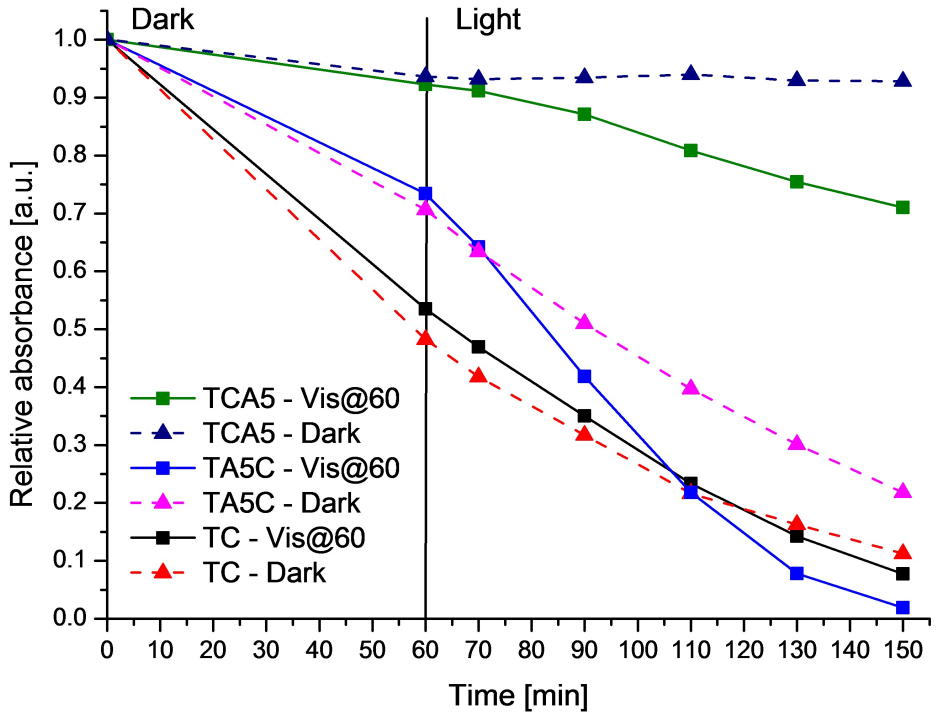

Fig. 5.8 Apparent visible activities of TC, TA5C and TCA5 nanomaterials after 60 min dark stirring shown with solid lines and dark activity shown with dotted lines

Following the *Kinetic concepts of heterogeneous photocatalysis* book chapter published by Springer, the evaluation of the kinetic data was based on classical graphical methods. The concentration-time plot was used to determine the kinetics rate values for the disappearance of the orange colour of MO dye in the case of the different catalysts [264, 265].

Heterogeneous photocatalytic reactions commonly follow pseudo-zero and pseudo-first order models. In the pseudo-zero order model the rate of reaction does not significantly depend on the concentration of the target chemical. This is commonly the finding for systems where the catalyst surface is saturated by the dye or when the reactant is present in large excess in the solution. For systems obeying the pseudo-first order model, effectively a single reactant is influencing the rate of the disappearance of the dye while the variance of catalyst concentration remains negligible. Most photocatalytic systems using inorganic semiconductors were reported to fall into the category of either pseudo-zero or pseudo-first order kinetics [109, 74, 138, 266–271].

Catalyst	Pseudo-zero order		Pseudo-first order	
	k_0 [mg L^{-1} min^{-1}]	R^2 [-]	k_1 [min^{-1}]	R^2 [-]
TA5C	0.1742	0.985	0.0332	0.950
TA3C	0.1777	0.982	0.0323	0.958
TA1C	0.1176	0.998	0.0255	0.890
TC	0.1124	0.982	0.0192	0.988
TCA1	0.0735	0.994	0.0042	0.990
TCA5	0.0557	0.989	0.0028	0.989

Table 5.3 Kinetic model parameters for the apparent visible activities after 60 min dark stirring

In this work, TC and TAC catalysts showed good affinity to adsorb MO to its surface while TCA catalysts showed more limited dye adsorption by one hour dark stirring. Considering the local dye concentration by the catalyst surface pseudo-zero or -first order kinetics may be followed under visible light exposure. It is also noted that in the current systems dye adsorption and dye conversion could also take place under visible light irradiation. Keeping this in mind the approximation of the overall process was attempted with power law kinetics such as pseudo-zero or pseudo-first order models. The aim was to allow comparison of the performance of the different catalysts under current operational conditions.

The linearized forms of the pseudo-zero and pseudo-first order kinetic models are shown in Equation 5.6 and 5.7 [272, 273]. The calculated parameters and regression coefficients for the models are summarized in Table 5.3.

$$c_0 - c_t = kt \tag{5.6}$$

$$-ln\frac{c_t}{c_0} = kt \tag{5.7}$$

After fitting the experimental data with the different kinetics models, both visual observation and the correlation coefficients confirmed that the pseudo-zero order model could

Concentration [ppm]	TC	TA5C	TA3C	TA1C	TCA5	TCA1
t0	11.7	15.3	15.7	10.9	20.2	19.2
t10	10.3	13.4	13.5	9.6	19.9	18.6
t20	8.7	10.8	11.2	8.2	19.5	18.0
t30	7.7	8.7	9.0	7.4	19.0	17.4
t40	6.3	6.5	6.7	6.0	18.4	16.8
t50	5.1	4.5	4.6	4.9	17.7	16.0
t60	3.8	3.0	2.9	3.6	16.9	15.0
t70	3.1	1.6	1.6	2.3	16.5	14.3
t80	2.4	0.7	1.0	1.4	16.0	13.4
t90	1.7	0.4	0.4	0.4	15.5	12.8

Table 5.4 MO concentrations in the Visible process of the different photocatalysts tabulated in the function of irradiation times

adequately describe the process for all samples. The kinetics models are depicted in Figure 5.9 a)- b) and the concentration of MO solution derived from the UV-visible spectra is listed in Table 5.4.

Based on the pseudo-zero order rate constants, the following decoloration efficiencies could be established for the catalysts: TA3C > TA5C > TA1C > TC > TCA1 > TCA5. In general, it could be seen that TAC catalysts showed the highest while TCA catalysts the lowest rate constants in the visible process.

It could be noticed that catalysts with the lowest dark adsorption by 60 min (TCA1 and TCA5) showed the lowest rate constants (*circa* 0.06-0.07 $mgL^{-1}min^{-1}$). Whereas catalysts with medium level of dark adsorption (TA5C and TA3C) exhibited the highest rate constants of *circa* 0.17-0.18 $mgL^{-1}min^{-1}$ under visible light irradiation. TC and TA1C showed the highest dark adsorption, yet they exhibited medium efficiency under visible light.

Correlation between the amount of pre-adsorbed dye and the apparent photoefficiency could be noticed for the nanocomposites. TC catalyst with highest dye uptake did not favour further improvement under light irradiation. This may suggest that excessive dye adsorption on the catalyst surface could exert an extensive shadowing effect. By absorbing an appreciable amount of visible light less light may have reached the catalyst surface which inhibited the

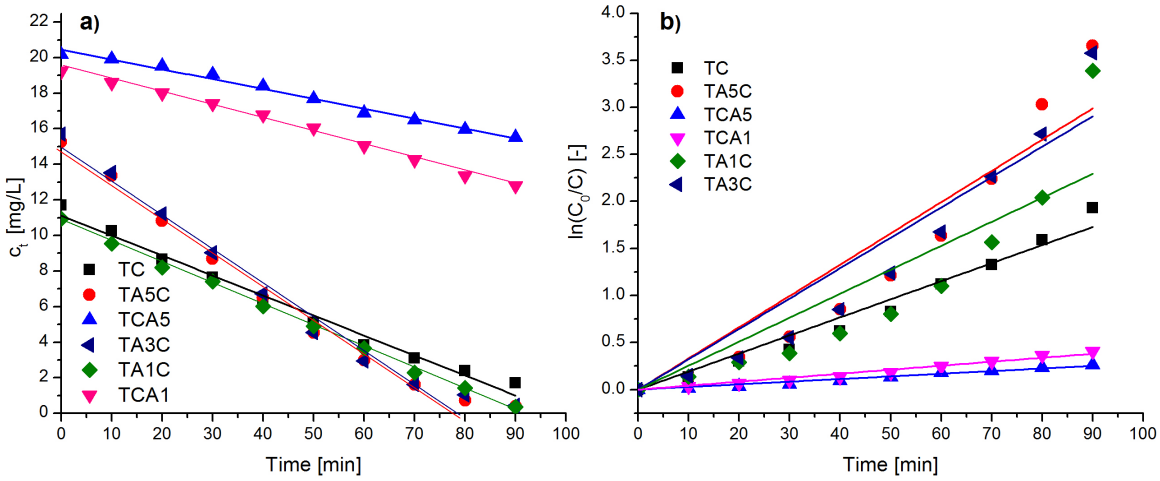

Fig. 5.9 a) Pseudo-zero order kinetic model and b) pseudo-first order model tested for the catalysts

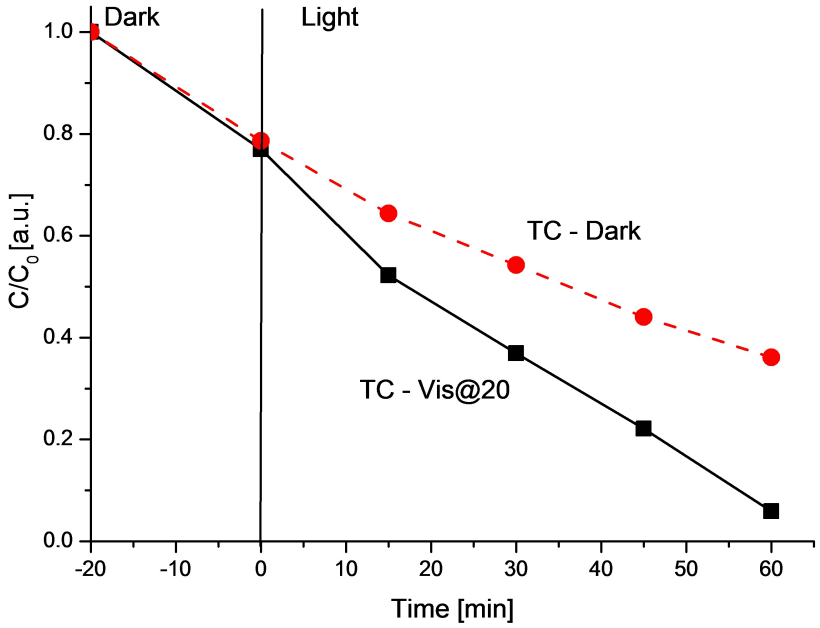

Fig. 5.10 Apparent visible activity of TC nanostructure after 20 min dark stirring shown with solid line and reference dark activity shown with dotted line

photocatalytic reactions. Similar phenomenon was noticed by *Sajjad* and his co-workers who tested the photocatalytic efficiencies of a WO_x/TiO_2 nanocomposite in varied concentration of MO solutions. They found that beyond an optimal dye concentration the photobleaching process was inhibited and lower efficiencies were measured [274]. They argued that the path length of photons were reduced which could affect the performance of the catalyst

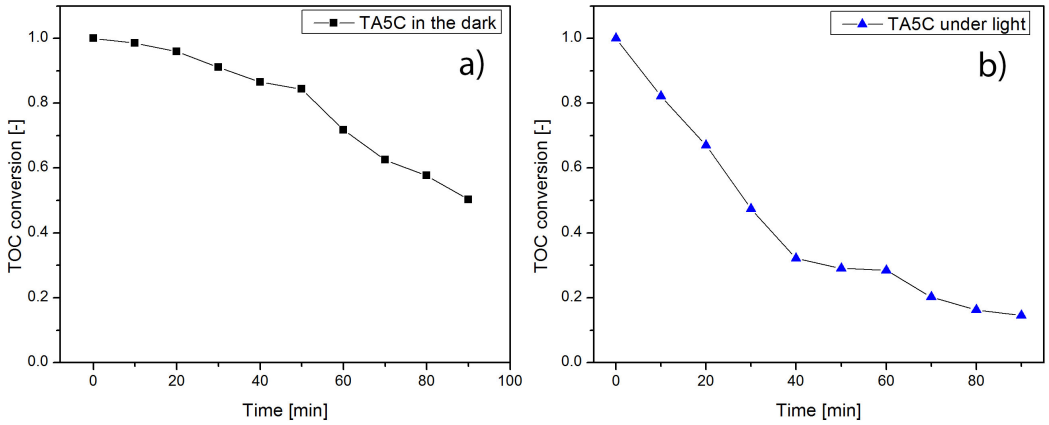

Fig. 5.11 TOC conversion showed for TA5C catalyst in the function of time a) when it is stirred in darkness and b) when exposed to visible light

detrimentally. They also mentioned possible competing effect of the dye adsorption with other species such as with oxygen or OH^- that play a key role in the photocatalytic process. Similarly, *Li et al.* also reported that increased initial dye concentration (RhB) resulted in lowered photoactivity of a magnetic $Fe_3O_4/TiO_2/SiO_2$ aerogel. The reduced efficiency was explained by blocked active sites and the fraction of the light absorbed by the dye itself [275]. Although in our test the initial dye concentration was not directly altered, still the different amount of MO adsorbed onto the surface of different catalysts may have led to similar effects on the apparent photoefficiency. In oder to test if the apparent visible activity of TC was affected by the amount of adsorbed dye, an additional experiment was conducted. In this experiment, TC catalyst was only allowed 20 min of dark stirring. This limited the amount of adsorbed MO to 23% from the previous *circa* 47%. As a result of reduced dye adsorption, significant improvement was noticed under visible light irradiation compared to the dark measurement as it can be seen from Figure 5.10. This finding further supported that the level of dark adsorption could play an important role in the overall performance of the catalyst under visible light irradiation which could be further investigated in the future.

In order to learn more about the underlying mechanism of the photocatalytic process further investigations were carried out. Typically, TOC analysis is undertaken in order to

provide insights in the nature of MO degradation considering complete mineralization and the formation of other intermediates [276, 277]. TA5C was selected among the catalysts for further analysis as one of the most active catalyst under visible light irradiation. It is worth mentioning that due to the limited batch size of the photochemical reaction, the samples needed to be diluted for the TOC measurements. This could reduce the certainty of detection by the TOC analyzer which could especially affect the lower concentration region. Therefore at this region the measurement may carry higher uncertainties. For reference, the dark stirred TA5C liquid samples were also analysed by TOC. However, in the dark process, no light-induced mineralization is expected nor the generation of organic degradation products. Therefore, similarly to the UV-visible spectrum, the decrease of the MO concentration could be attributed to the adsorption process. This is shown in Figure 5.11 a). The TOC conversion curve measured for TA5C catalyst under light irradiation is provided in Figure 5.11 b). For the TOC measurement the same testing and sampling conditions were employed as for the kinetical study of the apparent visible activities. From the TOC conversion plot it can be immediately seen that the total organic carbon content of the MO solution shows a declining trend over time similarly to the UV-visible curve of the solution using the same material (see in Figure 5.8). It could be also noticed that the TOC conversion curve levels off around 0.15 conversion and does not approach zero as closely as the UV-visible plot. The somewhat higher level of final conversion in the TOC measurement compared to the UV-visible conversion could indicate a degree of incomplete mineralization as opposed to full decomposition of the dye into CO_2 and H_2O. This TOC result also suggests that most of the MO removal in the case of TA5C under light exposure could be attributed to complete mineralization and/or adsorption processes generating limited amount of byproducts in the solution.

As a complementary technique, HPLC-MS analysis of TA5C was also performed in a qualitative manner to identify potential degradation products. Analysing the liquid sample

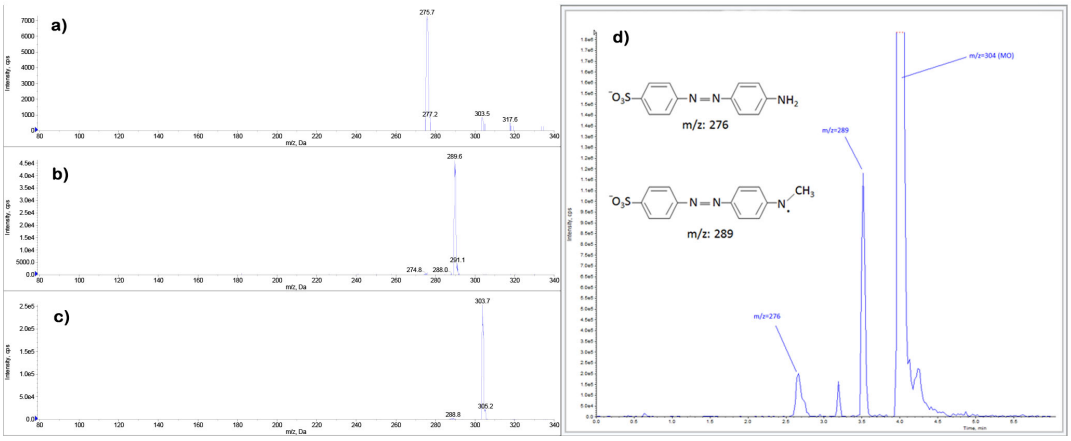

Fig. 5.12 HPLC-MS analysis of the MO solution after 90 min visible light irradiation when using TA5C catalyst, a)-c) MS spectra of the recognised products and d) HPLC chromatogram

after 90 min of light irradiation, from the MS spectrum the identification of two degradation products could be achieved. Their chemical formulas are displayed in Figure 5.12 d) along with the supporting chromatogram and MS spectrum a)-c). No other degradation product could be revealed from the light-irradiated intermediate samples. For reference, the HPLC chromatogram of the dark stirred samples are also shown in Figure 5.13 at 0 and 60 min of dark stirring along with the TA5C sample after 90 min of light irradiation. This supports that the dark stirring does not produce degradation products, only the presence of inherent chemicals can be discovered from both the 0 and 60 min dark-stirred liquid sample. However, the changing peak profile of the 90 min irradiated sample implies that some degradation products could be generated over the visible light irradiation. In agreement with the TOC results, the HPLC-MS analysis also suggested that the major form of MO removal could be attributed to the process of complete mineralization and adsorption. But, these results do not exclude the possibility that intermediate products generated by the photochemical process could also be physically adhered to the surface of the catalyst.

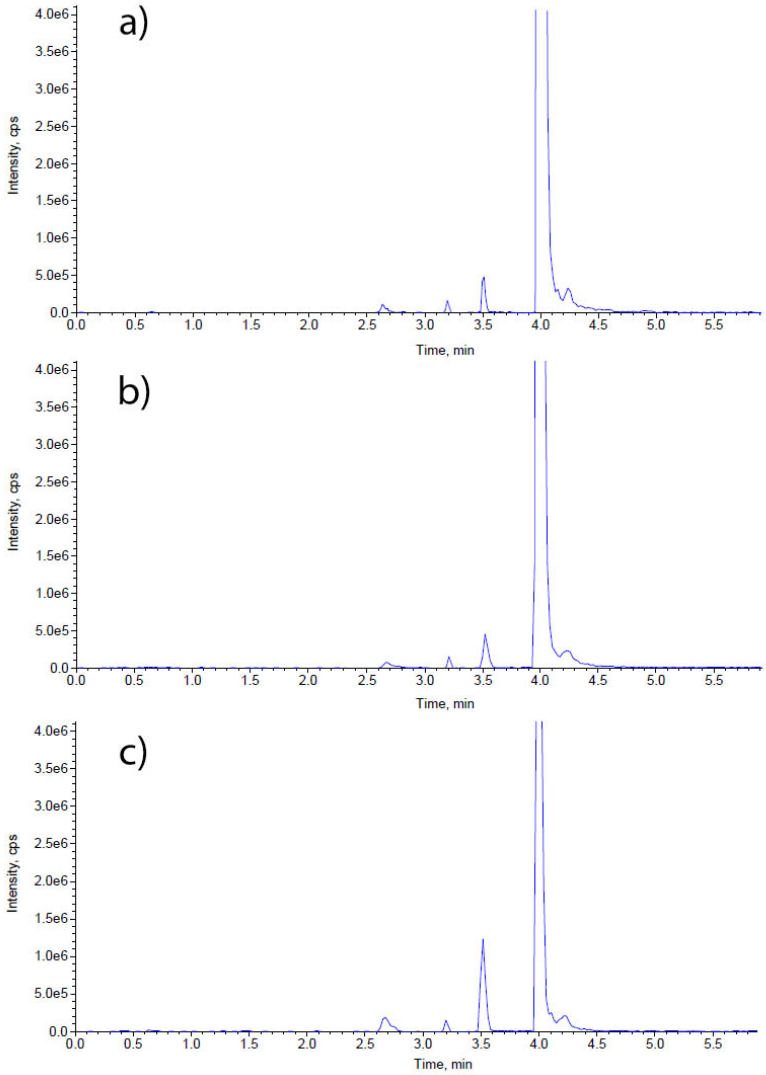

Fig. 5.13 HPLC chromatograms of the MO solutions when stirred in the dark for a) 0 min and b) 60 min and c) when irradiated with visible light for 90 min

The effect of Ag-modification

It was generally found that both the amount of Ag and the order of the synthesis process notably influenced the visible decoloration efficiencies of the materials.

In TAC catalysts, it was found that 1% Ag loading (TA1C) hardly changed the properties of TC and hence very close performance was noticed for both catalysts under visible light irradiation. However, 3% and 5% of Ag content, in TA3C and TA5C significantly enhanced the rates of the apparent visible process as can be seen in Table 5.3. For TCA catalysts, less effect was noticed when the amount of Ag content was varied. TCA1 which had 1% of Ag loading showed somewhat higher rate constant in the visible process than TCA5 catalyst with 5% of Ag loading.

When the order of the Ag-deposition step was altered, remarkable differences were noted in the material properties of TAC and TCA catalysts. While TAC catalysts were characterized as cubic Cu_2O by XRD, TCA catalysts in general contained mostly monoclinic CuO phase. The partial oxidation of Cu_2O into CuO in the TCA catalysts could be the result of the applied synthesis approach where the Ag-deposition step were conducted on TC under UV light irradiation. Other material properties such as the morphology and the optical properties were also affected by the order of the Ag-deposition step. As a result, TCA catalyst in general exhibited significantly lower apparent visible activities compared to TAC structures. This was reflected by the *circa* three times higher rate constant of TAC catalysts in the visible process. It is worth mentioning that the overall lower performance of TCA could originate from multiple factors. The restricted dye adsorption could limit the rate of the surface photoreactions and also the photoactivity of the oxidized CuO phase was reported to be different than that of the pure Cu_2O. Especially in CuO/TiO_2 systems, lowered photocatalytic activity was reported in the literature [278].

5.2.7 Mechanism

When TiO_2 and Cu_2O based heterostructures are fabricated a p-n junction is formed between the two semiconductors due to their different nature of conductivity [279]. As a result, the original valence and conduction bands are bended in order to reach equilibrium Fermi levels [95]. For a TiO_2-Cu_2O system diffusion of electrons from the CB of Cu_2O to the CB of TiO_2 is thermodynamically favoured whereas holes may accumulate on the VB of Cu_2O [22]. This way charge carrier separation could take place which is beneficial to produce longer-lived charges for photocatalytic surface reactions [16].

When Ag is incorporated into the system, in theory, the projection of Vis-light excited electrons from the conduction band of Cu_2O to metallic Ag could take place. Hence, in the ternary nanocomposites potentially both the Ag and the TiO_2 could serve as electron acceptors leaving the positive holes accumulate on the VB of Cu_2O. This way an even more sophisticated charge separation network may take place. In addition to the improved charge separation, Ag was reported to show plasmon resonant behaviour when interacting with visible light and was previously described as surface plasmonic co-catalyst. Several reports showed that Ag- or Au-modified plasmonic metallic nanostructures exhibited improved light absorption and/or photoactivities [94]. This may also contribute to the overall photo-efficiency of the ternary nanocomposites under visible light irradiation.

However, beyond the expected improvements from increased charge separation and Ag co-catalysis, our experimental results indicated the importance of the level of dye adsorption on the apparent visible activities of the catalysts. The pseudo-zero order kinetics implied a surface controlled process where surface chemical reactions directly between dye and catalyst may have dominated the visible activity rather than the release of radicals to the bulk solution. This hypothesis was further supported by the TOC analysis and HPLC-MS studies which suggested that the decoloration of the MO solution was mainly achieved by

complete mineralization and adsorption instead of the release or generation of intermediate degradation products to the solution.

5.3 Conclusion

It was found that the TiO_2/Cu_2O and Ag-modified TiO_2/Cu_2O hybrid structures consisted of smaller and bigger nanocrystals exhibiting less than a 100 nm in size regardless of the order of synthesis or the amount of Ag.

The XRD studies revealed that the order of Ag-deposition significantly affected the crystal phase composition of the ternary nanostructures. In TAC catalysts cubic Cu_2O, anatase and rutile TiO_2 and cubic metallic Ag was formed whereas in TCA samples part of the cubic Cu_2O got oxidized yielding face-centered monoclinic CuO phase.

Because CuO exhibits smaller band gap than Cu_2O the light harvesting ability of TCA was affected considerably. The diffuse reflectance measurements showed that significant visible light absorption could be achieved by TC and TAC catalysts while the light absorption of TCA catalysts were extended to the whole visible region. The band gap estimation of TC and TAC catalyst was performed by both direct and indirect Tauc plot and differential reflectance method. It was found that two distinct band gaps could be estimated from the Tauc model. Close agreement in the estimated band gap values were typically found between differential reflectance method and indirect Tauc plot for the higher band gap and between differential reflectance method and direct Tauc plot for the smaller band gap. This result correlated well with the indirect transition of major anatase phase in TiO_2 (higher band gap) and the direct transition of Cu_2O (smaller band gap).

The dark adsorption properties of the catalysts varied greatly between TAC and TCA catalyst. TCA exhibited limited but fast adsorption of methyl orange to its surface while TAC showed high adsorption uptake level and slower kinetics. As a reference, the adsorption of TC was also performed which followed pseudo-second order kinetics. In contrast, TAC

catalyst could not be described by pseudo-first nor pseudo-second order kinetics because uniquely the dye uptake was delayed until the first 25 min. This characteristics suggested that the presence of Ag could influence the dye adsorption character of the material in a unique way.

The decoloration efficiencies of the catalysts under visible light irradiation were studied using methyl orange dye. It was found that both the amount of Ag content and the order of the Ag-deposition step affected substantially the overall dye removal. The most effective catalysts were TAC with 3% and 5% of Ag loading. And the lowest performing catalyst was TCA with 5% of Ag-content. The apparent visible activities could be approximated by pseudo-zero order kinetics and it was found that the level of dark adsorption could be correlated to the apparent visible activities. The lower general performance of TCA may be due to the increased level of charge recombination at CuO-TiO_2 interphases. In contrast a sophisticated charge separation network could be established in TAC catalyst. Furthermore, it was revealed by TOC and HPLC-MS analysis that in the case of TA5C catalyst the total organic carbon content of the final MO solution was significantly reduced which suggested that the MO removal could mainly involve complete mineralization and adsorption.

Chapter 6

TiO_2/Cu_2O nanofilms

6.1 Introduction

Water scarcity is seen as one of the leading global problems in the 21th century. One of the most affected places on the planet by drinking water shortage is Africa. According to the United Nations, about 300 million people, almost half of the continent's population were affected by the lack of safe drinking water in 2006 [280]. Developing sustainable, robust and easy-to-operate water treatment methods are essential to address water shortage problems in developing countries such as Africa.

Due to their large surface area and good mass transfer character, photocatalysts in powder form have been widely investigated and synthesized with abundant structural diversity and tuned physico-chemical properties [281, 282]. However, for visible light aided water purification for developing countries, powders are not an ideal form. The separation step of powder catalysts from liquid medium is highly energy and time intensive process and their complete separation from liquid medium is challenging [283, 116]. Downstream processes may also require expensive equipments for membrane filtration or microfiltration processes [9]. The immobilization of powder catalysts could be one attractive option for facilitated operation and recycling of photocatalytic materials.

Cu_2O-based heterostructures have attracted substantial interest in the past in visible photocatalysis and a TiO_2-Cu_2O system has been investigated in the previous chapter by us as well. In addition to the powder form, immobilized Cu_2O nanostructures have been also reported in the literature. One promising approach to immobilize photocatalyst is to deposit thin films onto solid substrates such as glass or polymers. TiO_2/Cu_2O has been commonly fabricated in layer-by-layer arrangement by electrodeposition, reactive magnetron sputtering or chemical vapour deposition techniques [284, 285]. However, some authors argue that the layered configuration limits the surface area and the contact between the semiconductors which could influence the effective charge carrier migration to the surface and charge separation [125, 285, 74]. Moreover only the top layer is in direct contact with the liquid interphase which could affect the photocatalytic performance of the film [125]. Therefore other thin film designs have been adopted as well.

For example, *Zhang et al.* presented a surface masking approach to synthesize Cu_2O textured TiO_2 thin film. In their procedure, prior to Cu_2O sputtering, the surface of the TiO_2 thin film was masked by a monolayer of polystyrene spheres which were finally removed by sonication. The patterned surface allowed good contact between TiO_2 and Cu_2O and at the same time allowed the exposure of light and adsorbates to both semiconductors surfaces. The positive effect of these was reflected by the photocatalytic test results where enhanced photoactivity was measured for the TiO_2/Cu_2O microgrid heterojunction compared to TiO_2 or Cu_2O nanofilms [125]. Elsewhere, a TiO_2 nanotube array has been loaded with Cu_2O nanocrystals. Electrochemical anodization and deposition techniques were used to fabricate TiO_2 nanotubes and load them with Cu_2O nanocrystals. The as-prepared thin film exhibited record fast bacterial inactivation towards *Esherichia coli* which was attributed to the efficient charge separation and $OH^{\cdot}$ radical generation [286].

A simple, low-cost, yet effective alternative method to fabricate high-performance thin films is the doctor-blade coating technique. One of its key advantages is that it allows

the direct immobilization of powder catalysts with versatile material properties providing *e.g.* good contact between the heterostructures. TiO_2-Cu_2O hybrid structures showing inherent contact between the semiconductors were presented in the literature. Among others, Cu_2O/TiO_2 hollow spheres, Cu_2O/TiO_2 core-shell nanocomposites with octahedral structure, Cu_2O nanoparticles loaded TiO_2 nanobelts and Cu_2O nanospheres decorated with TiO_2 have been prepared by hydrothermal, chemical precipitation and hydrolysis methods in the past [287, 84, 288, 89]. An additional benefit of the doctor-blade coating technique is that it allows the fabrication of porous films by using organic additives in the photocatalyst paste that are burnt out over the thermal treatment step. Thin films fabricated by this method have been already utilized in photocatalytic systems and in dye-sensitized solar cell application. For example $InVO_4/BiVO_4$ composite film and CeO_2/Bi_2WO_6 thin films has been tested in photocatalysis while ZnO/TiO_2 and various TiO_2/dye composites were prepared in the past for solar cell application [143, 289–291]. To fabricate hollow sphere Cu_2O thin films *Choi et al.* reported a doctor-blading procedure using a copper(II) complex ink [292]. They tested the as-prepared thin films in gas sensing application which showed good performance.

Despite the benefits of this technique, to the best of our knowledge up to date there has been no report on Cu_2O/TiO_2 thin films prepared by doctor-blade coating technique for photocatalytic application. Therefore, in this work we pursued to study the deposition of a previously prepared and characterized TiO_2/Cu_2O powder (presented in Chapter 5) as an example for the fabrication of a TiO_2/Cu_2O thin film by doctor-blading method. The effect of process parameters such as the temperature treatment and the organic composition of the precursor paste was evaluated on the material properties and visible photocatalytic activities. The TiO_2/Cu_2O thin films have been characterized by SEM, TEM, XRD, XPS, ATR-FTIR and UV-vis DR. For the photocatalytic test methyl orange was used as a model compound.

6.2 Results and Discussion

6.2.1 Nomenclature

The TiO_2/Cu_2O nanofilms were named based on the composition of the TC paste and on the applied temperature over the heat treatment step. TC-0-350 and TC-100-550 nanofilms indicates that the TC paste contained no ethyl cellulose and was heat treated at 350 °C under nitrogen atmosphere, and that the TC paste contained the maximum amount of ethyl cellulose and was heat treated at 550 °C under nitrogen atmosphere, respectively. Following the same nomenclature TC-0-300, TC-0-350, TC-100-350 and TC-100-550 thin films have been fabricated.

6.2.2 Crystal structure and surface properties

X-Ray Powder Diffraction

The TC powder used for the nanofilm preparation had a typical yellow colour and it comprised of cubic Cu_2O, anatase TiO_2 and rutile TiO_2 as it was confirmed by XRD in the previous Chapter. However, after preparing and treating the TC nanofilms at different temperatures their colour changed significantly. Figure 6.1 depicts the remarkable colour changes of the nanofilms between no heat treatment and 550 °C. Knowing that Cu_2O and its potential oxidized form, CuO exhibits different colours (yellow and black, respectively), it was reasonable to hypothesise alteration in the crystal phase and oxidation state of the nanofilm constituents [293, 294]. To confirm this XRD and XPS studies were performed.

In general, TC nanofilms treated at 300 °C and 350 °C exhibited light or medium brownish colour, respectively. Figure 6.2 b) - d) shows their diffraction patterns. In all three patterns (TC-0-300, TC-0-350 and TC-100-350) anatase (a-) and rutile (r-) phases of TiO_2 and cubic (c-)Cu_2O could be identified by the JCPDS cards of 21-1271, 72-7374 and 71-3645, respectively. No other crystalline structure could be derived from the XRD patterns. Moreover,

there was no clear indication of the presence of oxidized forms of Cu_2O in the nanofilms treated at up to 350 °C by XRD. Therefore, the nature of the colour change remained unexplained. Similarly to our finding, *Nair et al.* reported that annealing Cu_2O thin films in nitrogen atmosphere up to 400 °C preserved the original composition of the films as indicated by the XRD patterns. Same authors also found that annealing at 350 °C in air resulted in the complete conversion of Cu_2O nanostructures into CuO [136].

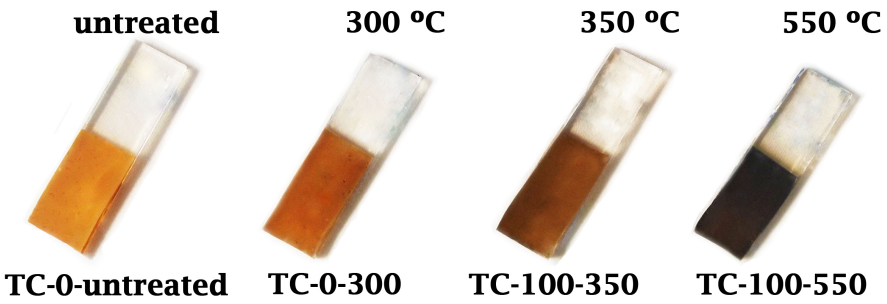

Fig. 6.1 Images showing the colour evolution of TC thin films treated at different temperatures

Increasing the sintering temperature to 550 °C showed clear evidence for the oxidation of Cu_2O into CuO in the XRD pattern of TC-100-550 (Figure 6.2 a)). This was also reflected from the dark brown/black colour of the nanofilm which has been previously associated with CuO in the literature [293]. In TC-100-550, characteristic peaks of face-centered monoclinic CuO appeared at 2θ = 35.5°, 38.7° and 48.8° which were assigned to (-111), (111) and (-202) hkl planes by 073-6023 JCPDS card, respectively. There was no indication of cubic Cu_2O in the XRD pattern and all the other diffraction peaks could be assigned to anatase or rutile TiO_2 as expected. This is in good agreement with other literature reports [136].

Scherrer-Debye calculation

Based on the Bragg's reflections of the particular material, the Scherrer-Debye equation (Equation 3.6) was used to estimate the mean crystallite sizes of the nanostructures.

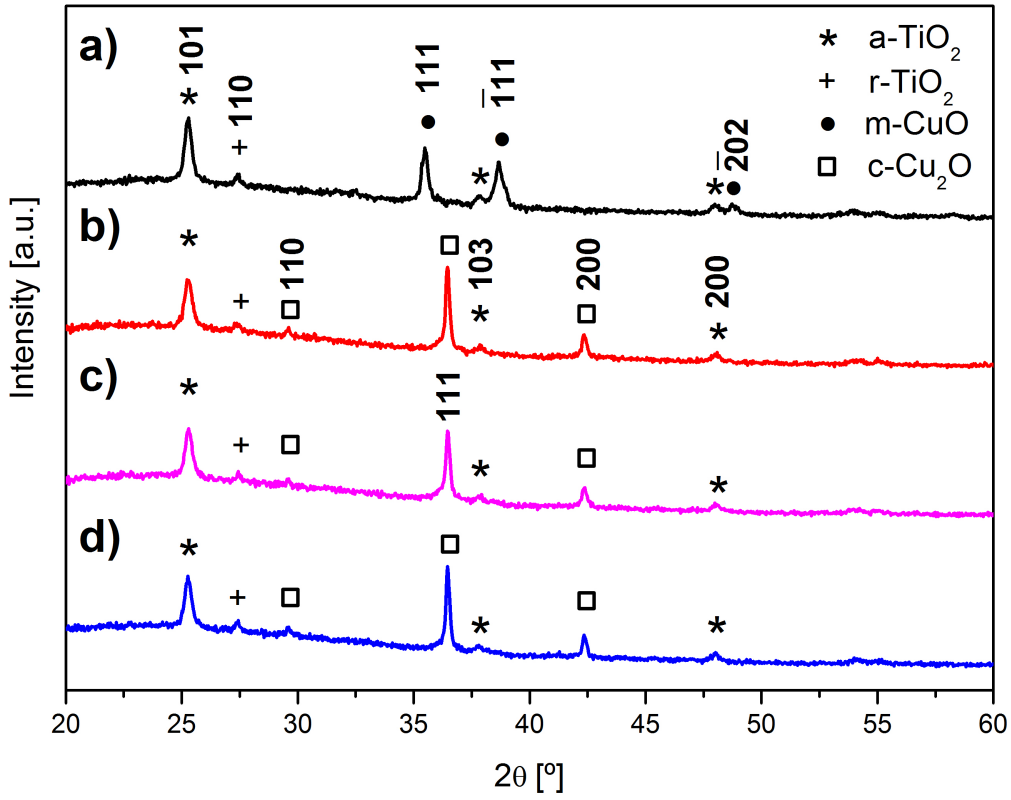

Fig. 6.2 XRD patterns of (a) TC-100-550 b) TC-100-350 c) TC-0-350 and d) TC-0-300 nanofilms

Nanofilm	hkl	Crystal phase	2θ [°]	Scherrer dimension [nm]
TC-0-300	101	anatase TiO_2	25.3	32
	110	rutile TiO_2	27.4	49
	111	cubic Cu_2O	36.5	68
	200	cubic Cu_2O	42.4	60
TC-0-350	101	anatase TiO_2	25.3	33
	110	rutile TiO_2	27.4	51
	111	cubic Cu_2O	36.5	59
	200	cubic Cu_2O	42.4	54
TC-100-350	101	anatase TiO_2	25.3	29
	110	rutile TiO_2	27.4	38
	111	cubic Cu_2O	36.5	61
	200	cubic Cu_2O	42.4	54
TC-100-550	101	anatase TiO_2	25.3	28
	110	rutile TiO_2	27.4	54
	111	monoclinic CuO	35.5	41
	-111	monoclinic CuO	38.7	29

Table 6.1 Scherrer dimensions calculated based on specific peaks from the XRD pattern of nanofilms of TC-0-300, TC-0-350, TC-100-350 and TC-100-550

In the crystallite size estimation the shape factor k was assumed as unity which is a commonly used value in the literature [295, 152]. In the Scherrer dimension calculation individual peaks were selected at positions where no other characteristic diffraction is expected from other materials. Table 6.1 summarizes the details of the Scherrer size calculation for the nanofilms. It is worth mentioning that the determination of peak broadening for the less intense peaks such as the selected peak for rutile TiO_2 at 27.4° position were more challenging due to the relatively higher noise/peak ratio. Therefore some of the variation in the crystallite size estimation of these peaks could be attributed to the reduced resolution.

It was found that the crystallite sizes of anatase TiO_2 did not change significantly in the different nanofilms. The mean of the Scherrer dimensions was calculated to be 30.5 ± 2.1 nm based on the most intense peak of (101) at 25.3° position. The narrow standard deviation suggests that the heat treatment and the paste composition did not have significant influence on the mean crystallite size of the anatase phase. At the same time, more variation was

found for the rutile phase of TiO_2. The calculated Scherrer dimensions were found to be 48.0 ± 6.0 nm across all the nanofilms. The higher standard deviation might be accounted for the relatively higher noise/peak ratio in the rutile peak as discussed above. It can be noted that the mean crystallite size of rutile TiO_2 was larger than that of the anatase TiO_2 which is in good agreement with the analytical record of P25 [159].

Similarly to TiO_2, cubic Cu_2O also exhibited comparable crystallite sizes across the different nanofilms. Its value varied around *circa* 60 nm which was generally higher than both anatase or rutile phases of TiO_2.

In TC-100-550 nanofilm the crystallite size of monoclinic CuO could be calculated instead of Cu_2O. It was found that the characteristic peaks of CuO in the XRD pattern were broadened which suggested smaller crystallite sizes relative to Cu_2O. Based on the (111) and (-111) hkl planes 41 and 29 nm mean crystallite sizes were calculated for CuO, respectively which is considerably smaller than the *circa* 60 nm mean crystallite size of Cu_2O. This finding is also confirmed by the SEM image of TC-100-550 (in Figure 6.3 d)) where more uniform size distribution and fewer bigger nanoparticles could be seen compared to the SEM images of TC-0-300 or TC0-350 nanofilms.

6.2.3 Morphological structure

The morphology of the nanostructures was studied by SEM and TEM in order to investigate the effect of the heat treatment and the TC paste composition on the size and shape of the nanostructures.

In general, it was found that the films were uniformly deposited onto the glass substrates and they exhibited a porous structure with pore sizes in the range of a couple of hundreds nanometers (see e.g. Figure 6.3 a)). No cracks or peeling-off from the surface of the FTO substrate was observed. This could indicate good dispersion and limited aggregation of the nanostructures. In the literature, aggregation issues of TiO_2 in the micrometer range

was reported to cause cracking and peeling-off effects resulting in poor quality thin films. However, when the size of the aggregates were limited to about 200 nm no detrimental effect on the film characteristics was observed by the same researchers [133].

It was noted from the SEM images shown in Figure 6.3, that the nanofilms typically consisted of smaller than 100 nm nanostructures except for TC-100-350 where the nanoparticles clustered to form blackberry-like spherical superstructures.

It was found that the nanofilms prepared from the cellulose-free paste (TC-0-300 and TC-0-350 shown in Figure 6.3 a) and b)) exhibited very similar morphologies with two main crystal sizes regardless of the applied temperature (up to 350 °C). The characteristic dimension of the irregularly-shaped smaller nanocrystals measured *circa* 20-40 nm. Whereas the bigger nanostructures fall typically in the range of 70-90 nm in size and resembled irregular cubic-like shapes. Globally, the smaller and bigger nanostructures were found to be uniformly dispersed.

When the nanofilm contained cellulose and was treated at 350 °C (TC-100-350), unique features were observed in the morphology. Figure 6.3 c) shows that the surface of the nanofilm was densily covered by larger spherical structures measuring typically 150-250 nm in diameter. The rough surface resembling a blackberry suggested that possibly smaller nanocrystals may have self-assembled to form larger nanostructures which appeared as a closely packed well-defined entity. To gain more understanding on the nature of the spherical assemblies TEM images were captured and electron diffraction (ED) pattern was recorded which can be viewed in Figure 6.4. The TEM image confirmed the rugged surface of the larger clusters and also highlighted the co-existence of smaller nanostructures which could be situated mainly in the pore-structure and subsurface areas of the film. The selected-area ED pattern of a spherical assembly shown in Figure 6.4 b) revealed that the nanocluster contained both Cu_2O and TiO_2 nanostructures. For example, the diffraction spot assigned to

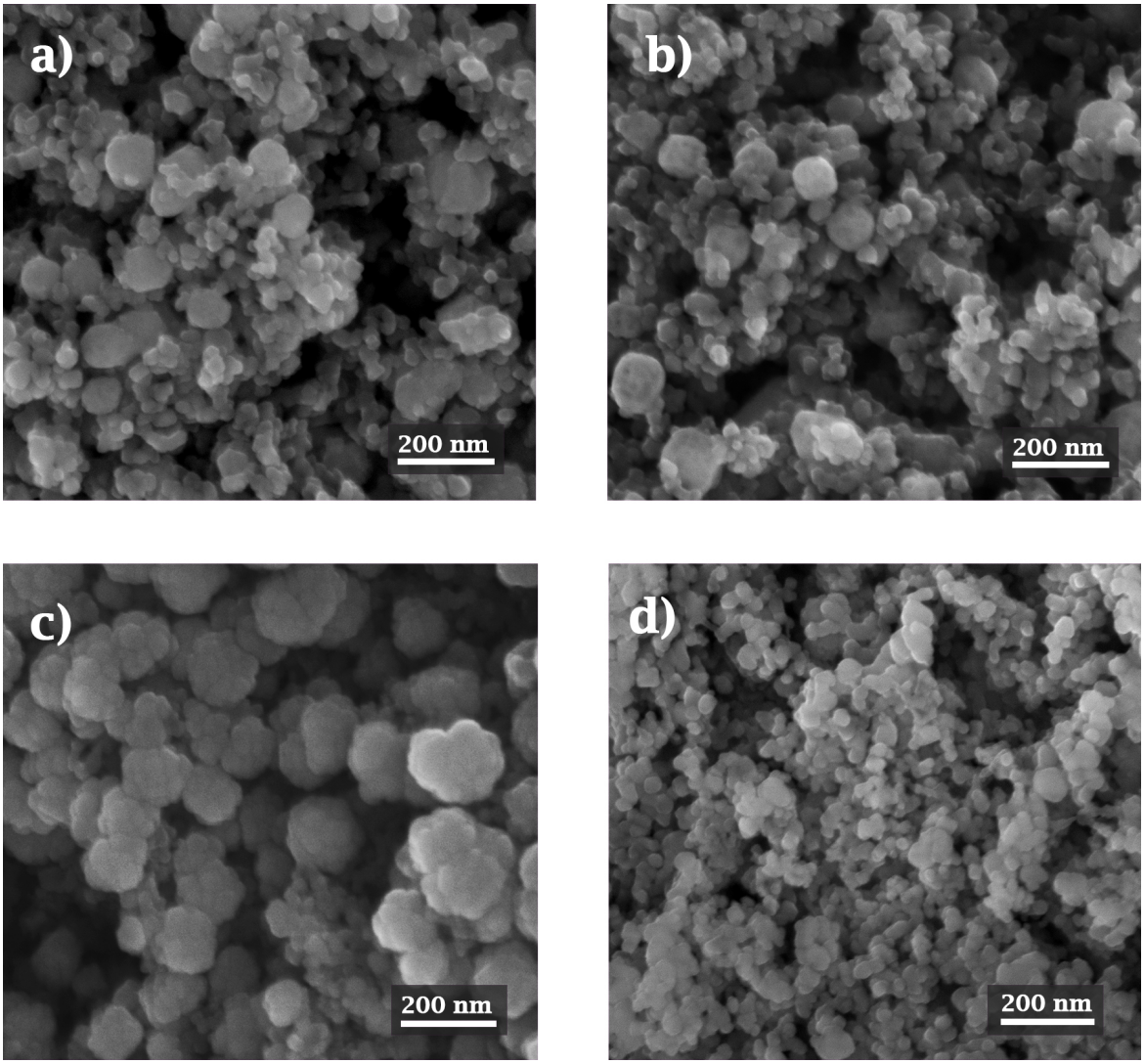

Fig. 6.3 SEM images of a) TC-0-300, b) TC-0-350, c) TC-100-350 and d) TC-100-550 nanofilms

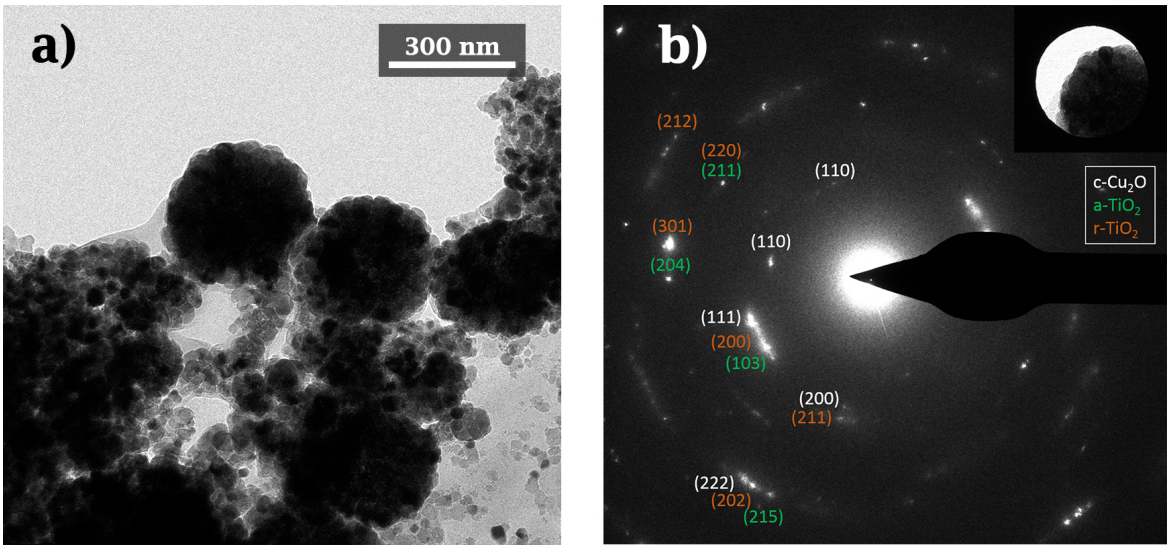

Fig. 6.4 (a) TEM image of TC-100-350 and (b) SAED pattern of TC-100-350 colour-coded for cubic Cu_2O (white), anatase TiO_2 (green) and rutile TiO_2 (orange), selected area is shown in the top-right corner

(110) hkl plane was characteristic to cubic Cu_2O. Other diffraction spots could be uniquely assigned to anatase or rutile TiO_2 such as (204) or (301) hkl planes, respectively.

Figure 6.3 d) shows TC-100-550 sample when the cellulose containing nanofilm was treated at 550 °C. It can be noted that the *circa* 250 nm assemblies formed at 350 °C completely disappeared leaving smaller, typically less than 100 nm nanoparticles behind. This further supports the possibility that the blackberry-like spherical structures in TC-100-350 nanofilm were made of smaller crystals which could disassemble when heat treated at 550 °C. The differently shaped and sized nanocrystals in TC-100-550 were uniformly dispersed and were closely interconnected. The unique morphology of TC-100-550 to other samples could be additionally related to the change in crystal phase and form of copper oxide which was confirmed by XRD and XPS and is discussed in Section 6.2.2.

X-ray photoelectron spectroscopy

To further investigate the colour change of the nanofilms, the chemical states of surface Cu, Ti and O elements were analysed by XPS. The high resolution XPS spectra of Cu 2p, Ti 2p

and O 1s is shown in Figure 6.5 and 6.6. The characteristic core levels of Cu^+ and Cu^{2+} in the Cu 2p XPS spectra allowed us to assess the presence of different oxidation forms of copper on the surface of the nanofilms. In the XPS spectrum of TC-0-300 the peaks located at 932.7 eV and 952.5 eV were assigned to the binding energies of Cu $2p_{3/2}$ and Cu $2p_{1/2}$ of Cu^+, respectively. This agrees well with literature data [296, 297]. Whereas the peaks positioned at 933.8 eV and 953.8 eV evidenced the presence of Cu^{2+} oxidation state which corresponded to binding energies of Cu $2p_{3/2}$ and Cu $2p_{1/2}$, respectively. Cu^{2+} was further supported by the characteristic satellite peak at 962.5 eV which originates from the Cu $3d^9$ unfilled shell [296, 298]. From the Cu 2p spectra of TC-0-300 (shown in Figure 6.5 a)) it could be concluded that both Cu_2O and CuO core levels were present in the thin film. The presence of CuO may explain to the deepening of yellow colour of the TC-0-300 nanofilm. Other researchers also reported that even low temperature treatment of Cu_2O (synthesis and drying under 100 °C at ambient conditions) yielded the formation of small portion of CuO in the nanostructures which was detectable by XPS [89, 299].

Similar peak deconvolutions and analysis revealed that the surface of TC-0-350 and TC-100-350 (shown in Figure 6.5 b) and c)) also composed of CuO and Cu_2O with increasing amount of Cu(II) compared to TC-0-300. The increasing Cu^{2+} content was clearly indicated by the characteristic peak positioned at around 933.8 eV which was more intense in both cases than in TC-0-300 nanofilm. Furthermore, the more enhanced satellite multipeak-complex situated between 944 and 941 eV binding energies also suggested increased amount of Cu^{2+} species. It was also noted that the higher percentage of CuO in TC-0-350 and TC-100-350 was consistent with the dark brown appereance of the samples as shown in Figure 6.2. This is speculated to be caused by the increased sintering temperature of 350 °C.

Finally, the Cu 2p XPS spectrum of TC-100-550 showed that both Cu_2O and CuO were present in the nanofilm although CuO appeared as major phase from the peak areas. This was reflected primarily from the more intense photoelectron peaks positioned at 934.1 and

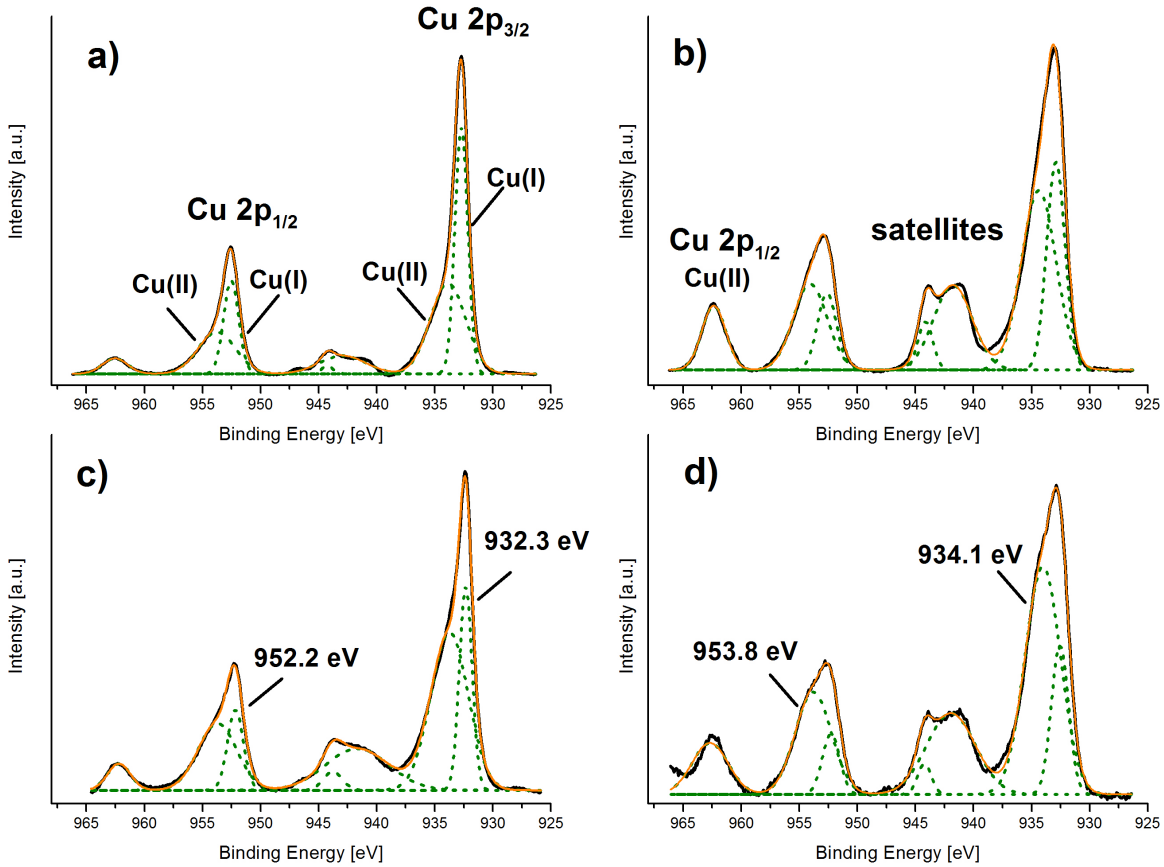

Fig. 6.5 XPS spectra of Cu 2p of a) TC-0-300 b) TC-0-350 c) TC-100-350 d) TC-100-550 where the black line represents the measured spectra, the orange line shows the theoretical overall fit and the dotted green lines show the fitted peaks

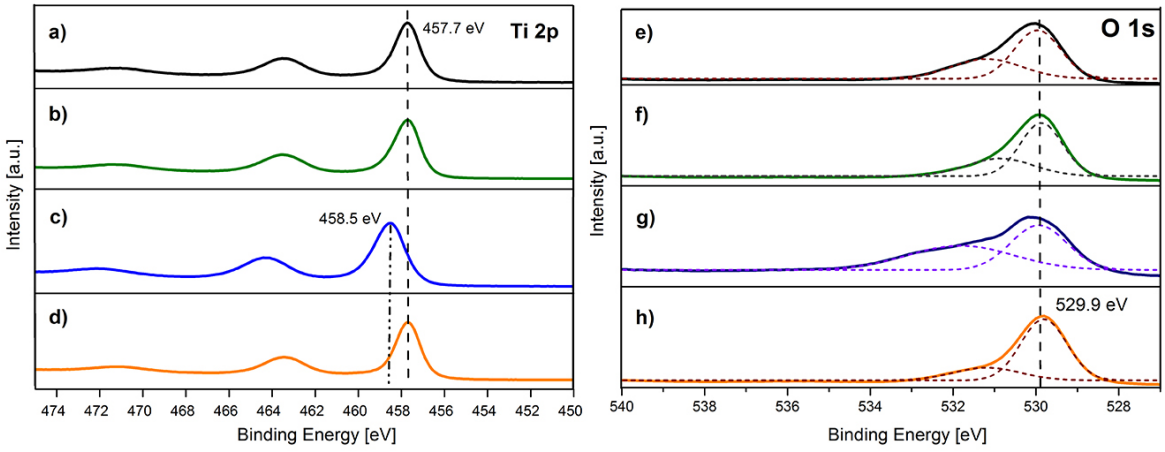

Fig. 6.6 XPS spectra of Ti 2p of a) TC-0-300 b) TC-0-350 c) TC-100-350 and d) TC-100-550 along with the O 1s XPS spectra of e) TC-0-300 f) TC-0-350 g) TC-100-350 and h) TC-100-550

953.8 eV which corresponded to Cu $2p_{3/2}$ and Cu $2p_{1/2}$ of Cu(II), respectively. The increased intensities caused the overlapping peaks to be skewed towards lower binding energies suggesting more dominant CuO composition in the nanofilm. This is in good agreement with the XRD result which revealed monoclinic CuO phase in TC-100-550. However, the Cu 2p spectrum also revealed the co-existence of Cu_2O which was not indicated by XRD. Similarly to *e.g.* TC-0-350, where the presence of CuO could not be detected from XRD but it was evidenced from XPS, this might be caused by the low content or small crystallite sizes of the particular crystal phase, perhaps due to high dispersity [287, 89].

The Ti 2p XPS spectra shown in Figure 6.6 a)-d) revealed two main peaks. The peak at lower binding energies could be assigned to Ti $2p_{3/2}$ whereas the peak appearing at higher binding energies belonged to Ti $2p_{1/2}$ [287, 300]. It was also noted that the Ti 2p binding energies of TC-100-350 was uniquely shifted towards higher energies. It may be assumed that this shift is induced by the bigger blackberry-like assemblies that could allow stronger connections between the constituents due to the closely packed arrangement. This may in part change the local bonding enviroment of Ti. Other researchers also experienced a shift in the binding energies of metal atoms when they closely interacted with other materials. *Jing et al.* found that the Cu $2p_{3/2}$ peak of Cu_2O appeared at higher binding energies when the catalyst interacted with humic acid [256]. Elsewhere, similar shift towards higher energies was realised when a Ag-modified Cu_2O interacted with reduced graphene oxide which served as support for the catalyst [96].

The high resolution O 1s XPS scan can be viewed in Figure 6.6 e)-h). In general, the asymmetric peaks in the O 1s XPS scan reflected the different Cu-O and Ti-O bonding enviroments. For example in TC-0-300 nanofilm it was found that the peak appearing at higher binding energy of 531.1 eV could possibly belong to Cu-O, whereas the peak positioned at lower binding energy of 530.0 eV to Ti-O bonds. These binding energies are in good agreement with literature data [299, 296, 301].

6.2.4 Optical properties

The light harvesting properties of the thin films was investigated by recording the UV-vis diffuse reflectance spectra.

It was generally found that the absorbance of the coloured films increased in the 500-850 nm region when the thin films were treated at higher temperatures. This finding is in good correlation with the colours and the composition of the films.

It was seen that the untreated TC film and TC-0-300 sample exhibited similar light absorption character. In both diffuse-reflectance spectra the band edges of TiO_2 and Cu_2O were reflected in the 400-500 nm and 500-600 nm regions, respectively. The heterostructure formation resulted in significant enhancement in the visible light absorption in good agreement with the optical properties of the powder TC catalyst that was presented in the previous chapter. This absorption pattern is also matching the literature references of similar nanocomposite thin films [230, 302].

By increasing the temperature to 350 °C further increase in the light absorption was noted in the far red region of the visible spectrum for both TC-0-350 and TC-100-350 films. This phenomenon could reflect the increasing amount of oxidized copper oxide (CuO) ratio in the thin films that was characterized by typical absorption in the 500-800 nm region in previous studies [303]. This is further supported by the result of the XPS analysis which confirmed that heat treatment performed at 350 °C resulted in higher portion of CuO in the thin films. The brownish colour of the 350 °C treated films is also in alignment with this.

Finally the darkest thin film, TC-100-550 showed no clear evidence of typical Cu_2O absorption that formed a shoulder in the previous samples on the TiO_2 absorbance curve. At the same time the highest increase in the 500-800 nm region was noted for this sample which suggested that Cu_2O has been mostly transformed into CuO. This is also in agreement with the XRD and XPS characterization of the thin film.

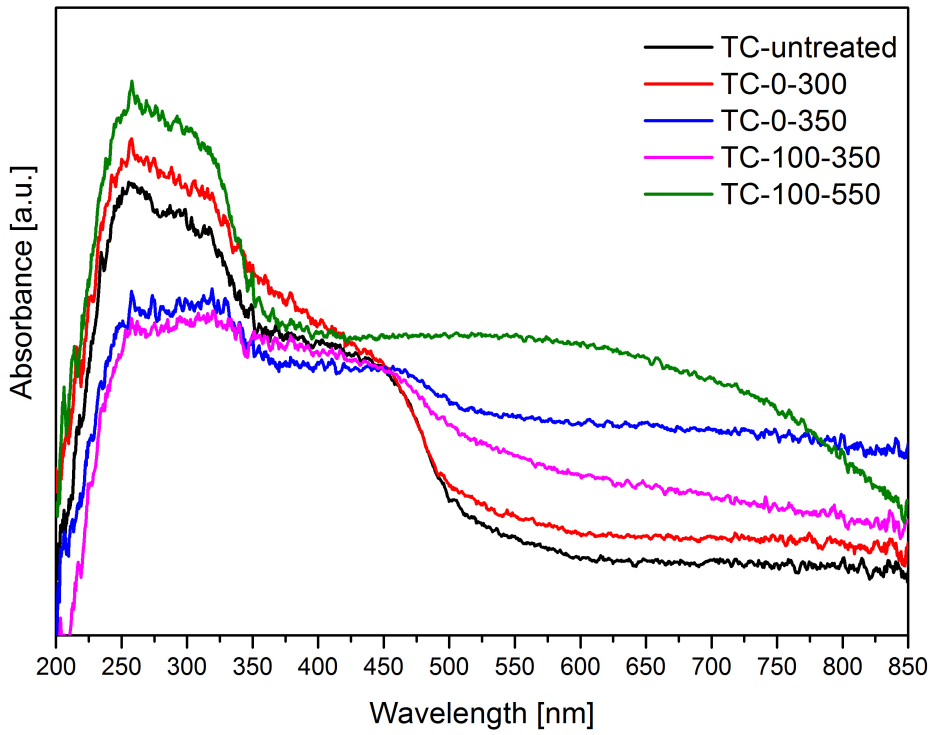

Fig. 6.7 UV-vis diffuse reflectance spectra shown for the unheated TC film along with TC-0-300, TC-0-350, TC-100-350 and TC-100-550 thin films

6.2.5 Temperature effect on the organic composition of the nanofilm

ATR-FTIR (shortly referred as ATR) is a commonly used technique to map *e.g.* the adsorption of dyes to the catalyst surface during the photocatalytic test or to assess the presence of other IR-active co-catalysts or substrates such as graphite oxides or chitosan *etc.* in the nanostructures [256, 304, 305].

In this work, ethyl cellulose and/or alpha terpineol were used as additives to prepare TC paste for the fabrication of the nanofilms. Both chemicals exhibit typical IR bands in the range of 3000-2800 cm^{-1} and 1500-900 cm^{-1} (see Figure 6.8) which allowed us to study their presence in the nanofilms after heat treatment at different temperatures. Because Cu_2O was proved to be sensitive to the applied temperature (by *e.g.* XPS) we wished to study the effect of the heat treatment step at different temperatures on the organic composition of the nanofilm to optimise its performance.

In general, typical Cu-O, O-Cu-O and Cu-O-Cu lattice vibrations could be find in the ATR spectra of the nanofilms in the 500-800 cm^{-1} range which is in agreement with other reports [301, 256].

Figure 6.8 a) shows the effect of heat treatment at or below 300 °C on a cellulose-free nanofilm. It was found that a temperature treatment less than 300 °C could not efficiently remove the alpha terpineol content of the nanofilm. The ATR spectrum of the film treated at 300 °C shows that the characteristic peaks of alpha terpineol (*e.g.* between 2975-2847 cm^{-1}) disappeared. As a reference, the ATR spectrum of alpha terpineol is shown on the same Figure.

Similarly, the temperature effect on the the cellulose containing nanofilm was also studied. Figure 6.8 b) shows the spectrum of the 100% cellulose nanofilm treated at or below 350 °C. It can be seen that residues of cellulose was still present in the nanofilm below 350 °C which was indicated by the peaks appearing between 1190 and 945 cm^{-1} in the ATR spectra of the nanofilm. This is in good agreement with other literature reports. For example, *Choi et al.* reported that residues of ethyl cellulose were found in Cu_xO nanofilms that were calcinated between 200 °C and 300 °C [292].

The termal treatment not only plays role in the removal of organic additives from the thin film but it also ensures adequate binding of the nanostructures with the substrate surface [116]. *Ito* and his coworkers proposed that the chemical binding between the FTO substrate and the catalyst involves the dehydration of surface -OH groups into M-O-M bonds over the sintering process where M is a generalized form of metal atoms [133].

As a conclusion, the cellulose-free nanofilms could be treated as low as 300 °C whereas the cellulose containing films should be treated at minimum 350 °C in order to remove the organic additives from the nanofilms. Ethyl cellulose is typically added to *e.g.* TiO_2 pastes to enhance film porosity whereas terpineol is normally used to adjust viscosity and stabilize the suspension [133]. Omitting cellulose from the paste formulation allowed us to apply

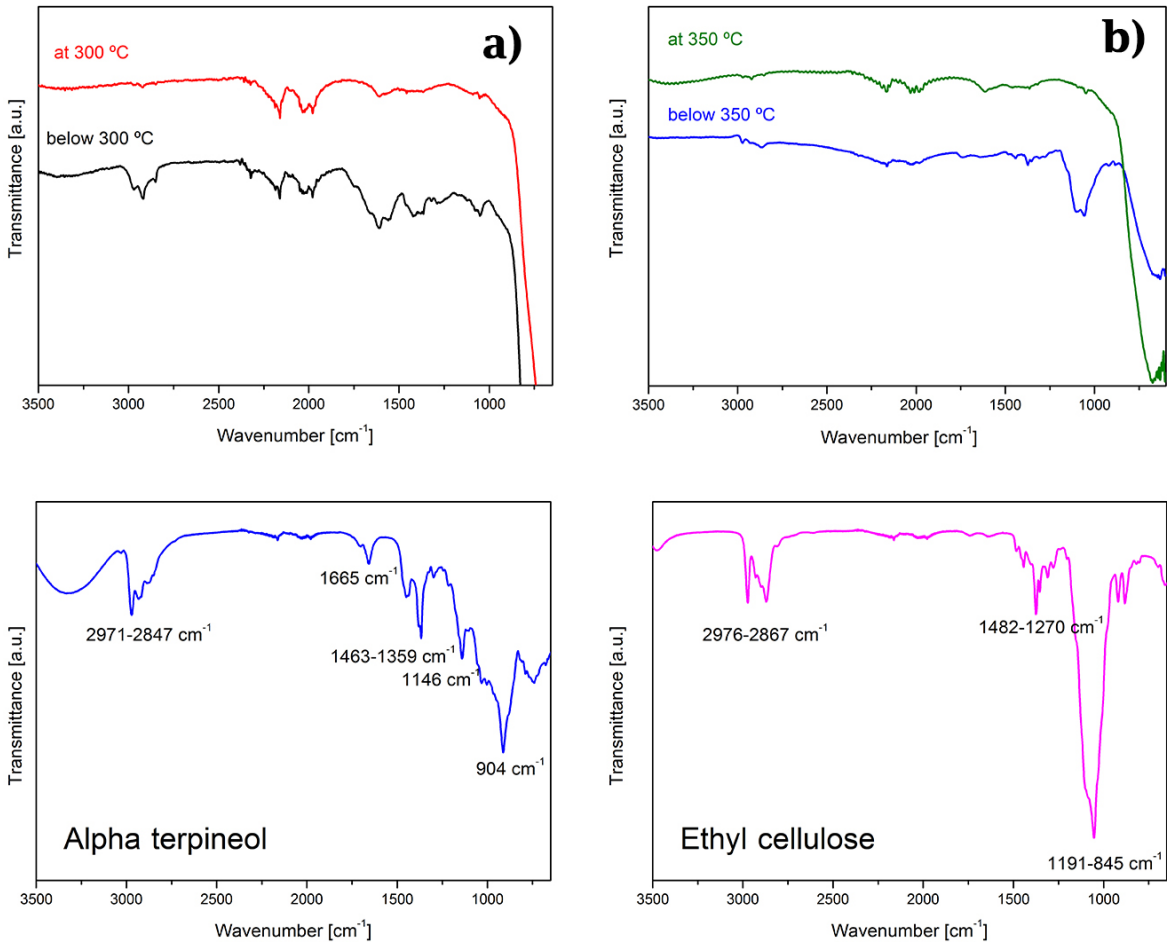

Fig. 6.8 ATR spectra revealing the effect of temperature treatment on the organic composition of the nanofilms a) sintering at or below 300 °C the cellulose-free nanofilm and b) sintering at or below 350 °C the cellulose-containing nanofilm. In the bottom row the ATR spectrum of alpha-terpineol and ethyl-cellulose is shown from the left to the right, respectively.

lower temperature treatment which was shown to contain the highest cubic Cu_2O crystal phase content among the nanofilms. In contrast, the 350 °C heat treatment resulted in a more substantial part of the original Cu_2O crystal phase to oxidize into CuO as it was confirmed by XPS and the colour change of the nanofilms discussed in Section 6.2.2.

6.2.6 Visible photocatalytic activities and dark adsorption

The visible response of the nanofilms was investigated in a stirred quartz cell using methyl orange (MO) as a model compound. For visible light source a white LED which has emission

in the visible region from 400 nm to was used to irradiate the quartz cell from a perpendicular direction.

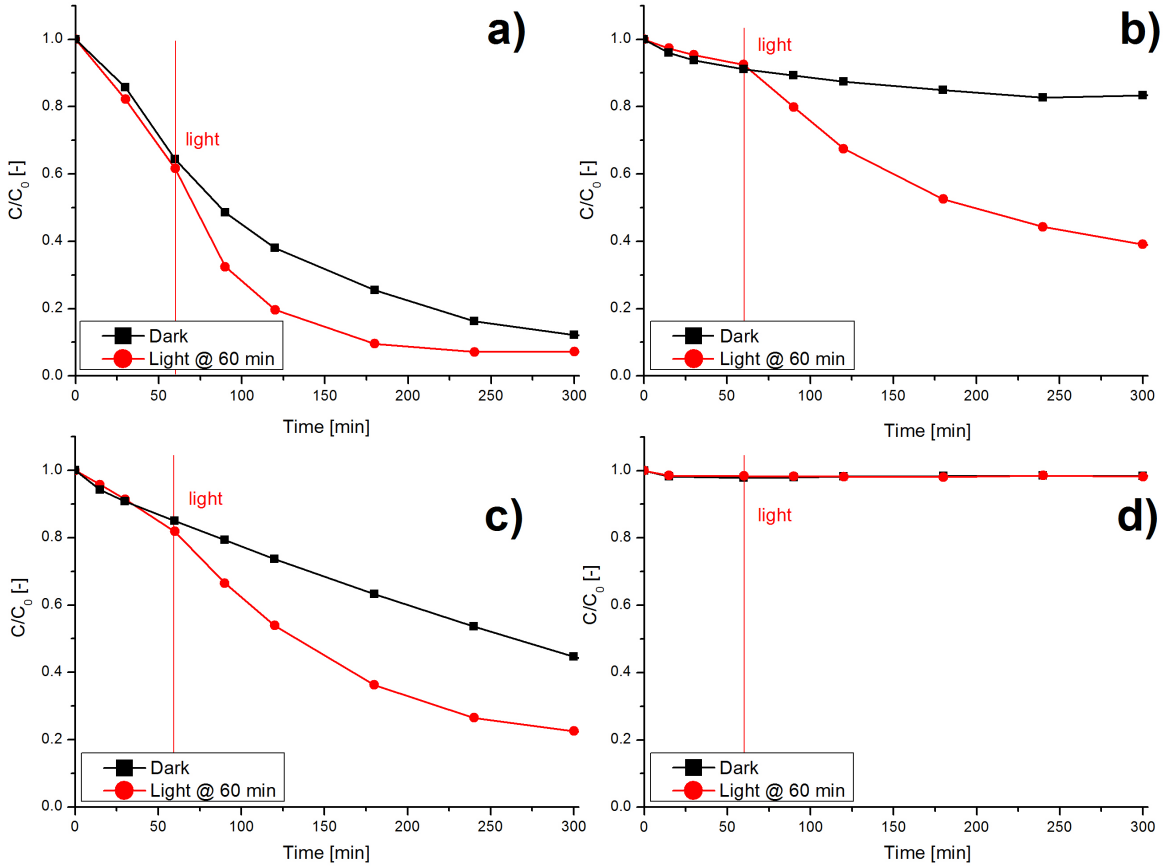

Fig. 6.9 Apparent visible photoactivity measured after 60 min dark stirring is shown with red line and as a reference dark stirring is shown with black line for a) TC-0-300 b) TC-0-350 c) TC-100-350 and D) TC-100-550 nanofilms

In general, it was found that the nanofilms that were free from organic additives exhibited substantial MO adsorption in darkness. The only exemption was TC-100-550 nanofilm where only a few percentage of MO adsorption was measured in the dark reference experiment. It was also generally found that the nanofilms did not exhibit further visible activity once the adsorption/desorption equilibrium has been reached. This is not unusual for Cu_2O related nanostructures and similar findings has been reported in some cases. In fact, *Zhang et al.* reported that a Cu_2O@TiO_2 nanobelts exhibited weak photoactivity beyond the adsorption of metyl orange dye [288]. Elsewhere, *Dong* and his coworkers found that a

Cu_2O thin film exhibited only a few percent of MO removal in the absence of H_2O_2 after the adsorption/desorption equilibrium has been reached [36]. The limited photoactivity after reaching adsorption/desorption equilibrium might be due to unfavored conditions for the photocatalytic surface reactions such as competitive surface occupation or extensive light absorption by the surface adsorbed dye [274, 275]. However, we found that light irradiation after 60 minutes of dark stirring could significantly enhance the MO removal for most of the nanofilms as it can be seen on Figure 6.9.

Figure 6.9 a) depicts the apparent visible activity and dark adsorption of TC-0-300 nanofilm. By 60 minutes of dark adsorption *circa* 40% of the initial MO was adhered to the surface of the nanostructures. When the visible light was turned on the apparent visible activity exhibited close to 20% better performance when compared to the dark measurement. After 2 hours of light irradiation the MO concentration dropped to about 10% and the MO removal rate started to level off. By the end, 93% of the initial MO was removed from the solution by TC-0-300. Other researchers found similar behaviour in *e.g.* the photocatalysis of 4-nitrophenol by Cu_2O-TiO_2 nanocomposites under simulated sunlight irradiation where the removal of the organic compound stopped at the concentration of *circa* 10% [87].

The performance of TC-0-350 nanofilm is shown on Figure 6.9 b). It can be seen that the adsorbed amount of MO was much lower than that of the TC-0-300. Only 10% of the dye was adsorbed by the nanofilm in 60 minutes as opposed to 40% for TC-0-300. Similarly to the nanofilm treated at 300 °C, the visible light resulted in a significant improvement in the performance of TC-0-350. By the end of the 5 hours test, the dye concentration was reduced by 60% while only 18% of the initial dye concentration was removed in the reference dark test. The overall dye removal efficiency of TC-0-350 was moderated relative to TC-0-300.

The cellulose containing films are shown on Figure 6.9 c) and d). For TC-100-350 the initial dye adsorption was measured to be around 15% over the first hour of dark stirring. This value was close to the dark adsorption of TC-0-350 which was treated at the same

temperature but prepared from the cellulose-free paste. However, unlike TC-0-350 the dark adsorption of TC-100-350 showed a continuous steady dye removal tendency throughouth the dark reference experiment reaching as low as 55% MO removal by the end of 5 hour. When the visible light was turned on the TC-0-350 nanofilm showed improved performance compared to the dark measurement and achieved the removal of 78% of the initial MO. The overall efficiency of TC-100-350 was in between TC-0-350 and TC-0-300. When the cellulose containing nanofilm was treated at the highest temperature of 550 °C, nor the level of dark adsorption, nor the apparent visible activity was shown to be significantly improved. This can be viewed on Figure 6.9 d).

From the photocatalytic experiments it can be noted that the highest level of dark adsorption and visible activity has been achieved when the nanofilm was treated at the lowest temperature of 300 °C and it contained no cellulose. Increasing the sintering temperature to 350 °C for both cellulose free and cellulose containing film and finally to 550 °C for the cellulose containing film resulted in lower level of dark adsorption and moderated visible activities. Over the heat treatment it was evidenced by the XRD and XPS results that the composition of the nanofilms has changed. When the thin films have been treated at 350 °C regardless the cellulose content higher portion of the cubic Cu_2O was converted to monoclinic CuO compared to TC-0-300 film. And finally in TC-100-550, the majority of Cu_2O was coverted to CuO. It is known that CuO and Cu_2O exhibits different physico-chemical properties. For example, they possess distinct band gaps of 2.0-2.2 and 1.4-1.6 eV and hence different colours of yellow and black for Cu_2O and CuO, respectively [306, 307, 87]. Due to the different positions of their respective valence and conduction band edges it was reported by many researchers that CuO had detrimental effect on the photocatalytic performance of *e.g.* TiO_2/CuO heterostructures where CuO may have acted as a recombination center for the photo-generated charges. Some researchers believe that CuO could exhibit a remarkable "shading effect" [308, 74, 309]. In view of this, both adsorption and visible activities of the

nanofilms with higher CuO portion could be influenced by the different properties of CuO relative to Cu_2O.

In addition to the effect of the crystal phase and oxidation state, the morphology has been affected appreciably over the course of different fabrication conditions, too. For example, in TC-100-350 bigger polycrystalline assemblies were formed than in either TC-0-300 or TC-0-350. The altered morphology could affect the surface area of the nanostructures, the sizes and structures of the pores and the spherical assemblies could provide a more intimate contact between the different semiconductor crystallites. It was pointed out in earlier research that the intimate contact between coupled semiconductors could have a great significance in the effectiveness of interfacial charge carrier transfer and separation [74]. The overall effect of these factors could also play role in the dark adsorption character and the visible activity of the thin films.

Since the photocatalytic test involved both adsorption and photoactivity the underlying mechanism of photocatalysis is difficult to interpret. Although it could be suggested that the visible light ($\lambda > 400$ nm) can excite electrons from the valence band of Cu_2O to its respective conduction band. Between the Cu_2O-TiO_2 interphase the electrons are thermodinamically favoured to migrate to the conduction band of TiO_2 due to its less negative band edge position than that of the Cu_2O. This charge separation between Cu_2O and TiO_2 could play an important role in enhancing the lifetime of the photo-induced charges. On the contrary, on a CuO-TiO_2 interphase both electrons and holes are favoured to accumulate on the conduction and valence band of CuO, respectively [309]. This could facilitate the recombination of charges which may negatively affect the photoactivity.

When all three semiconductor phases are present multiple charge transfer is possible. Figure 6.10 shows the band alignment between the three semiconductor phases. In the literature it was found that the conduction band edge of CuO could vary between -0,2 and 0,1 eV, whereas its valence band edge normally takes 1,4-1,5 eV values [310, 311]. The

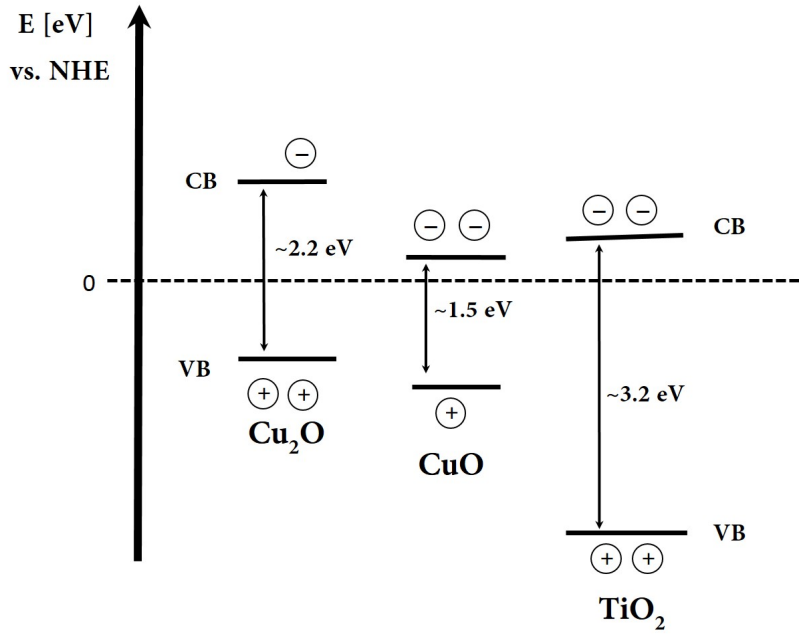

Fig. 6.10 Theoretical band structure alignment between CuO, TiO_2 and Cu_2O when all three semiconductor phases are present at the heterointerface.

differences in the reported CB and VB values of CuO could arise from the various synthesis conditions applied or the possible defect states, oxidation levels or chemical residues of the samples ... *etc* [311]. Regardless of the exact value, it is likely that in our system the photo-generated electrons would travel to the CB of CuO or TiO_2 while the migration of holes would thermodinamically be favoured to the VB of CuO or Cu_2O. More exact charge separation scheme is difficult to be given without further measurements. Moreover, due to the different nature of *p* and *n* conductivity of the semiconductors, bending of the band structure is possible. This could further modify the band edge positions. *Huang et al.* for example reported that in a $Cu_2O/CuO/TiO_2$ ternary photocathode the conduction band edges are approaching zero in the Cu_2O, CuO and TiO_2 order. Therefore the electrons were shown to accumulate on the CB of TiO_2, while the holes rested on the VB of Cu_2O [278].

It is also worth noting that the visible photons could excite the molecules of the orange coloured dye (MO) which could potentially also transfer electons between the semiconduc-

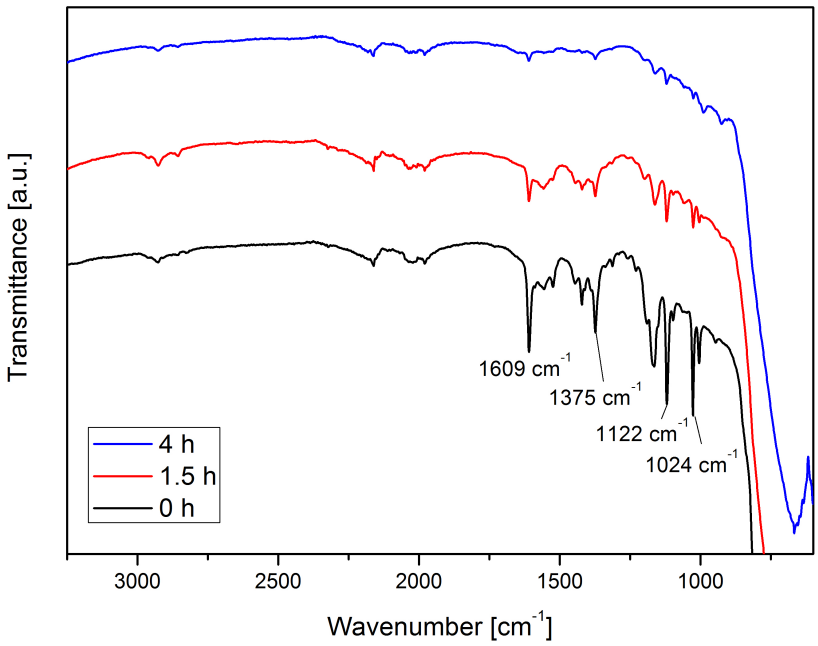

Fig. 6.11 ATR-IR spectrum showing the effect of 0, 1.5 and 4 hours of NaCl soaking of TC-0-300 nanofilm after the visible photocatalysis test

tors. These electrons may contribute in the overall photocatalytic activities as well. This phenomenon is known as photosensitization in the literature and it is a commonly used technique to fabricate visible response solar cells [102].

6.2.7 Recycling test

In potential industrial application the efficiency of photocatalysts over repeated use is an important feature. In order to study the reusability of the nanofilms recycling tests were performed.

TC-0-300 was selected as one of the best performing catalyst to demonstrate the apparent visible activities over multiple cycles. Following the visible photocatalytic test the TC-0-300 nanofilm was recovered by a 9% NaCl solution until full desorption of the dye was achieved. The successful recovery of the nanofilm was confirmed by ATR which is shown in Figure 6.11. The main characteristic peaks of methyl orange were assigned as follows. The region between 1447 and 1609 cm^{-1} could be assigned to the stretching vibrations

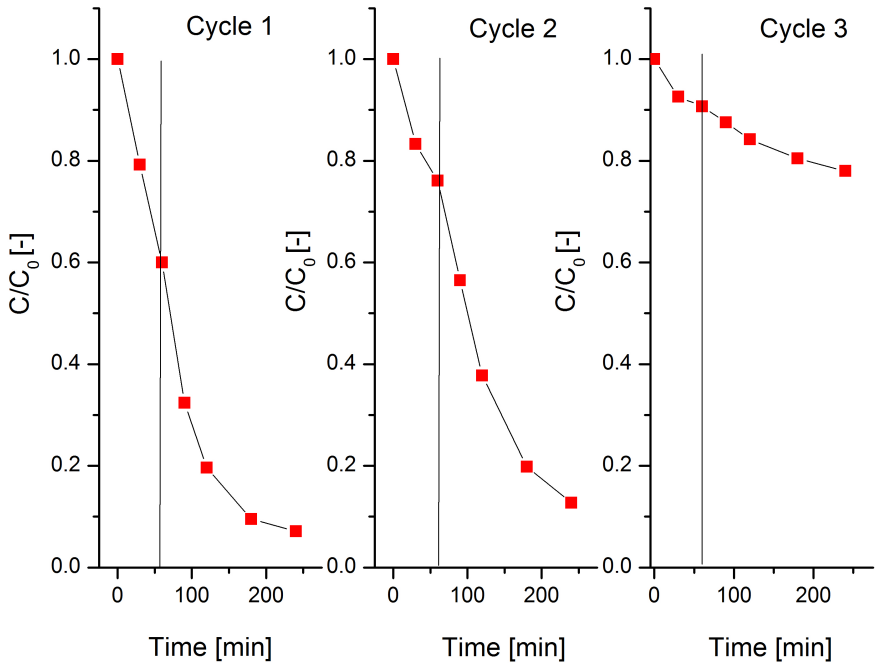

Fig. 6.12 Recycling experiments showing the apparent visible efficiency of TC-0-300 nanofilm over three repeated cycles, the vertical lines indicate the points when the visible ligth was turned on

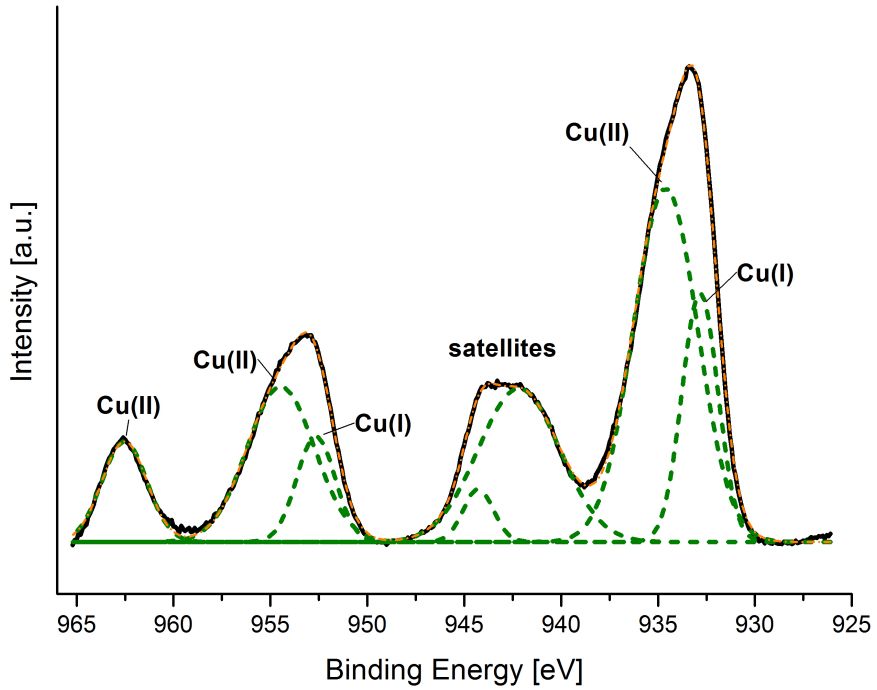

Fig. 6.13 XPS spectrum of TC-100-350 as recorded after the first photocatalytic test followed by recovery, the black line represents the measured spectra, the orange line shows the theoretical overall fit and the dotted green lines show the fitted peaks

of the aromatic ring. The stretching vibrations of -N=N- group could be found at 1420 cm^{-1}, whereas the sulfonil group of MO is located at 1122 and 1024 cm^{-1} [288]. After one and a half hour stirring in NaCl solution most of the dye molecules left the surface of the nanostructures which was indicated by the diminished characteristic peaks of MO in the whole 1609-1024 cm^{-1} range.

The desorption of MO from the nanostructure surface is believed to be achieved by the increased ionic strenght of the solution [97]. *Liu et al.* reported that with increasing ionic strength the adsorption capacity of Cu_2O drops dramatically. This was explained by the newly created negatively charged Cl^- atmosphere around the positively charged Cu_2O surface which could make the adsorption of anionic dyes such as MO unfavored.

The recycling test revealed that the TC-0-300 nanofilm could undergo considerable activity loss under repeated use. The level of dark adsorption gradually dropped from *circa* 40% to *circa* 10% over the three cycles (Figure 6.12). The decreased efficiency over the dark stirring could imply increased CuO ratio in the nanofilm which was also suggested by the deepening of the colour of the thin film after photocatalysis and recovery. XPS spectra performed after the first cycle also confirmed increased ratio of CuO on the surface of TC-100-350 film compared to before the photocatalytic test. This can be viewed in Figure 6.13.

Narrow band gap semiconductors (typically $E_g < 2.0$ eV) such as Cu_2O or CuO were reported to be more likely to suffer from photocorrosion which affects significantly their recyclability in photocatalysis. This can occur due to the more positive or more negative position of their self-reduction/oxidation potential levels compared to that of the water [278]. In the literature most of the activity loss of Cu_2O-related nanostructures were associated with the accumulation of holes on the valence band of Cu_2O which were shown to be responsible for the self-oxidation of Cu_2O into CuO [89, 312].

6.3 Conclusion

In this work, the fabrication of TiO_2/Cu_2O thin films on FTO glass substrates has been presented by doctor-blade coating technique for the first time. This technique provided a facile and cost-effective way to deposite powder TiO_2/Cu_2O nanostructures onto FTO. The effect of the paste composition and the sintering temperature has been investigated with respect to the material properties and the visible and dark activity.

The XRD results confirmed that the films treated at or below 350 °C mainly composed of cubic Cu_2O beside anatase and rutile TiO_2 regardless of the cellulose content of the paste. The XRD diffractogram of TC-100-550 could be assigned to face-centered monoclinic CuO and anatase and rutile TiO_2. XPS studies further revealed that TC-0-350 and TC-100-350 films exhibited higher CuO ratios on the surface of the films than TC-0-300 but CuO could be detected in TC-0-300 as well. With good agreement with XRD, TC-100-550 was found to compose of mainly CuO based on the XPS spectrum.

The SEM images confirmed that the nanostructures in TC-0-300 and TC-0-350 nanofilms exhibited similar morphologies and dimensions and they were typically less than 100 nm. Uniquely, in TC-100-350 larger spherical assemblies appeared that were in the range of 150-250 nm in size. TEM-SAED revealed that the assemblies composed of both cubic Cu_2O and anatase and rutile phases of TiO_2. The polycrystalline nature of the large spherical nanostructures were suggested by SEM and TEM as well. Additionally, the Scherrer-Debye calculation revealed that the crystallite sizes of Cu_2O were typically bigger than those of TiO_2 which may indicate that the bigger cubic-shaped structures in the SEM belonged to Cu_2O. Finally, the TC-100-550 thin film exhibited uniformly distributed irregularly shaped nanostructures where no bigger nanocrystals were evident. In agreement with this, the Scherrer calculation revealed that the CuO phase exhibited smaller crystallite sizes than Cu_2O.

The optical properties of the thin films were investigated by UV-vis diffuse reflectace. It was found that absorption pattern of the thin films could be well-correlated to their colours and to their composition confirmed by XRD and XPS analysis.

The different sintering temperatures were found to be important not only for the material properties but also for the removal of the organic additives of the paste. It was revealed by ATR that at least 300 °C was necessary to remove the alpha terpineol, whereas 350 °C to remove the ethyl cellulose content of the thin films.

It was found that the apparent visible activity and dark adsorption character of the films significantly varied by the fabrication procedure. Among all the films, TC-0-300 exhibited the highest total MO removal of *circa* 90% in 5 hours. The least effective thin film was TC-100-550 with only a few percent of MO removal. Along with the visible activities, the dark adsorption properties of the thin films were found to be different for the 300 and 350 °C treated samples. Regardless the paste composition the 350 °C treated films adsorbed less MO by 60 min. It was concluded that the dark and visible activities of the films could be modulated by the material properties including the crystal phase, oxidation state and structural properties of Cu_2O and TiO_2. These properties were greatly affected by the thermal treatment and the composition of the doctor-blading paste.

The recycling test revealed that the film could loose considerable activity over repeated use.

Chapter 7

Conclusion

In this thesis different aspects and stages of the development of photocatalytic materials have been considered. Research investigations were carried out from the study of single materials (WO_3 nanostructures), through the study of more complex material systems (Ag-cocatalysed TiO_2/Cu_2O systems), to the investigation of immobilization methods of a powder catalyst (TiO_2/Cu_2O thin films).

WO_3 nanostructures were synthesized by hydrothermal processes and the effect of process parameters such as the solution pH, EtOH and the polymeric surface modulator was studied on the material properties and on the photocatalytic activities. It was found that monoclinic, hexagonal and orthorombic WO_3 and $WO_3 \cdot 0.33H_2O$ could be synthesised by adjusting the solution pH from 0.10 up to 2.01. Monoclinic WO_3 formation was favoured at lower pH levels whereas hexagonal phase WO_3 at higher pH levels. Orthorombic $WO_3 \cdot 0.33H_2O$ was formed at medium pH levels between 0.51 and 1.52. The solution pH not only influenced the crystal phase but also the morphological structure and the band gap energies. As the pH was increased cuboidal nanoplates, nanorods and finally fine nanoneedles and nanowires were formed. The evolution of the morphological structure was discussed with respect to the nucleation theory proposed by LaMer and Dinegar. It was found that the fine nanoneedle formation at pH 1.05 could not be explained by the level of supersaturation. Instead it is

speculated that the metastable hexagonal phase could potentially impact the morphology of WO_3 by means of stabilisation effects. The band gap energies ranged from 2.70±0.03 eV to 3.25±0.03 eV. The highest value was reached at pH 1.05. The variation in the forbidden band gap energies could be attributed to quantum confinement effect and to the crystal structure. The most significant effect of using EtOH in the synthesis procedure was found in the optical properties and in the photocatalytic activities of the nanostructures. The W-EtOH sample exhibited distinct absorption spectrum and blue colour instead of pale yellow. Despite its extended light absorption in the far-red region of the visible spectrum it did not enhance the photocatalytic activity compared to the pale yellow samples. This was suggested by the formation of interband states that may have acted as recombination centers. The highest photoactivities were noted for W-1.52-P20E and W-0.10-P20E samples. It was concluded that the photocatalytic performance of WO_3 nanostructure is a compromise of the material properties including the energy band, crystal structure and the morphology.

The amount of Ag content between 1% and 5% and the effect of the synthesis sequence was investigated on the material properties and on the apparent visible activities of Ag-modified TiO_2/Cu_2O hybrid structures. It was found that the amount of Ag content has not significantly affected the crystal phase, the morphology or the optical properties of the ternary nanomaterials neither in TAC nor in TCA catalysts. However, it was revealed that the dark adsorption and apparent visible activities of the materials were influenced by the amount of deposited Ag. Increasing Ag ratio in TAC catalyst resulted in higher level of dye adsorption to the catalyst surface and at the same time higher rate constants in the apparent visible activities. For TCA catalyst it was found that increased amount of Ag caused a slight decrease in both the dark adsorption and in the rate constants of dye removal of the catalyst under visible light. When the order of the Ag-modification step was altered in the synthesis process, significant impact on the material properties was found. It was revealed that uniquely in TCA catalyst the co-existence of both cubic Cu_2O and face-centered monoclinic CuO

crystal phases was confirmed by the XRD diffragtograms. In contrast, TAC catalyst exhibited pure cubic phase Cu_2O. The partial oxidation of Cu_2O in TCA catalyst was proposed to be caused by the synthesis conditions of the final Ag-deposition step. The morphologycal structure of TAC and TCA catalysts were similar. Both hybrid structure contained smaller (20-30 nm) and bigger (70-80 nm) nanocrystals, however in TCA samples fewer bigger nanostructures were found. It was found that the light absorption properties of TAC and TCA catalyst were significantly different. TAC samples showed extended light absorption to the visible range whereas TCA catalyst exhibited light absorption in the whole visible region. The dark adsorption studies revealed that the TAC ternary structures exhibited delayed dye adsorption in the first 25 minutes while TCA nanomaterials showed rapid although limited dye adsorption to its surface. Under visible light irradiation it was found that TAC catalyst in general showed higher rate constants in the decoloration of methyl orange than TCA samples.

TiO_2/Cu_xO thin films were prepared on FTO substrates by doctor-blade coating technique. The effect of the applied temperature treatment between 300 °C and 550 °C and the chemical composition (cellulose or cellulose-free) of the paste was investigated. It was suggested by ATR-FTIR that the lowest temperature treatment of 300 °C was only effective to remove the alpha-terpineol content from the thin films but not the ethyl cellulose. Temperature treatments above 350 °C were found to adequately eliminate both the alpha-terpineol and ethyl cellulose content. XRD and XPS studies revealed that increasing sintering temperatures yielded higher ratio of face-centered monoclinic CuO beside cubic Cu_2O. At the highest temperature treatment at 550 °C most of the cubic Cu_2O was converted into CuO. The change in the crystal structure and oxidation state of the copper oxide was also evidenced by the colour change of the thin films from yellow to dark brown/black as the temperature was elevated from 300 °C to 550 °C. It was found that the morphology of the thin films was significantly influenced by the heat treatment and the composition of the doctor-blading paste. Beside smaller nanocrystals, TC-350-100 thin film uniquely exhibited 150-250 nm big

polycrystalline spherical assemblies which were evidenced to consist of both TiO_2 and Cu_2O by TEM-SAED. Additionally, in TC-550-100 sample fewer 70-90 nm big nanocrystals were present which was reflected by the SEM image and also suggested by the Scherrer-Debye crystallite size calculation. The apparent visible activities of the nanofilms revealed that TC-0-300 could remove the highest amount of methyl orange dye after 4 hours of visible light irradiation whereas TC-100-550 was the least efficient. When increasing the temperature of the heat treatment for the cellulose-free thin film to 350 °C (TC-0-350), both the dark adsorption and apparent visible activities were found to decrease. However, the cellulose-containing film treated at the same temperature (TC-100-350) showed improved efficiencies under both dark conditions and light irradiation. It is suggested that the material properties such as the crystal structure, oxidation state, structural properties could play a significant role in the decoloration efficiencies of the thin films.

All in all,the author's opinion is that all the studied nanostructures carried positive and negative features, as well. With respect to stability and recyclability, WO_3 catalysts like W-0.1-P20E were found to be the best among the studied systems. In terms of fastest decoloration, the Ag-modified TA5C and TA3C were shown to be the best powder catalysts. It was seen that the final MO solution contained only minimal degradation products. Most of the dye or its degradation products were mineralized and/or adsorbed to the catalyst surface under visible light irradiation.

7.1 Future improvements

As a final remark, future improvements for the better evaluation of photocatalytic performance are proposed.

In order to assess the photocatalytic activities of the nanomaterials dye target molecules are commonly used. However, most often these coloured chemicals like methyl orange can absorb part of the incident light. In this event, it is hard to exclude or estimate the extent of

photosensitization by the dye itself in the overall photocatalytic degradation. To overcome this limitation in the future colourless, UV-active model compounds could be also used to evaluate the photoactivity under visible light irradiation such as 4-chloro-fenol or sodium dodecylbenzenesulfonate.

In this work, only one target molecule has been used to describe the photoactivity. In the future it may be beneficial to employ a range of UV-active compounds for example with different adsorption abilities towards the photocatalyst that could provide further insights in the mechanism and effectiveness of the photocatalyst. For example toluene or isoproturon herbicide could be tested in the future for Cu_2O based materials.

In addition to the target molecule, also the effect of process parameters of the photocatalytic test could be systematically mapped in the future to allow optimised working conditions for specific photocatalyst that could allow better comparison of benefits and weaknesses of different structures.

Stability measurements would be beneficial to be carried out to test the material capability to be used in multiple cycles. This is an important property when considering industrial application of a material.

To learn more about the underlying mechanism of the photocatalytic process it is advisable to investigate both the remaining solution and the material after visible irradiation. The solid material could provide information on the changes of the material crystal or morphological structure. Also potential photocorrosion could be identified and further justified. HPLC-MS and TOC analysis of the solution could reveal potential degradation products and serve information on the mineralization and photobleaching processes.

Improvement on the catalytic material might be achieved by considering the following. In the ternary TiO_2-Cu_2O-Ag composite system the surface chemical properties of the materials could be fine-tuned for purpose when considering the use of capping agents such as polymers or organic surface modulators (like 1-dodecyl-3-methylimidazolium chloride) in the reaction

mixture. This way the surface charge of composite material can be modified and its effect studied with respect to the target molecule.

Also in this work, the partial oxidation of Cu_2O into CuO was experienced when Ag was deposited onto the surface of TiO_2-Cu_2O material. By using different approaches for the Ag-deposition the extent of the oxidation process might be limited or eliminated. This could be possibly achieved by working under milder conditions or at lower temperature and allowing fewer contact time. This way the effect of the partial oxidation could be minimized when comparing to other ternary systems.

TA5C was identified as one of the best catalysts to remove MO from aqueous solution by visible light. It is proposed that the performance of this material could be further enhanced if H_2O_2 is added to the reaction mixture during photocatalytic testing. It is believed that peroxide could considerably aid the release of $OH^{\cdot}$ to the bulk solution and thus promote photocatalytic processes including full mineralization of contaminants.

References

[1] D. Khetarpal, N. Yassaa, and U. Nzotcha. World energy resources. Technical report, 2016.

[2] H. Zhu and T. Lian. Wavefunction engineering in quantum confined semiconductor nanoheterostructures for efficient charge separation and solar energy conversion. *Energy & Environmental Science*, 5(11):9406–9418, 2012.

[3] M. Kummu, P. J. Ward, H. de Moel, and O. Varis. Is physical water scarcity a new phenomenon? Global assessment of water shortage over the last two millennia. *Environmental Research Letters*, 5(3), 2010.

[4] S. Diop, P. M'mayi, D. Lisbjerg, R. Johnstone, United Nations Environment Programme, and GRID-Arendal. *Vital Water Graphics: An Overview of the State of the World's Fresh and Marine Waters*. United Nations Environment Programme, 2nd edition, 2008.

[5] R. Das, Sh. B. Abd Hamid, Md E. Ali, A. F. Ismail, M. S. M. Annuar, and S. Ramakrishna. Multifunctional carbon nanotubes in water treatment: The present, past and future. *Desalination*, 354(0):160–179, 2014.

[6] J. Trujillo-Reyes, J. R. Peralta-Videa, and J. L. Gardea-Torresdey. Supported and unsupported nanomaterials for water and soil remediation: Are they a useful solution for worldwide pollution? *Journal of Hazardous Materials*, 280(0):487–503, 2014.

[7] M. Hosenuzzaman, N. A. Rahim, J. Selvaraj, M. Hasanuzzaman, A. B. M. A. Malek, and A. Nahar. Global prospects, progress, policies, and environmental impact of solar photovoltaic power generation. *Renewable and Sustainable Energy Reviews*, 41(0):284–297, 2015.

[8] A. Fujishima and K. Honda. Electrochemical photolysis of water at a semiconductor electrode. *Nature*, 238(5358):37, 1972.

[9] S. Malato, P. Fernández-Ibáñez, M. I. Maldonado, J. Blanco, and W. Gernjak. Decontamination and disinfection of water by solar photocatalysis: Recent overview and trends. *Catalysis Today*, 147(1):1–59, 2009.

[10] S. Malato, P. Fernández-Ibáñez, M. I. Maldonado, and I. Oller. *Chapter 15 - Solar Photocatalytic Processes: Water Decontamination and Disinfection A2 - Suib, Steven L*, pages 371–393. Elsevier, Amsterdam, 2013.

[11] H.-E. Cheng, C.-Y. Lin, and C.-M. Hsu. Fabrication of SnO_2-TiO_2 core-shell nanopillar-array films for enhanced photocatalytic activity. *Applied Surface Science*, 396:393–399, 2017.

[12] M. Qamar, Z. H. Yamani, M. A. Gondal, and K. Alhooshani. Synthesis and comparative photocatalytic activity of Pt/WO_3 and Au/WO_3 nanocomposites under sunlight-type excitation. *Solid State Sciences*, 13(9):1748–1754, 2011.

[13] Y. L. Pan, S. Z. Deng, L. Polavarapu, N. Y. Gao, P. Y. Yuan, C. H. Sow, and Q. H. Xu. Plasmon-enhanced photocatalytic properties of Cu_2O nanowire-Au nanoparticle assemblies. *Langmuir*, 28(33):12304–12310, 2012.

[14] S. Singh, H. Mahalingam, and P. K. Singh. Polymer-supported titanium dioxide photocatalysts for environmental remediation: A review. *Applied Catalysis A: General*, 462–463(0):178–195, 2013.

[15] Y. Lan, Y. Lu, and Z. Ren. Mini review on photocatalysis of titanium dioxide nanoparticles and their solar applications. *Nano Energy*, 2(5):1031–1045, 2013.

[16] A. Talebian, M. H. Entezari, and N. Ghows. Complete mineralization of surfactant from aqueous solution by a novel sono-synthesized nanocomposite (TiO_2-Cu_2O) under sunlight irradiation. *Chemical Engineering Journal*, 229:304–312, 2013.

[17] Z. Zhang and P. Wang. Optimization of photoelectrochemical water splitting performance on hierarchical TiO_2 nanotube arrays. *Energy & Environmental Science*, 5(4):6506–6512, 2012.

[18] P. Salvador. Hole diffusion length in n-TiO_2 single-crystals and sintered electrodes - photoelectrochemical determination and comparative-analysis. *Journal of Applied Physics*, 55(8):2977–2985, 1984.

[19] Z. H. Zhang, R. Dua, L. B. Zhang, H. B. Zhu, H. N. Zhang, and P. Wang. Carbon-layer-protected cuprous oxide nanowire arrays for efficient water reduction. *ACS Nano*, 7(2):1709–1717, 2013.

[20] B. Ohtani. *Design and Development of Active Titania and Related Photocatalysts*, pages 73–102. Wiley-VCH Verlag GmbH & Co. KGaA, 2013.

[21] H. Tong, S. Ouyang, Y. Bi, N. Umezawa, M. Oshikiri, and J. Ye. Nano-photocatalytic materials: Possibilities and challenges. *Advanced Materials*, 24(2):229–251, 2012.

[22] C.-Y. Kuo, C.-H. Wu, and H.-Y. Lin. Synergistic effects of TiO_2 and Cu_2O in UV/TiO_2/zeolite-based systems on photodegradation of bisphenol A. *Environmental Technology*, 35(15):1851–1857, 2014.

[23] Y. J. Wang, Q. S. Wang, X. Y. Zhan, F. M. Wang, M. Safdar, and J. He. Visible light driven type II heterostructures and their enhanced photocatalysis properties: a review. *Nanoscale*, 5(18):8326–8339, 2013.

[24] Z. Ren, Y. Guo, C.-H. Liu, and P.-X. Gao. Hierarchically nanostructured materials for sustainable environmental applications. *Frontiers in Chemistry*, 1, 2013.

[25] H. Ruda, J. Polanyi, J. Yang, Z. Wu, U. Philipose, T. Xu, S. Yang, K. L. Kavanagh, J. Q. Liu, L. Yang, Y. Wang, K. Robbie, J. Yang, K. Kaminska, D. G. Cooke, F. A. Hegmann, A. J. Budz, and H. K. Haugen. Developing 1D nanostructure arrays for future nanophotonics. *Nanoscale Research Letters*, 1(2):99 – 119, 2006.

[26] H. Zheng, J. Z. Ou, M. S. Strano, R. B. Kaner, A. Mitchell, and K. Kalantarzadeh. Nanostructured tungsten oxide – properties, synthesis, and applications. *Advanced Functional Materials*, 21(12):2175–2196, 2011.

[27] A. M. Tripathi and S. Mitra. Tin sulfide (SnS) nanorods: structural, optical and lithium storage property study. *RSC Advances*, 4(20):10358–10366, 2014.

[28] M. I. Dyakonov. *Basics of Semiconductor and Spin Physics*, pages 1–28. Springer Berlin Heidelberg, 2008.

[29] H. M. Chen, C. K. Chen, Y.-C. Chang, C.-W. Tsai, R.-S. Liu, S.-F. Hu, W.-S. Chang, and K.-H. Chen. Quantum dot monolayer sensitized ZnO nanowire-array photoelectrodes: True efficiency for water splitting. *Angewandte Chemie International Edition*, 49(34):5966–5969, 2010.

[30] F. Amano, E. Ishinaga, and A. Yamakata. Effect of particle size on the photocatalytic activity of WO_3 particles for water oxidation. *The Journal of Physical Chemistry C*, 117(44):22584–22590, 2013.

[31] X. Zhang, V. Thavasi, S. G. Mhaisalkar, and S. Ramakrishna. Novel hollow mesoporous 1D TiO_2 nanofibers as photovoltaic and photocatalytic materials. *Nanoscale*, 4(5):1707–1716, 2012.

[32] J. Huang, X. Xu, C. Gu, G. Fu, W. Wang, and J. Liu. Flower-like and hollow sphere-like WO_3 porous nanostructures: Selective synthesis and their photocatalysis property. *Materials Research Bulletin*, 47(11):3224–3232, 2012.

[33] J. Y. Ho and M. H. Huang. Synthesis of submicrometer-sized Cu_2O crystals with morphological evolution from cubic to hexapod structures and their comparative photocatalytic activity. *Journal of Physical Chemistry C*, 113(32):14159–14164, 2009.

[34] Y. Cui, G. Zhang, Z. Lin, and X. Wang. Condensed and low-defected graphitic carbon nitride with enhanced photocatalytic hydrogen evolution under visible light irradiation. *Applied Catalysis B: Environmental*, 181:413–419, 2016.

[35] A. B. Murphy. Band-gap determination from diffuse reflectance measurements of semiconductor films, and application to photoelectrochemical water-splitting. *Solar Energy Materials and Solar Cells*, 91(14):1326–1337, 2007.

[36] J. Dong, H. Xu, F. Zhang, C. Chen, L. Liu, and G. Wu. Synergistic effect over photocatalytic active Cu_2O thin films and their morphological and orientational transformation under visible light irradiation. *Applied Catalysis A: General*, 470:294–302, 2014.

[37] K. Byrappa, A. K. Subramani, S. Ananda, K. M. Lokanatha Rai, R. Dinesh, and M. Yoshimura. Photocatalytic degradation of Rhodamine B dye using hydrothermally synthesized ZnO. *Bulletin of Materials Science*, 29(5):433–438, 2006.

[38] Y. X. Zhao, H. C. Pan, Y. B. Lou, X. F. Qiu, J. J. Zhu, and C. Burda. Plasmonic $Cu_{2-x}S$ nanocrystals: Optical and structural properties of copper-deficient copper(I) sulfides. *Journal of the American Chemical Society*, 131(12):4253–4261, 2009.

[39] D. Chen and Y. Wang. Impurity doping: a novel strategy for controllable synthesis of functional lanthanide nanomaterials. *Nanoscale*, 5(11):4621–4637, 2013.

[40] W. Choi, A. Termin, and M. R. Hoffmann. The role of metal ion dopants in quantum-sized TiO_2: Correlation between photoreactivity and charge carrier recombination dynamics. *The Journal of Physical Chemistry*, 98(51):13669–13679, 1994.

[41] S. Martha, P. C. Sahoo, and K. M. Parida. An overview on visible light responsive metal oxide based photocatalysts for hydrogen energy production. *RSC Advances*, 5(76):61535–61553, 2015.

[42] G. S. Shao, Q. R. Deng, L. Wan, M. L. Guo, X. H. Xia, and Y. Gao. Molecular design of TiO_2 for gigantic red shift via sub lattice substitution. *Journal of Nanoscience and Nanotechnology*, 10(11):7092–7096, 2010.

[43] K. Obata, K. Kishishita, A. Okemoto, K. Taniya, Y. Ichihashi, and S. Nishiyama. Photocatalytic decomposition of NH_3 over TiO_2 catalysts doped with Fe. *Applied Catalysis B-Environmental*, 160:200–203, 2014.

[44] T. L. Thompson and J. T. Yates. Surface science studies of the photoactivation of TiO_2-new photochemical processes. *Chemical Reviews*, 106(10):4428–4453, 2006.

[45] R. F. Yuan, B. H. Zhou, D. Hua, C. H. Shi, and L. Ma. Effect of metal-ion doping on the characteristics and photocatalytic activity of TiO_2 nanotubes for the removal of toluene from water. *Water Science and Technology*, 69(8):1697–1704, 2014.

[46] M. Khan, W. Cao, N. Chen, Z. Usman, D. F. Khan, A. M. Toufiq, and M. A. Khaskheli. Influence of tungsten doping concentration on the electronic and optical properties of anatase TiO_2. *Current Applied Physics*, 13(7):1376–1382, 2013.

[47] N. Venkatachalam, M. Palanichamy, B. Arabindoo, and V. Murugesan. Enhanced photocatalytic degradation of 4-chlorophenol by Zr^{4+} doped nano TiO_2. *Journal of Molecular Catalysis A: Chemical*, 266(1–2):158–165, 2007.

[48] I. Cimieri, H. Poelman, N. Avci, J. Geens, S. Lambert, B. Heinrichs, and D. Poelman. Sol–gel preparation of pure and doped TiO_2 films for the photocatalytic oxidation of ethanol in air. *Journal of Sol-Gel Science and Technology*, 63(3):526–536, 2012.

[49] N. Shaham-Waldmann and Y. Paz. *Modified Photocatalysts*, pages 103–143. Wiley-VCH Verlag GmbH & Co. KGaA, 2013.

[50] H. Q. Sun, G. L. Zhou, S. Z. Liu, H. M. Ang, M. O. Tade, and S. B. Wang. Visible light responsive titania photocatalysts codoped by nitrogen and metal (Fe, Ni, Ag, or Pt) for remediation of aqueous pollutants. *Chemical Engineering Journal*, 231:18–25, 2013.

[51] Y. Bessekhouad, D. Robert, J. V. Weber, and N. Chaoui. Effect of alkaline-doped TiO_2 on photocatalytic efficiency. *Journal of Photochemistry and Photobiology A-Chemistry*, 167(1):49–57, 2004.

[52] S. S. Srinivasan, J. Wade, E. K. Stefanakos, and Y. Goswami. Synergistic effects of sulfation and co-doping on the visible light photocatalysis of TiO_2. *Journal of Alloys and Compounds*, 424(1-2):322–326, 2006.

[53] C.-C. Hu, T.-C. Hsu, and S.-Y. Lu. Effect of nitrogen doping on the microstructure and visible light photocatalysis of titanate nanotubes by a facile cohydrothermal synthesis via urea treatment. *Applied Surface Science*, 280(0):171–178, 2013.

[54] Y. Yalcin, M. Kilic, and Z. Cinar. The role of non-metal doping in TiO_2 photocatalysis. *Journal of Advanced Oxidation Technologies*, 13(3):281–296, 2010.

[55] T. Q. Lin, C. Y. Yang, Z. Wang, H. Yin, X. J. Lu, F. Q. Huang, J. H. Lin, X. M. Xie, and M. H. Jiang. Effective nonmetal incorporation in black titania with enhanced solar energy utilization. *Energy & Environmental Science*, 7(3):967–972, 2014.

[56] G. Liu, L.-C. Yin, J. Wang, P. Niu, C. Zhen, Y. Xie, and H.-M. Cheng. A red anatase TiO_2 photocatalyst for solar energy conversion. *Energy & Environmental Science*, 5(11):9603–9610, 2012.

[57] E. M. Neville, J. M. D. MacElroy, K. R. Thampi, and J. A. Sullivan. Visible light active C-doped titanate nanotubes prepared via alkaline hydrothermal treatment of C-doped nanoparticulate TiO_2: Photo-electrochemical and photocatalytic properties. *Journal of Photochemistry and Photobiology A: Chemistry*, 267(0):17–24, 2013.

[58] C. Di Valentin and G. Pacchioni. Trends in non-metal doping of anatase TiO_2: B, C, N and F. *Catalysis Today*, 206(0):12–18, 2013.

[59] M. V. Dozzi and E. Selli. Doping TiO_2 with p-block elements: Effects on photocatalytic activity. *Journal of Photochemistry and Photobiology C: Photochemistry Reviews*, 14:13–28, 2013.

[60] X. Zhou, F. Peng, H. Wang, H. Yu, and J. Yang. Effect of nitrogen-doping temperature on the structure and photocatalytic activity of the B,N-doped TiO_2. *Journal of Solid State Chemistry*, 184(1):134–140, 2011.

[61] F. Spadavecchia, M. Ceotto, L. Lo Presti, C. Aieta, I. Biraghi, D. Meroni, S. Ardizzone, and G. Cappelletti. Second generation nitrogen doped titania nanoparticles: A comprehensive electronic and microstructural picture. *Chinese Journal of Chemistry*, 32(12):1195–1213, 2014.

[62] H. Wang, T. Lin, G. Zhu, H. Yin, X. Lü, Y. Li, and F. Huang. Colored titania nanocrystals and excellent photocatalysis for water cleaning. *Catalysis Communications*, 60(0):55–59, 2015.

[63] X. Liu and M. T. Swihart. Heavily-doped colloidal semiconductor and metal oxide nanocrystals: an emerging new class of plasmonic nanomaterials. *Chemical Society Reviews*, 43(11):3908–3920, 2014.

[64] F. Zuo, L. Wang, T. Wu, Z. Y. Zhang, D. Borchardt, and P. Y. Feng. Self-doped Ti^{3+} enhanced photocatalyst for hydrogen production under visible light. *Journal of the American Chemical Society*, 132(34):11856–11857, 2010.

[65] H. Y. Yin, X. L. Wang, L. Wang, Q. L. N, and H. T. Zhao. Self-doped TiO_2 hierarchical hollow spheres with enhanced visible-light photocatalytic activity. *Journal of Alloys and Compounds*, 640:68–74, 2015.

[66] Z. H. Zhang, X. L. Yang, M. N. Hedhili, E. Ahmed, L. Shi, and P. Wang. Microwave-assisted self-doping of TiO_2 photonic crystals for efficient photoelectrochemical water splitting. *Acs Applied Materials & Interfaces*, 6(1):691–696, 2014.

[67] Z. H. Zhang, M. N. Hedhili, H. B. Zhu, and P. Wang. Electrochemical reduction induced self-doping of Ti^{3+} for efficient water splitting performance on TiO_2 based photoelectrodes. *Physical Chemistry Chemical Physics*, 15(37):15637–15644, 2013.

[68] C. Y. Yang, Z. Wang, T. Q. Lin, H. Yin, X. J. Lu, D. Y. Wan, T. Xu, C. Zheng, J. H. Lin, F. Q. Huang, X. M. Xie, and M. H. Jiangl. Core-shell nanostructured "black" rutile titania as excellent catalyst for hydrogen production enhanced by sulfur doping. *Journal of the American Chemical Society*, 135(47):17831–17838, 2013.

[69] A. L. Routzahn, S. L. White, L. K. Fong, and P. K. Jain. Plasmonics with doped quantum dots. *Israel Journal of Chemistry*, 52(11-12):983–991, 2012.

[70] Y. Liu, Y. H. Deng, Z. K. Sun, J. Wei, G. F. Zheng, A. M. Asiri, S. B. Khan, M. M. Rahman, and D. Y. Zhao. Hierarchical Cu_2S microsponges constructed from nanosheets for efficient photocatalysis. *Small*, 9(16):2702–2708, 2013.

[71] S. C. Li, K. Yu, Y. Wang, Z. L. Zhang, C. Q. Song, H. H. Yin, Q. Ren, and Z. Q. Zhu. Cu_2S@ZnO hetero-nanostructures: facile synthesis, morphology-evolution and enhanced photocatalysis and field emission properties. *Crystengcomm*, 15(9):1753–1761, 2013.

[72] H. L. Chen, S. Y. Xu, J. B. Cui, and L. Y. Wang. $Cu_{2-x}S$/graphene oxide nanocomposites for efficient photocatalysis driven by real sunlight. *RSC Advances*, 5(114):94375–94379, 2015.

[73] R. S. Selinsky, Q. Ding, M. S. Faber, J. C. Wright, and S. Jin. Quantum dot nanoscale heterostructures for solar energy conversion. *Chemical Society Reviews*, 42(7):2963–2985, 2013.

[74] S. Lopez-Ayala and M. E. Rincon. Catalytic and photocatalytic performance of mesoporous Cu_xO-TiO_2. *Journal of Photochemistry and Photobiology A-Chemistry*, 222(1):249–257, 2011.

[75] K. F. Wu, L. J. Hill, J. Q. Chen, J. R. McBride, N. G. Pavlopolous, N. E. Richey, J. Pyun, and T. Q. Lian. Universal length dependence of rod-to-seed exciton localization efficiency in type I and quasi-type II CdSe@CdS nanorods. *ACS Nano*, 9(4):4591–4599, 2015.

[76] J. Chen, S. H. Shen, P. H. Guo, M. Wang, P. Wu, X. X. Wang, and L. J. Guo. In-situ reduction synthesis of nano-sized Cu_2O particles modifying g-C_3N_4 for enhanced photocatalytic hydrogen production. *Applied Catalysis B-Environmental*, 152:335–341, 2014.

[77] Chuan Li, J. H. Hsieh, J. C. Cheng, and C. C. Huang. Optical and photoelectrochemical studies on Ag_2O/TiO_2 double-layer thin films. *Thin Solid Films*, 570, Part B:436–444, 2014.

[78] Y. Zheng, L. Zheng, Y. Zhan, X. Lin, Q. Zheng, and K. Wei. Ag/ZnO heterostructure nanocrystals: Synthesis, characterization, and photocatalysis. *Inorganic Chemistry*, 46(17):6980–6986, 2007.

[79] Y. Myung, D. M. Jang, T. K. Sung, Y. J. Sohn, G. B. Jung, Y. J. Cho, H. S. Kim, and J. Park. Composition-tuned ZnO-CdSSe core-shell nanowire arrays. *ACS Nano*, 4(7):3789–3800, 2010.

[80] Y. L. Liu, G. J. Yang, H. Zhang, Y. Q. Cheng, K. Q. Chen, Z. Y. Peng, and W. Chen. Enhanced visible photocatalytic activity of Cu_2O nanocrystal/titanate nanobelt heterojunctions by a self-assembly process. *RSC Advances*, 4(46):24363–24368, 2014.

[81] Y. N. Huo, X. L. Yang, J. Zhu, and H. X. Li. Highly active and stable $CdS - TiO_2$ visible photocatalyst prepared by in situ sulfurization under supercritical conditions. *Applied Catalysis B-Environmental*, 106(1-2):69–75, 2011.

[82] J. Mioduska, A. Zielinska-Jurek, M. Janczarek, and J. Hupka. The effect of calcination temperature on structure and photocatalytic properties of WO_3/TiO_2 nanocomposites. *Journal of Nanomaterials*, 2016:8, 2016.

[83] Q. Zhang, I. Lee, J. B. Joo, F. Zaera, and Y. D. Yin. Core-shell nanostructured catalysts. *Accounts of Chemical Research*, 46(8):1816–1824, 2013.

[84] X. Su, J. Zhao, Y. Li, Y. Zhu, X. Ma, F. Sun, and Z. Wang. Solution synthesis of Cu_2O/TiO_2 core-shell nanocomposites. *Colloids and Surfaces A: Physicochemical and Engineering Aspects*, 349(1–3):151–155, 2009.

[85] N. M. Vuong, D. Kim, and H. Kim. Electrochromic properties of porous WO_3-TiO_2 core-shell nanowires. *Journal of Materials Chemistry C*, 1(21):3399–3407, 2013.

[86] I. M. Szilágyi, E. Santala, M. Heikkilä, M. Pore, V.and Kemell, T. Nikitin, G. Teucher, T. Firkala, L. Khriachtchev, M. Räsänen, M. Ritala, and M. Leskelä. Photocatalytic properties of WO_3/TiO_2 core/shell nanofibers prepared by electrospinning and atomic layer deposition. *Chemical Vapor Deposition*, 19(4-6):149–155, 2013.

[87] S. Chu, X. M. Zheng, F. Kong, G. H. Wu, L. L. Luo, Y. Guo, H. L. Liu, Y. Wang, H. X. Yu, and Z. G. Zou. Architecture of $Cu_2O@TiO_2$ core-shell heterojunction and photodegradation for 4-nitrophenol under simulated sunlight irradiation. *Materials Chemistry and Physics*, 129(3):1184–1188, 2011.

[88] Y. Liu, B. Zhang, L. Luo, X. Chen, Z. Wang, E. Wu, D. Su, and W. Huang. TiO_2/Cu_2O core/ultrathin shell nanorods as efficient and stable photocatalysts for water reduction. *Angewandte Chemie International Edition*, 54(50):15260–15265, 2015.

[89] L. M. Liu, W. Y. Yang, Q. Li, S. A. Gao, and J. K. Shang. Synthesis of Cu_2O nanospheres decorated with TiO_2 nanoislands, their enhanced photoactivity and stability under visible light illumination, and their post-illumination catalytic memory. *ACS Applied Materials & Interfaces*, 6(8):5629–5639, 2014.

[90] Z. Xie, X. Liu, W. Wang, X. Wang, C. Liu, Q. Xie, Z. Li, and Z. Zhang. Enhanced photoelectrochemical and photocatalytic performance of TiO_2 nanorod arrays/CdS quantum dots by coating TiO_2 through atomic layer deposition. *Nano Energy*, 11:400–408, 2015.

[91] M. Liu, X. Xie, L. Chen, X. Wang, Y. Cheng, F. Lu, W.-H. Wang, J. Yang, X. Du, J. Zhu, H. Liu, H. Dong, W. Wang, and H. Liu. A rational design of heterojunction photocatalyst CdS interfacing with one cycle of ALD oxide. *Journal of Materials Science & Technology*, 32(6):489–495, 2016.

[92] L. G. Devi and R. Kavitha. A review on plasmonic metal-TiO_2 composite for generation, trapping, storing and dynamic vectorial transfer of photogenerated electrons across the schottky junction in a photocatalytic system. *Applied Surface Science*, 360:601–622, 2016.

[93] N. Zhou, V. Lopez-Puente, Q. Wang, L. Polavarapu, I. Pastoriza-Santos, and Q.-H. Xu. Plasmon-enhanced light harvesting: applications in enhanced photocatalysis, photodynamic therapy and photovoltaics. *RSC Advances*, 5(37):29076–29097, 2015.

[94] S. Linic, P. Christopher, and D. B. Ingram. Plasmonic-metal nanostructures for efficient conversion of solar to chemical energy. *Nature Materials*, 10(12):911–921, 2011.

[95] R. E. Hummel. *Electronic Properties of Materials*. Springer-Verlag New York, 4 edition, 2011.

[96] L. Xu, F. Zhang, Z. Song, X.and Yin, and Y. Bu. Construction of reduced graphene oxide-supported Ag-Cu_2O composites with hierarchical structures for enhanced photocatalytic activities and recyclability. *Journal of Materials Chemistry A*, 3(11):5923–5933, 2015.

[97] J. Liu, Z. Gao, H. Han, D. Wu, F. Xu, H. Wang, and K. Jiang. Mesoporous Cu_2O submicro-spheres, facile synthesis and the selective adsorption properties. *Chemical Engineering Journal*, 185–186:151–159, 2012.

[98] U. Habiba, M. S. Islam, T. A. Siddique, A. M. Afifi, and B. C. Ang. Adsorption and photocatalytic degradation of anionic dyes on Chitosan/PVA/Na–Titanate/TiO_2 composites synthesized by solution casting method. *Carbohydrate Polymers*, 149:317–331, 2016.

[99] C. Young, T. M. Lim, K. Chiang, J. Scott, and R. Amal. Photocatalytic oxidation of toluene and trichloroethylene in the gas-phase by metallised (Pt, Ag) titanium dioxide. *Applied Catalysis B-Environmental*, 78(1-2):1–10, 2008.

[100] V. P. Dinesh, P. Biji, A. Ashok, S. K. Dhara, M. Kamruddin, A. K. Tyagi, and B. Raj. Plasmon-mediated, highly enhanced photocatalytic degradation of industrial textile dyes using hybrid ZnO@Ag core-shell nanorods. *RSC Advances*, 4(103):58930–58940, 2014.

[101] Y. Li, W. Wu, P. Dai, L. Zhang, Z. Sun, G. Li, M. Wu, X. Chen, and C. Chen. WO_3 and Ag nanoparticle co-sensitized TiO_2 nanowires: preparation and the enhancement of photocatalytic activity. *RSC Advances*, 4(45):23831–23837, 2014.

[102] Z. Wang, C. Chen, W. Ma, and J. Zhao. *Sensitization of Titania Semiconductor: A Promising Strategy to Utilize Visible Light*, pages 199–240. Wiley-VCH Verlag GmbH & Co. KGaA, 2013.

[103] J. C. Zhao, C. C. Chen, and W. H. Ma. Photocatalytic degradation of organic pollutants under visible light irradiation. *Topics in Catalysis*, 35(3-4):269–278, 2005.

[104] S. Wahyuningsih, A. H. Ramelan, R. Hidayat, G. Fadillah, H. Munawaroh, Lnmz Saputri, and Q. A. Hanif. *Alternative natural dyes in water purification: anthocyanin as TiO_2-sensitizer in Rhodamine B photoelectrodegradation*, volume 9792 of *Proceedings of SPIE*. Spie-Int Soc Optical Engineering, Bellingham, 2015.

[105] J. A. Fernandez, A. Suan, J. C. Ramirez, J. Robles, J. C. Salcedo, A. M. Pedroza, and C. E. Daza. Treatment of real wastewater with TiO_2-films sensitized by a natural-dye obtained from picramnia sellowii. *Journal of Environmental Chemical Engineering*, 4(3):2848–2856, 2016.

[106] Z. L. Jin, X. J. Zhang, Y. X. Li, S. B. Li, and G. X. Lu. 5.1% apparent quantum efficiency for stable hydrogen generation over eosin-sensitized CuO/TiO_2 photocatalyst under visible light irradiation. *Catalysis Communications*, 8(8):1267–1273, 2007.

[107] D. Chatterjee. Effect of excited state redox properties of dye sensitizers on hydrogen production through photo-splitting of water over TiO_2 photocatalyst. *Catalysis Communications*, 11(5):336–339, 2010.

[108] W. S. Han, K. R. Wee, H. Y. Kim, C. Pac, Y. Nabetani, D. Yamamoto, T. Shimada, H. Inoue, H. Choi, K. Cho, and S. O. Kang. Hydrophilicity control of visible-light hydrogen evolution and dynamics of the charge-separated state in $Dye/TiO_2/Pt$ hybrid systems. *Chemistry-A European Journal*, 18(48):15368–15381, 2012.

[109] Z. Jin, W. B. Duan, B. Liu, X. D. Chen, F. H. Yang, and J. P. Guo. Fabrication of efficient visible light activated Cu-P25-graphene ternary composite for photocatalytic degradation of methyl blue. *Applied Surface Science*, 356:707–718, 2015.

[110] T. G. Kim, H. Ryu, W.-J. Lee, and J.-H. Yoon. Effects of graphene oxide (GO) on GO-Cu_2O composite films grown by using electrochemical deposition for a pec photoelectrode. *Journal of the Korean Physical Society*, 66(10):1586–1592, 2015.

[111] R. Vinoth, P. Karthik, C. Muthamizhchelvan, B. Neppolian, and M. Ashokkumar. Carrier separation and charge transport characteristics of reduced graphene oxide supported visible-light active photocatalysts. *Physical Chemistry Chemical Physics*, 18(7):5179–5191, 2016.

[112] X. J. Liu, L. K. Pan, T. Lv, Z. Sun, and C. Q. Sun. Enhanced photocatalytic reduction of Cr(VI) by $ZnO - TiO_2 -$ CNTs composites synthesized via microwave-assisted reaction. *Journal of Molecular Catalysis A-Chemical*, 363:417–422, 2012.

[113] T. S. Natarajan, J. Y. Lee, H. C. Bajaj, W. K. Jo, and R. J. Tayade. Synthesis of multiwall carbon nanotubes/TiO_2 nanotube composites with enhanced photocatalytic decomposition efficiency. *Catalysis Today*, 282:13–23, 2017.

[114] S. Park, S. K. Choo, G. R. Choi, Y. J. Chung, D. Oh, Y. C. Kim, and J.-H. Lee. Photocatalytic and immobilization characteristics of immobilized zno and TiO_2 nanopowders. *Research on Chemical Intermediates*, 36(6):843–849, 2010.

[115] J. Geltmeyer, H. Teixido, M. Meire, T. Van Acker, K. Deventer, F. Vanhaecke, S. Van Hulle, K. De Buysser, and K. De Clerck. TiO_2 functionalized nanofibrous membranes for removal of organic (micro)pollutants from water. *Separation and Purification Technology*, 179:533–541, 2017.

[116] D. Robert, V. Keller, and N. Keller. *Immobilization of a Semiconductor Photocatalyst on Solid Supports: Methods, Materials, and Applications*, pages 145–178. Wiley-VCH Verlag GmbH & Co. KGaA, 2013.

[117] F. Montecchio, D. Chinungi, R. Lanza, and K. Engvall. Surface treatments of metal supports for photocatalysis applications. *Applied Surface Science*, 401:283–296, 2017.

[118] M. Tasbihi, A. Călin, I.and Šuligoj, M. Fanetti, and U. Lavrenčič Štangar. Photocatalytic degradation of gaseous toluene by using TiO_2 nanoparticles immobilized on fiberglass cloth. *Journal of Photochemistry and Photobiology A: Chemistry*, 336:89–97, 2017.

[119] N. M. Mahmoodi and M. Arami. Bulk phase degradation of Acid Red 14 by nanophotocatalysis using immobilized titanium(IV) oxide nanoparticles. *Journal of Photochemistry and Photobiology A-Chemistry*, 182(1):60–66, 2006.

[120] S. S. Chin, K. Chiang, and A. G. Fane. The stability of polymeric membranes in a TiO_2 photocatalysis process. *Journal of Membrane Science*, 275(1–2):202–211, 2006.

[121] H. Han and R. B. Bai. Highly effective buoyant photocatalyst prepared with a novel layered-TiO_2 configuration on polypropylene fabric and the degradation performance for methyl orange dye under UV-vis and vis lights. *Separation and Purification Technology*, 73(2):142–150, 2010.

[122] F. Magalhaes, F. C. C. Moura, and R. M. Lago. TiO_2/LDPE composites: A new floating photocatalyst for solar degradation of organic contaminants. *Desalination*, 276(1–3):266–271, 2011.

[123] I. Altin and M. Sökmen. Buoyant photocatalyst based on zno immobilized on polystyrene beads for pollutants treatment. *CLEAN – Soil, Air, Water*, 43(7):1025–1030, 2015.

[124] A. Y. Shan, T. I. M. Ghazi, and S. A. Rashid. Immobilisation of titanium dioxide onto supporting materials in heterogeneous photocatalysis: A review. *Applied Catalysis A: General*, 389(1–2):1–8, 2010.

[125] J. Zhang, H. Zhu, S. Zheng, F. Pan, and T. Wang. TiO_2 film/Cu_2O microgrid heterojunction with photocatalytic activity under solar light irradiation. *ACS Applied Materials & Interfaces*, 1(10):2111–2114, 2009.

[126] C. Shen, Y. J. Wang, J. H. Xu, and G. S. Luo. Facile synthesis and photocatalytic properties of TiO_2 nanoparticles supported on porous glass beads. *Chemical Engineering Journal*, 209:478–485, 2012.

[127] A. S. Zoolfakar, R. A. Rani, A. J. Morfa, A. P. O'Mullane, and K. Kalantarzadeh. Nanostructured copper oxide semiconductors: a perspective on materials, synthesis methods and applications. *Journal of Materials Chemistry C*, 2(27):5247–5270, 2014.

[128] A. Zolanvari, H. Sadeghi, R. Norouzi, and A. Ranjgar. Surface plasmons and optical properties of TiO_2/X(X = Au and Ag) nanostructure thin films. *Chinese Physics Letters*, 30(9), 2013.

[129] J. Medina-Valtierra, C. Frausto-Reyes, G. Camarillo-Martinez, and J. A. Ramirez-Ortiz. Complete oxidation of isopropanol over Cu_4O_3 (paramelaconite) coating deposited on fiberglass by CVD. *Applied Catalysis A-General*, 356(1):36–42, 2009.

[130] H. M. Yates, L. A. Brook, D. W. Sheel, I. B. Ditta, A. Steele, and H. A. Foster. The growth of copper oxides on glass by flame assisted chemical vapour deposition. *Thin Solid Films*, 517(2):517–521, 2008.

[131] M. Leskelä and M. Ritala. Atomic layer deposition (ALD): from precursors to thin film structures. *Thin Solid Films*, 409(1):138–146, 2002.

[132] I. Levchuk, C. Guillard, F. Dappozze, S. Parola, D. Leonard, and M. Sillanpaa. Photocatalytic activity of TiO_2 films immobilized on aluminum foam by atomic layer deposition technique. *Journal of Photochemistry and Photobiology A-Chemistry*, 328:16–23, 2016.

[133] S. Ito, P. Chen, P. Comte, M. K. Nazeeruddin, P. Liska, P. Péchy, and M. Grätzel. Fabrication of screen-printing pastes from TiO_2 powders for dye-sensitised solar cells. *Progress in Photovoltaics: Research and Applications*, 15(7):603–612, 2007.

[134] H. Nan, W. Wu, K. Feng, B. Shan, and Y. Qiu, Y.and Zhang. Improved photocatalytic efficiency and stability of CdS/ZnO shell/core nanoarrays with high coverage and enhanced interface combination. *International Journal of Hydrogen Energy*, 42(2):848–857, 2017.

[135] S. Ramkumar and G. Rajarajan. Enhanced visible light photocatalytic activity of pristine and silver (Ag) doped WO_3 nanostructured thin films. *Journal of Materials Science: Materials in Electronics*, 27(11):12185–12192, 2016.

[136] M. T. S. Nair, L. Guerrero, O. L. Arenas, and P. K. Nair. Chemically deposited copper oxide thin films: structural, optical and electrical characteristics. *Applied Surface Science*, 150(1-4):143–151, 1999.

[137] P. Lv, W. Y. Fu, H. B. Yang, H. R. Sun, Y. L. Chen, J. W. Ma, X. M. Zhou, L. C. Tian, W. J. Zhang, M. J. Li, H. Z. Yao, and D. Wu. Simple synthesis method of Bi_2S_3//CdS quantum dots cosensitized TiO_2 nanotubes array with enhanced photoelectrochemical and photocatalytic activity. *Crystengcomm*, 15(37):7548–7555, 2013.

[138] G. Odling and N. Robertson. $BiVO_4 - TiO_2$ composite photocatalysts for dye degradation formed using the SILAR method. *ChemPhysChem*, 17(18):2872–2880, 2016.

[139] H. Chen, S. Chen, X. Quan, H. Yu, H. Zhao, and Y. Zhang. Fabrication of $TiO_2 - Pt$ coaxial nanotube array Schottky structures for enhanced photocatalytic degradation of phenol in aqueous solution. *The Journal of Physical Chemistry C*, 112(25):9285–9290, 2008.

[140] S. Matsuzawa, C. Maneerat, Y. Hayata, T. Hirakawa, N. Negishi, and T. Sano. Immobilization of TiO_2 nanoparticles on polymeric substrates by using electrostatic interaction in the aqueous phase. *Applied Catalysis B: Environmental*, 83(1–2):39–45, 2008.

[141] I. Burgues-Ceballos, M. Stella, P. Lacharmoise, and E. Martinez-Ferrero. Towards industrialization of polymer solar cells: material processing for upscaling. *Journal of Materials Chemistry A*, 2(42):17711–17722, 2014.

[142] M. Jonstrup, M. Warjerstam, M. Murto, and B. Mattiasson. Immobilisation of TiO_2 for combined photocatalytic-biological azo dye degradation. *Water Science and Technology*, 62(3):525–531, 2010.

[143] U. Lamdab, K. Wetchakun, S. Phanichphant, W. Kangwansupamonkon, and N. Wetchakun. $InVO_4$-$BiVO_4$ composite films with enhanced visible light performance for photodegradation of methylene blue. *Catalysis Today*, 278, Part 2:291–302, 2016.

[144] A. Rachel, B. Lavedrine, M. Subrahmanyam, and P. Boule. Use of porous lavas as supports of photocatalysts. *Catalysis Communications*, 3(4):165–171, 2002.

[145] G. S. Shephard, S. Stockenstrom, D. de Villiers, W. J. Engelbrecht, and G. F. S. Wessels. Degradation of microcystin toxins in a falling film photocatalytic reactor with immobilized titanium dioxide catalyst. *Water Research*, 36(1):140–146, 2002.

[146] K. Tennakone, C. T. K. Tilakaratne, and I. R. M. Kottegoda. Photocatalytic degradation of organic contaminants in water with TiO_2 supported on polythene films. *Journal of Photochemistry and Photobiology A-Chemistry*, 87(2):177–179, 1995.

[147] J. Velasquez, S. Valencia, L. Rios, G. Restrepo, and J. Marin. Characterization and photocatalytic evaluation of polypropylene and polyethylene pellets coated with P25 TiO_2 using the controlled-temperature embedding method. *Chemical Engineering Journal*, 203:398–405, 2012.

[148] D. J. Ham, A. Phuruangrat, S. Thongtem, and J. S. Lee. Hydrothermal synthesis of monoclinic WO_3 nanoplates and nanorods used as an electrocatalyst for hydrogen evolution reactions from water. *Chemical Engineering Journal*, 165(1):365–369, 2010.

[149] J. Li, S. K. Cushing, J. Bright, F. Meng, T. R. Senty, P. Zheng, A. D. Bristow, and N. Wu. Ag@Cu_2O core-shell nanoparticles as visible-light plasmonic photocatalysts. *ACS Catalysis*, 3(1):47–51, 2012.

[150] E. F. Paulus and A. Gieren. *Structure Analysis by Diffraction*, pages 373–417. Wiley-VCH Verlag GmbH, 2008.

[151] G. Gauglitz. *Ultraviolet and Visible Spectroscopy*, pages 419–463. Wiley-VCH Verlag GmbH, 2008.

[152] M. Birkholz. *Line Profile Analysis*, pages 85–141. Wiley-VCH Verlag GmbH & Co. KGaA, 2006.

[153] S. Enzo, G. Fagherazzi, A. Benedetti, and S. Polizzi. A profile-fitting procedure for analysis of broadened X-ray diffraction peaks. *Journal of Applied Crystallography*, 21(5):536–542, 1988.

[154] B. E. Warren. *X-ray diffraction*. Addison-Wesley Pub. Co., Reading, Mass., 1969.

[155] J. I. Langford and A. J. C. Wilson. Scherrer after sixty years: A survey and some new results in the determination of crystallite size. *Journal of Applied Crystallography*, 11(2):102–113, 1978.

[156] C. G. Granqvist. *Tungsten Oxide Films: Ultraviolet Absorption and Semiconductor Bandgap*, pages 139–146. Elsevier Science B.V., Amsterdam, 1995.

[157] R. S. Vemuri, M. H. Engelhard, and C. V. Ramana. Correlation between surface chemistry, density, and band gap in nanocrystalline WO_3 thin films. *ACS Applied Materials & Interfaces*, 4(3):1371–1377, 2012.

[158] K. A. Michalow, D. Logvinovich, A. Weidenkaff, M. Amberg, G. Fortunato, A. Heel, T. Graule, and M. Rekas. Synthesis, characterization and electronic structure of nitrogen-doped TiO_2 nanopowder. *Catalysis Today*, 144(1-2):7–12, 2009.

[159] P. Apopei, C. Catrinescu, C. Teodosiu, and S. Royer. Mixed-phase TiO_2 photocatalysts: Crystalline phase isolation and reconstruction, characterization and photocatalytic activity in the oxidation of 4-chlorophenol from aqueous effluents. *Applied Catalysis B-Environmental*, 160:374–382, 2014.

[160] F. Jentoft. Diffuse reflectance IR and UV-vis spectroscopy, 2004.

[161] D. Nagy, D. Nagy, I. M. Szilágyi, and X. Fan. Effect of the morphology and phases of WO_3 nanocrystals on their photocatalytic efficiency. *RSC Advances*, 6(40):33743–33754, 2016.

[162] A. Aubry, D. Y. Lei, A. I. Fernandez-Domínguez, Y. Sonnefraud, S. A. Maier, and J. B. Pendry. Plasmonic light-harvesting devices over the whole visible spectrum. *Nano Letters*, 10(7):2574–2579, 2010.

[163] E. Hulicius and V. Kubecek. *Semiconductor lasers for medical applications*, pages 222–250. Woodhead Publishing, 2013.

[164] L. E. Brus. Electron–electron and electron-hole interactions in small semiconductor crystallites: The size dependence of the lowest excited electronic state. *The Journal of Chemical Physics*, 80(9):4403–4409, 1984.

[165] A. Govindaraj and C. N. R. Rao. *Nanotubes and Nanowires*, pages 208–284. Wiley-VCH Verlag GmbH & Co. KGaA, 2005.

[166] H. Dong, Z. Wu, F. Lu, Y. Gao, A. El-Shafei, B. Jiao, S. Ning, and X. Hou. Optics–electrics highways: Plasmonic silver nanowires@TiO_2 core–shell nanocomposites for enhanced dye-sensitized solar cells performance. *Nano Energy*, 10(0):181–191, 2014.

[167] J. Y. Luo, S. Z. Deng, Y. T. Tao, F. L. Zhao, L. F. Zhu, L. Gong, J. Chen, and N. S. Xu. Evidence of localized water molecules and their role in the gasochromic effect of WO_3 nanowire films. *The Journal of Physical Chemistry C*, 113(36):15877–15881, 2009.

[168] T.-D. Nguyen. From formation mechanisms to synthetic methods toward shape-controlled oxide nanoparticles. *Nanoscale*, 5(20):9455–9482, 2013.

[169] K. Byrappa and T. Adschiri. Hydrothermal technology for nanotechnology. *Progress in Crystal Growth and Characterization of Materials*, 53(2):117–166, 2007.

[170] L. Liu and Y. Yang. Shape-controlled synthesis of *MnCo* complex oxide nanostructures via a polyol-based precursor route and their catalytic properties. *Superlattices and Microstructures*, 54(0):26–38, 2013.

[171] F. Zheng, M. Zhang, and M. Guo. Controllable preparation of WO_3 nanorod arrays by hydrothermal method. *Thin Solid Films*, 534(0):45–53, 2013.

[172] V. B. Patil, P. V. Adhyapak, S. S. Suryavanshi, and I. S. Mulla. Oxalic acid induced hydrothermal synthesis of single crystalline tungsten oxide nanorods. *Journal of Alloys and Compounds*, 590(0):283–288, 2014.

[173] J. M. Wang, E. Khoo, P. S. Lee, and J. Ma. Controlled synthesis of WO_3 nanorods and their electrochromic properties in H_2SO_4 electrolyte. *The Journal of Physical Chemistry C*, 113(22):9655–9658, 2009.

[174] S. Adhikari and D. Sarkar. Hydrothermal synthesis and electrochromism of WO_3 nanocuboids. *RSC Advances*, 4(39):20145–20153, 2014.

[175] S. Bai, K. Zhang, R. Luo, D. Li, A. Chen, and C. C. Liu. Low-temperature hydrothermal synthesis of WO_3 nanorods and their sensing properties for NO_2. *Journal of Materials Chemistry*, 22(25):12643–12650, 2012.

[176] T. Peng, D. Ke, J. Xiao, L. Wang, J. Hu, and L. Zan. Hexagonal phase WO_3 nanorods: Hydrothermal preparation, formation mechanism and its photocatalytic O_2 production under visible-light irradiation. *Journal of Solid State Chemistry*, 194(0):250–256, 2012.

[177] A. Sonia, Y. Djaoued, B. Subramanian, R. Jacques, M. Eric, B. Ralf, and B. Achour. Synthesis and characterization of novel nanorod superstructures and twin octahedral morphologies of WO_3 by hydrothermal treatment. *Materials Chemistry and Physics*, 136(1):80–89, 2012.

[178] X. Wang, X. Meng, M. Zhong, F. Wu, and J. Li. Hydrothermal synthesis of $WO_3 \cdot 0.5H_2O$ microtubes with excellent photocatalytic properties. *Applied Surface Science*, 282(0):826–831, 2013.

[179] J. Zhang, X. L. Wang, X. H. Xia, C. D. Gu, and J. P. Tu. Electrochromic behavior of WO_3 nanotree films prepared by hydrothermal oxidation. *Solar Energy Materials and Solar Cells*, 95(8):2107–2112, 2011.

[180] E. E. Finney and R. G. Finke. Nanocluster nucleation and growth kinetic and mechanistic studies: A review emphasizing transition-metal nanoclusters. *Journal of Colloid and Interface Science*, 317(2):351–374, 2008.

[181] T. Sugimoto. Underlying mechanisms in size control of uniform nanoparticles. *Journal of Colloid and Interface Science*, 309(1):106–118, 2007.

[182] G. Salas, R. Costo, and M. d. P. Morales. *Synthesis of Inorganic Nanoparticles*, volume Volume 4, pages 35–79. Elsevier, 2012.

[183] J. Wang, E. Khoo, P. S. Lee, and J. Ma. Synthesis, assembly, and electrochromic properties of uniform crystalline WO_3 nanorods. *The Journal of Physical Chemistry C*, 112(37):14306–14312, 2008.

[184] Z. Q. Li, Y. J. Xiong, and Y. Xie. Selected-control synthesis of *ZnO* nanowires and nanorods via a *PEG*-assisted route. *Inorganic Chemistry*, 42(24):8105–8109, 2003.

[185] A. Wolcott, T. R. Kuykendall, W. Chen, S. Chen, and J. Z. Zhang. Synthesis and characterization of ultrathin WO_3 nanodisks utilizing long-chain poly(ethylene glycol). *The Journal of Physical Chemistry B*, 110(50):25288–25296, 2006.

[186] C. Balázsi, K. Sedlácková, J. Pfeifer, A. L. Tóth, E. O. Zayim, I. M. Szilágyi, L. Wang, K. Kalyanasundaram, and P.-I. Gouma. *Synthesis and Examination of Hexagonal Tungsten Oxide Nanocrystals for Electrochromic and Sensing Applications*, chapter 5, pages 77–91. NATO Science for Peace and Security Series C: Environmental Security. Springer Netherlands, 2009.

[187] I. M. Szilágyi, E. Santala, M. Heikkil a, M. Kemell, T. Nikitin, L. Khriachtchev, M. R as anen, M. Ritala, and M. Leskel a. Thermal study on electrospun polyvinylpyrrolidone/ammonium metatungstate nanofibers: optimising the annealing conditions for obtaining WO_3 nanofibers. *Journal of Thermal Analysis and Calorimetry*, 105(1):73–81, 2011.

[188] X. He, C. Hu, Q. Yi, X. Wang, H. Hua, and X. Li. Preparation and improved photocatalytic activity of $WO_3 \cdot 0.33H_2O$ nanonetworks. *Catalysis Letters*, 142(5):637–645, 2012.

[189] T. Peng, D. Ke, J. Xiao, L. Wang, J. Hu, and L. Zan. Hexagonal phase WO_3 nanorods: Hydrothermal preparation, formation mechanism and its photocatalytic O_2 production under visible-light irradiation. *Journal of Solid State Chemistry*, 194(0):250–256, 2012.

[190] J.-H. Ha, P. Muralidharan, and D. K. Kim. Hydrothermal synthesis and characterization of self-assembled h-WO_3 nanowires/nanorods using *EDTA* salts. *Journal of Alloys and Compounds*, 475(1–2):446–451, 2009.

[191] Z. Gu, H. Li, T. Zhai, W. Yang, Y. Xia, Y. Ma, and J. Yao. Large-scale synthesis of single-crystal hexagonal tungsten trioxide nanowires and electrochemical lithium intercalation into the nanocrystals. *Journal of Solid State Chemistry*, 180(1):98–105, 2007.

[192] P. Van Tong, N. D. Hoa, V. Van Quang, N. Van Duy, and N. Van Hieu. Diameter controlled synthesis of tungsten oxide nanorod bundles for highly sensitive NO_2 gas sensors. *Sensors and Actuators B: Chemical*, 183(0):372–380, 2013.

[193] Z. Gu, T. Zhai, B. Gao, X. Sheng, Y. Wang, H. Fu, Y. Ma, and J. Yao. Controllable assembly of WO_3 nanorods/nanowires into hierarchical nanostructures. *The Journal of Physical Chemistry B*, 110(47):23829–23836, 2006.

[194] S. Salmaoui, F. Sediri, N. Gharbi, C. Perruchot, S. Aeiyach, I. A. Rutkowska, P. J. Kulesza, and M. Jouini. Hexagonal nanorods of tungsten trioxide: Synthesis, structure, electrochemical properties and activity as supporting material in electrocatalysis. *Applied Surface Science*, 257(19):8223–8229, 2011.

[195] J. Y. Zheng, G. Song, Chang W. K., and Y. S. Kang. Fabrication of (001)-oriented monoclinic WO_3 films on *FTO* substrates. *Nanoscale*, 5(12):5279–5282, 2013.

[196] C. Y. Ng, K. A. Razak, A. A. Aziz, and Z. Lockman. The formation of WO_3 nanorods using the surfactant-assisted hydrothermal reaction. *Journal of Experimental Nanoscience*, 9(1):9–16, 2013.

[197] K. O. Iwu, A. Galeckas, P. Rauwel, A. Y. Kuznetsov, and T. Norby. One-dimensional WO_3 and its hydrate: One-step synthesis, structural and spectroscopic characterization. *Journal of Solid State Chemistry*, 185(0):245–252, 2012.

[198] K. Huang, Q. Zhang, F. Yang, and D. Y. He. Ultraviolet photoconductance of a single hexagonal WO_3 nanowire. *Nano Research*, 3(4):281–287, 2010.

[199] J. Yu, L. Qi, B. Cheng, and X. Zhao. Effect of calcination temperatures on microstructures and photocatalytic activity of tungsten trioxide hollow microspheres. *Journal of Hazardous Materials*, 160(2–3):621–628, 2008.

[200] M. Gillet, K. Aguir, C. Lemire, E. Gillet, and K. Schierbaum. The structure and electrical conductivity of vacuum-annealed WO_3 thin films. *Thin Solid Films*, 467(1-2):239–246, 2004.

[201] G. A. de Wijs, P. K. de Boer, R. A. de Groot, and G. Kresse. Anomalous behavior of the semiconducting gap in WO_3 from first-principles calculations. *Physical Review B*, 59(4):2684–2693, 1999. PRB.

[202] S. K. Deb. Opportunities and challenges in science and technology of WO_3 for electrochromic and related applications. *Solar Energy Materials and Solar Cells*, 92(2):245–258, 2008.

[203] J. Su, X. Feng, J. D. Sloppy, L. Guo, and C. A. Grimes. Vertically aligned WO_3 nanowire arrays grown directly on transparent conducting oxide coated glass: Synthesis and photoelectrochemical properties. *Nano Letters*, 11(1):203–208, 2010.

[204] S. K. Gullapalli, R. S. Vemuri, and C. V. Ramana. Structural transformation induced changes in the optical properties of nanocrystalline tungsten oxide thin films. *Applied Physics Letters*, 96(17), 2010.

[205] A. Gupta, P. Ifeacho, C. Schulz, and H. Wiggers. Synthesis of tailored WO_3 and WO_x ($2.9<x<3$) nanoparticles by adjusting the combustion conditions in a $H_2/O_2/Ar$ premixed flame reactor. *Proceedings of the Combustion Institute*, 33(2):1883–1890, 2011.

[206] I. M. Szilágyi, B. Fórizs, O. Rosseler, Á. Szegedi, P. Németh, P.and Király, G. Tárkányi, B. Vajna, K. Varga-Josepovits, K. László, A. L. Tóth, P. Baranyai, and M. Leskel a. WO_3 photocatalysts: Influence of structure and composition. *Journal of Catalysis*, 294(0):119–127, 2012.

[207] C. Y. Ng, K. Abdul Razak, and Z. Lockman. WO_3 nanorods prepared by low-temperature seeded growth hydrothermal reaction. *Journal of Alloys and Compounds*, 588(0):585–591, 2014.

[208] M. Kurumada, O. Kido, T. Sato, H. Suzuki, Y. Kimura, K. Kamitsuji, Y. Saito, and C. Kaito. Structure of WO_3 ultrafine particles and their characteristic solid states. *Journal of Crystal Growth*, 275(1–2):e1673–e1678, 2005.

[209] T. H. Fleisch and G. J. Mains. An XPS study of the UV reduction and photochromism of MoO_3 and WO_3. *The Journal of Chemical Physics*, 76(2):780–786, 1982.

[210] S. Zhang, H. Li, and Z. Yang. Controllable synthesis of WO_3 with different crystalline phases and its applications on methylene blue removal from aqueous solution. *Journal of Alloys and Compounds*, 722(Supplement C):555–563, 2017.

[211] M. Vasilopoulou, A. Soultati, D. G. Georgiadou, T. Stergiopoulos, L. C. Palilis, S. Kennou, N. A. Stathopoulos, D. Davazoglou, and P. Argitis. Hydrogenated understoichiometric tungsten oxide anode interlayers for efficient and stable organic photovoltaics. *Journal of Materials Chemistry A*, 2(6):1738–1749, 2014.

[212] D. F. Sun, J. G. Liu, J. P. Li, Z. H. Feng, L. He, B. Zhao, T. Y. Wang, R. X. Li, S. Yin, and T. Sato. Solvothermal synthesis of spindle-like WO_3/TiO_2 particles with enhanced photocatalytic activity. *Materials Research Bulletin*, 53:163–168, 2014.

[213] A. K. L. Sajjad, S. Shamaila, B. Z. Tian, F. Chen, and J. L. Zhang. One step activation of WO_x/TiO_2 nanocomposites with enhanced photocatalytic activity. *Applied Catalysis B-Environmental*, 91(1-2):397–405, 2009.

[214] M. Farhadian, P. Sangpour, and G. Hosseinzadeh. Preparation and photocatalytic activity of WO_3-MWCNT nanocomposite for degradation of naphthalene under visible light irradiation. *RSC Advances*, 6(45):39063–39073, 2016.

[215] F. G. Han, H. P. Li, L. Fu, J. Yang, and Z. Liu. Synthesis of S-doped WO_3 nanowires with enhanced photocatalytic performance towards dye degradation. *Chemical Physics Letters*, 651:183–187, 2016.

[216] A. P. Shpak, A. M. Korduban, M. M. Medvedskij, and V. O. Kandyba. XPS studies of active elements surface of gas sensors based on WO_3-x nanoparticles. *Journal of Electron Spectroscopy and Related Phenomena*, 156-158(Supplement C):172–175, 2007.

[217] L. Su, L. Zhang, J. Fang, M. Xu, and Z. Lu. Electrochromic and photoelectrochemical behavior of electrodeposited tungsten trioxide films. *Solar Energy Materials and Solar Cells*, 58(2):133–140, 1999.

[218] C. Yu, W. Zhou, J. C. Yu, H. Liu, and L. Wei. Design and fabrication of heterojunction photocatalysts for energy conversion and pollutant degradation. *Chinese Journal of Catalysis*, 35(10):1609–1618, 2014.

[219] J. Yu and L. Qi. Template-free fabrication of hierarchically flower-like tungsten trioxide assemblies with enhanced visible-light-driven photocatalytic activity. *Journal of Hazardous Materials*, 169(1–3):221–227, 2009.

[220] Z. H. Zhang, R. Dua, L. B. Zhang, H. B. Zhu, H. N. Zhang, and P. Wang. Carbon-layer-protected cuprous oxide nanowire arrays for efficient water reduction. *ACS Nano*, 7(2):1709–1717, 2013.

[221] H. Zhu and T. Lian. Wavefunction engineering in quantum confined semiconductor nanoheterostructures for efficient charge separation and solar energy conversion. *Energy & Environmental Science*, 5(11):9406–9418, 2012.

[222] J. Xiao, X. Zhang, and Y. Li. A ternary g-C_3N_4/Pt/ZnO photoanode for efficient photoelectrochemical water splitting. *International Journal of Hydrogen Energy*, 40(30):9080–9087, 2015.

[223] D. Chaudhary, N. Khare, and V. D. Vankar. Ag nanoparticles loaded TiO_2/MWCNT ternary nanocomposite: A visible-light-driven photocatalyst with enhanced photocatalytic performance and stability. *Ceramics International*, 42(14):15861–15867, 2016.

[224] P. Chen, T.-Y. Xiao, H.-H. Li, J.-J. Yang, Z. Wang, H.-B. Yao, and S.-H. Yu. Nitrogen-doped graphene/ZnSe nanocomposites: Hydrothermal synthesis and their enhanced electrochemical and photocatalytic activities. *ACS Nano*, 6(1):712–719, 2012.

[225] T.-D. Nguyen-Phan, V. H. Pham, J. S. Chung, M. Chhowalla, T. Asefa, W.-J. Kim, and E. W. Shin. Photocatalytic performance of Sn-doped TiO_2/reduced graphene oxide composite materials. *Applied Catalysis A: General*, 473:21–30, 2014.

[226] J. Kneer, M. Boxberg, and J. Wöllenstein. Optical properties of copper oxide thin films as selective sensing principle for hydrogen sulfide detection. volume 8763, pages 87630E–87630E–9, 2013.

[227] Y. Liu, F. Ren, S. H. Shen, Y. M. Fu, C. Chen, C. Liu, Z. Xing, D. Liu, X. H. Xiao, W. Wu, X. D. Zheng, Y. C. Liu, and C. Z. Jiang. Efficient enhancement of hydrogen production by ag/Cu_2O/ZnO tandem triple-junction photoelectrochemical cell. *Applied Physics Letters*, 106(12), 2015.

[228] S. M. Majhi, P. Rai, S. Raj, B.-S. Chon, K.-K. Park, and Y.-T. Yu. Effect of Au nanorods on potential barrier modulation in morphologically controlled Au@Cu_2O core–shell nanoreactors for gas sensor applications. *ACS Applied Materials & Interfaces*, 6(10):7491–7497, 2014.

[229] X. Liu, L. Cao, W. Sun, Z. Zhou, and J. Yang. A p/n type compounded Cu_2O/TiO_2 photo-catalytic membrane for organic pollutant degradation. *Research on Chemical Intermediates*, 42(7):6289–6300, 2016.

[230] L. Yang, M. Zhang, K. Zhu, J. Lv, G. He, and Z. Sun. Electrodeposition of flake-like Cu_2O on vertically aligned two-dimensional TiO_2 nanosheet array films for enhanced photoelectrochemical properties. *Applied Surface Science*, 391, Part B:353–359, 2017.

[231] X.-W. Liu, W.-W. Li, and H.-Q. Yu. Cathodic catalysts in bioelectrochemical systems for energy recovery from wastewater. *Chemical Society Reviews*, 43(22):7718–7745, 2014.

[232] X. Deng, C. Wang, E. Zhou, J. Huang, M. Shao, X. Wei, X. Liu, M. Ding, and X. Xu. One-step solvothermal method to prepare Ag/Cu_2O composite with enhanced photocatalytic properties. *Nanoscale Research Letters*, 11(1):29, 2016.

[233] S. Y. Yang, S. S. Zhang, H. J. Wang, H. Yu, Y. P. Fang, and F. Peng. Controlled preparation of Ag-Cu_2O nanocorncobs and their enhanced photocatalytic activity under visible light. *Materials Research Bulletin*, 70:296–302, 2015.

[234] H. Wang, N. Liu, J. Lu, S. Yao, S. Jiang, and W. Zhang. Template synthesis and characterization of Cu_2O/TiO_2 coaxial nanocable for photocatalysis. *Chemical Research in Chinese Universities*, 31(5):846–850, 2015.

[235] T. F. Jiang, T. F. Xie, L. P. Chen, Z. W. Fu, and D. J. Wang. Carrier concentration-dependent electron transfer in Cu_2O/ZnO nanorod arrays and their photocatalytic performance. *Nanoscale*, 5(7):2938–2944, 2013.

[236] Y. M. Liu, W. G. Zhang, W. Liang, H. X. Wang, and B. Yu. Structure and performance of Cu_2O/ag/TiO_2 three-layered nanocomposite films. *Rare Metal Materials and Engineering*, 44(7):1754–1757, 2015.

[237] L. Li, F. Jiang, J. Liu, H. Wan, Y. Wan, and S. Zheng. Enhanced photocatalytic reduction of aqueous Pb(II) over Ag loaded TiO_2 with formic acid as hole scavenger. *Journal of Environmental Science and Health, Part A*, 47(3):327–336, 2012.

[238] T. Liu, B. Li, Y. Hao, F. Han, L. Zhang, and L. Hu. A general method to diverse silver/mesoporous–metal–oxide nanocomposites with plasmon-enhanced photocatalytic activity. *Applied Catalysis B: Environmental*, 165(0):378–388, 2015.

[239] J. F. Wang, H. J. Li, Z. Y. Zhou, X. Y. Li, J. Liu, and H. Y. Yang. Tunable surface-plasmon-resonance wavelength of silver island films. *Chinese Physics B*, 19, 2010.

[240] V. Madhavi, P. Kondaiah, H. Shaik, and G. M. Rao. Phase dependent photocatalytic activity of Ag loaded TiO_2 films under sun light. *Applied Surface Science*, 364:732–739, 2016.

[241] C. H. B. Ng and W. Y. Fan. Shape evolution of Cu_2O nanostructures via kinetic and thermodynamic controlled growth. *Journal of Physical Chemistry B*, 110(42):20801–20807, 2006.

[242] C. H. Kuo, C. H. Chen, and M. H. Huang. Seed-mediated synthesis of monodispersed Cu_2O nanocubes with five different size ranges from 40 to 420 nm. *Advanced Functional Materials*, 17(18):3773–3780, 2007.

[243] O. Messaoudi, H. Makhlouf, A. Souissi, I. Ben Assaker, M. Karyaoui, A. Bardaoui, M. Oueslati, and R. Chtourou. Correlation between optical and structural properties of copper oxide electrodeposited on ITO glass. *Journal of Alloys and Compounds*, 611:142–148, 2014.

[244] J. N. Gao, Q. S. Li, H. B. Zhao, L. S. Li, C. L. Liu, Q. H. Gong, and L. M. Qi. One-pot synthesis of uniform Cu_2O and CuS hollow spheres and their optical limiting properties. *Chemistry of Materials*, 20(19):6263–6269, 2008.

[245] M. Perez-Gonzalez, S. A. Tomas, M. Morales-Luna, M. A. Arvizu, and M. M. Tellez-Cruz. Optical, structural, and morphological properties of photocatalytic TiO_2-ZnO thin films synthesized by the sol-gel process. *Thin Solid Films*, 594:304–309, 2015.

[246] J. Iqbal, T. Jan, S. Ul-Hassan, I. Ahmed, Q. Mansoor, M. U. Ali, F. Abbas, and M. Ismail. Facile synthesis of Zn doped CuO hierarchical nanostructures: Structural, optical and antibacterial properties. *Aip Advances*, 5(12), 2015.

[247] J. Wu, K. S. Hui, K. N. Hui, L. Li, H. H. Chun, and Y. R. Cho. Characterization of Sn-doped CuO thin films prepared by a sol-gel method. *Journal of Materials Science-Materials in Electronics*, 27(2):1719–1724, 2016.

[248] S. K. Sonar, R. V. Wagh, P. S. Niphadkar, P. N. Joshi, S. S. Deshpande, and S. V. Awate. Enhanced dual-effect of adsorption and photodegradation of SiO2 embedded TiO_2 hybrid catalyst for improved decolourization of methylene blue. *Water, Air, & Soil Pollution*, 224(9):1–12, 2013.

[249] K. V. Kumar and S. Sivanesan. Pseudo second order kinetic models for safranin onto rice husk: Comparison of linear and non-linear regression analysis. *Process Biochemistry*, 41(5):1198–1202, 2006.

[250] Y. S. Ho and G. McKay. The kinetics of sorption of divalent metal ions onto sphagnum moss peat. *Water Research*, 34(3):735–742, 2000.

[251] J. Shu, Z. Wang, Y. Huang, N. Huang, C. Ren, and W. Zhang. Adsorption removal of congo red from aqueous solution by polyhedral Cu_2O nanoparticles: Kinetics, isotherms, thermodynamics and mechanism analysis. *Journal of Alloys and Compounds*, 633:338–346, 2015.

[252] M. Kosmulski. Isoelectric points and points of zero charge of metal (hydr)oxides: 50 years after Parks' review. *Advances in Colloid and Interface Science*, 238:1–61, 2016.

[253] Z. Gao, J. Liu, F. Xu, D. Wu, Z. Wu, and K. Jiang. One-pot synthesis of graphene–cuprous oxide composite with enhanced photocatalytic activity. *Solid State Sciences*, 14(2):276–280, 2012.

[254] P. Kumar, M. Govindaraju, S. Senthamilselvi, and K. Premkumar. Photocatalytic degradation of methyl orange dye using silver (Ag) nanoparticles synthesized from ulva lactuca. *Colloids and Surfaces B: Biointerfaces*, 103(0):658–661, 2013.

[255] I. Sur, M. Altunbek, M. Kahraman, and M. Culha. The influence of the surface chemistry of silver nanoparticles on cell death. *Nanotechnology*, 23(37), 2012.

[256] H. Y. Jing, T. Wen, C. M. Fan, G. Q. Gao, S. L. Zhong, and A. W. Xu. Efficient adsorption/photodegradation of organic pollutants from aqueous systems using Cu_2O nanocrystals as a novel integrated photocatalytic adsorbent. *Journal of Materials Chemistry A*, 2(35):14563–14570, 2014.

[257] R. Liang, A. Hu, W. Li, and Y. N. Zhou. Enhanced degradation of persistent pharmaceuticals found in wastewater treatment effluents using TiO_2 nanobelt photocatalysts. *Journal of Nanoparticle Research*, 15(10):1–13, 2013.

[258] F. Zhang, J. Lan, Y. Yang, T. Wei, R. Tan, and W. Song. Adsorption behavior and mechanism of methyl blue on zinc oxide nanoparticles. *Journal of Nanoparticle Research*, 15(11):1–10, 2013.

[259] J. Huang, Y. Cao, Z. Liu, Z. Deng, and W. Wang. Application of titanate nanoflowers for dye removal: A comparative study with titanate nanotubes and nanowires. *Chemical Engineering Journal*, 191:38–44, 2012.

[260] Y.-S. Ho. Review of second-order models for adsorption systems. *Journal of Hazardous Materials*, 136(3):681–689, 2006.

[261] Y. Li, Q. Du, T. Liu, J. Sun, Y. Jiao, Y. Xia, L. Xia, Z. Wang, W. Zhang, K. Wang, H. Zhu, and D. Wu. Equilibrium, kinetic and thermodynamic studies on the adsorption of phenol onto graphene. *Materials Research Bulletin*, 47(8):1898–1904, 2012.

[262] V. Fierro, V. Torné-Fernández, D. Montané, and A. Celzard. Adsorption of phenol onto activated carbons having different textural and surface properties. *Microporous and Mesoporous Materials*, 111(1–3):276–284, 2008.

[263] G. McKay, M. S. Otterburn, and J. A. Aga. Intraparticle diffusion process occurring during adsorption of dyestuffs. *Water, Air, and Soil Pollution*, 36(3):381–390, 1987.

[264] I. U. Gaya. *Kinetic Concepts of Heterogeneous Photocatalysis*, pages 43–71. Springer Netherlands, Dordrecht, 2014.

[265] D. Y. Murzin and T. Salmi. *Chapter 11 - Kinetic Modeling*, pages 665–721. Elsevier, Amsterdam, 2016.

[266] J. Varghese and K. T. Varghese. Graphene/CuS/ZnO hybrid nanocomposites for high performance photocatalytic applications. *Materials Chemistry and Physics*, 167:258–264, 2015.

[267] M. Shirzad-Siboni, A Jonidi-Jafari, M Farzadkia, A Esrafili, and M Gholami. Enhancement of photocatalytic activity of Cu-doped ZnO nanorods for the degradation of an insecticide: Kinetics and reaction pathways. *Journal of Environmental Management*, 186:1–11, 2017.

[268] A. E. Regazzoni, P. Mandelbaum, M. Matsuyoshi, S. Schiller, S. A. Bilmes, and M. A. Blesa. Adsorption and photooxidation of salicylic acid on titanium dioxide: A surface complexation description. *Langmuir*, 14(4):868–874, 1998.

[269] Y. Li, H. Li, N. Zhong, G. X. Quan, and Y. Q. Lan. Catalytic roles of Mn(II) and Fe(III) in the reduction of Cr(VI) by mandelic acid under an irradiation of simulated solar light. *Water Environment Research*, 87(5):450–460, 2015.

[270] L. Li, W. Zhu, P. Zhang, Z. Chen, and W. Han. Photocatalytic oxidation and ozonation of catechol over carbon-black-modified nano-TiO_2 thin films supported on Al sheet. *Water research*, 37(15):3646–3651, 2003.

[271] E. Benavente, F. Duran, C. Sotomayor-Torres, and G. Gonzalez. Heterostructured layered hybrid ZnO/MoS_2 nanosheets with enhanced visible light photocatalytic activity. *Journal of Physics and Chemistry of Solids*, 113:119–124, 2018.

[272] L. Yan, Y. Cheng, S. Yuan, X. Yan, X. Hu, and K. Oh. Photocatalytic degradation kinetics of methyl orange in TiO_2–SiO_2–$NiFe_2O_4$ aqueous suspensions. *Research on Chemical Intermediates*, 39(4):1673–1684, 2013.

[273] S. Saha, J. M. Wang, and A. Pal. Nano silver impregnation on commercial TiO_2 and a comparative photocatalytic account to degrade malachite green. *Separation and Purification Technology*, 89:147–159, 2012.

[274] A. K. L. Sajjad, S. Shamaila, B. Z. Tian, F. Chen, and J. L. Zhang. Comparative studies of operational parameters of degradation of azo dyes in visible light by highly efficient WO_x/TiO_2 photocatalyst. *Journal of Hazardous Materials*, 177(1-3):781–791, 2010.

[275] Z.-D. Li, H.-L. Wang, X.-N. Wei, X.-Y. Liu, Y.-F. Yang, and W.-F. Jiang. Preparation and photocatalytic performance of magnetic Fe_3O_4@TiO_2 core-shell microspheres supported by silica aerogels from industrial fly ash. *Journal of Alloys and Compounds*, 659:240–247, 2016.

[276] S. J. A. Moniz, S. A. Shevlin, X. An, Z.-X. Guo, and J. Tang. Fe_2O_3–TiO_2 nanocomposites for enhanced charge separation and photocatalytic activity. *Chemistry – A European Journal*, 20(47):15571–15579, 2014.

[277] Z. J. Zhang, W. Z. Wang, M. Shang, and W. Z. Yin. Photocatalytic degradation of rhodamine B and phenol by solution combustion synthesized $BiVO_4$ photocatalyst. *Catalysis Communications*, 11(11):982–986, 2010.

[278] Q. Huang, F. Kang, H. Liu, Q. Li, and X. D. Xiao. Highly aligned $Cu_2O/CuO/TiO_2$ core/shell nanowire arrays as photocathodes for water photoelectrolysis. *Journal of Materials Chemistry A*, 1(7):2418–2425, 2013.

[279] S. F. Chen, S. J. Zhang, W. Liu, and W. Zhao. Study on the photocatalytic activity of p-n junction photocatalyst Cu_2O/TiO_2. *Journal of Nanoscience and Nanotechnology*, 9(7):4397–4403, 2009.

[280] United Nations Department of Economic and Social Affairs. International decade for action 'Water for life' 2005-2015, 2014.

[281] X. F. Yang, Z. P. Chen, J. S. Xu, H. Tang, K. M. Chen, and Y. Jiang. Tuning the morphology of g-C_3N_4 for improvement of Z-Scheme photocatalytic water oxidation. *ACS Applied Materials & Interfaces*, 7(28):15285–15293, 2015.

[282] A. S. Ganeshraja, K. Rajkumar, K. Zhu, X. Li, S. Thirumurugan, W. Xu, J. Zhang, M. Yang, K. Anbalagan, and J. Wang. Facile synthesis of iron oxide coupled and doped titania nanocomposites: tuning of physicochemical and photocatalytic properties. *RSC Advances*, 6(76):72791–72802, 2016.

[283] M. Matsuoka, T. Toyao, Y. Horiuchi, M. Takeuchi, and M. Anpo. *Wastewater Treatment Using Highly Functional Immobilized TiO_2 Thin-Film Photocatalysts*, pages 179–197. Wiley-VCH Verlag GmbH & Co. KGaA, 2013.

[284] A. Paracchino, N. Mathews, T. Hisatomi, M. Stefik, S. D. Tilley, and M. Gratzel. Ultrathin films on copper(I) oxide water splitting photocathodes: a study on performance and stability. *Energy & Environmental Science*, 5(9):8673–8681, 2012.

[285] W. Siripala, A. Ivanovskaya, T. F. Jaramillo, S. H. Baeck, and E. W. McFarland. A Cu_2O/TiO_2 heterojunction thin film cathode for photoelectrocatalysis. *Solar Energy Materials and Solar Cells*, 77(3):229–237, 2003.

[286] S. Zhang, C. Liu, X. Liu, H. Zhang, P. Liu, S. Zhang, F. Peng, and H. Zhao. Nanocrystal Cu_2O-loaded TiO_2 nanotube array films as high-performance visible-light bactericidal photocatalyst. *Applied Microbiology and Biotechnology*, 96(5):1201–1207, 2012.

[287] H. Yin, X. Wang, L. Wang, Q. Nie, Y. Zhang, and W. Wu. Cu_2O/TiO_2 heterostructured hollow sphere with enhanced visible light photocatalytic activity. *Materials Research Bulletin*, 72:176–183, 2015.

[288] J. Zhang, W. Liu, X. Wang, X. Wang, B. Hu, and H. Liu. Enhanced decoloration activity by $Cu_2O@TiO_2$ nanobelts heterostructures via a strong adsorption-weak photodegradation process. *Applied Surface Science*, 282(0):84–91, 2013.

[289] S. Issarapanacheewin, K. Wetchakun, S. Phanichphant, W. Kangwansupamonkon, and N. Wetchakun. Efficient photocatalytic degradation of Rhodamine B by a novel CeO_2/Bi_2WO_6 composite film. *Catalysis Today*, 278, Part 2:280–290, 2016.

[290] A. X. Wei, W. Zhao, J. Liu, Z. X. Ge, and C. B. Liu. Dye-sensitized solar cells based on the composites photoanodes of ZnO microrods/TiO_2 nanoparticles. *Integrated Ferroelectrics*, 127:157–163, 2011.

[291] C. S. Chou, R. Y. Yang, M. H. Weng, and C. H. Yeh. Study of the applicability of TiO_2/dye composite particles for a dye-sensitized solar cell. *Advanced Powder Technology*, 19(6):541–558, 2008.

[292] Y.-H. Choi, D.-H. Kim, H. S. Han, S. Shin, S-H Hong, and K. S. Hong. Direct printing synthesis of self-organized copper oxide hollow spheres on a substrate using copper(II) complex ink: Gas sensing and photoelectrochemical properties. *Langmuir*, 30(3):700–709, 2014.

[293] V. Prakash, R. K. Diwan, and U. K. Niyogi. Characterization of synthesized copper oxide nanopowders and their use in nanofluids for enhancement of thermal conductivity. *Indian Journal of Pure & Applied Physics*, 53(11):753–758, 2015.

[294] W. C. Huang, L. M. Lyu, Y. C. Yang, and M. H. Huang. Synthesis of Cu_2O nanocrystals from cubic to rhombic dodecahedral structures and their comparative photocatalytic activity. *Journal of the American Chemical Society*, 134(2):1261–1267, 2012.

[295] V. Uvarov and I. Popov. Metrological characterization of X-ray diffraction methods for determination of crystallite size in nano-scale materials. *Materials Characterization*, 58(10):883–891, 2007.

[296] Z. H. Zhang and P. Wang. Highly stable copper oxide composite as an effective photocathode for water splitting via a facile electrochemical synthesis strategy. *Journal of Materials Chemistry*, 22(6):2456–2464, 2012.

[297] H. X. Chen, T. Tu, M. Wen, and Q. S. Wu. Assembly synthesis of Cu_2O-on-Cu nanowires with visible-light-enhanced photocatalytic activity. *Dalton Transactions*, 44(35):15645–15652, 2015.

[298] Q. Wang, Y. L. Jia, M. P. Wang, W. H. Qi, Y. Pang, X. M. Cui, W. H. Ji, and J. Yi. Synthesis of Cu_2O nanotubes with efficient photocatalytic activity by electrochemical corrosion method. *Journal of Physical Chemistry C*, 119(38):22066–22071, 2015.

[299] X. Xu, Z. H. Gao, Z. D. Cui, Y. Q. Liang, Z. Y. Li, S. L. Zhu, X. J. Yang, and J. M. Ma. Synthesis of Cu_2O octadecahedron/TiO_2 quantum dot heterojunctions with high visible light photocatalytic activity and high stability. *Acs Applied Materials & Interfaces*, 8(1):91–101, 2016.

[300] S. Y. Zhu, S. J. Liang, Y. C. Tong, X. H. An, J. L. Long, X. Z. Fu, and X. X. Wang. Photocatalytic reduction of CO_2 with H_2O to CH_4 on Cu(I) supported TiO_2 nanosheets with defective 001 facets. *Physical Chemistry Chemical Physics*, 17(15):9761–9770, 2015.

[301] M. A. Bhosale and B. M. Bhanage. A simple approach for sonochemical synthesis of Cu_2O nanoparticles with high catalytic properties. *Advanced Powder Technology*, 27(1):238–244, 2016.

[302] H. Dongliang, H. Jiahai, Q. Long, P. Jiangrui, and S. Zhenji. Optical and photocatalytic properties of Cu-Cu_2O/TiO_2 two-layer nanocomposite films on Si substrates. *Rare Metal Materials and Engineering*, 44(8):1888–1893, 2015.

[303] S. Sohrabnezhad and A. Valipour. Synthesis of Cu/CuO nanoparticles in mesoporous material by solid state reaction. *Spectrochimica Acta Part A: Molecular and Biomolecular Spectroscopy*, 114:298–302, 2013.

[304] C. Cao, L. Xiao, L. Liu, H. Zhu, C. Chen, and L. Gao. Visible-light photocatalytic decolorization of reactive brilliant red x-3b on Cu_2O/crosslinked-chitosan nanocomposites prepared via one step process. *Applied Surface Science*, 271(0):105–112, 2013.

[305] A. Abulizi, G.-H. Yang, and J.-J. Zhu. One-step simple sonochemical fabrication and photocatalytic properties of Cu_2O-rGO composites. *Ultrasonics Sonochemistry*, 21(1):129–135, 2014.

[306] G. Dong, B. Du, L. Liu, W. Zhang, Y. Liang, H. Shi, and W. Wang. Synthesis and their enhanced photoelectrochemical performance of ZnO nanoparticle-loaded CuO dandelion heterostructures under solar light. *Applied Surface Science*, 399:86–94, 2017.

[307] J. Y. Zheng, G. Song, C. Woo Kim, and Y. S. Kang. Facile preparation of p-CuO and p-CuO/n-$CuWO_4$ junction thin films and their photoelectrochemical properties. *Electrochimica Acta*, 69:340–344, 2012.

[308] M. Ichimura and Y. Kato. Fabrication of TiO_2/Cu_2O heterojunction solar cells by electrophoretic deposition and electrodeposition. *Materials Science in Semiconductor Processing*, 16(6):1538–1541, 2013.

[309] G. Li, N. M. Dimitrijevic, L. Chen, T. Rajh, and K. A. Gray. Role of surface/interfacial Cu^{2+} sites in the photocatalytic activity of coupled CuO-TiO_2 nanocomposites. *Journal of Physical Chemistry C*, 112(48):19040–19044, 2008.

[310] S. J. A. Moniz and J. W. Tang. Charge transfer and photocatalytic activity in CuO-TiO_2 nanoparticle heterojunctions synthesised through a rapid, one-pot, microwave solvothermal route. *Chemcatchem*, 7(11):1659–1667, 2015.

[311] A. L. Luna, M. A. Valenzuela, C. Colbeau-Justin, P. Vazquez, J. L. Rodriguez, J. R. Avendano, S. Alfaro, S. Tirado, A. Garduno, and J. M. De la Rosa. Photocatalytic degradation of gallic acid over CuO-TiO_2 composites under UV/Vis LEDs irradiation. *Applied Catalysis A-General*, 521:140–148, 2016.

[312] C.-M. Wang and C.-Y. Wang. Photocorrosion of plasmonic enhanced Cu_xO photocatalyst. *Journal of Nanophotonics*, 8(1):084095–084095, 2014.